Photocatalytic methane conversion into chemicals and fuels under mild conditions

Di Hu

To cite this version:

Di Hu. Photocatalytic methane conversion into chemicals and fuels under mild conditions. Catalysis. Université de Lille, 2022. English. NNT : 2022ULILR034 . tel-04379284

HAL Id: tel-04379284
https://theses.hal.science/tel-04379284

Submitted on 8 Jan 2024

THÈSE DE DOCTORAT

Université de Lille

Photocatalytic Methane Conversion into Chemicals and Fuels Under Mild Conditions

Di HU

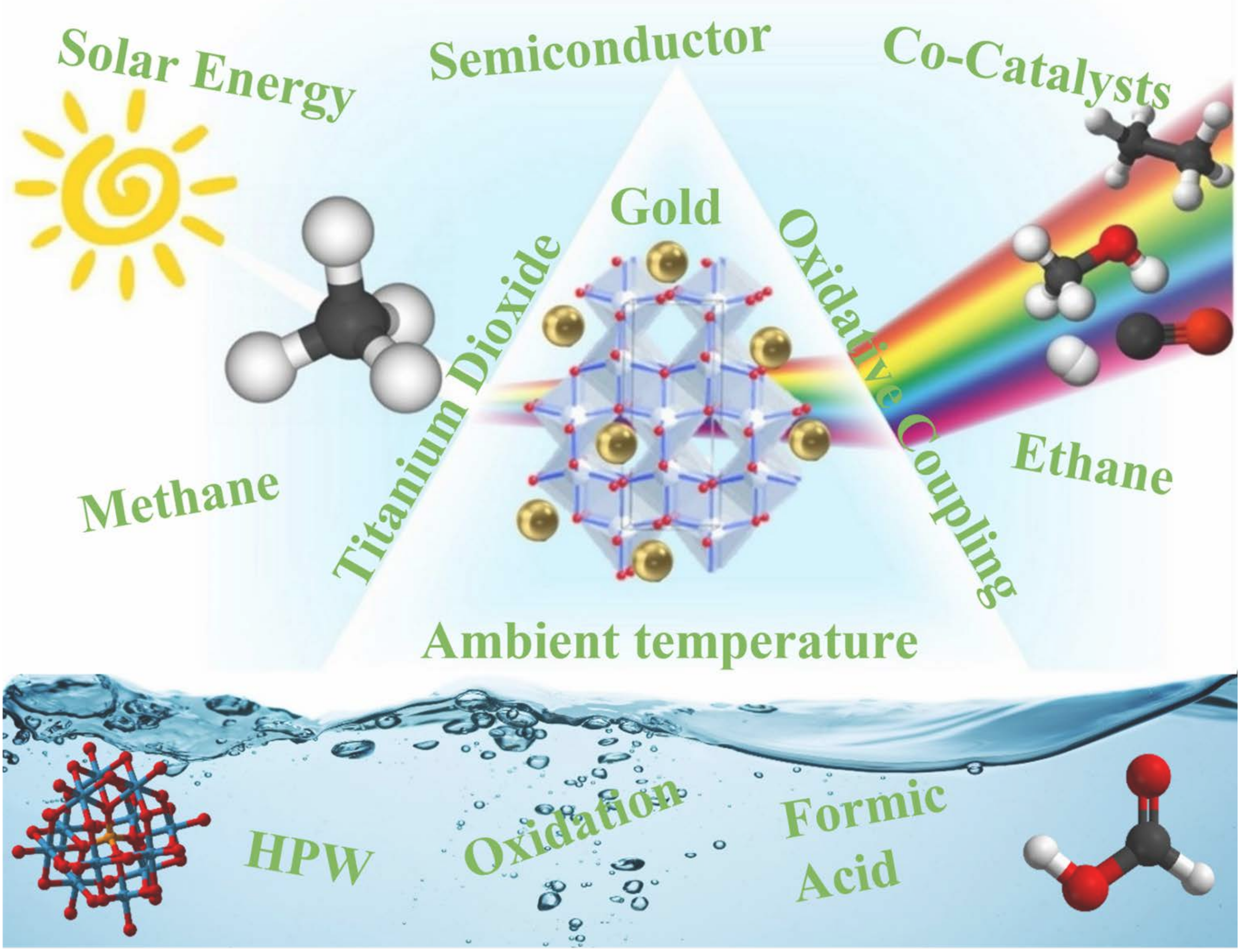

THÈSE DE DOCTORAT

Di HU

POUR L'OBTENTION DU TITRE DE

DOCTEUR DE L'UNIVERSITÈ DE LILLE

Ecole Doctorale : Science de la Matière, du Rayonnement et de L'Environnement

- Spécialité : Chimie théorique, physique, analytique

Conversion photocatalytique du méthane en produits chimiques et en carburants dans des conditions douces

Soutenue le 7th Octobre 2022

Rapporteurs	DR. Nicolas Keller, Université de Strasbourg (France)
	Pr. Nathalie Job, Université de Liège (Belgique)
Examinateurs	Pr. Marc Robert, Université de Paris (France)
	Dr HDR. Bruno Grandidier, Université de Lille (France)
	Dr HDR. Vitaly Ordomsky, Université de Lille (France)
	Dr. Dorota Rutkowska-Zbik, Jerzy Haber Institute of Catalysis and Surface Chemistry, Polish Academy of Science (Pologne)
Président du jury	DR. Hynd Remita, Université Paris-Saclay (France)
Invité	Pr. Pedro Camargo, Université de Helsinki (Finland)
Directeur	DR. Andrei Khodakov, Université de Lille (France)

Content

Abstract

Methane is one of the most abundant molecules on Earth. Most of the state-of-the-art methane chemical conversion technologies require high temperatures, they are accompanied by insufficient selectivity, carbon deposition and major production of carbon dioxide. Development of the methane conversion technologies at mild conditions is important for the rational utilization of renewable and fossil feedstocks and for the environment. Photocatalysis, converting solar energy into chemical energy, is a promising alternative for direct methane conversion at ambient temperature in the future.

Direct oxidation of methane into value-added fuels and chemicals remains a major challenge in modern science, due to the inertness of methane and insufficient selectivity of methane chemical conversion. A comparative analysis of low temperature methane photocatalytic conversion routes has been performed, such as methane oxidation, methane reforming and methane coupling. Methane photocatalytic oxidation currently exhibits the highest conversion rate, while methane coupling shows the highest selectivity. The most promising routes could be methane oxidation to methanol and methane coupling to ethane with higher value, which simultaneously exhibits higher productivity and selectivity.

Silver salt of phosphotungstic aicd (AgPW) mechanically mixed with titania has been prepared for photochemical methane coupling. Introducing even small amount of AgPW to TiO_2 significantly enhanced the coupling rate. The chemical looping process achieved ethane production of 64 μmol/g with coupling selectivity above 95%. The in-situ XAS revealed the gradual reduction of cationic Ag^+ species to metallic Ag at room temperature in the presence of methane, which resulted in methane coupling slowing down, while their subsequent re-oxidation to silver cations in the presence of air can regenerate methane coupling activity. The silver reduction-oxidation cycles in methane and air under irradiation can be repeated several times.

Gold nanoparticles with a size from 6 to 29 nm supported on titania have been prepared for photocatalytic non-oxidative and oxidative methane coupling in both batch and continuous gas flow reactors. The photocatalytic performance is not affected by the nanoparticles size. The methane conversion requires band gap transition in TiO_2 excited by UV irradiation. No methane conversion was observed after activation of plasmonic gold nanoparticles by visible light. The plasmonic effect of gold nanoparticles cannot alone drive the methane photocatalytic conversion. The methane activation and oxidation occur over titania oxygen vacancies, while oxygen is likely activated by gold nanoparticles. The methane conversion was facilitated by slower electron-hole recombination in the presence of gold nanoparticles. A hydrocarbon productivity of 1864 μmol g^{-1} h^{-1} with a coupling selectivity higher than 86% was achieved in the continuous oxidative methane coupling flow process.

A cascade one-pot photo-chemocatalytic process for methane oxidation to formic acid has been proposed. A specifically designed photocatalyst and a commercial heterogeneous catalyst were used together in the cascade process. The methane selective conversion into formic acid proceeds first over caesium salt of phosphotungstic acid (CsPW) supported on titania, which photocatalytically oxidizes methane under irradiation into a mixture of C_1 liquid oxygenates. The C_1 liquid oxygenates produced by photocatalysis are then selectively converted into formic acid over the heterogeneous alumina supported ruthenium catalyst. All reactions of selective oxidation of methane to formic acid occur in the cascade process at room temperature in the same reactor. The cascade process produced formic acid with a productivity of 5000 $\mu mol_{\text{formic acid}}\ g^{-1}_{\text{photocatalyst}}$ and a selectivity of 85 %, as well as a concentration of up to 1.1 mmol L^{-1}. Methane photocatalytic oxidation results in a mixture of C_1 oxygenates in water using O_2 as an oxidant, which then are selectively oxidized to formic acid.

Keywords: methane activation; photocatalysis; mild conditions; methane coupling;

ethane; methane oxidation; formic acid.

Résumé

Le méthane est l'une des molécules les plus abondantes sur Terre. La plupart des technologies de pointe de conversion chimique du méthane nécessitent des températures élevées, elles s'accompagnent d'une sélectivité insuffisante, d'un dépôt de carbone et d'une production importante de dioxyde de carbone. Le développement des technologies de conversion du méthane dans des conditions douces est important pour l'utilisation rationnelle des matières premières renouvelables et fossiles et pour l'environnement. La photocatalyse, qui convertit l'énergie solaire en énergie chimique, est une alternative prometteuse pour la conversion directe du méthane à température ambiante dans le futur.

L'oxydation directe du méthane en carburants et produits chimiques à valeur ajoutée reste un défi majeur de la science moderne, en raison de l'inertie du méthane et de la sélectivité insuffisante de la conversion chimique du méthane. Une analyse comparative des voies de conversion photocatalytique du méthane à basse température a été réalisée, telles que l'oxydation du méthane, le reformage du méthane et le couplage du méthane. L'oxydation photocatalytique du méthane présente actuellement le taux de conversion le plus élevé, tandis que le couplage du méthane présente la plus grande sélectivité. Les voies les plus prometteuses pourraient être l'oxydation du méthane en méthanol et le couplage du méthane en éthane de valeur supérieure, qui présente simultanément une productivité et une sélectivité plus élevées.

Le sel d'argent de l'aicd phosphotungstique (AgPW) mélangé mécaniquement avec l'oxyde de titane a été préparé pour le couplage photochimique du méthane. L'introduction d'une quantité même faible d'AgPW dans le TiO_2 a permis d'augmenter significativement le taux de couplage. Le processus de bouclage chimique a atteint une production d'éthane de 64 μmol/g avec une sélectivité de couplage supérieure à 95 %. La XAS in situ a révélé la réduction progressive des espèces Ag^+ cationiques en Ag métallique à température ambiante en présence de méthane, ce qui a entraîné un ralentissement du couplage du méthane, tandis que leur réoxydation ultérieure en cations d'argent en présence d'air peut régénérer l'activité de couplage du méthane. Les cycles de réduction-oxydation de l'argent dans le méthane et l'air sous irradiation peuvent être répétés plusieurs fois.

Des nanoparticules d'or d'une taille de 6 à 29 nm supportées sur de l'oxyde de titane ont été préparées pour le couplage photocatalytique non oxydant et oxydant du méthane dans des réacteurs à flux gazeux discontinus et continus. La performance photocatalytique n'est pas affectée par la taille des nanoparticules. La conversion du méthane nécessite une transition de bande interdite dans le TiO_2 excité par une irradiation UV. Aucune conversion du méthane n'a été observée après l'activation des nanoparticules d'or plasmoniques par la lumière visible. L'effet plasmonique des nanoparticules d'or ne peut pas à lui seul conduire la conversion photocatalytique du méthane. L'activation et l'oxydation du méthane se produisent sur les lacunes en oxygène de l'oxyde de titane, tandis que l'oxygène est probablement activé par les nanoparticules d'or. La conversion du méthane a été facilitée par une recombinaison électron-trou plus lente en présence de nanoparticules d'or. Une productivité d'hydrocarbures de 1864 μmol g^{-1} h^{-1} avec une sélectivité de couplage supérieure à 86 % a été atteinte dans le procédé de couplage oxydatif continu du méthane en flux.

Un processus photo-chemo-catalytique en cascade à un pot pour l'oxydation du méthane en acide formique a été proposé. Un photocatalyseur spécialement conçu et un catalyseur hétérogène commercial ont été utilisés ensemble dans le processus en cascade. La conversion sélective du méthane en acide formique s'effectue d'abord sur le sel de césium de l'acide phosphotungstique (CsPW) supporté par l'oxyde de titane, qui oxyde le méthane par photocatalyse sous irradiation en un mélange de composés oxygénés liquides C_1. Les composés oxygénés liquides C_1 produits par photocatalyse sont ensuite convertis sélectivement en acide formique sur le catalyseur hétérogène au ruthénium supporté par de l'alumine. Toutes les réactions d'oxydation sélective du méthane en acide formique ont lieu dans le processus en cascade à température ambiante dans le même réacteur. Le processus en cascade a produit de l'acide formique avec une productivité de 5000 $\mu mol_{\text{acide formique}}$ $g^{-1}_{\text{photocatalyseur}}$ et une sélectivité de 85 %, ainsi qu'une concentration allant jusqu'à 1.1 mmol L^{-1}.

Mots clés: activation du méthane; photocatalyse; conditions douces; couplage du méthane; éthane; oxydation du méthane; acide formique.

Chapter 1. General Introduction

1.1 Introduction

1.1.1 Vast and diverse methane feedstocks

Methane comes from renewable and fossil resources: biogas, natural gas, coal gas, shale gas and clathrates in the ocean floors. In recent years, abundant feedstocks of unconventional shale gas, coalbed gas and tight gas have doubly overwhelmed the proven conventional natural gas reserves [1]. Methane is an important source of energy. It is used as a fuel for electricity generation, industry, heating and transport. Methane combustion corresponds to 20-25% of the global emission of carbon dioxide. Significant amounts of methane are nowadays burned out at the oil production sites. Methane “flaring” consumes 3.5 % of the global natural gas production. Methane is itself a greenhouse gas (GHG) with an effect 30 times higher than carbon dioxide. In terms of warming potential, methane global emissions to the atmosphere since 2000, correspond to putting 350 million more cars on the world’s roads. Methane is also involved in the ground-level formation of ozone, which is an air pollutant and bad for human health. Elaboration of new sustainable technologies of methane chemical conversion can, therefore, solve both the problems of rational utilization of fossil and renewable resources and address the global warming and environmental concerns.

1.1.2 State of the art methane conversion

The state-of-the-art chemical conversion (**Figure 1**) can be divided into direct and indirect routes [2–4]. In the indirect methane conversion, methane is first transformed to syngas (a mixture of carbon monoxide and hydrogen) and then syngas is used in numerous processes such as methanol synthesis, Fischer-Tropsch reaction, hydroformylation, hydrogen production etc. The indirect conversion of methane to fuels and chemicals via intermediate formation of syngas currently corresponds to large industrial units. The conventional methane indirect conversion technologies include steam reforming of methane (SRM), partial oxidation of methane (POM), autothermal reforming (ATR) and dry reforming of methane (DRM).

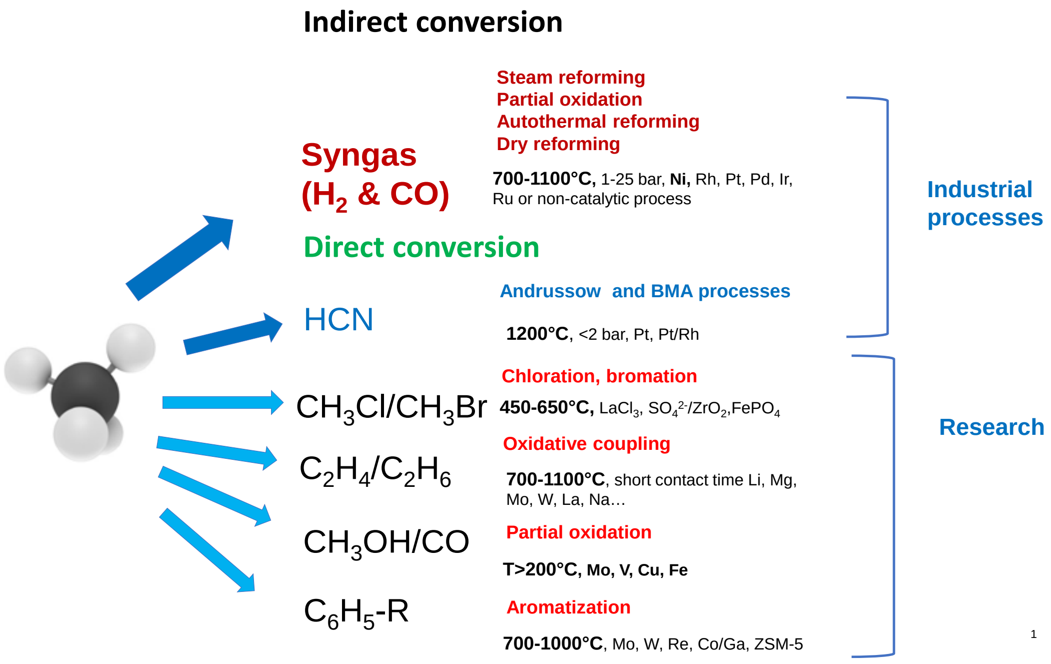

Figure 1. The state of the art direct and indirect methane chemical conversion. All the processes require high temperatures

SRM (Eq. 1) is an endothermic reaction, which has been effectively performed at high temperatures (above 800 °C) and pressures between 2 and 3.5 MPa:

$$CH_4 + H_2O\ (g) \rightarrow CO + 3H_2,\ \Delta H^0_{298K} = 205.9\ kJ\cdot mol^{-1} \qquad (1)$$

The process yields syngas with the H_2/CO ratio of about 3, which is too high for either Fischer-Tropsch or methanol synthesis. SRM in combination with the water gas shift reaction (WGS, $H_2O+CO \rightarrow H_2+CO_2$) is also employed for industrial hydrogen production. Currently, 95% of the world's hydrogen is produced by SRM. The process is generally carried out in large multi-tubular fixed-bed reactors with supported nickel catalysts.

In POM, methane is oxidized to syngas with a sub-stoichiometric amount of oxygen either with or without catalyst:

$$CH_4 + 1/2O_2 \rightarrow CO + 2H_2,\ \Delta H^{0}_{298K} = -36\ kJ\ mol^{-1} \qquad (2)$$

Non-catalytic POM typically requires harsh conditions and high temperature (T>1200°C) and is often accompanied by undesired methane combustion, while catalytic POM operates efficiently in the range of 750-950 °C and pressure of 2.5-3.5 MPa. The exothermicity of POM may lead to the formation of hot spots inside the reactor. The use of oxygen for POM presents nonnegligible risks of explosion and catalyst oxidation. The ATR process, which represents a combination of SRM and POM, is performed at temperatures above 850 °C and pressure of 0.1-8 MPa.

In addition to the industrial syngas production processes, DRM (Eq. 3) is considered as a potential alternative to simultaneously convert two greenhouse gases (methane and carbon dioxide) into syngas with the H_2/CO ratio of about 1. DRM is generally carried out at ambient pressure and temperature higher than 800 °C.

$$CH_4+CO_2 \rightarrow 2\ H_2 + 2\ CO,\ \Delta H^{0}_{298K} = 247 kJ/mol \qquad (3)$$

Huge energy requirement, coke deposition and catalyst sintering are three main thorny problems of DRM.

The direct methane conversion [2] includes (**Figure 1**) non-oxidative (NOCM) and oxidative coupling of methane (OCM), partial oxidation of methane (POM) to oxygenates, methane aromatization, oxidative Andrussow and non-oxidative BMA (or Degussa) processes. Among direct methane conversion routes, only the Andrussow (Eq. 4) and BMA (Eq. 5) processes, which produce hydrogen cyanide, have been commercialized[5]:

$$CH_4 + NH_3 + 3/2O_2 \rightarrow 3H_2O + HCN,\ \Delta H^{0}_{298K} = -483\ kJ{\cdot}mol^{-1} \qquad (4)$$

$$CH_4 + NH_3 \rightarrow 3H_2 + HCN,\ \Delta H^{0}_{298K} = 251\ kJ{\cdot}mol^{-1} \qquad (5)$$

Thermodynamic limitations hinder direct nonoxidative methane coupling to the C_2 hydrocarbons. The coupling reaction requires extremely high temperatures, generates aromatics as byproducts and is accompanied by rapid carbon deposition. The exothermic oxidative coupling of methane (OCM, Eq. 6) with oxidants (such as oxygen, water and N_2O) can be performed at 750-950 °C:

$$2CH_4 + O_2 \rightarrow C_2H_4 + 2H_2O,\ \Delta H^0_{298K} = -280\ kJ \cdot mol^{-1} \quad (6)$$

Production of major amounts of undesirable carbon dioxide and carbon deposition over catalysts are major drawbacks of both the NOCM and OCM reactions. None of the developed catalysts and processes have fulfilled so far the industrial demands in terms of selectivity, conversion and stability [2].

Methane catalytic aromatization (Eq. 7) is also an extremely thermodynamically unfavorable reaction [6]:

$$6CH_4 \rightarrow C_6H_6 + 9H_2,\ \Delta H^0_{298K} = 531\ kJ \cdot mol^{-1} \quad (7)$$

The maximum thermodynamically possible benzene yield of about 12% can be obtained at 700 °C. Though the addition of hydrogen or oxidants (O_2, CO, CO_2, NO and steam) may limit carbon formation, the major barriers for its practical application are insufficient selectivity and inevitable overoxidation of reaction products in the presence of oxidizing agents.

The direct methane oxidation to the C_1 oxygenates (methanol, formaldehyde or formic acid) has been widely studied in both gaseous and liquid phases on various catalytic systems. The oxygenates generated in direct methane oxidation can be more easily over-oxidized to carbon dioxide than methane. A wide range of oxidants have been involved in this process, such as O_2, N_2O, H_2O_2 and even water. It was shown that H_2O_2 might elevate [7–10] the selectivity of methane oxidation toward methanol and can be used at relatively mild conditions. Recently, binuclear [11] and trinuclear [12] copper oxo-clusters in zeolites have shown noticeable activity in the methane oxidation to methanol. Because of thermodynamic limitations [13–15], the reaction has to be performed using chemical looping and temperature swings. Formaldehyde is another possible product of POM. The best reported results [2] correspond, however, to the maximum formaldehyde selectivity of 50% at the methane conversion below 3%.

1.1.3 Challenges in methane chemical conversion

The state of state-of-the-art methane direct or indirect chemical conversion suffers from the following shortcomings:

- high energy consumption, which is required to conduct the methane conversion at high temperatures or to use temperature and pressure swings in the chemical looping processes;
- insufficient selectivities to the target products and emission of large amounts of carbon dioxide;
- rapid catalyst deactivation at high reaction temperatures in both oxidizing and non-oxidizing atmospheres, due to extensive carbon deposition and catalyst sintering;
- thermodynamic limitations for the methane conversion in the absence of oxidizing agents.

In order to improve the efficiency of methane conversion, two main challenges should be considered: methane activation and instability of the reaction intermediates and products. The high energy consumption associated with the methane conversion should be addressed by conducting the reaction at mild conditions and if possible, even at ambient temperature [16–18]. In the low temperature processes, the energy for methane activation can be provided either by the external energy (light, electricity) or by the reacting agents with high energy density, such as oxygen, hydrogen peroxide.

Methane is an extremely inert molecule. Methane activation has been for a long time a “holy grail” [3,17,19,20] of modern science. The C-H bond energy of methane is about 434 $kJ \cdot mol^{-1}$ (4.5 eV), which is the highest among all alkanes. The chemical stability of methane is also closely related to the symmetric tetrahedral molecular geometry, which leads to low polarizability, weak acidity and low affinity for electrons and protons. Most of the products of methane conversion (ethane, ethylene, methanol, formaldehyde, formic acid, carbon monoxide etc.) are more reactive than methane. This results in their overoxidation and reduces the selectivities to the target products. Consequently, the methane conversion is usually accompanied by the production of large amounts of more stable and kinetically inert carbon dioxide and carbon.

1.1.4 Photocatalysis

Solar energy, which is cheap, non-polluting and abundant, provides a potential way to solve both environmental and energy challenges of methane activation and conversion. Photocatalysis, converting the light energy into chemical energy of various chemicals, could occur at mild conditions and under ambient temperature [17,21–23].

Photocatalysts refer to a class of semiconductor materials that can induce photocatalytic redox reactions upon irradiation. In general, heterogeneous photocatalysts can be divided into two main categories. The first category is the bulk semiconductor photocatalysts, such as TiO_2, ZnO, CdS, and WO_3 [24]. The second category is supported or highly dispersed photocatalysts, such as Pd/TiO_2 [25], MgO/TiO_2 [26], TiO_2/SiO_2 [27], and La/WO_3 [28].

The semiconductor (**Figure 2**) is characterized by its electronic band structure constituted of the valence band (VB) and conduction band (CB). The VB electrons firstly absorb incident light with energy equivalent or/and exceeding the bandgap, resulting in charge transfer from VB to CB. The electrons (e^-) and holes (h^+), also called photogenerated charge carriers, are formed in VB and CB, respectively, and then migrate to the surface of photocatalytic materials. Subsequently, the interaction of the photogenerated charge carriers with reacting molecules strongly depends on their redox potential and energies of the conduction band minimum (CBM) and valence band maximum (VBM) [29]. The lifetime of the photogenerated charge carriers is also a critical characteristic determining the photocatalytic efficiency. The electron–hole pairs usually have a lifetime of about 10^{-9} s, while the chemical process requires between 10^{-8} and 10^{-3} s. Most of photogenerated charge carriers undergo recombination processes on the surface and/or in the volume or can be captured by the defect sites in semiconductors, releasing the recombination energy as heat or photons. This inevitably decreases the availability of photogenerated charge carriers for the photoactivation of reacting molecules. The recombination of the photo-excited electron-hole pairs should be, therefore, retarded.

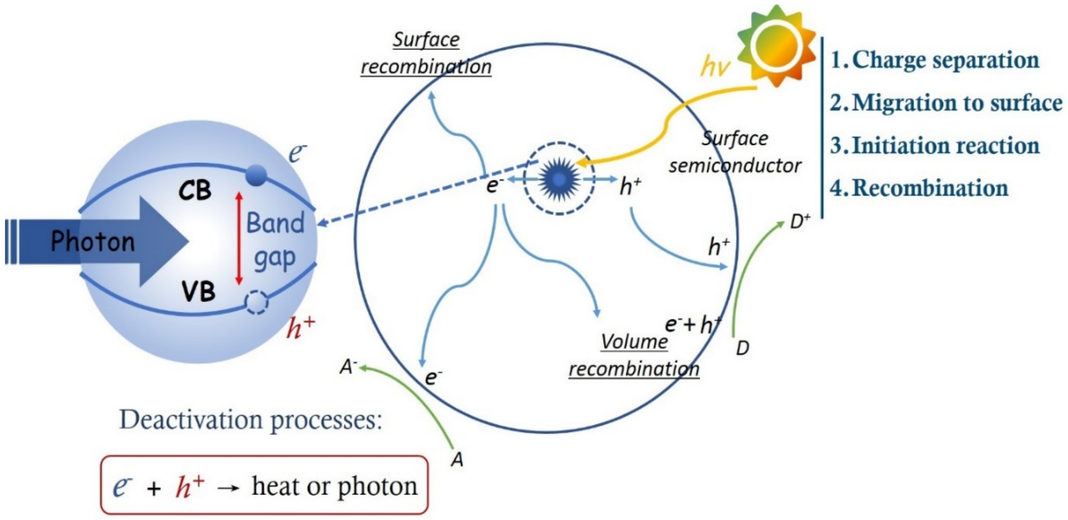

Figure 2. Photocatalytic excitation processes over semiconductors

Addition of metal nanoparticles (Pt, Au, Ag and Ru [30,31]) results in significant improvement of photocatalytic performance. The Schottky barriers formed between the intimate interface of metal nanoparticles and semiconductors favor separation and transfer of photogenerated charge carriers to active sites. Besides, metal nanoparticles can also operate as co-catalysts for the photocatalytic reactions [32,33]. The most efficient are usually noble metals. Rarity and high prices restrict, however, the extensive application of noble metals for photocatalysis. Finally, adding electron scavengers such as Fe^{3+}, Cu^{2+}, Ag^{+}

or H_2O_2 is also helpful for the separation and transfer of photogenerated charge carriers, thus enhancement of the photocatalytic efficiency [34].

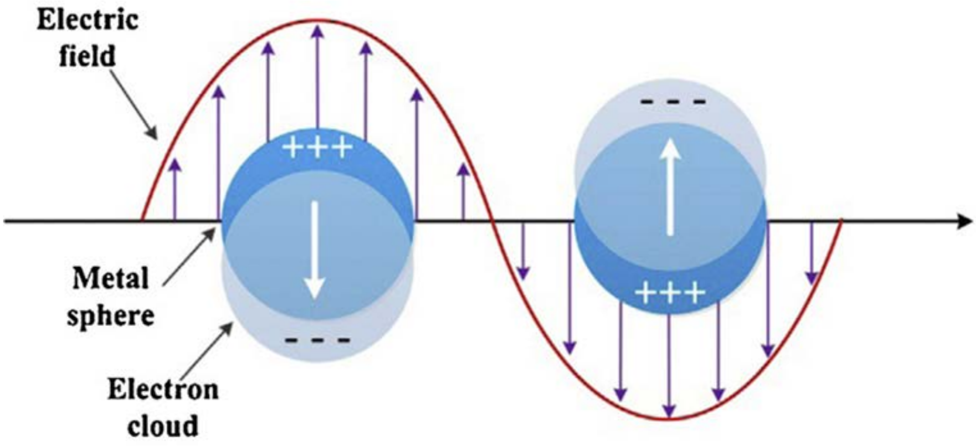

Figure 3. Schematic illustration of LSPR of metal NPs

Under UV and/or visible light irradiation, the interband and/or intraband electronic excitations can occur in some particular metal nanostructures, such as Au [35], Ag [36], Cu [37] and Ni [38] nanoparticles, the latter producing a localized surface plasmon resonance (LSPR) accompanied with significantly enhanced light absorption (**Figure 3**). LSPR is the collective free electron charge oscillation in the metallic nanoparticles that are excited by light [39], such as a collective oscillation of the conduction electrons and large absorption cross-section – that occur when the light frequency is resonant with the metal's size-dependent plasma oscillation frequency. LSPR results in a strong electromagnetic field around metal particles and can accelerates charge separation. Electromagnetic simulations using the finite-difference time-domain (FDTD) methods have shown that the electric field intensity can be > 10^3 times that of the incident light at the surface of a single NP and rise to > 10^6 times stronger in the "hot spots" between two NPs separated by a narrow gap ~ 1 nm. The intensity and resonance wavelength of LSPR over plasmonic metal nanostructures are tunable by modifying their morphology and particle size.

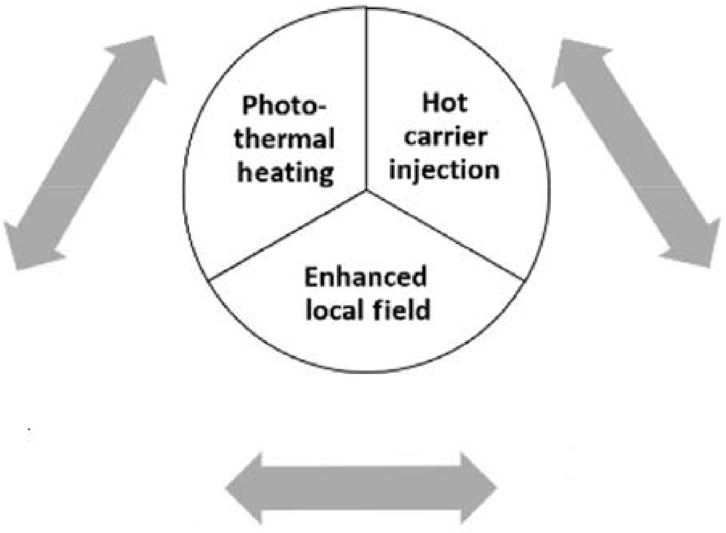

Figure 4. Different photo-induced effects

Following photoexcitation (**Figure. 4**), the plasmon decay generates energetic hot electrons and hot holes, photothermal heating, and local enhancement of electric field around the plasmonic metal nanostructures [40]. Under illumination, temperature is especially significant for the photocatalysts with the LSPR metals and the real surface temperature over the LSPR metals can be significantly higher [41–43] compared to the average temperature in the photoreactor. Photogenerated hot carriers and increased surface temperatures provide energy to induce and accelerate a chemical reaction under milder thermal conditions than possible with catalysts in the dark. At the same time, intense and confined electromagnetic fields near plasmonic NP surfaces enhance the probability that adsorbed molecules may absorb a photon. Additionally, the increased rate of electron-hole pair generation near the NP surface provides free carriers that can ionize adsorbed molecules, weaken chemical bonds, accelerate bond scission, and promote selective chemical reactions.

By contrast, hot carrier-mediated and local enhanced processes do more than just increase reaction rate; they can selectively alter reaction pathways, even opening reaction pathways that are not accessible under purely thermal conditions. Hot carriers generated in the plasmonic nanostructure can do this in a number of ways, most commonly of free sites. For example, hot electrons excited to the lowest unoccupied molecular orbital (LUMO) of surface adsorbed molecules might mediate the first mechanism. For each photocatalytic reaction, there exists a photon energy threshold, and only photoexcited electrons with energies at least as high as the LUMO energy can initiate reactions. Conversely, for the second mechanism, hot holes below the Fermi level can accept electrons from surface-attached catalytic intermediates, thus desorbing them from the catalytic surface and recovering active sites. Accordingly, the unique control of plasmonic photocatalysis hinges on the design of materials that selectively deposit the energy of photons into photoexcited carriers injected into targeted adsorbate orbitals associated with the activation of selected bonds.

While there is a consensus that all three plasmonic photocatalytic effects in **Figure 4** can enhance reaction rates, there is no clear consensus about the extent to which each contributes. All three mechanisms may operate simultaneously. There is growing evidence that they can work together, synergistically. Therefore, a grand challenge facing the plasmonic photocatalysis research community is to identify and quantify the extent to which each of these intertwined effects contributes.

These effects can be enhanced by the Schottky barrier created at the interface between metal catalysts and semiconductor support materials (**Figure 5**), leading to enhanced hot hole or hot electron collection for p-type or n-type semiconductors, respectively, depending on the band alignment. In this way, reaction pathways that are limited by or closed to purely thermal methods can be accessed in plasmonic photocatalysis.

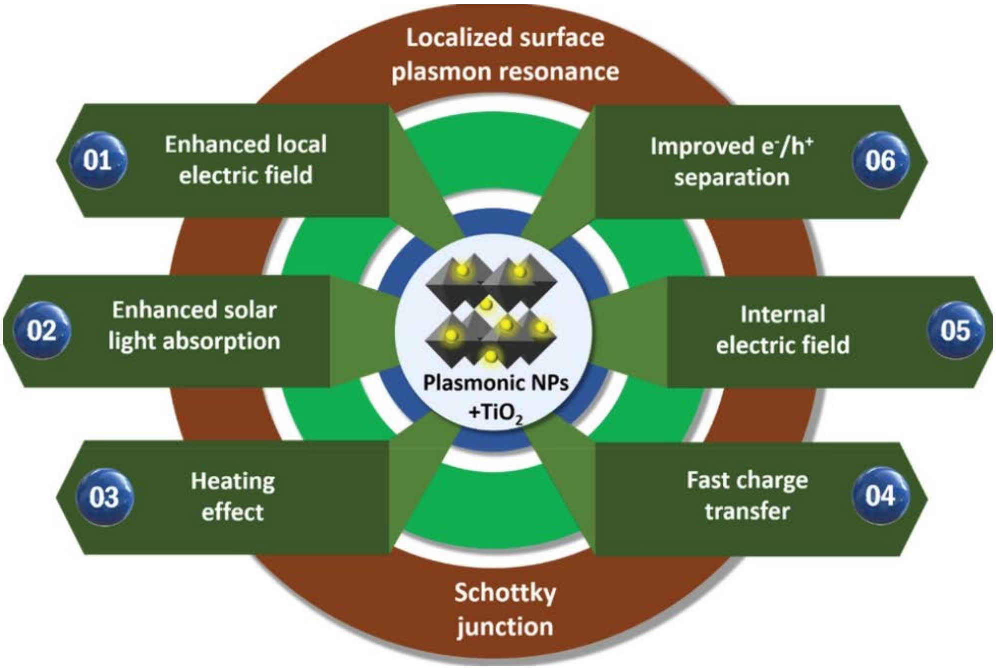

Figure 5. Different strategies and concepts employed in the design and development of photocatalysts based on a semiconductor, such as TiO_2; and plasmonic NPs

The photocatalytic reactions may have rather complex mechanisms and usually involve several elementary steps and intermediates. These reaction steps can be affected by different extent by charge separation, migration and lifetime. The overall selectivity of methane conversion is a function of the rate of these different steps and would be affected by the presence of co-catalysts.

The performance of photocatalysts principally depends on the following characteristics:

- Band gap energy;
- Energy position of the conduction band minimum (CBM) and valence band maximum (VBM);
- Life time of electrons and holes;
- Presence of a co-catalyst.

In the last decades, photocatalysis has been shown to be very promising for water decomposition and environmental remediation. Since a few years, a large number of publications have addressed photocatalytic reduction of carbon dioxide. Recently, photocatalysis has also demonstrated a great potential for the selective methane conversion to fuels and chemicals occurring under mild conditions. The number of publications dedicated to photocatalytic methane conversion is exponentially growing in the last two decades **(Figure 6**).

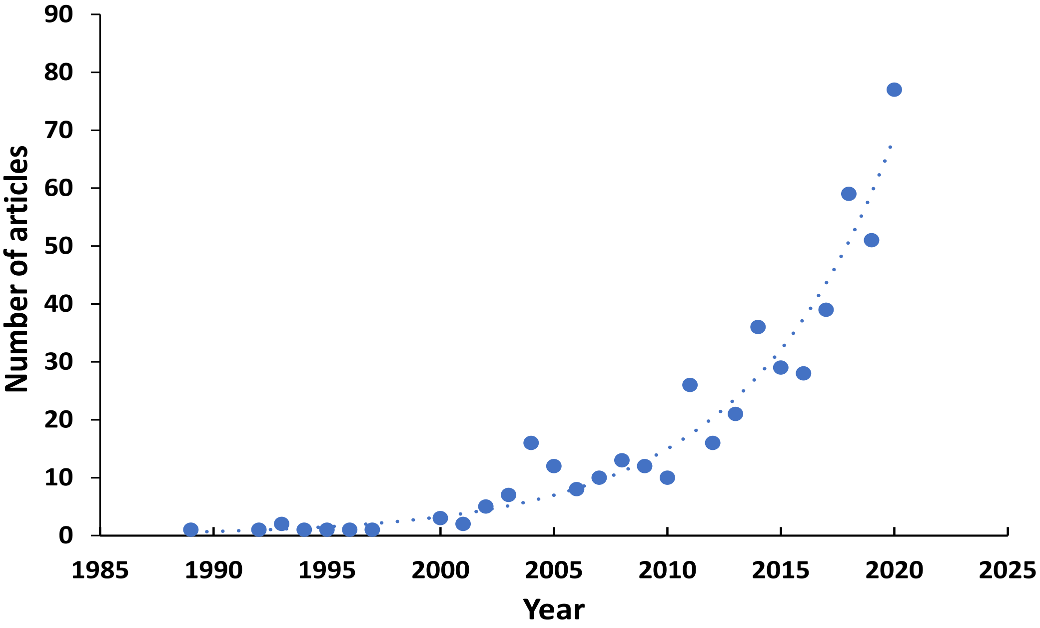

Figure 6. Evolution of the number of publications dedicated to methane photocatalytic conversion. Search results in Scopus using “methane” and “photocatalysis” as search item.

1.2 Photocatalysis for selective methane conversion

One of the first stages of methane chemical conversion is its activation, requires a significant energy supply. Direct methane ionization or direct C-H bond cleavage in the gaseous methane both require very high energy, which is obviously impractical for real use. The role of any catalyst is, therefore, to reduce the activation energy of methane activation and to shift the reaction selectivity to a specific target product. In classical thermal catalysis, activation of the C-H bond in the methane molecule requires high temperature (>500 °C). In photocatalysis, the energy of photons provides an alternative energy source for methane activation, which may occur under irradiation even at room temperature. Photocatalysts, which decrease the energy of methane photocatalytic activation and enable efficient selective methane conversion at ambient temperatures under irradiation, are therefore considered as critical factors.

The C-H bond cleavage is usually strongly associated with the generation of the reaction intermediates upon light irradiation [44]. There have been generally two main mechanisms of methane photocatalytic activation [17]. The first mechanism involves the formation of electrophilic oxygen-centered radicals (such as O^-, OH•, •O-R, etc.), which react and abstract a H atom from methane. The activation barriers for abstracting a H atom and for the methane activation are lowered in this way [45]. The second mechanism considers the metal-CH_3 species as the reaction intermediates. These species form via methane dissociation over a photocatalyst.

The goal of our review is to perform a comparative and extensive analysis of methane photocatalytic conversion occurring at mild conditions and often at ambient temperature. More specifically, we consider three methane photocatalytic conversion routes: partial oxidation, reforming and coupling. The methane photocatalytic reactions are discussed together and compared using quantitative criteria such as selectivity to the target products and productivity. The analysis of current trends in the chemistry and catalysis of methane photocatalytic activation and conversion is principally performed based on the literature published in the last 10 years.

1.2.1 Photocatalytic methane oxidation

1.2.1.1 Complete oxidation of methane (COM) and Partial oxidation of methane (POM) to carbon monoxide and methanol

The partial oxidation of methane (POM) provides an opportunity for direct selective production of various value-added chemicals. Very often, methanol is the target product of methane photocatalytic oxidation. In addition, complete oxidation of methane (COM) to carbon dioxide is also considered as a promising approach for reducing global warming. Methane is a greenhouse gas with a potential 30 times higher than that of CO_2 and can be present in small amounts in the atmosphere. It can be expected, therefore, that COM could reduce global warming. Titania [46] and zinc oxide [47] promoted with silver nanoparticles showed a good photocatalytic activity in methane complete oxidation. The photocatalysis can therefore clean [48] the atmosphere from non-CO_2 GHGs such as methane, reduce the global warming effect and simultaneously generate renewable electricity.

Molecular oxygen is prevalent among all the oxidants for the photocatalytic methane oxidation, due to its easy availability and economic superiority. Various O radicals formed from molecular oxygen under irradiation play an important role in methane activation and conversion. In the pioneering work, Kazansky et al. [49] studied reactions of methane with the photogenerated hole centers over TiO_2 and V/SiO_2 in the presence and absence of molecular oxygen under UV irradiation at mild temperature. The methane conversion resulted in the production of formaldehyde, ethane and CO_x. It was revealed that the photogenerated O^- hole centers were consumed in the absence of oxygen. They were responsible for the formation of methyl radicals and alkoxide intermediate species (CH_3O^- and $C_2H_5O^-$), while the surface ions Ti^{4+} and V^{5+} were simultaneously reduced by electrons.

In the presence of oxygen, both COM and POM were enhanced, but POM was predominant. Additional oxygen was suggested to easily trap free electrons and formed more active oxygen species. Moreover, oxygen also played a key role in hindering metal reduction, which caused catalyst deactivation. Similarly, the O^- radicals of transition metal oxides, such as WO_3, V_2O_5, ZnO and MoO_3, played an important role in methane oxidation. Chen and co-workers [50] reported that the nano-scaled zinc oxide effectively oxidized methane in the presence of oxygen under UV-visible light at ambient conditions. The photogenerated surface O^- species and molecular oxygen were responsible for the formation of formaldehyde intermediates and for the complete oxidation to carbon dioxide. It was found that smaller zinc oxide nanoparticles favored the photocatalytic methane oxidation. Moreover, additional silver decoration further enhanced the catalytic performance due to the silver LSPR. Ward et al. [31] reported that MoO_3 catalyzed selective oxidation of methane into methanol in the presence of oxygen at 100 °C under UV irradiation. The authors suggested that the surface absorbed H_2O was possibly involved in methanol production through the methyl radical pathway. Furthermore, additional doping with the Cu^{2+} cations made the photocatalyst sensitive to the visible light, due to the narrowed O 2*p*→Cu 3*d* excitations in $CuMoO_4$. The electron trapping capability of Cu^{2+} lengthened the lifetime of O^- radicals. Sastre and co-workers [51] discovered methane oxidation with molecular oxygen to the liquid C_1 oxygenates with the selectivity above 95% over zeolites at room temperature under deep UV irradiation. The methanol productivity was about 194 $\mu mol \cdot g_{cat}^{-1} \cdot h^{-1}$ with a selectivity of 40.5%. They suggested that upon irradiation the surface silyloxyl radicals (Si-O•) derived from surface silanol groups generated methyl radicals, and then further formed the silyl methyl ethers ($Si-OCH_3$). Their decomposition yielded methanol. Moreover, the pore structure played an important role in providing silanol groups and confined space for methane activation. The presence of oxygen was critical for determining the reaction pathway of methyl radicals, thus directly influenced the selectivity. Highly selective CH_3OH production was achieved [52] in aerobic photocatalytic CH_4 oxidation by $Au_{0.75}/ZnO$ at atmospheric temperature. The Au nanoparticles were involved in the plasmonic affect, maximizing the electron and hole utilization. Isotopic tests showed that CH_3OH was produced from the combination of the CH_3 radicals with either O_2 or OH•.

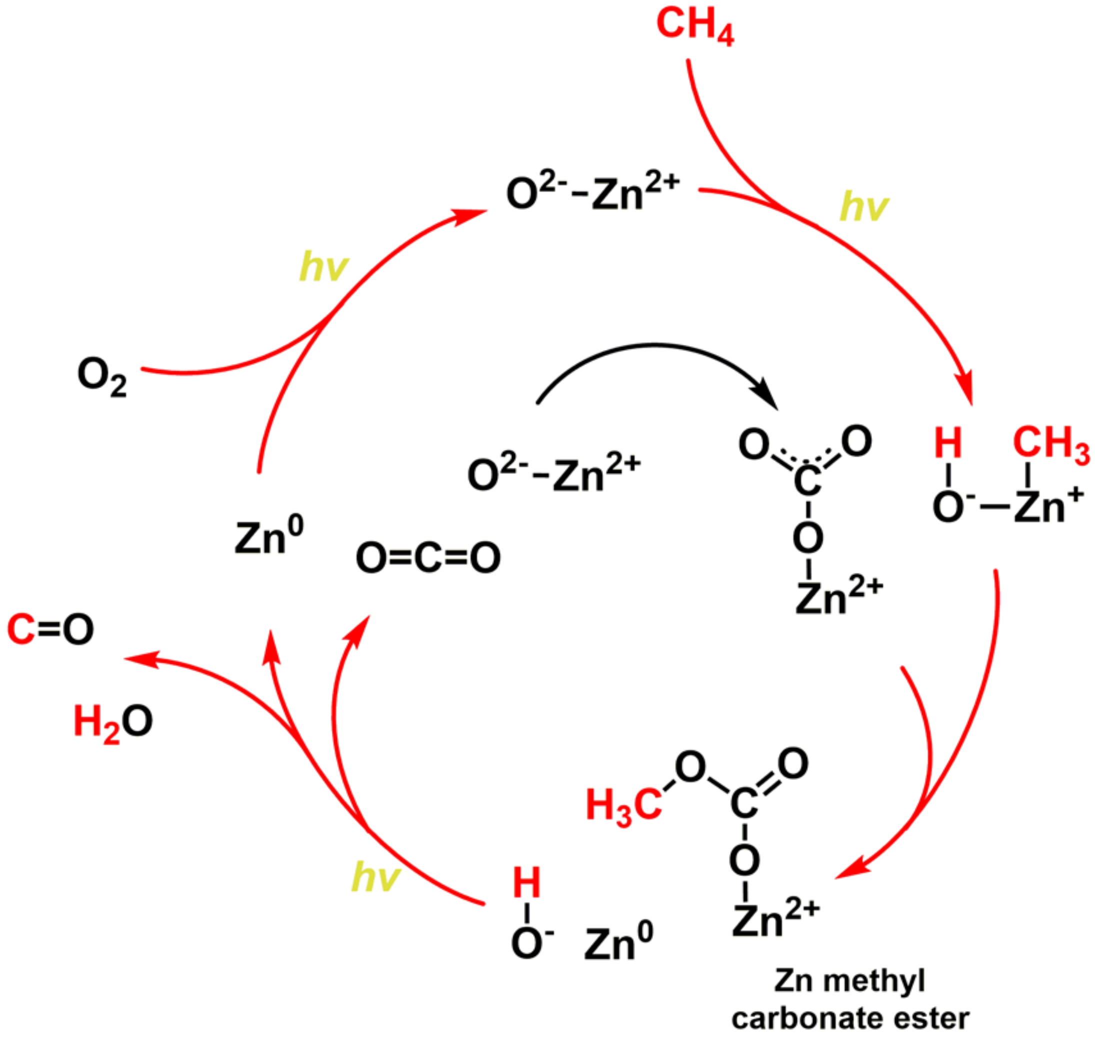

Figure 7. Reaction steps in methane oxidation with O_2 over Zn-HPW/TiO_2.

Recently, our group discovered that zinc-heteropolyacid-titania nanocomposites catalyzed selective oxidation of methane into carbon monoxide using a 300 W Xe lamp at ambient temperature in the presence of molecular oxygen [53]. The optimized Zn-HPW/TiO_2 nanocomposite exhibited a high carbon monoxide productivity of 429 μmol·g_{cat}^{-1}·h^{-1} in the batch reactor containing 3 bar of methane and 1 bar of oxygen. It turned out that all the three TiO_2, HPW and Zn components of the nanocomposites were essential for selective carbon monoxide production. TiO_2 harvested photons and achieved charge separation, HPW then promoted the transfer of photogenerated charge carriers, and Zn thus provided efficient active sites in the form of the charge-transfer excited complex [Zn^+–$O^−$] for the formation of methyl carbonate intermediates (**Figure 7**). The decomposition of methyl carbonate intermediates generated from the zinc carbonates produced carbon monoxide, and zinc was simultaneously reduced by electrons.

Water was found to be a very promising agent for methane selective oxidation. The promoting effect of water on methane activation is usually attributed to the formation of OH• radicals. Chen and Li [54] reported the methane oxidation over the water preabsorbed TiO_2 and Mo/TiO_2 at mild conditions under UV irradiation in the presence of oxygen with the methanol productivity of 12.5 μmol·g_{cat}^{-1}·h^{-1}.The dehydrated counterparts only produced CO_x. It seems that water could be a critical factor for selective oxidation of methane into methanol over some catalysts. Gondal et al. [55] studied methane oxidation induced by UV laser beam over the WO_3, TiO_2 and NiO semiconductors at room temperature in aqueous solution. The strong laser beam resulted in more efficient electron-hole excitation and water oxidation to hydroxyl radicals. This enhanced the methane conversion to above 20% over all samples. Among them, the maximum methanol productivity (529 μmol·g_{cat}^{-1}·h^{-1}) followed by a decrease with the irradiation time, was observed for WO_3, the decrease resulted from the methanol degradation in which a high concentration of methanol competitively donated electron to holes due to the band structure of WO_3. They further reported even higher methanol production rate over Ag impregnated WO_3 at room temperature under laser irradiation, in the presence of water [56]. The surface Ag^+ ions enhanced the formation of hydroxyl radicals by suppressing charge carrier recombination upon both the Ag_2O and WO_3 nanoparticles. However, besides the methanol degradation, the non-selective oxidation of excessive hydroxyl radicals also resulted in further methanol oxidation and produced a variety of by-products. Recently, Du et al. [57] discovered that in the presence of water, the CeO_2 nanoparticles calcined at high-temperatures selectively catalyzed methane oxidation into ethanol and aldehyde at ambient conditions under simulated solar light. The concentration of oxygen vacancies in the catalysts was critical for the formation of hydroxyl radicals upon irradiation, and a higher Ce^{III}/Ce^{IV} ratio favored ethanol formation. The optimized CeO_2 nanoparticles achieved the ethanol productivity of 11.4 $\mu mol \cdot g_{cat}^{-1} \cdot h^{-1}$ with the selectivity of 91.5%. Zhu and co-workers [58] fabricated bipyramidal $BiVO_4$ and achieved methanol productivity (112 $\mu mol \cdot g_{cat}^{-1} \cdot h^{-1}$, selectivity over 85%) at mild temperature under simulated solar irradiation in the presence of water. The intermediate reactivity of exposed facets and easier formation of photoexcited holes in the bipyramid structure favored selective methane oxidation, while the larger amount of CO_2 was detected over plate-like $BiVO_4$. Villa et al. [34] compared methane oxidation in various aqueous suspensions containing mesoporous WO_3 at mild temperature under UVC-visible light irradiation. The methanol production rate of 27.1 $\mu mol \cdot g_{cat}^{-1} \cdot h^{-1}$ with a selectivity of 46.2% was obtained in the presence of methane and pure water, while the presence of the Fe^{3+} electron scavenger in the aqueous solution increased the methanol production rate to 67.5 $\mu mol \cdot g_{cat}^{-1} \cdot h^{-1}$ with a selectivity of 58.5%. It was proposed [59] that the addition of Fe^{3+} not only improved charge separation, which favored the production of $HO\bullet_{ads}$, but also enhanced production of free hydroxyl radicals via photolysis ($Fe^{3+} + H_2O \rightarrow Fe^{2+} + HO\bullet + H^+$). The H_2O_2 aqueous solutions have enhanced capability to provide abundant hydroxyl radicals [60]. For the WO_3 counterpart, in the presence of methane and H_2O_2 aqueous solution, the ethane production predominated instead of methanol. The formation of methanol was favored by adsorbed surface hydroxyl species, Thus the methyl radicals generated by free hydroxyl radicals mainly went for the methane coupling. The proposed mechanism was further confirmed in another work [61].

Xie and co-workers [62] discovered that an optimized FeO_x/TiO_2 nanocomposite consisted of highly dispersed iron species anchored on TiO_2 achieved a methanol productivity of 1056 $\mu mol \cdot g_{cat}^{-1}$ with a selectivity over 90% at ambient conditions under simulated sunlight irradiation in the presence of H_2O_2, and only produced a trace amount of CO_x. They suggested that Fe^{3+} species not only improved the electron-hole separation, but also lowered the overpotential for H_2O_2 reduction, which avoided the formation of O_2^- and over-oxidation coincided with the formation of CO_2 (**Figure 8)**. The photoexcitation occurred upon TiO_2 and photogenerated holes were left in the VB of TiO_2 to form methyl radicals, while the photogenerated electrons were transferred to the surface iron species to participate in the H_2O_2 reduction with a lowered energy barrier.

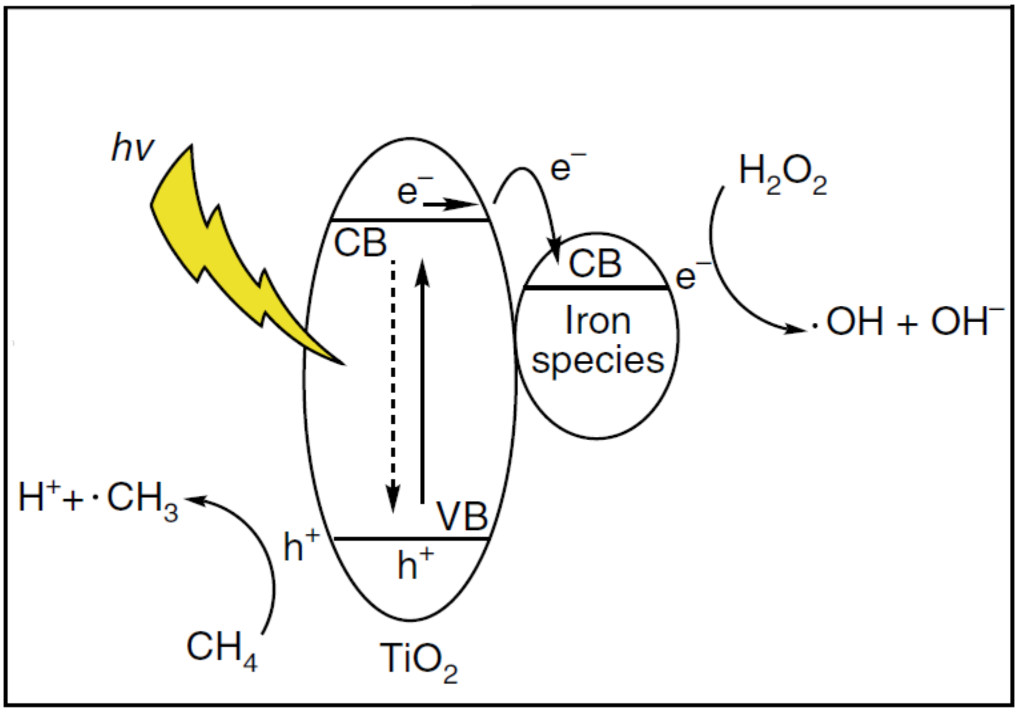

Figure 8. Reaction steps in methane oxidation with H_2O_2 over FeO_x/TiO_2

1.2.1.2 Partial oxidation of methane (POM) to formaldehyde and formic acid

In addition to the major production of methanol, several photocatalytic systems and oxidants have been explored for methane oxidation to high-value formaldehyde and formic acid. **Table 1** shows the representative methane oxidation to liquid products cases, most of them produce methanol as the major products in a C_1 oxygenate mixture including methanol, methyl hydroperoxide and formaldehyde and sometimes a small amount of C_2 oxygenate, such as ethanol and acetaldehyde are even produced, which results in low selectivity. Thus, the selective methane oxidation to formaldehyde and/or formic acid would be more attractive than producing methanol with unsatisfying selectivity and lower value.

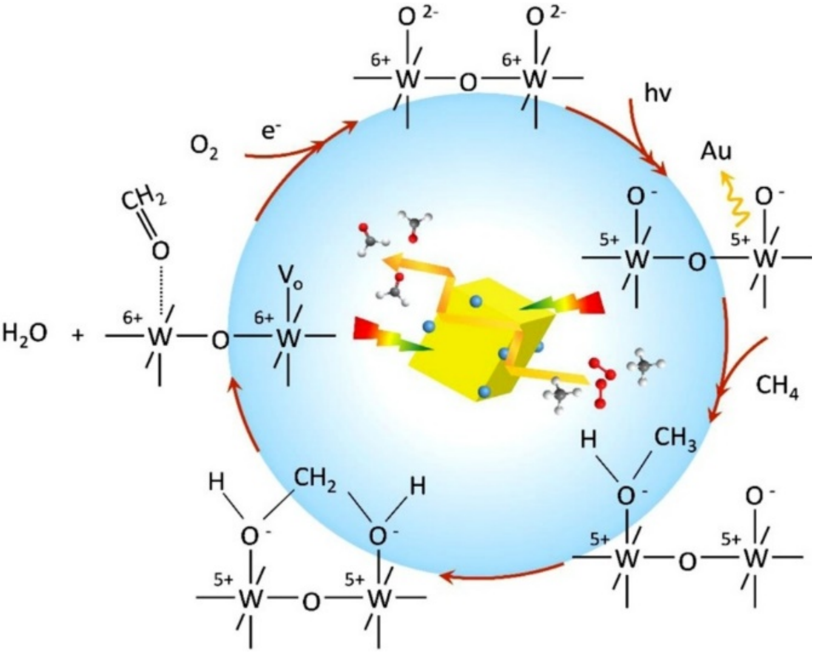

Figure 9. Proposed reaction mechanism for HCHO generation over c-WO_3

Niu et al. [63] reported a direct photocatalytic aerobic oxidation of methane to formaldehyde process over Au_x/c-WO_3 with selectivity higher than 99%. They demonstrated that the electrophilic terminal O^- ion (hole) from the exposed (002), (020) and (200) facets of c-WO_3 can not only abstract the H-atom from CH_4 molecule but also donate an O-atom to form HCHO (**Figure 9**). Consumed O can be timely restored by molecular O_2 as oxidant, thus ensuring the sustained generation of HCHO. As the effective electron transfer media, Au nanoparticles can extract the photoexcited electrons to promote O^- ion generation, thus accelerate the formation of HCHO in c-WO_3 system.

Hu et al. [64] reported a photocatalytic conversion of methane to liquid oxygenates with selectivity of 82.4% containing mainly formaldehyde and formic acid over HSiMo/TiO_2. In addition, small amount of methanol and acetaldehyde were also produced simultaneously. They demonstrated that the synergetic effect of HSiMo and TiO_2 plays an important role in the photocatalytic process, in which HSiMo can promote C-H breaking and methane oxidation would take place at the interface between HSiMo and TiO_2.

Toxic and unstable chlorine dioxide radical was also used[65] for the non-catalytic synthesis of formic acid from methane (**Figure 10**). The methane oxygenation is initiated by the photochemical Cl−O bond cleavage of $ClO_2\cdot$ to generate Cl· and O_2. The produced Cl· reacts with CH_4 to form a methyl radical ($CH_3\cdot$). Finally, the oxygenated products such as methanol and formic acid were given by the radical chain reaction. A fluorous solvent plays an important role of inhibiting the deactivation of reactive radical species such as Cl· and $CH_3\cdot$. The yields of methanol and formic acid were 14% and 85 %, respectively, with a methane conversion of 99 % without formation of the further oxygenated products such as CO_2 and CO.

The process producing formaldehyde or formic acid, however, required either high pressure or elevated temperature. Multiple liquid oxygenates (methyl hydroperoxide, methanol, formaldehyde, formic acid, etc.) are usually simultaneously produced and can be hardly separated. Most of the current photocatalytic methane oxidation routes suffer, therefore, from low productivity and insufficient selectivity or require highly reactive, unstable and toxic oxidants (H_2O_2, ClO_2 etc).

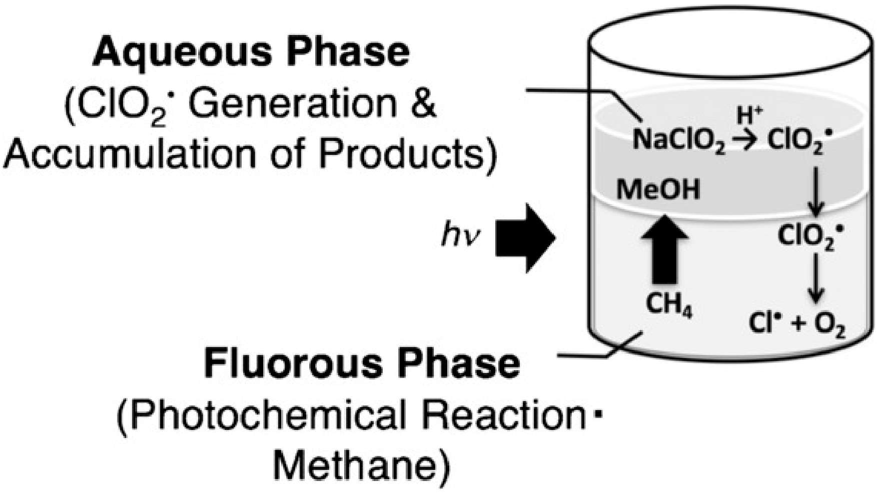

Figure 10. Two-phase photooxidation of CH_4 by $NaClO_2$. $NaClO_2$ is dissolved in an aqueous phase and CH_4 is dissolved in fluorous phase

Table 1. Representative photocatalytic methane oxidation to liquid products

Photocatalyst	Reaction conditions	Liquid Products			Overall selectivity of main liquid product
		Main liquid product		Liquid By-products and productivity	
		Productivity	Selectivity (in liquid)		
TiO_2 [59]	300 W Xe lamp, 20 mg catalyst, 3 MPa CH_4, 20 ml H_2O, 2 ml $FeCl_2$ (0.01M), 20 μl H_2O_2, 303 K, reaction time 1 h	CH_3OH 471 μmol g^{-1}	84.4%	CH_3CHO 53 μmol g^{-1} HCOOH 34 μmol g^{-1}	84%

FeOx/TiO_2 [66]	300 W Xe lamp, 10 mg catalyst, 20% CH_4, 80% Ar, 6 ml H_2O, 4 ml 2 m M H_2O_2, 298 K, reaction time 3 h	CH_3OH 1056 μmol g^{-1}	93.7%	CH_3CH_2OH 70 μmol g^{-1}	90%
q-$BiVO_4$ [67]	Hg lamp, 10 mg catalyst, 1 MPa CH_4, 1 MPa O_2, 10 ml H_2O, 298 K, reaction time 3 h	CH_3OH 2300 μmol g^{-1}	56.1%	HCHO 1800μmol g^{-1}	52.3%
Cu-0.5/PCN [68]	500 W Xe lamp, 20 mg catalyst, 25 ml H_2O, $CH_4/N_2=1/9$, flow rate 100 ml min^{-1}, room temperature, reaction time 1 h	CH_3CH_2OH 106 μmol g^{-1}	81.2%	CH_3OH 24.5 μmol g^{-1}	-

Au/ZnO [69]	300 W Xe lamp, 10 mg catalyst, 2 MPa CH_4, 0.1 MPa O_2, 100 ml H_2O, 298 K, reaction time 2 h	CH_3OOH 12340 μmol g^{-1} CH_3OH 4120 μmol g^{-1}	65.6%	HCHO 8630 μmol g^{-1}	62.6%
Au-CoO_x/TiO_2 [70]	300 W Xe lamp, 10 mg catalyst, 2 MPa CH_4, 0.1 MPa O_2, 100 ml H_2O, 298 K, reaction time 2 h	CH_3OOH 2200 μmol g^{-1} CH_3OH 2880 μmol g^{-1}	99.9%	Trace HCHO	95%
$Au_{0.2}Cu_{0.15}$-ZnO [71]	300 W Xe lamp, 20 mg catalyst, 1.9 MPa CH_4, 0.1 MPa O_2, 100 ml H_2O, 298 K, reaction time 2 h	CH_3OH 12906 μmol g^{-1} CH_3OOH 4870 μmol g^{-1}	79.2%	HCHO 4673 μmol g^{-1}	79.0%
$Au_{0.3}$/c-WO_3 [63]	300 W Xe lamp, 10 mg catalyst, 1.9 MPa CH_4, 0.1 MPa O_2, 150 ml H_2O, 298 K, reaction time 3 h	HCHO 1300 μmol g^{-1}	99.9%	-	99.8%

Au-Pd/TiO$_2$[72]	Xe lamp, 5 mg catalyst, 3 MPa CH$_4$, 1 MPa O$_2$, 30 ml H$_2$O, 315 K, reaction time 1 h	CH$_3$OH 8600 µmol g^{-1} CH$_3$OOH 6200 µmol g^{-1}	75.1%	HCHO 4500 µmol g^{-1} HCOOH 400 µmol g^{-1}	73.6%
Perfluorinated Solvent[65]	500 W Xe lamp, NaClO$_2$ (0.1 mM), 298 K, 1 atm, reaction time 0.25 h	HCOOH yield 85%	85.9%	CH$_3$OH yield 14%	9%
HSiMo/TiO$_2$[64]	AM 1.5G sunlight, 20 mg catalyst, 3 MPa CH$_4$, 2 MPa O$_2$, 20 ml H$_2$O, 423 K, reaction time 2 h	HCOOH 1359 µmol g^{-1}	46.1%	CH$_3$OH 190 µmol g^{-1} HCHO 1350 µmol g^{-1} CH$_3$CHO 50 µmol g^{-1}	41.8%

1.2.2 Photocatalytic methane reforming

Steam reforming and dry reforming of methane (SRM and DRM) are promising ways to directly convert methane into valuable syngas, a mixture of carbon monoxide and hydrogen. Conventional methane reforming involves heterogeneous catalysts and requires higher temperatures. Thermocatalytic methane reforming is often accompanied by rapid catalyst deactivation due to sintering and carbon deposition. Photocatalytic methane reforming occurring under mild conditions appears as a promising strategy, which can reduce energy consumption, improve the selectivity to CO and hydrogen and largely avoid coke formation and sintering.

1.2.2.1 Dry reforming of methane (DRM)

There have been so far several reports about the photocatalytic DRM process. Tanaka and co-workers [73,74] discovered that methane reacted with carbon dioxide over ZrO and MgO and selectively produced carbon monoxide under irradiation at room temperature. A very small amount of hydrogen was observed relative to carbon monoxide. The isotopic experiments uncovered that carbon monoxide originated from carbon dioxide instead of methane, while the methane conversion resulted in carbonaceous residues on the surface. The proposed mechanism [75] suggests that carbon dioxide is firstly photoexcited to the $\bullet CO_2^-$ anion radicals, which then activate methane and form the surface acetate species and formate intermediates. The electron transfer to carbon dioxide is an energy consuming process and requires -1.9 eV [76], but it can be facilitated by the presence of water vapor [75]. Cu/CdS–TiO_2/SiO_2 was reported to selectively convert methane and carbon dioxide into acetone with selectivity of 92.3% under UV irradiation at the temperature of 120 °C [77]. The authors suggested that both methyl radicals and $\bullet CO_2^-$ anion radicals were responsible for the formation of acetone, while ethane and carbon monoxide were originated from methane and carbon dioxide, respectively.

Yoshida and co-workers [78] discovered that both hydrogen and carbon monoxide were simultaneously produced via photocatalytic DRM under UV irradiation over Ga_2O_3. The mild reaction temperature of 200 °C was essential to drive the photocatalytic DRM. In order to further improve the efficiency of the photocatalytic DRM process, several strategies including doping with Cu, Pt and Ag, La and montmorillonite have been exploited to accelerate charge transfer and promote the reactant conversion. Besides, narrow bandgap materials (such as black TiO_2 and graphitic carbon nitride) have also been developed to extend the range of light absorption.

In addition to the wide bandgap photocatalyst, the narrow bandgap materials have been exploited to make photocatalytic DRM feasible under simulated light or visible solar light. Hu and co-workers [79] reported an efficient photocatalytic DRM over Pt/black TiO_2 under visible light at catalyst surface temperature of 550 °C, and achieved a hydrogen and carbon monoxide productivities of 71 $\text{mmol}\cdot g_{cat}^{-1}\cdot h^{-1}$ and 158 $\text{mmol}\cdot g_{cat}^{-1}\cdot h^{-1}$, respectively. It was found that the enhanced yields under irradiation were due to the photocatalytic reaction. On the basis of FT-NIR and EPR characterization, they suggested that the oxygen vacancies of the black TiO_2 formed a donor level (Ti^{3+}) below the CB of TiO_2, thus an additional energy bandgap of 1.3 eV enabled the absorption of visible light. Moreover, Pt loading greatly accelerated the charge transfer and contributed to the C-H bond cleavage.

In addition to noble metals such as platinum, Ni and Cu are potential plasmonic promoters for photocatalytic methane activation. Nickel has been widely studied in thermocatalytic methane conversion due to its high activity and lower price. Ye and co-workers [38,80] discovered that Ni effectively promoted DRM over Ni/Al_2O_3 and Ni/SiO_2 nanocomposites under light irradiation at 550 °C, in which Ni nanoparticles acted as both the catalytically active sites and a plasmonic promoter. Li and co-workers [81] reported a Ni/CeO_2 nanocomposite for light-driven DRM under focalized UV-vis-Infrared irradiation without any other heater, which achieved hydrogen and carbon monoxide productivities of

391.8 $\mu mol \cdot g_{cat}^{-1} \cdot h^{-1}$ and 376.2 $\mu mol \cdot g_{cat}^{-1} \cdot h^{-1}$, respectively, with the light to fuel efficiency of 11.1%. They suggested that LSPR on the Ni nanoparticles and significant IR heating effect causing the equilibrium temperature increase up to 807 °C on the nanocomposite, CeO_2 also played an important role for reactant activation and durability enhancement due to its intrinsic activity for DRM and carbon elimination ability by the abundant lattice oxygen. Nevertheless, their reaction conditions were still harsh, especially for necessary huge thermal energy input. Yoshida et al. [82] reported plasma-assisted DRM over Ni/Al_2O_3 under visible light irradiation at 200 °C, with carbon monoxide and hydrogen productivities of 1.87 and 1.20 $mmol \cdot h^{-1}$, respectively. Moreover, Ni/Al_2O_3 was inactive in the same thermal condition without light irradiation, thus metallic Ni nanoparticles were responsible for the photocatalytic DRM performance under visible light irradiation.

Ye and co-workers [40] reported for the first time that plasmonic promoter Au was effective in the activity enhancement of thermocatalytic DRM over Rh-Au/SBA-15 under low intensive visible light irradiation at 500 °C, with the hydrogen and carbon monoxide productivities of 3700.0 and 4050.0 $\mu mol \cdot g_{cat}^{-1} \cdot s^{-1}$, respectively. The productivities were higher than the sum of that of Au/SBA-15 and Rh/SBA-15 under the same conditions. The UV/VIS spectra showed that the Au containing samples exhibited visible light absorption due to the Au LSPR, and the intensity of electromagnetic field around metal nanoparticles in Rh-Au/SBA-15 was much enhanced due to the near field coupling effect. High temperature increased the energy of the photoinduced hot electrons, while plasmonic metal nanoparticles contributed to the reactant polarization and the energetic hot electrons enhanced molecular activation. Afterwards, similarly, bimetallic alloy nanocomposites Pd-Au/Al_2O_3 [83] and Pt-Au/SiO_2 [84] all exhibited considerably enhanced catalytic performance in DRM under visible light irradiation at milder temperature largely due to the strong LSPR of plasmonic metal nanostructures.

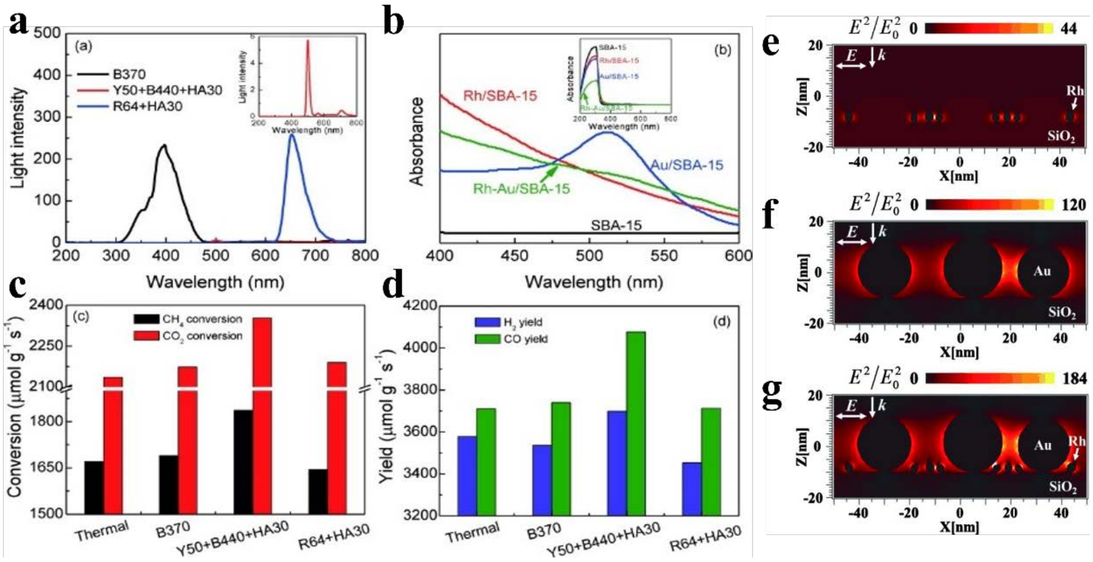

Figure 11. (a) Incident light with different wavelength region over filters. (b) UV/Vis spectra of catalysts. (c) methane and carbon dioxide conversions and (d) carbon monoxide and hydrogen yield counterparts under various irradiation conditions. (e-g) electric field distribution of the catalyst under visible-light excitation of 530 nm, the color scale bar shows the electric field enhancement. (e) Rh/SBA-15. (f) Au/SBA-15. (g) Rh-Au/SBA-15.

Recently, Zhou and co-workers [85] fabricated a Cu-Ru single-atom alloy, which consisted of catalytic single-Ru atoms supported on Cu nanoparticles for DRM under laser without external heating and achieved a long-term stability for 50 hours with methane conversion of 220 $\mu mol \cdot g_{cat}^{-1} \cdot s^{-1}$ and selectivity of above 99%. They suggested that single-Ru atom active sites, together with the Cu nanoparticle LSPR, were responsible for the prominent photocatalytic performance, in which plasmonic Cu nanoparticles facilitated the generation of hot electrons, while the single-Ru atoms provided highly active sites for methane dehydrogenation and carbon dioxide activation as shown in **Figure 11a**. Moreover, a proper single-atom structure was essential. Calculations showed that the structure consisting of isolated Ru atoms on Cu surface was optimal for lowering molecular activation barriers and resisting other processes such as reverse water gas shift reaction and coke formation. Coke produced upon Ru ensembles and Cu surface blocked the active sites and caused the catalyst deactivation (**Figure 11b**). Note that the Cu-Ru single-atom alloy showed much higher activity and longer durability in photocatalytic DRM than in thermo-catalytic DRM.

1.2.2.2 Steam reforming of methane (SRM)

Yoshida et al. [86] discovered photocatalytic SRM over Pt/TiO_2 under UV irradiation at room temperature. Hydrogen and carbon dioxide were observed as main products with trace amounts of ethane and carbon monoxide. The isotopic experiments suggested that the interaction of methane and water firstly generated the [CH_2O] intermediates, which then further reacted with water and produced hydrogen and carbon dioxide. Similarly, they further investigated β-Ga_2O_3 and Pt/β-Ga_2O_3 in photocatalytic SRM using 300 W Xe lamp at mild temperature. Hydrogen and carbon dioxide were detected as products. An improved hydrogen productivities of 1 μmol·min^{-1} g^{-1} was obtained in the steady state over Pt/β-Ga_2O_3 [87]. Besides, $NaTaO_3$ with high photoactivity in the water decomposition was used for photocatalytic SRM using 300 W Xe lamp at mild temperature. Compared to bare $NaTaO_3$, enhanced photocatalytic SRM performances were observed over the samples modified either by Pt or La, while the Ni-loaded sample could not activate methane and just showed high photoactivity for the water decomposition [88,89]. Li et al. [90] reported an enhanced photocatalytic hydrogen evolution over Pt/TiO_2 under UV irradiation (wavelength centered at 254 nm) at mild temperature by integrating water splitting with methane conversion. The hydrogen productivity of 200 μmol·g_{cat}^{-1}·h^{-1} was achieved, ethane and carbon dioxide were simultaneously produced with the rates of 53.3 μmol·g_{cat}^{-1}·h^{-1} and 28.9 μmol·g_{cat}^{-1}·h^{-1}, respectively. Pt sites seem to play an important role in the methane activation, and ethane comes from the coupling of methyl radicals.

In another work, Yoshida et al. [91] reported that compared to bare $K_2Ti_6O_{13}$, Pt loaded

$K_2Ti_6O_{13}$ showed significantly enhanced photocatalytic SRM performance in the same conditions using a 300 W Xe lamp at mild temperature, and Rh loaded $K_2Ti_6O_{13}$ exhibited two times higher activity than Pt loaded $K_2Ti_6O_{13}$. It was found that not only the type of loaded metal but also the loading method influenced the photocatalytic SRM performance. They suggested that metallic rhodium nanoparticles and rhodium oxide nanoparticles coexisted in Rh loaded $K_2Ti_6O_{13}$ and promoted the transfer and separation of charge carriers. They proposed that photogenerated holes and electrons are transferred to rhodium oxide nanoparticles and metallic rhodium nanoparticles, respectively. This could efficiently prevent the charge recombination and cooperatively promoted the reduction and oxidation processes.

Amin et al. [92] discovered a photocatalytic bi-reforming of methane (BRM) process combined by photocatalytic DRM and SRM over Ag loaded protonated graphitic carbon nitride (Ag/pg-C_3N_4) under UV irradiation (wavelength centered at 254 nm) at mild conditions. It was found that carbon monoxide, hydrogen and methanol were the main products, in addition to traces of ethane in all the photocatalytic SRM, DRM and BRM processes. Interestingly, pure g-C_3N_4 was favorable for CO evolution, while pg-C_3N_4 promoted both H_2 and CH_3OH production. Compared to the photocatalytic SRM and DRM processes, in photocatalytic BRM, the production of methanol almost remained unchanged with the rate of 365 $\mu mol \cdot g_{cat}^{-1} \cdot h^{-1}$, while that of carbon monoxide and hydrogen increased to 1211 $\mu mol \cdot g_{cat}^{-1} \cdot h^{-1}$ and 344 $\mu mol \cdot g_{cat}^{-1} \cdot h^{-1}$, respectively. Ag loading and protonation of g-C_3N_4 promoted charge separation and thus improved reactant adsorption.

1.2.3 Photocatalytic coupling of methane

Methane coupling could be an efficient way to selectively convert methane into higher hydrocarbons, such as ethane and propane. Methane coupling includes the non-oxidative coupling of methane (NOCM) and oxidative coupling of methane (OCM). In addition to hydrocarbons, OCM can also produce carbon monoxide and carbon dioxide as by-products.

NOCM: $2CH_4 \rightarrow C_2H_6 + H_2$ (8)

OCM: $4CH_4 + O_2 \rightarrow 2C_2H_6 + 2H_2O$ (9)

$2CH_4 + O_2 \rightarrow C_2H_4 + 2H_2O$ (10)

The production of ethylene (Eq. 10) does not usually occur in the photochemical coupling. Ethane seems, to be one of the primary products of the photocatalytic coupling. Ethane dehydrogenation to ethylene is thermodynamically unfavorable at ambient temperature and does not seem to be catalyzed by photocatalysts.

The photoinduced centers of some metal oxides, such as of Zn, Ti, Al and Ga oxides, are capable to dissociate methane under mild conditions with the role of photogenerated O^- holes. Among them, TiO_2 was studied in methane coupling and showed predominant CO_x production and low methane conversion in both OCM and NOCM [93,94].

Ga_2O_3 has been investigated as a promising material in NOCM under UV irradiation at mild temperature and exhibited much higher methane conversion and higher ethane selectivity (up to 96%) than other oxide semiconductors, with high stability in the reductive atmosphere [78,95]. Silica materials were also exhibiting NOCM activity after high temperature pretreatment, which generated $\equiv Si-O\bullet$ as photoactive sites via the dehydroxylation of surface hydroxyl groups [96]. More often, promotion with metals could further improve the photocatalytic NOCM performance by enhancing charge separation, accelerating charge transfer and acting as a co-catalyst.

Highly dispersed mixed metal oxide species, such as SiO_2-Al_2O_3-TiO_2, ZrO_2/SiO_2,

MgO/SiO_2 Ce/Al_2O_3 and $Ce/Ti/SiO_2$ have been investigated in NOCM at mild conditions. They exhibited higher photoactivity and ethane selectivity of above 90% [26,95,97,98]. These highly dispersed metal oxide species showed different electronic and local structures from the original bulk materials [95,99]. Among them, the SiO_2-Al_2O_3-TiO_2 ternary oxide has been reported as one of the most effective photocatalysts for NOCM with the methane conversion rate of around 1.40 $\mu mol \cdot g_{cat}^{-1} \cdot h^{-1}$, corresponding to the ethane productivity of 0.69 $\mu mol \cdot g_{cat}^{-1} \cdot h^{-1}$. However, the total C_{2+} yield of 3.74% was still very low even after 90 h of reaction [97].

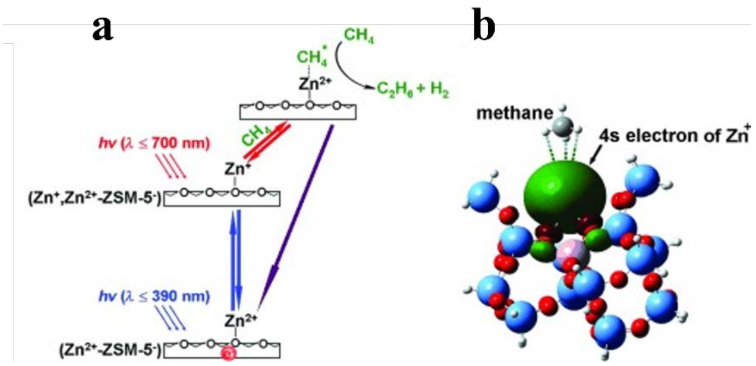

Figure 12. (a) Proposed photocatalytic mechanism over Zn-ZSM-5 catalysts and (b) geometry of the adsorbed methane molecule attracted by the Zn^+ active site (red: O, blue: Si, pink: Al, gray: C, white: H, and green: the 4s electron of Zn^+).

Chen et al [100]. investigated a zinc modified medium pore ZSM-5 zeolite photocatalysts, which achieved prominent photocatalytic NOCM performance under UV irradiation at room temperature. The methane conversion of 23.8% was achieved in 8 h and ethane selectivity was above 99.0%, corresponding to the ethane production rate of 5.95 $\mu mol \cdot g_{cat}^{-1} \cdot h^{-1}$. Note that the photocatalyst operated without obvious deactivation and coke deposition for 16 h. They suggested that the existence of univalent zinc species (Zn^+) played a key role in the efficient methane activation through the photoinduced electron attack from

Zn 4s orbital to the empty C-H σ^*-antibonding orbital (**Figure 12b**). Besides, the pores with an approximate size of 0.55 nm restricted the formation of longer chain C_{3+} hydrocarbons. Thus, a higher selectivity towards ethane was achieved. A two-stage photocatalytic process was proposed, in which UV and visible light accomplished the charge transfer from oxygen of the zeolite framework to Zn^{2+} and the methane activation upon the Zn^{+} species (**Figure 12a)**. Consequently, the photocatalyst still exhibited outstanding performance under sunlight irradiation, with the methane conversion of 0.63 $\mu mol \cdot g_{cat}^{-1} \cdot h^{-1}$ and ethane selectively above 99.9%. The activity of the photocatalyst decreased in the presence of water, which limited its application in the water-based photocatalytic systems.

Li et al. [44] further investigated the Ga^{3+} modified ETS-10 titanosilicate in photocatalytic NOCM under UV irradiation at mild temperature and achieved methane conversion rate of 29.8 $\mu mol \cdot g_{cat}^{-1} \cdot h^{-1}$ without the CO_x formation, corresponding to the methane conversion of 14.9% and ethane selectivity higher than 70%. Furthermore, the Ga^{3+} modified sample could be regenerated after thermal treatment in moist air without noticeable deactivation for 5 cycles. It revealed that only after the ion-exchange of ETS-10 with the particular metal ions such as Ga^{3+}, Al^{3+}, Zn^{2+} and Fe^{3+}, the enhanced photocatalytic activity could be observed. Among them, the Ga^{3+} modified sample showed the best performance, the Al^{3+}, Zn^{2+} and Fe^{3+} modified samples were inferior, while the Cu^{2+} modified sample was inactive. They suggested that the ion-exchange treatment formed the structure defects in the framework of ETS-10 and thus, resulted in the abundant Ti-OH groups. Besides, the modified metal cations played an important role in polarizing methane and thus reduced the activation energy for C-H cleavage. The photoexcitation firstly occurs upon the titanate composite in ETS-10. The Ti-OH groups then trap the photogenerated holes to generate active hydroxyl radicals for the H abstraction. The Ti-OH groups could be then regenerated in the presence of water and oxygen under high temperature.

In another work, Zhang and co-workers [32] fabricated a Pt loaded hierarchical macro-mesoporous structure (HGTS) consisting of Ga dopant and porous TiO_2-SiO_2 for photocatalytic NOCM using a 300 W Xe lamp under mild temperature. The methane conversion of 6.24% was achieved in 4 h, corresponding to the methane conversion rate of 3.48 $\mu mol \cdot g_{cat}^{-1} \cdot h^{-1}$ and 90% selectivity toward ethane. It was found that the optimized Ga doping was beneficial for promoting charge separation, while doping with Pt further significantly accelerated charge transfer from TiO_2 to the Pt sites due to the Mott−Schottky junction between Pt and TiO_2. Interestingly, Ga substitution in the framework reduced the electron transfer from surface oxygen vacancy to the Pt site. Methane was more easily activated by the electron-enriched metallic Pt, while the cationic Pt helped to abstract H atoms. However, the photocatalytic activity decreased by almost a half after four cycles.

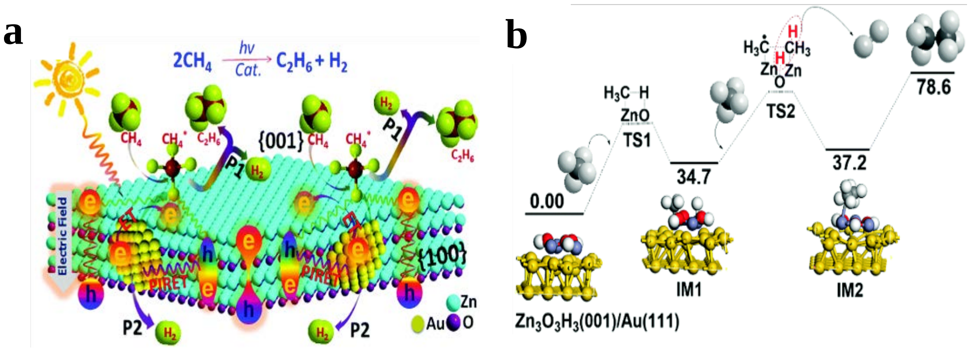

Figure 13. (a) Schematic description of the idealized Au/ZnO (001) nanocomposite for the dehydrogenative coupling of methane into ethane. (b) Potential energy diagram for the methane coupling reaction on Au/ZnO (001) clusters (energy in $kJ \cdot mol^{-1}$).

Combining of semiconductor and plasmonic nanostructures can also contribute to the enhancement of methane coupling. Long et al. [101] reported Au/ZnO nanocomposite consisting of plasmonic Au nanoparticles and ZnO nanosheets with polar 001 plane in light-driven NOCM process under simulated solar light irradiation at room temperature. The optimized Au/ZnO (001) nanocomposite exhibited ethane and hydrogen productivities of 11.0 $\mu mol \cdot g_{cat}^{-1} \cdot h^{-1}$ and 10.0 $\mu mol \cdot g_{cat}^{-1} \cdot h^{-1}$, respectively. They suggested that the coupling of the intrinsic inner electric field (IEF) of ZnO nanosheets and LSPR field of Au nanoparticles significantly accelerated the charge separation in photoexcited ZnO and promoted the electron transfer to Au nanoparticles. This makes the ZnO surface more electron poor and favored methane chemisorption and dissociation (**Figure 13a**). The proposed mechanism was shown in **Figure 13b**. Methane was firstly polarized in the ZnO surface and then oxidized by the holes to form $\text{Zn-CH}_3\bullet$ and H^+ species. Ethane was finally produced by the coupling of two methyl radicals, while the electrons were injected into the molecular orbitals of H^+ to generated hydrogen. A similar strategy was effective for methane coupling over Au/TiO_2 (001).

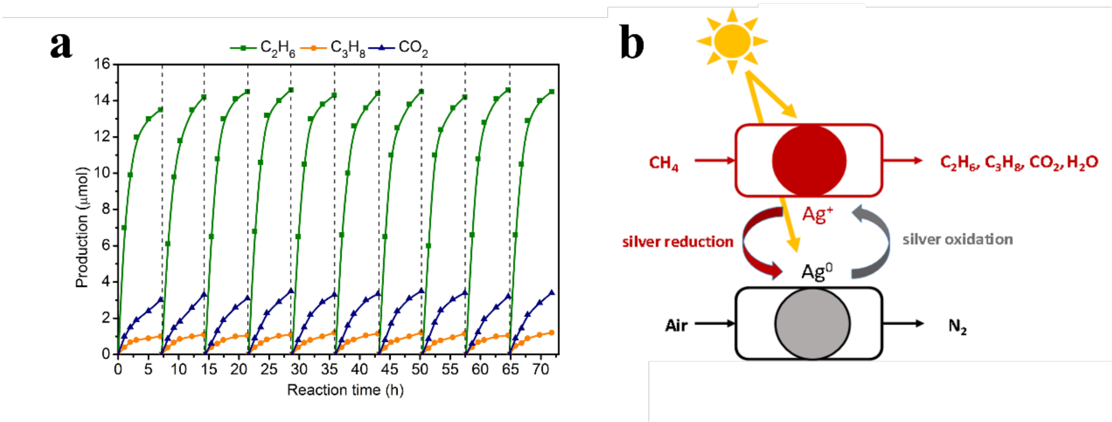

Figure 14. (a) Reaction–regeneration cycles in methane photochemical coupling on $Ag–HPW/TiO_2$. The solid lines are guides to the eye. Dashed lines represent nanocomposite regeneration and (b) Schematic description of photochemical looping process.

Recently, our group proposed [102] photochemical looping for methane coupling at room temperature over the silver-heteropolyacid-titania nanocomposites ($Ag-HPW/TiO_2$). We suggested that the n-type semiconductor TiO_2 and the p-type semiconductor HPW created a p-n heterojunction between their interfaces. Under the irradiation, photogenerated electrons were rapidly transferred from TiO_2 to HPW and resulted in silver reduction, while the abundant photogenerated holes were accumulated in TiO_2 and enhanced methane oxidation. The coupling reaction involves two methyl radicals produced via methane activation over silver sites. The reaction slowed down with the reduction of silver cations. Promisingly, the nanocomposite can be reversibly regenerated by exposing it to air under irradiation at room temperature, after which the nanocomposite still exhibited the original performance for methane coupling in numerous cycles (**Figure 14a)**. The amount of the produced ethane exactly corresponds to the silver content in the nanocomposite. The photochemical looping process achieves methane coupling selectivity over 90%, quantitative yield of ethane over 9%, high quantum efficiency (3.5% at 362 nm) and excellent stability. (**Figure 14b)**.

1.3 Major routes of methane photocatalytic conversion: challenges and outlook

A sharp increase in the interest to the methane photocatalytic conversion has been observed in the last decade (**Figure 6**). Three major routes of methane photocatalytic conversion have attracted particular attention. They involve

- methane selective oxidation with the methanol being the principal reaction product;
- methane photocatalytic dry or steam reforming to hydrogen and carbon monoxide;
- methane coupling leading to the formation of ethane and higher hydrocarbons.

The semiconductors, co-catalysts and products obtained in these three major methane photocatalytic conversion routes are displayed in **Figure 15**. Much less information is available about other methane conversion reactions. A recent paper by Hu [103] et al reports the possible use of methane and other light alkanes in the amination, alkylation, and arylation reaction over ceria photocatalysts. Direct methane aromatization with simultaneous hydrogen production was recently uncovered [104] over Si-doped GaN nanowires under ultraviolet illumination at ambient temperature.

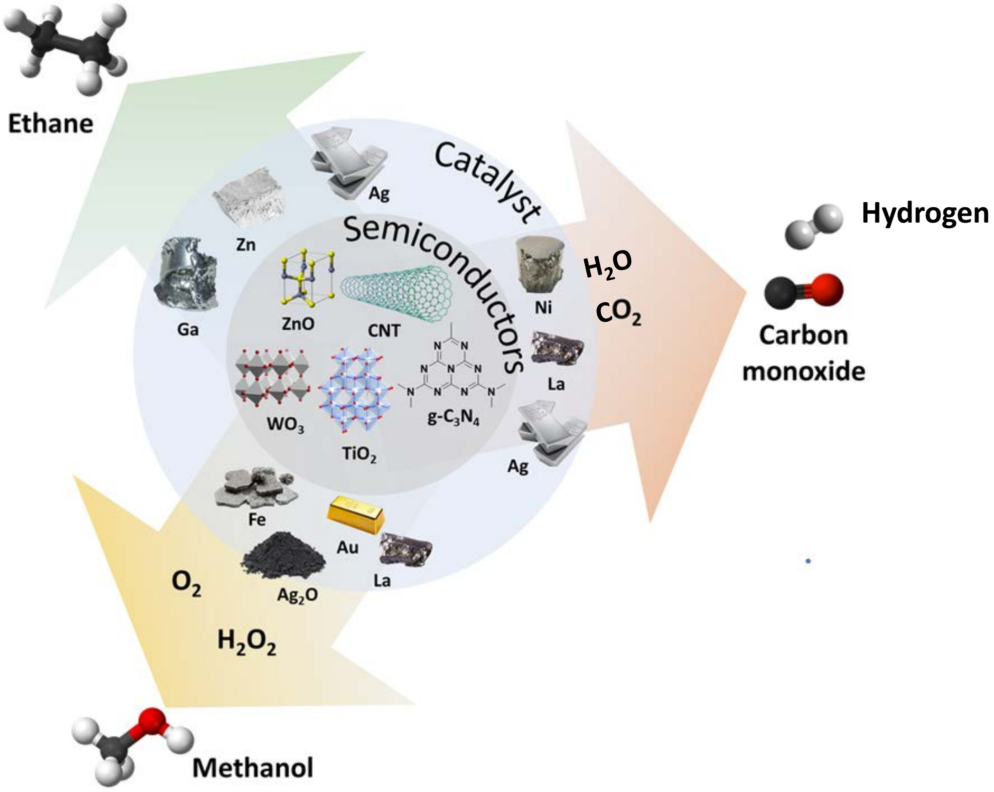

Figure 15. Semiconductors and co-catalysts for three major routes of methane photocatalytic conversion.

Let us discuss the advantages and drawbacks of each methane conversion route. Methane photocatalytic oxidation may lead to methanol, formaldehyde, formic acid, CO and CO_2. Extremely low yields of formaldehyde and formic acid were reported in the methane photocatalytic conversion. Among different oxidation processes, methane partial oxidation to methanol and methane complete oxidation to CO_2 have attracted particular attention. The complete oxidation of methane to CO_2 seems to be an attractive option to reduce the concentrations of methane present in the atmosphere. Note that methane is a GHG, which is 30 times more potent than carbon dioxide. Methane photocatalytic oxidation is an exothermic process. The methane photocatalytic oxidation to CO_2 can reduce, on the one hand, global warming and on other hand, because of the exothermic effect, it can produce renewable electricity under mild conditions.

Methanol is the target product in most of the publications dedicated to methane photocatalytic oxidation. The photocatalytic oxidation to methanol requires oxidizing agents, such as molecular oxygen, hydrogen peroxide, water or NO. The use of different oxidizing agents leads to different methanol productivities. Important, methane oxidation with water or hydrogen peroxide results in several times higher productivities compared to the methane oxidation in the presence of molecular oxygen. Since the methane photocatalytic oxidation commonly proceeds with the radical mechanisms, the reasons of a higher rate of methane conversion in the presence of water or hydrogen peroxide can be due to the much easier generation of oxygen or hydroxyl radicals for the methane activation. The selectivity of methane conversion to a larger extent depends on the concentration and reactivity of the generated radical species. Among the methane oxidizing agents, water seems to be the most efficient. It enables at the same time, the highest methane conversion rate and high selectivity to methanol. A much higher cost of hydrogen peroxide compared to methane and methanol hinders its utilization for methane photocatalytic conversion. The reactive oxygen for methane photocatalytic oxidation can be also provided by the semiconductor or cocatalysts. In this case, the reaction proceeds according to the Mars-van Krevelen mechanism [53] with periodic reduction and re-oxidation of photocatalysts. This mechanism was clearly identified over silver [50] and zinc [53] catalysts.

The literature shows a major progress in productivity of methane to methanol conversion. Thus, from 2005 to 2022 the productivity for the best catalysts known so far increased from 529 to 6453 μmol g^{-1} h^{-1}. The highest efficiency has been observed over oxides like WO_3, TiO_2, NiO, Ag/WO_3, Au supported over ZnO and Au-Cu supported over ZnO.

Methane photocatalytic reforming usually leads to hydrogen and carbon monoxide. Direct synthesis of oxygenates from methane and carbon dioxide currently seems to be highly challenging, though production of small amounts of acetone was reported by Shi [77] et al. over the Cu/CdS–TiO_2/SiO_2 catalyst under ultraviolet irradiation. The characteristic productivities for methane photocatalytic reforming are much lower than for methane oxidation to methanol. The methane dry photocatalytic reforming has been investigated in greater detail compared to the steam reforming process. Very often, the photocatalytic reforming proceeds at elevated temperatures (>100°C and even >550°C), when a contribution of thermal activation to the methane conversion rate cannot be excluded. Important, the composition of syngas produced via methane dry photocatalytic reforming is different from that, which could be expected from the stoichiometric reaction: $H_2/CO=1$; $CH_4+CO_2 \rightarrow H_2+CO$. This suggests a possible contribution of water gas shift and other processes to the methane photocatalytic reforming. Methane photocatalytic reforming to syngas can also simultaneously involve CO_2 and structural water of photocatalyst [105]. Methane photocatalytic reforming coincides with other methane reactions such as methane partial oxidation to methanol or methane coupling. That is also the reason, why the selectivity to carbon monoxide and hydrogen in methane photocatalytic reforming is rarely higher than 60-70%. The relatively rapid increase in the productivity of methane photocatalytic reforming has been observed recently. Thus, for the several last years, the productivity increased almost ten times from 142 to 1211 μmol g^{-1} h^{-1}. The highest efficiency has been observed over silver supported nanoporous graphitic carbon nitride sheets.

Photocatalytic coupling to ethane and higher hydrocarbons represents an interesting path to upgrade methane. Indeed, ethane has a higher value than methane. Moreover, ethane can be converted via cracking/dehydrogenation to ethylene, which is an important platform molecule for many chemical processes. Different to the widely studied process of high temperature methane oxidative or non-oxidative [106] couplings (OCM and NOCM), methane photochemical coupling proceeds at lower temperatures. Low temperature photocatalytic coupling of methane produces mainly ethane, while ethylene, the building block of many daily basis plastic products, is commonly produced in high temperature methane oxidative coupling [3]. Both thermally activated and photoactivated methane coupling reactions proceed via the generation of CH_3 radicals. The primary product in both coupling processes is ethane. Note that in the higher temperature process, ethane is dehydrogenated to ethylene. At high temperatures, the ethylene formation from ethane is favored by thermodynamics. In contrast, ethane is primarily produced in the low temperature photocatalytic methane coupling. At low temperatures, dehydrogenation of ethane to ethylene is thermodynamically unfavorable and does not seem to be enhanced by photocatalysis.

Relatively high selectivity to ethane (often >70% and sometimes >90%) in the photochemical and photocatalytic methane coupling has been reported in many works. A trace amount of propane and even butane are often observed. The presence of propane and higher hydrocarbons arises from the coupling reaction of methane with ethane and other produced hydrocarbons. Despite better selectivity, the main challenge of methane photocatalytic coupling seems to be lower productivity compared to the methane partial oxidation or reforming. Recently, we suggested a new concept of photochemical looping for stoichiometric synthesis of ethane from methane on the silver-based nanocomposites containing titania and heteropolyacids. The ethane productivity attained 20 μmol g^{-1} h^{-1} in this process.

The photocatalytic coupling of methane to ethane demonstrates significantly lower productivities in comparison with the methane oxidation to methanol or methane reforming. However, a gradual increase in the ethane productivity of ethane with time has been observed. Supported Au, Ag, Zn and Ga based materials demonstrate productivities of ethane in the range 5 to 5000 μmol g^{-1} h^{-1}.

Table 2. Selectivity and productivity of different methane photocatalytic conversion routes

	Selectivity to the target products, %	Productivity, $\mu mol \cdot g_{cat}^{-1} \cdot h^{-1}$
Photocatalytic methane oxidation - to methanol	>40	5-20 (in air) and 6453 (in H_2O/O_2 or H_2O_2)
-to carbon monoxide	>80	430 (in air)
Photocatalytic methane reforming DRM	>60-70	for H_2/CO >600-1200
Photocatalytic coupling of methane	>70-90	10-5000

The characteristic state-of the art productivities and selectivities of the major routes of methane photocatalytic conversion are summarized in **Table 2**. In terms of productivity, the three routes of methane photochemical conversion can be ranked in the following order: methane partial oxidation > methane coupling > methane reforming. The productivity ranges from >1000-6000 μmol g^{-1} h^{-1} in methane reforming or methane oxidation to methanol to 5000 μmol g^{-1} h^{-1} in methane coupling. The opposite trend is observed for the selectivity of methane photocatalytic conversion processes. Higher selectivity is observed (**Table 2**) in the methane coupling to ethane followed by methane partial oxidation and then by methane reforming. Almost stoichiometric conversion of methane to ethane can be achieved in the photocatalytic process, while the selectivity of methane reforming is usually about 60-70%.

Higher selectivity and productivity seem to be major challenges for the photocatalytic methane conversion. The photo-conversion efficiencies of photochemical methane conversions are generally lower than 10%. Higher solar-to-fuel efficiency of 12.5% has been reported [107] for DRM and that of 11.7% for photocatalytic oxidation of methane to methanol [69]. The photo-conversion efficiencies have been however generally lower than 5% or even 1% for photochemical methane coupling [101,102].

Currently, the majorities of photocatalytic methane conversion reactions are carried out in home-made or commercial batch reactors with various volumes. Relatively high residence time in batch reactors leads to the overoxidation of the methane conversion intermediates. Design of new photoreactors such as fluidized, slurry, fixed bed, membrane, optical-fiber, monolith or internally illuminated monolith photoreactors [108–111] can also enhance the efficiency of light collection, exposure of the photocatalyst to the irradiation, heat and mass transfer. Particular attention should be paid to the absence of even very tiny leaks. Even a very small amount of excess oxygen can affect the reaction rate and selectivity.

The current scientific immaturity of the methane photochemical conversion processes does not allow to envision industrial or practical utilization in the future. Among the discussed methane photocatalytic conversion routes, the most promising could be photocatalytic methane oxidation to methanol. Methanol is a valuable platform molecule, it has a much higher cost compared to ethane produced by methane coupling or to syngas, which is manufactured by methane reforming. The methane partial oxidation to methanol exhibits relatively higher productivity and selectivity.

Direct mild conversion of methane is one of the main targets in the modern society. The photochemical processes such as methane partial oxidation, methane reforming and methane coupling should provide opportunities to perform methane conversion to value-added products, under mild conditions, instead of methane combustion. This should significantly decrease the GHG effects due to the uncontrollable emission of methane and carbon dioxide and will contribute to the optimized utilization of fossil and renewable methane feedstocks.

1.4 Objective of thesis

The photocatalytic methane partial oxidation to methanol exhibits relatively higher productivity and selectivity as reviewed above. Some expensive and non-environmentally friendly oxidants are used necessary for achieving higher productivity. Photocatalytic oxidation of methane in water to high value oxygenates (formaldehyde, formic acid) have been rarely reported. Even methanol has been the main product in very limited works. The photocatalytic coupling of methane to ethane often demonstrates significantly lower productivities in comparison with the other processes but exhibits highest selectivity. The photocatalytic oxidative coupling of methane to ethane has been rarely studied and indicates a potential route to achieve both higher coupling productivity and selectivity.

This thesis aims to develop and propose new efficient photocatalysts and photocatalytic processes to utilize methane. We focus on the photocatalytic oxidative/non-oxidative coupling of methane to hydrocarbons and photocatalytic methane oxidation in water to valuable oxygenates, to study effective way to activate methane and provide new ideas for its photocatalytic conversion. Our goal is to develop environmental, sustainable and efficient photocatalytic processes to selectively convert methane to ethane and formic acid under mild conditions.

The simple oxide, TiO_2, which has been demonstrated as efficient photocatalysts among various semiconductors, has been used for photocatalytic methane conversion in this work. In addition, the cocatalysts have been introduced into TiO_2 semiconductor substrate forming composite photocatalysts to promote the charge transfer/separation, improve light absorption and lower the activation energy for methane conversion.

The Au NPs, which is a stable and interesting metal of visible light utilization with plasmonic effect as introduced above and charge transfer/separation, has been studied as a cocatalyst. Additional, heteropolyacids (HPAs) has been used as a material for the preparation of the other cocatalysts. HPAs, possessing characteristics of strong Brønsted acidity and easily tunable acidity, have been demonstrated to display outstanding catalytic performance in a wide range of acid-catalyzed reactions as well as oxidation reactions. However, the lack of thermal stability and high solubility in polar media of HPAs has limited their further applications in heterogeneous reactions. In contrast to coating HPAs onto semiconductor substrate, it is more effective to exchange protons of HPAs with different cations (e.g., Cs^+, Ag^+) to form insoluble salts, which can tune and amplify HPAs reactivity, prevent HPAs leaching out from catalysts or even result in the appearance of bifunctional or multifunctional catalysis. Such a conceptual strategy would lead to offer a new class of tunable and recoverable HPA salts catalysts with high efficiency and heterogeneity, providing versatile applications in sustainable chemistry. Compared to $H_4SiW_{12}O_{40}$ and other HPAs such as $H_3PMo_{12}O_{40}$, $H_3PW_{12}O_{40}$ (HPW) presents stronger Brønsted acidity and thermal stability, because of the weak interaction between acidic protons and large Keggin anion. Furthermore, we have recently demonstrated that HPW is capable in promoting metal dispersion and enhancing charge separation as introduced above, which results in better methane conversion compared with other HPAs.

Thereby, in this work, we have focused on designing silver and cesium modified HPW cocatalysts (CsPW and AgPW) prepared by an ion-exchanged method and Au NPs cocatalyst with average particle size ranging from 6 nm to 30 nm prepared by seeded growth method. After which CsPW and AgPW have been mechanically mixed with TiO_2 to form heteropolyacid salt-TiO_2 composite, while Au NPs have been supported on TiO_2 by impregnation to form Au/TiO_2.

1.5 References

[1] E. McFarland, Unconventional chemistry for unconventional natural gas, Science (80-.). 338 (2012) 341–342. https://doi.org/10.1126/science.1226840.

[2] E. V. Kondratenko, T. Peppel, D. Seeburg, V.A. Kondratenko, N. Kalevaru, A. Martin, S. Wohlrab, Methane conversion into different hydrocarbons or oxygenates: Current status and future perspectives in catalyst development and reactor operation, Catal. Sci. Technol. 7 (2017) 366–381. https://doi.org/10.1039/c6cy01879c.

[3] R. Horn, R. Schlögl, Methane Activation by Heterogeneous Catalysis, Catal. Letters. 145 (2015) 23–39. https://doi.org/10.1007/s10562-014-1417-z.

[4] P. Schwach, X. Pan, X. Bao, Direct Conversion of Methane to Value-Added Chemicals over Heterogeneous Catalysts: Challenges and Prospects, Chem. Rev. 117 (2017) 8497–8520. https://doi.org/10.1021/acs.chemrev.6b00715.

[5] G.E. Johnson, W.A. Decker, A.J. Forney, J.H. Field, Hydrogen cyanide produced from coal and ammonia, Ind. Eng. Chem. Process Des. Dev. 7 (1968) 137–143. https://doi.org/10.1021/i260025a027.

[6] J.J. Spivey, G. Hutchings, Catalytic aromatization of methane, Chem. Soc. Rev. 43 (2014) 792–803. https://doi.org/10.1039/c3cs60259a.

[7] M.H. Ab Rahim, M.M. Forde, R.L. Jenkins, C. Hammond, Q. He, N. Dimitratos, J.A. Lopez-Sanchez, A.F. Carley, S.H. Taylor, D.J. Willock, D.M. Murphy, C.J. Kiely, G.J. Hutchings, Oxidation of methane to methanol with hydrogen peroxide using supported gold-palladium alloy nanoparticles, Angew. Chemie - Int. Ed. 52 (2013) 1280–1284. https://doi.org/10.1002/anie.201207717.

[8] C. Hammond, M.M. Forde, M.H. Ab Rahim, A. Thetford, Q. He, R.L. Jenkins, N. Dimitratos, J.A. Lopez-Sanchez, N.F. Dummer, D.M. Murphy, A.F. Carley, S.H. Taylor, D.J. Willock, E.E. Stangland, J. Kang, H. Hagen, C.J. Kiely, G.J.

Hutchings, Direct catalytic conversion of methane to methanol in an aqueous medium by using copper-promoted Fe-ZSM-5, Angew. Chemie - Int. Ed. 51 (2012) 5129–5133. https://doi.org/10.1002/anie.201108706.

[9] P. Tomkins, M. Ranocchiari, J.A. Van Bokhoven, Direct Conversion of Methane to Methanol under Mild Conditions over Cu-Zeolites and beyond, Acc. Chem. Res. 50 (2017) 418–425. https://doi.org/10.1021/acs.accounts.6b00534.

[10] N. Agarwal, S.J. Freakley, R.U. McVicker, S.M. Althahban, N. Dimitratos, Q. He, D.J. Morgan, R.L. Jenkins, D.J. Willock, S.H. Taylor, C.J. Kiely, G.J. Hutchings, Aqueous Au-Pd colloids catalyze selective CH 4 oxidation to CH 3 OH with O 2 under mild conditions, Science (80-.). 358 (2017) 223–227. https://doi.org/10.1126/science.aan6515.

[11] M.H. Groothaert, P.J. Smeets, B.F. Sels, P.A. Jacobs, R.A. Schoonheydt, Selective Oxidation of Methane by the Bis(μ-oxo)dicopper Core Stabilized on ZSM-5 and Mordenite Zeolites, J. AM. CHEM. SOC. 127 (2005) 1394–1395. https://doi.org/10.1021/ja047158u.

[12] S. Grundner, M.A.C. Markovits, G. Li, M. Tromp, E.A. Pidko, E.J.M. Hensen, A. Jentys, M. Sanchez-Sanchez, J.A. Lercher, Single-site trinuclear copper oxygen clusters in mordenite for selective conversion of methane to methanol, Nat. Commun. 6 (2015). https://doi.org/10.1038/ncomms8546.

[13] V.L. Sushkevich, D. Palagin, M. Ranocchiari, J.A. van Bokhoven, Selective anaerobic oxidation of methane enables direct synthesis of methanol, Science (80-.). 356 (2017) 523–527. https://doi.org/10.1126/science.aam9035.

[14] D. Palagin, V.L. Sushkevich, J.A. Van Bokhoven, Water Molecules Facilitate Hydrogen Release in Anaerobic Oxidation of Methane to Methanol over Cu/Mordenite, ACS Catal. 9 (2019) 10365–10374. https://doi.org/10.1021/acscatal.9b02702.

[15] J. Zhu, V.L. Sushkevich, A.J. Knorpp, M.A. Newton, S.C.M. Mizuno, T. Wakihara, T. Okubo, Z. Liu, J.A. Van Bokhoven, Cu-Erionite Zeolite Achieves High Yield in Direct Oxidation of Methane to Methanol by Isothermal Chemical Looping, Chem. Mater. 32 (2020) 1448–1453. https://doi.org/10.1021/acs.chemmater.9b04223.

[16] P. Tang, Q. Zhu, Z. Wu, D. Ma, Methane activation: the past and future, Energy Environ. Sci. 7 (2014) 2580–2591. https://doi.org/10.1039/C4EE00604F.

[17] X. Meng, X. Cui, N.P. Rajan, L. Yu, D. Deng, X. Bao, Direct Methane Conversion under Mild Condition by Thermo-, Electro-, or Photocatalysis, Chem. 5 (2019) 2296–2325. https://doi.org/10.1016/j.chempr.2019.05.008.

[18] L. Sun, Y. Wang, N. Guan, L. Li, Methane Activation and Utilization: Current Status and Future Challenges, Energy Technol. (2019). https://doi.org/10.1002/ente.201900826.

[19] B. Wang, S. Albarracín-Suazo, Y. Pagán-Torres, E. Nikolla, Advances in methane conversion processes, Catal. Today. 285 (2017) 147–158. https://doi.org/10.1016/j.cattod.2017.01.023.

[20] F. Roudesly, J. Oble, G. Poli, Metal-catalyzed C H activation/functionalization: The fundamentals, J. Mol. Catal. A Chem. 426 (2017) 275–296. https://doi.org/10.1016/j.molcata.2016.06.020.

[21] L. Yuliati, H. Yoshida, Photocatalytic conversion of methane, Chem. Soc. Rev. 37 (2008) 1592. https://doi.org/10.1039/b710575b.

[22] X. Cai, Y.H. Hu, Advances in catalytic conversion of methane and carbon dioxide to highly valuable products, Energy Sci. Eng. 7 (2019) 4–29. https://doi.org/10.1002/ese3.278.

[23] L. Pan, M. Ai, C. Huang, L. Yin, X. Liu, R. Zhang, S. Wang, Z. Jiang, X. Zhang, J.J. Zou, W. Mi, Manipulating spin polarization of titanium dioxide for efficient

photocatalysis, Nat. Commun. 11 (2020). https://doi.org/10.1038/s41467-020-14333-w.

[24] U.G. Akpan, B.H. Hameed, Parameters affecting the photocatalytic degradation of dyes using TiO2-based photocatalysts: A review, J. Hazard. Mater. 170 (2009) 520–529. https://doi.org/10.1016/j.jhazmat.2009.05.039.

[25] Q. Li, H. Yue, C. Liu, K. Ma, S. Zhong, B. Liang, S. Tang, A Photocatalytic Transformation Realized by Pd/TiO2 Particle Size Modulation: from Oxidative Ethane Dehydrogenation to Direct Ethane Dehydrogenation, Chem. Eng. J. 395 (2020) 125120. https://doi.org/10.1016/j.cej.2020.125120.

[26] L. Yuliati, T. Hattori, H. Yoshida, Highly dispersed magnesium oxide species on silica as photoactive sites for photoinduced direct methane coupling and photoluminescence, Phys. Chem. Chem. Phys. 7 (2005) 195–201. https://doi.org/10.1039/b410089a.

[27] L. Yuliati, H. Itoh, H. Yoshida, Preparation of isolated highly dispersed titanium oxides on silica by sol-gel method for photocatalytic non-oxidative direct methane coupling, Stud. Surf. Sci. Catal. 162 (2006) 961–968. https://doi.org/10.1016/S0167-2991(06)81003-7.

[28] C.E. Taylor, R.P. Noceti, New developments in the photocatalytic conversion of methane to methanol, Catal. Today. 55 (2000) 259–267. https://doi.org/10.1016/S0920-5861(99)00244-8.

[29] E. Kowalska, Z. Wei, M. Janczarek, Band-gap Engineering of Photocatalysts: Surface Modification versus Doping, in: Visible Light. Photocatal., Wiley-VCH Verlag GmbH & Co. KGaA, Weinheim, Germany, 2018: pp. 447–484. https://doi.org/10.1002/9783527808175.ch16.

[30] B. Han, W. Wei, L. Chang, P. Cheng, Y.H. Hu, Efficient Visible Light Photocatalytic CO2 Reforming of CH4, ACS Catal. 6 (2016) 494–497.

https://doi.org/10.1021/acscatal.5b02653.

[31] M.D. Ward, J.F. Brazdil, S.P. Mehandru, A.B. Anderson, Methane photoactivation on copper molybdate. An experimental and theoretical study, J. Phys. Chem. 91 (1987) 6515–6521. https://doi.org/10.1021/j100310a019.

[32] S. Wu, X. Tan, J. Lei, H. Chen, L. Wang, J. Zhang, Ga-Doped and Pt-Loaded Porous TiO 2 –SiO 2 for Photocatalytic Nonoxidative Coupling of Methane, J. Am. Chem. Soc. 141 (2019) 6592–6600. https://doi.org/10.1021/jacs.8b13858.

[33] Y. Ben-Shahar, F. Scotognella, I. Kriegel, L. Moretti, G. Cerullo, E. Rabani, U. Banin, Optimal metal domain size for photocatalysis with hybrid semiconductor-metal nanorods, Nat. Commun. 7 (2016) 1–7. https://doi.org/10.1038/ncomms10413.

[34] K. Villa, S. Murcia-López, T. Andreu, J.R. Morante, Mesoporous WO3 photocatalyst for the partial oxidation of methane to methanol using electron scavengers, Appl. Catal. B Environ. 163 (2015) 150–155. https://doi.org/10.1016/j.apcatb.2014.07.055.

[35] S. Mukherjee, F. Libisch, N. Large, O. Neumann, L. V. Brown, J. Cheng, J.B. Lassiter, E.A. Carter, P. Nordlander, N.J. Halas, Hot electrons do the impossible: Plasmon-induced dissociation of H 2 on Au, Nano Lett. 13 (2013) 240–247. https://doi.org/10.1021/nl303940z.

[36] P. Christopher, H. Xin, S. Linic, Visible-light-enhanced catalytic oxidation reactions on plasmonic silver nanostructures, Nat. Chem. 3 (2011) 467–472. https://doi.org/10.1038/nchem.1032.

[37] A. Marimuthu, J. Zhang, S. Linic, Tuning selectivity in propylene epoxidation by plasmon mediated photo-switching of Cu oxidation state, Science (80-.). 340 (2013) 1590–1593. https://doi.org/10.1126/science.1231631.

[38] H. Liu, X. Meng, T.D. Dao, L. Liu, P. Li, G. Zhao, T. Nagao, L. Yang, J. Ye,

Light assisted CO2 reduction with methane over SiO2 encapsulated Ni nanocatalysts for boosted activity and stability, J. Mater. Chem. A. 5 (2017) 10567–10573. https://doi.org/10.1039/c7ta00704c.

[39] B. László, K. Baán, E. Varga, A. Oszkó, A. Erdőhelyi, Z. Kónya, J. Kiss, Photo-induced reactions in the CO2-methane system on titanate nanotubes modified with Au and Rh nanoparticles, Appl. Catal. B Environ. 199 (2016) 473–484. https://doi.org/10.1016/j.apcatb.2016.06.057.

[40] H. Liu, X. Meng, T.D. Dao, H. Zhang, P. Li, K. Chang, T. Wang, M. Li, T. Nagao, J. Ye, Conversion of Carbon Dioxide by Methane Reforming under Visible-Light Irradiation: Surface-Plasmon-Mediated Nonpolar Molecule Activation, Angew. Chemie - Int. Ed. 54 (2015) 11545–11549. https://doi.org/10.1002/anie.201504933.

[41] G. Baffou, R. Quidant, Thermo-plasmonics: using metallic nanostructures as nano-sources of heat, Laser Photon. Rev. 7 (2013) 171–187. https://doi.org/10.1002/lpor.201200003.

[42] G. Baffou, R. Quidant, Nanoplasmonics for chemistry, Chem. Soc. Rev. 43 (2014) 3898. https://doi.org/10.1039/c3cs60364d.

[43] S. Linic, U. Aslam, C. Boerigter, M. Morabito, Photochemical transformations on plasmonic metal nanoparticles, Nat. Mater. 14 (2015) 567–576. https://doi.org/10.1038/nmat4281.

[44] L. Li, Y.Y. Cai, G.D. Li, X.Y. Mu, K.X. Wang, J.S. Chen, Synergistic effect on the photoactivation of the methane C-H bond over Ga 3+-modified ETS-10, Angew. Chemie - Int. Ed. 51 (2012) 4702–4706. https://doi.org/10.1002/anie.201200045.

[45] H. Song, X. Meng, Z. Wang, H. Liu, J. Ye, Solar-Energy-Mediated Methane Conversion, Joule. 3 (2019) 1606–1636.

https://doi.org/10.1016/j.joule.2019.06.023.

[46] I. Grčić, J. Marčec, L. Radetić, A.-M. Radovan, I. Melnjak, I. Jajčinović, I. Brnardić, Ammonia and methane oxidation on TiO2 supported on glass fiber mesh under artificial solar irradiation, Environ. Sci. Pollut. Res. (2020). https://doi.org/10.1007/s11356-020-09561-y.

[47] X. Chen, Y. Li, X. Pan, D. Cortie, X. Huang, Z. Yi, Photocatalytic oxidation of methane over silver decorated zinc oxide nanocatalysts, Nat. Commun. 7 (2016). https://doi.org/10.1038/ncomms12273.

[48] R. de Richter, T. Ming, P. Davies, W. Liu, S. Caillol, Removal of non-CO 2 greenhouse gases by large-scale atmospheric solar photocatalysis, Prog. Energy Combust. Sci. 60 (2017) 68–96. https://doi.org/10.1016/j.pecs.2017.01.001.

[49] S.L. Kaliaguine, B.N. Shelimov, V.B. Kazansky, Reactions of methane and ethane with hole centers O-, J. Catal. 55 (1978) 384–393. https://doi.org/10.1016/0021-9517(78)90225-7.

[50] X. Chen, Y. Li, X. Pan, D. Cortie, X. Huang, Z. Yi, Photocatalytic oxidation of methane over silver decorated zinc oxide nanocatalysts, Nat. Commun. 7 (2016) 1–8. https://doi.org/10.1038/ncomms12273.

[51] F. Sastre, V. Fornés, A. Corma, H. García, Selective, room-temperature transformation of methane to C1 oxygenates by deep UV photolysis over zeolites, J. Am. Chem. Soc. 133 (2011) 17257–17261. https://doi.org/10.1021/ja204559z.

[52] W. Zhou, X. Qiu, Y. Jiang, Y. Fan, S. Wei, D. Han, L. Niu, Z. Tang, Highly selective aerobic oxidation of methane to methanol over gold decorated zinc oxide: Via photocatalysis, J. Mater. Chem. A. 8 (2020) 13277–13284. https://doi.org/10.1039/d0ta02793f.

[53] X. Yu, V. De Waele, A. Löfberg, V. Ordomsky, A.Y.A.Y. Khodakov, V. De Waele, A. Löfberg, V. Ordomsky, A.Y.A.Y. Khodakov, Selective photocatalytic

conversion of methane into carbon monoxide over zinc-heteropolyacid-titania nanocomposites, Nat. Commun. 10 (2019) 700. https://doi.org/10.1038/s41467-019-08525-2.

[54] X. Chen, S. Li, Photooxidation of methane to methanol by molecular oxygen on water-preadsorbed porous TiO2-based catalysts, Chem. Lett. (2000) 314–315. https://doi.org/10.1246/cl.2000.314.

[55] M.A. Gondal, A. Hameed, Z.H. Yamani, A. Arfaj, Photocatalytic transformation of methane into methanol under UV laser irradiation over WO3, TiO2 and NiO catalysts, Chem. Phys. Lett. 392 (2004) 372–377. https://doi.org/10.1016/j.cplett.2004.05.092.

[56] A. Hameed, I.M.I. Ismail, M. Aslam, M.A. Gondal, Photocatalytic conversion of methane into methanol: Performance of silver impregnated WO3, Appl. Catal. A Gen. 470 (2014) 327–335. https://doi.org/10.1016/j.apcata.2013.10.045.

[57] J. Du, W. Chen, G. Wu, Y. Song, X. Dong, G. Li, J. Fang, W. Wei, Y. Sun, Evoked methane photocatalytic conversion to C2 oxygenates over ceria with oxygen vacancy, Catalysts. 10 (2020). https://doi.org/10.3390/catal10020196.

[58] W. Zhu, M. Shen, G. Fan, A. Yang, J.R. Meyer, Y. Ou, B. Yin, J. Fortner, M. Foston, Z. Li, Z. Zou, B. Sadtler, Facet-Dependent Enhancement in the Activity of Bismuth Vanadate Microcrystals for the Photocatalytic Conversion of Methane to Methanol, ACS Appl. Nano Mater. 1 (2018) 6683–6691. https://doi.org/10.1021/acsanm.8b01490.

[59] Y. Zeng, H.C. Liu, J.S. Wang, X.Y. Wu, S.L. Wang, Synergistic photocatalysis-Fenton reaction for selective conversion of methane to methanol at room temperature, Catal. Sci. Technol. 10 (2020) 2329–2332. https://doi.org/10.1039/d0cy00028k.

[60] S. Shi, Z. Sun, C. Bao, T. Gao, Y.H. Hu, The special route toward conversion of

methane to methanol on a fluffy metal-free carbon nitride photocatalyst in the presence of H2O2, Int. J. Energy Res. (2020). https://doi.org/10.1002/er.5088.

[61] K. Villa, S. Murcia-López, T. Andreu, J.R. Morante, On the role of WO3 surface hydroxyl groups for the photocatalytic partial oxidation of methane to methanol, Catal. Commun. 58 (2015) 200–203. https://doi.org/10.1016/j.catcom.2014.09.025.

[62] J. Xie, R. Jin, A. Li, Y. Bi, Q. Ruan, Y. Deng, Y. Zhang, S. Yao, G. Sankar, D. Ma, J. Tang, Highly selective oxidation of methane to methanol at ambient conditions by titanium dioxide-supported iron species, Nat. Catal. 1 (2018) 889–896. https://doi.org/10.1038/s41929-018-0170-x.

[63] S. Wei, X. Zhu, P. Zhang, Y. Fan, Z. Sun, X. Zhao, D. Han, L. Niu, Aerobic oxidation of methane to formaldehyde mediated by crystal-O over gold modified tungsten trioxide via photocatalysis, Appl. Catal. B Environ. 283 (2021) 119661. https://doi.org/10.1016/j.apcatb.2020.119661.

[64] Z. Sun, C. Wang, Y.H. Hu, Highly selective photocatalytic conversion of methane to liquid oxygenates over silicomolybdic-Acid/TiO2under mild conditions, J. Mater. Chem. A. 9 (2021) 1713–1719. https://doi.org/10.1039/d0ta09226f.

[65] K. Ohkubo, K. Hirose, Light-Driven C−H Oxygenation of Methane into Methanol and Formic Acid by Molecular Oxygen Using a Perfluorinated Solvent, Angew. Chemie - Int. Ed. 57 (2018) 2126–2129. https://doi.org/10.1002/anie.201710945.

[66] J. Xie, R. Jin, A. Li, Y. Bi, Q. Ruan, Y. Deng, Y. Zhang, S. Yao, G. Sankar, D. Ma, J. Tang, Highly selective oxidation of methane to methanol at ambient conditions by titanium dioxide-supported iron species, Nat. Catal. 1 (2018) 889–896. https://doi.org/10.1038/s41929-018-0170-x.

[67] Y. Fan, W. Zhou, X. Qiu, H. Li, Y. Jiang, Z. Sun, D. Han, L. Niu, Z. Tang, Selective photocatalytic oxidation of methane by quantum-sized bismuth vanadate, Nat. Sustain. 4 (2021) 509–515. https://doi.org/10.1038/s41893-021-00682-x.

[68] Y. Zhou, L. Zhang, W. Wang, Direct functionalization of methane into ethanol over copper modified polymeric carbon nitride via photocatalysis, Nat. Commun. 10 (2019) 1–8. https://doi.org/10.1038/s41467-019-08454-0.

[69] H. Song, X. Meng, S. Wang, W. Zhou, X. Wang, T. Kako, J. Ye, Direct and Selective Photocatalytic Oxidation of CH4 to Oxygenates with O2 on Cocatalysts/ZnO at Room Temperature in Water, J. Am. Chem. Soc. 141 (2019) 20507–20515. https://doi.org/10.1021/jacs.9b11440.

[70] H. Song, X. Meng, S. Wang, W. Zhou, S. Song, T. Kako, J. Ye, Selective Photo-oxidation of Methane to Methanol with Oxygen over Dual-Cocatalyst-Modified Titanium Dioxide, ACS Catal. 10 (2020) 14318–14326. https://doi.org/10.1021/acscatal.0c04329.

[71] L. Luo, Z. Gong, Y. Xu, J. Ma, H. Liu, J. Xing, J. Tang, Binary Au–Cu Reaction Sites Decorated ZnO for Selective Methane Oxidation to C1 Oxygenates with Nearly 100% Selectivity at Room Temperature, J. Am. Chem. Soc. 144 (2022) 740–750. https://doi.org/10.1021/jacs.1c09141.

[72] X. Cai, S. Fang, Y.H. Hu, Unprecedentedly high efficiency for photocatalytic conversion of methane to methanol over Au-Pd/TiO2-what is the role of each component in the system?, J. Mater. Chem. A. 9 (2021) 10796–10802. https://doi.org/10.1039/d1ta00420d.

[73] Y. Kohno, T. Tanaka, T. Funabiki, S. Yoshida, Photoreduction of Carbon Dioxide with Methane over ZrO 2, Chem. Lett. 26 (1997) 993–994. https://doi.org/10.1246/cl.1997.993.

[74] K. Teramura, T. Tanaka, H. Ishikawa, Y. Kohno, T. Funabiki, Photocatalytic Reduction of CO 2 to CO in the Presence of H 2 or CH 4 as a Reductant over MgO, J. Phys. Chem. B. 108 (2004) 346–354. https://doi.org/10.1021/jp0362943.

[75] Y. Kohno, T. Tanaka, T. Funabiki, S. Yoshida, Reaction mechanism in the photoreduction of CO2 with CH4 over ZrO2, Phys. Chem. Chem. Phys. 2 (2000) 5302–5307. https://doi.org/10.1039/b005315p.

[76] S.N. Habisreutinger, L. Schmidt-Mende, J.K. Stolarczyk, Photocatalytic reduction of CO2 on TiO2 and other semiconductors, Angew. Chemie - Int. Ed. 52 (2013) 7372–7408. https://doi.org/10.1002/anie.201207199.

[77] D. Shi, Y. Feng, S. Zhong, Photocatalytic conversion of CH4 and CO2 to oxygenated compounds over Cu/CdS-TiO2/SiO2 catalyst, in: Catal. Today, 2004: pp. 505–509. https://doi.org/10.1016/j.cattod.2004.09.004.

[78] L. Yuliati, H. Itoh, H. Yoshida, Photocatalytic conversion of methane and carbon dioxide over gallium oxide, Chem. Phys. Lett. 452 (2008) 178–182. https://doi.org/10.1016/j.cplett.2007.12.051.

[79] B. Han, W. Wei, L. Chang, P. Cheng, Y.H. Hu, Efficient Visible Light Photocatalytic CO2 Reforming of CH4, ACS Catal. 6 (2016) 494–497. https://doi.org/10.1021/acscatal.5b02653.

[80] H. Liu, T.D. Dao, L. Liu, X. Meng, T. Nagao, J. Ye, Light assisted CO2 reduction with methane over group VIII metals: Universality of metal localized surface plasmon resonance in reactant activation, Appl. Catal. B Environ. 209 (2017) 183–189. https://doi.org/10.1016/j.apcatb.2017.02.080.

[81] Q. Zhang, M. Mao, Y. Li, Y. Yang, H. Huang, Z. Jiang, Q. Hu, S. Wu, X. Zhao, Novel photoactivation promoted light-driven CO2 reduction by CH4 on Ni/CeO2 nanocomposite with high light-to-fuel efficiency and enhanced stability, Appl. Catal. B Environ. 239 (2018) 555–564.

https://doi.org/10.1016/j.apcatb.2018.08.052.

[82] D. Takami, Y. Ito, S. Kawaharasaki, A. Yamamoto, H. Yoshida, Low temperature dry reforming of methane over plasmonic Ni photocatalysts under visible light irradiation, Sustain. Energy Fuels. 3 (2019) 2968–2971. https://doi.org/10.1039/c9se00206e.

[83] H. Liu, M. Li, T.D. Dao, Y. Liu, W. Zhou, L. Liu, X. Meng, T. Nagao, J. Ye, Design of PdAu alloy plasmonic nanoparticles for improved catalytic performance in CO2 reduction with visible light irradiation, Nano Energy. 26 (2016) 398–404. https://doi.org/10.1016/j.nanoen.2016.05.045.

[84] H. Song, X. Meng, T.D. Dao, W. Zhou, H. Liu, L. Shi, H. Zhang, T. Nagao, T. Kako, J. Ye, Light-Enhanced Carbon Dioxide Activation and Conversion by Effective Plasmonic Coupling Effect of Pt and Au Nanoparticles, ACS Appl. Mater. Interfaces. 10 (2018) 408–416. https://doi.org/10.1021/acsami.7b13043.

[85] L. Zhou, J.M.P. Martirez, J. Finzel, C. Zhang, D.F. Swearer, S. Tian, H. Robatjazi, M. Lou, L. Dong, L. Henderson, P. Christopher, E.A. Carter, P. Nordlander, N.J. Halas, Light-driven methane dry reforming with single atomic site antenna-reactor plasmonic photocatalysts, Nat. Energy. 5 (2020) 61–70. https://doi.org/10.1038/s41560-019-0517-9.

[86] H. Yoshida, K. Hirao, J.I. Nishimoto, K. Shimura, S. Kato, H. Itoh, T. Hattori, Hydrogen production from methane and water on platinum loaded titanium oxide photocatalysts, J. Phys. Chem. C. 112 (2008) 5542–5551. https://doi.org/10.1021/jp077314u.

[87] K. Shimura, T. Yoshida, H. Yoshida, Photocatalytic activation of water and methane over modified gallium oxide for hydrogen production, J. Phys. Chem. C. 114 (2010) 11466–11474. https://doi.org/10.1021/jp1012126.

[88] H. Yoshida, S. Kato, K. Hirao, J.I. Nishimoto, T. Hattori, Photocatalytic steam

reforming of methane over platinum-loaded semiconductors for hydrogen production, Chem. Lett. 36 (2007) 430–431. https://doi.org/10.1246/cl.2007.430.

[89] K. Shimura, S. Kato, T. Yoshida, H. Itoh, T. Hattori, H. Yoshida, Photocatalytic steam reforming of methane over sodium tantalate, J. Phys. Chem. C. 114 (2010) 3493–3503. https://doi.org/10.1021/jp902761x.

[90] L. Yu, Y. Shao, D. Li, Direct combination of hydrogen evolution from water and methane conversion in a photocatalytic system over Pt/TiO2, Appl. Catal. B Environ. 204 (2017) 216–223. https://doi.org/10.1016/j.apcatb.2016.11.039.

[91] K. Shimura, H. Kawai, T. Yoshida, H. Yoshida, Bifunctional rhodium cocatalysts for photocatalytic steam reforming of methane over alkaline titanate, ACS Catal. 2 (2012) 2126–2134. https://doi.org/10.1021/cs2006229.

[92] B. Tahir, M. Tahir, N.A.S. Amin, Silver loaded protonated graphitic carbon nitride (Ag/pg-C3N4) nanosheets for stimulating CO2 reduction to fuels via photocatalytic bi-reforming of methane, Appl. Surf. Sci. 493 (2019) 18–31. https://doi.org/10.1016/j.apsusc.2019.06.257.

[93] K. Okabe, K. Sayama, H. Kusama, H. Arakawa, Photo-oxidative coupling of methane over TiO2-based catalysts, Chem. Lett. (1997) 457–458. https://doi.org/10.1246/cl.1997.457.

[94] G.N. Kuzmin, M. V. Knatko, S. V. Kurganov, Light and X-ray-induced chemistry of methane on TiO2, React. Kinet. Catal. Lett. 23 (1983) 313–317. https://doi.org/10.1007/BF02065581.

[95] L. Yuliati, T. Hattori, H. Itoh, H. Yoshida, Photocatalytic nonoxidative coupling of methane on gallium oxide and silica-supported gallium oxide, J. Catal. 257 (2008) 396–402. https://doi.org/10.1016/j.jcat.2008.05.022.

[96] L. Yuliati, M. Tsubota, A. Satsuma, H. Itoh, H. Yoshida, Photoactive sites on pure silica materials for nonoxidative direct methane coupling, J. Catal. 238

(2006) 214–220. https://doi.org/10.1016/j.jcat.2005.12.002.

[97] H. Yoshida, N. Matsushita, Y. Kato, T. Hattori, Synergistic active sites on SiO2-Al2O3-TiO2 photocatalysts for direct methane coupling, J. Phys. Chem. B. 107 (2003) 8355–8362. https://doi.org/10.1021/jp034458+.

[98] L. Yuliati, T. Hamajima, T. Hattori, H. Yoshida, Highly dispersed Ce(III) species on silica and alumina as new photocatalysts for non-oxidative direct methane coupling, Chem. Commun. (2005) 4824–4826. https://doi.org/10.1039/b507698f.

[99] H. Yoshida, M.G. Chaskar, Y. Kato, T. Hattori, Active sites on silica-supported zirconium oxide for photoinduced direct methane conversion and photoluminescence, J. Photochem. Photobiol. A Chem. 160 (2003) 47–53. https://doi.org/10.1016/S1010-6030(03)00220-X.

[100] L. Li, G.D. Li, C. Yan, X.Y. Mu, X.L. Pan, X.X. Zou, K.X. Wang, J.S. Chen, Efficient sunlight-driven dehydrogenative coupling of methane to ethane over a Zn+-modified zeolite, Angew. Chemie - Int. Ed. 50 (2011) 8299–8303. https://doi.org/10.1002/anie.201102320.

[101] L. Meng, Z. Chen, Z. Ma, S. He, Y. Hou, H.H. Li, R. Yuan, X.H. Huang, X. Wang, X. Wang, J. Long, Gold plasmon-induced photocatalytic dehydrogenative coupling of methane to ethane on polar oxide surfaces, Energy Environ. Sci. 11 (2018) 294–298. https://doi.org/10.1039/c7ee02951a.

[102] X. Yu, V.L. Zholobenko, S. Moldovan, D. Hu, D. Wu, V. V Ordomsky, A.Y. Khodakov, Stoichiometric methane conversion to ethane using photochemical looping at ambient temperature, Nat. Energy. 5 (2020) 511–519. https://doi.org/10.1038/s41560-020-0616-7.

[103] A. Hu, J.J. Guo, H. Pan, Z. Zuo, Selective functionalization of methane, ethane, and higher alkanes by cerium photocatalysis, Science (80-.). 361 (2018) 668–

672. https://doi.org/10.1126/science.aat9750.

[104] L. Li, S. Fan, X. Mu, Z. Mi, C.J. Li, Photoinduced conversion of methane into benzene over GaN nanowires, J. Am. Chem. Soc. 136 (2014) 7793–7796. https://doi.org/10.1021/ja5004119.

[105] B. László, K. Baán, A. Oszkó, A. Erdőhelyi, J. Kiss, Z. Kónya, Hydrogen evolution in the photocatalytic reaction between methane and water in the presence of CO2 on titanate and titania supported Rh and Au catalysts, Top. Catal. 61 (2018) 875–888. https://doi.org/10.1007/s11244-018-0936-z.

[106] X. Guo, G. Fang, G. Li, H. Ma, H. Fan, L. Yu, C. Ma, X. Wu, D. Deng, M. Wei, D. Tan, R. Si, S. Zhang, J. Li, L. Sun, Z. Tang, X. Pan, X. Bao, Direct, nonoxidative conversion of methane to ethylene, aromatics, and hydrogen, Science (80-.). 344 (2014) 616–619. https://doi.org/10.1126/science.1253150.

[107] H. Huang, M. Mao, Q. Zhang, Y. Li, J. Bai, Y. Yang, M. Zeng, X. Zhao, Solar-Light-Driven CO2 Reduction by CH4 on Silica-Cluster-Modified Ni Nanocrystals with a High Solar-to-Fuel Efficiency and Excellent Durability, Adv. Energy Mater. 8 (2018) 1–11. https://doi.org/10.1002/aenm.201702472.

[108] A.A. Khan, M. Tahir, Recent advancements in engineering approach towards design of photo-reactors for selective photocatalytic CO2 reduction to renewable fuels, J. CO2 Util. 29 (2019) 205–239. https://doi.org/10.1016/j.jcou.2018.12.008.

[109] P.Y. Liou, S.C. Chen, J.C.S. Wu, D. Liu, S. MacKintosh, M. Maroto-Valer, R. Linforth, Photocatalytic CO2 reduction using an internally illuminated monolith photoreactor, Energy Environ. Sci. 4 (2011) 1487–1494. https://doi.org/10.1039/c0ee00609b.

[110] O. Ola, M.M. Maroto-Valer, Review of material design and reactor engineering on TiO2 photocatalysis for CO2 reduction, J. Photochem. Photobiol. C

Photochem. Rev. 24 (2015) 16–42. https://doi.org/10.1016/j.jphotochemrev.2015.06.001.

[111] V.H. Nguyen, J.C.S. Wu, Recent developments in the design of photoreactors for solar energy conversion from water splitting and CO2 reduction, Appl. Catal. A Gen. 550 (2018) 122–141. https://doi.org/10.1016/j.apcata.2017.11.002.

Chapter 2. Experimental

2.1 Materials and experiments

2.1.1 Materials

Titanium (IV) oxide (P25, 99.5%, primary 21 nm), phosphotungstic acid hydrate ($H_3O_{40}PW_{12}·xH_2O$, HPW), phosphomolybic acid hydrate ($H_3(P(Mo_3O_{10})_4)·xH_2O$, HPMo), tungstosilicic acid hydrate ($H_4(Si(W_3O_{10})_4)·xH_2O$, HSiW), silicomolybdic acid solution ($H_4(Si(Mo_3O_{10})_4)·xH_2O$, HSiMo), HCHO solution (1000 μg/mL), silver nitrate ($AgNO_3$, ≥99.0%), caesium nitrate ($CsNO_3$, ≥99.0%), ammonium bicarbonate (NH_4HCO_3, ≥99.0%) and 5% Ru/Al_2O_3, Silicon dioxide (SiO_2, nanopowder, 10-20 nm particle size (BET), 99.5% trace metals basis), gold (III) chloride hydrate ($HAuCl_4·xH_2O$) and Tetraethyl orthosilicate (TEOS) were purchased from Sigma-Aldrich. Air and methane were supplied by Air Liquid and were used in the catalytic reactions. All chemicals were used without treatment.

2.1.2 Synthesis of phosphotungstic acid salt/TiO₂ composite catalysts

The different phosphotungstic salts (AgPW, CsPW and NH_4PW) were prepared by mixing HPW hydrate aqueous solution with the stoichiometric amount of $AgNO_3$, $CsNO_3$ and NH_4HCO_3 aqueous solution, respectively. The Cs salts of different heteropolyacids (CsPW, CsPMo, CsSiW and CsSiMo) were prepared by mixing $CsNO_3$ aqueous solution with the stoichiometric amount of heteropolyacids aqueous solution (HPW, HPMo, HSiW and HSiMo), respectively. All the precipitated salts were then washed by deionized water for three times and filtered out. They have a broad grain size distribution from tens of nanometers to hundreds of nanometers.

In **Chapter 3**. Preparation of AgPW-TiO_2: 0.1 g AgPW was mechanically mixed with a necessary amount of TiO_2 to provide specific AgPW mass ratio (10%, 30%, 60%, 90%, 95% and 99%); Preparation of composites containing AgPW mixed with other semiconductors (ZnO, PCN and $SrTiO_3$): 0.1 g AgPW was mechanically mixed with a necessary amount of ZnO, PCN and $SrTiO_3$ to provide AgPW mass ratio of 90%; Preparation of CsPW-TiO_2: 0.1 g CsPW was mechanically mixed with a necessary amount of TiO_2 to provide specific CsPW mass ratio of 90%; Preparation of HPW-TiO_2: 0.1 g HPW was mechanically mixed with a necessary amount of TiO_2 to provide specific HPW mass ratio of 90%; Preparation of Ag_2O/TiO_2: The Ag_2O/TiO_2 was prepared by incipient wetness impregnation of 0.1 g TiO_2 support with a necessary aqueous solutions of silver nitrate ($AgNO_3$) to provide the same Ag amount as in 90% AgPW-TiO_2. Unless otherwise specified in **Chapter 3**, the mass ratio of heteropolyacid salt (AgPW and CsPW) is 90% in all the heteropolyacid salt-semiconductor samples.

In **Chapter 5**. Preparation of CsPW-TiO_2: 0.1 g CsPW was mechanically mixed with a necessary amount of TiO_2 to provide specific CsPW mass ratio (10%, 30%, 60% and 80%); Preparation of the other heteropolyacid salts (AgPW, NH_4PW, CsPMo, CsSiW and CsSiMo)-TiO_2: 0.1 g heteropolyacid salts was mechanically mixed with a necessary amount of TiO_2 to provide 60% heteropolyacid salts mass ratio; Preparation of HPW-TiO_2: 0.5 g TiO_2 was mechanically mixed with a necessary amount of HPW hydrate to provide the corresponding HPW amount as in 60% CsPW-TiO_2; Preparation of Cs/TiO_2: The Cs/TiO_2 was prepared by incipient wetness impregnation of TiO_2 with aqueous solutions of caesium nitrate ($CeNO_3$) to provide the same amount of caesium as in CsPW-TiO_2. All the pre-synthesized samples were dried at 353 K overnight and calcined (except for NH_4PW and NH_4PW-TiO_2) at 573 K in air for 3 h with the 2 °C min^{-1} temperature ramp before using. Unless otherwise specified in **Chapter 5**, the mass ratio of heteropolyacid salt is 60% in all the heteropolyacid salt-TiO_2 samples.

2.1.3 Synthesis of Au/TiO$_2$ catalysts with a series of Au particle size

In **Chapter 4**. Au colloid solution with a range of average Au NPs sizes (6 nm, 14 nm, 22 nm, and 30 nm) were firstly prepared as the previous work [1] via the seeded growth method. Briefly, a seed solution was prepared by injecting 1 mL of chloroauric acid solution (25 mM) into 150 mL of a boiling solution of sodium citrate (2.2 mM) contained in a 3 neck round bottom flask and fitted with a reflux condenser and thermometer. The reaction was allowed to proceed for 15 min and then cooled to 90 °C. 1 mL of chloroauric acid solution (25 mM) was injected into the seed solution and allowed react for 30 min. This was repeated twice. After the third addition had reacted for 30 min, 55 mL of sample was harvested and replaced with 53 mL of ddH$_2$O and 2 mL of sodium citrate solution (60 mM). This acted as the seed solution for the next generation. This process was repeated four times. The electron microscopy images of the colloidal gold NPs are shown in **Figures 1**.

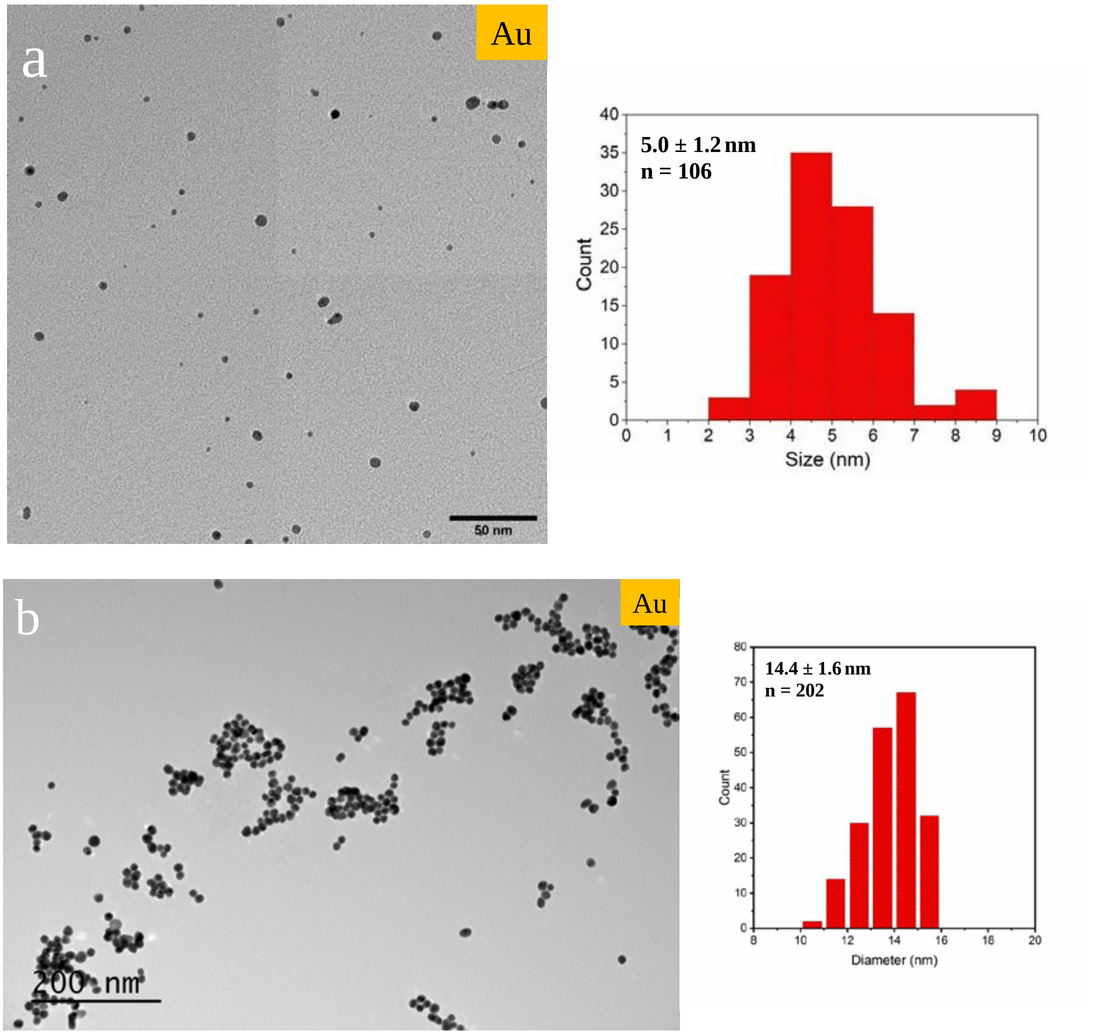

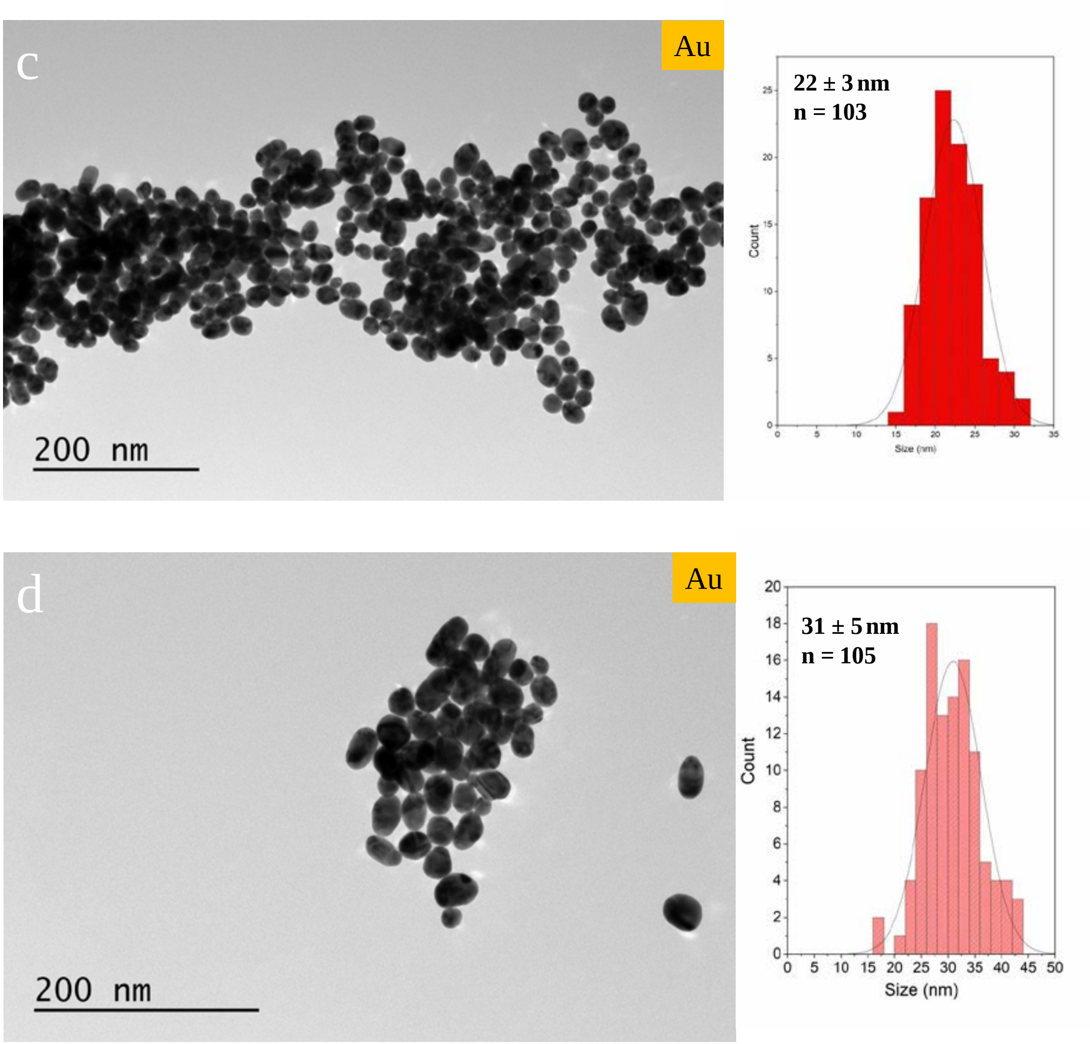

Figure 1. TEM images histograms of particle size distributions of Au nanoparticles (a) 6 nm (b) 14 nm, (c) 22 nm and (d) 30 nm in size.

The titania and silica supported catalysts with gold nanoparticles were synthesized by incipient wetness impregnation of TiO_2 and/or SiO_2 supports with the corresponding Au colloid solutions. The catalysts are labelled **x nm Au/TiO_2** or **x nm Au/SiO_2**, where **x** indicates the Au nanoparticle size. The Au/TiO_2 and Au/SiO_2 samples were dried at 60 °C overnight to have the fresh catalysts. The electron microscopy images of the fresh **Au/TiO_2** samples are shown in **Figures 2**.

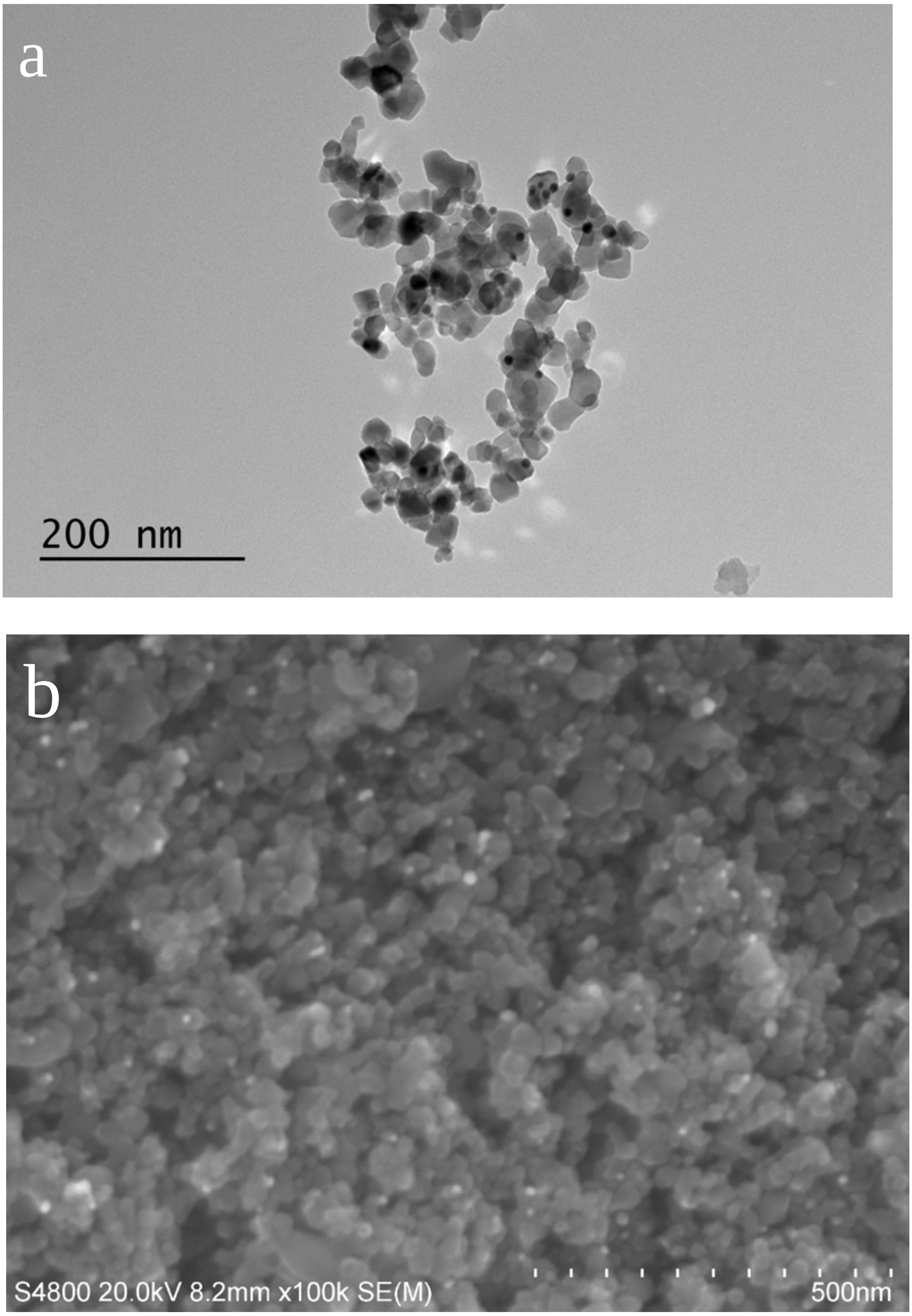
a
200 nm
b
S4800 20.0kV 8.2mm x100k SE(M)
500nm

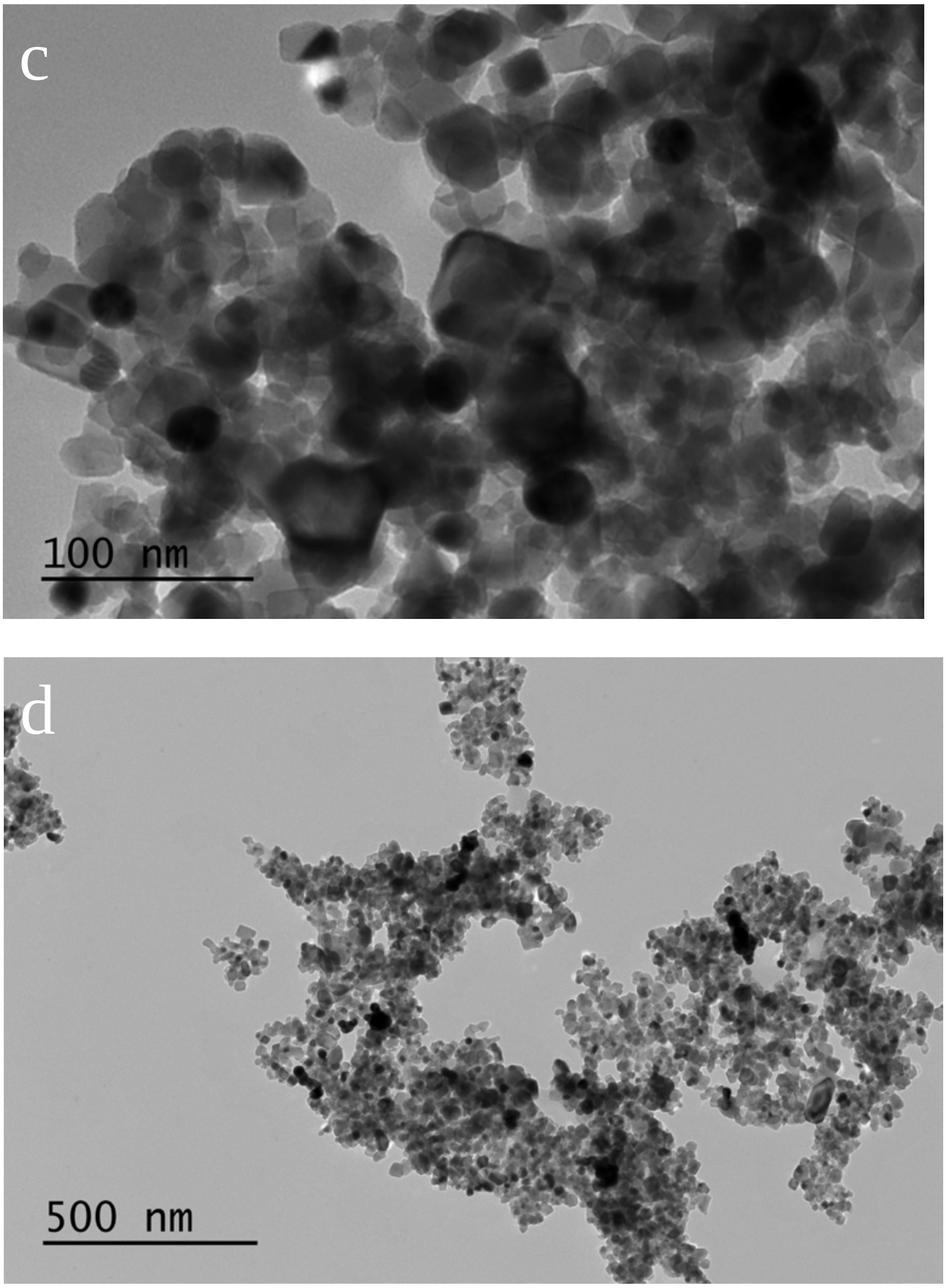

Figure 2. TEM and SEM images of fresh (a) 6 nm Au/TiO_2, (b) 14 nm Au/TiO_2, (c) 22 nm Au/TiO_2 and (d) 30 nm Au/TiO_2.

The fresh **Au/TiO$_2$** samples are then calcined at 300 ℃ for 6 h with a heating rate of 2 ℃ min^{-1} before use. The electron microscopy images of the calcined **Au/TiO$_2$** are shown in **Figures 1** in the **Chapter 4.** The theoretical loading of Au is 5 wt% for all samples and the actual Au loadings of samples obtained from X-Ray Fluorescence Spectrometer (XRF) are displayed in **Table 1**.

Table 1. Au loading in samples obtained from XRF

Samples	Au loadings (wt%)	
	Theoretical	XRF
6 nm Au/TiO$_2$	5	4.35
14 nm Au/TiO$_2$		4.26
14 nm Au/SiO$_2$		4.57
22 nm Au/TiO$_2$		4.74
30 nm Au/TiO$_2$		4.34

The **14 nm Au/TiO$_2$** sample was treated with TEOS using the following procedure: 0.2 g TEOS was firstly dissolved in 3.0 g n-hexane solution and stirred for 30 min. Next, 0.1 g **14 nm Au/TiO$_2$** was dispersed in above solution and stirred overnight. The sample was then centrifuged and calcined at 500 ℃ for 6 h with a heating rate of 2 ℃ min^{-1} before use.

2.2 Catalyst characterization

The X-ray diffraction patterns were recorded on a PANalytical Empyrean X-ray diffractometer in Bragg–Brentano configuration with a 0.02° step size and 1 s step time. Cu Kα radiation (40 kV and 30 mA) was used as the X-ray source. The crystalline phases were identified by comparing the diffraction patterns with those of the standard powder X-ray diffraction files (JCPDS).

The XPS analysis was performed in a Thermo Fisher ESCALAB 250Xi photoelectron spectrometer using monochromatic Al Kα (1,486.7 eV) X-ray irradiation and a 180° double-focusing hemispherical analyzer with a six-channel detector. The binding energy of the photoemission spectra was calibrated to C 1s peak with a binding energy of 284.8 eV.

The TEM analysis was carried out on a JEOL 2100 FEG S/TEM microscope operated at 200 kV and equipped with a spherical aberration probe corrector. Before analysis, the samples were dispersed in ethanol and deposited on a holey carbon-coated TEM grid. In STEM, the images were recorded using an HAADF detector with inner and outer diameters of about 73 and 194 mrad. EDS analyses allowing the elemental mapping were performed in the S/TEM using a JEOL Silicon Drift Detector (DrySD60GV, sensor size 60 mm) with a solid angle of approximately 0.6 srad.

The photoluminescence spectroscopy (PL) measurements were performed on a LabRam HR (Horiba Scientific). For excitation, 325 nm radiation from a diode-pumped solid-state 1 mW laser was used. The spectrophotometer has an entrance slit of 100 mm and is equipped with a 300 lines per mm grating that permits achieving a spectral resolution of 3.8 cm per pixel. The luminescence light was detected with a CCD camera operating at -135°C.

The electrochemical experiments were performed in a standard three–electrode configuration, where a glassy carbon (GC) electrode (0.28 cm^2 geometric area), a graphite rod and an Ag/AgCl electrode were used as working, counter, and reference electrodes, respectively. The GC surface was polished with 0.05 μm alumina slurry and kept in ultrasonic bath for 5 minutes in water and acetone before any modifications. Then, 28 μL of aqueous catalyst solution (2 mg/mL) was dripped on the clean GC surface, which was kept at room temperature until complete drying. The catalyst loading of 200 $\mu g/cm^2$ was achieved. The measured potentials were calibrated in relation to a reversible hydrogen electrode following the equation $E_{RHE} = E_{Ag/AgCl} + 0.059pH + E^0_{Ag/AgCl}$ ($E^0_{Ag/AgCl} = 0.197$ V at 25°C). Linear sweep voltammetry (LSV) was recorded in 0.5 M H_2SO_4 solution saturated with N_2, at a scan rate of 10 mV s^{-1}.

Chronoamperometry (CA) experiments were performed at –0.5 V using the same electrolyte. For light–induced experiments, the GC electrode was irradiated with 370 nm and 525 nm Kessil PR 160 LEDs (average intensity of 137 mW/cm^2).

TGA was performed under air flow (10 ml min−1) and nitrogen flow (10 ml min−1) in the temperature range 40–800 °C with a heating rate of 5 °C min−1 on a Mettler Toledo SMP/PF7458/MET/600W instrument.

The analysis of paramagnetic species has been performed by Continuous-Wave Electron Paramagnetic Resonance (CW–EPR). These experiments were performed on a Bruker ELEXSYS E500 spectrometer operating in X-band (9.5 GHz). The following conditions were used for the in-situ measurements: a microwave power of 2 mW, modulation amplitude of 1 G with a conversion time of 40 ms and 50 scans. The EPR spectra were recorded at 120 K to avoid electron-hole recombination. The spin trapping experiments are performed with [DMPO] = 80 mM, microwave power of 10mW, modulation amplitude of 0.2 G, a conversion time of 5 ms and 100 scans. An EPR quick pressure tube is used to work under a controlled atmosphere. Data were simulated using WinSim software.

Fourier transform infra-red (FTIR) spectra were recorded using a Thermo Fisher Scientific Nicolet 6700 FTIR (32 scans at a resolution of 4 cm^{-1} resolution) equipped with a mercury cadmium telluride detector. A self-supported wafer of catalysts (diameter, 13 mm, 40 mg catalyst) was heated at 200 °C to remove adsorbed water under vacuum (<10−5 torr) and subsequently cooled to room temperature for adsorption of CO and in-situ experiment with methane and air.

The *in-situ* time-resolved X-ray absorption spectra (XAS) in the transmission mode were measured at the SuperXAS beamline (Swiss Light Source) using a gas manifold system and a capillary reactor. The experimental setup was described in detail in previous reports. The Ag-HPW-TiO_2 nanocomposite (3-5 mg) was loaded in the quartz capillary (OD=1 mm, wall thickness=0.02 mm) and pressed from both sides with quartz wool. The setup has zero dead volume and allows maintaining constant very low gas velocities (~1-2 ncm^3/min). The sample was exposed to UV irradiation using a Hamamatsu Mercury-Xenon spot light source, equipped with a quartz light-guide to deliver a stable and uniform illumination. The schema and picture of the setup are shown in **Figure 3**. The *in-situ* time-resolved XAS data were recorded at room temperature. The measuring times of an XAS spectrum was 5 min.

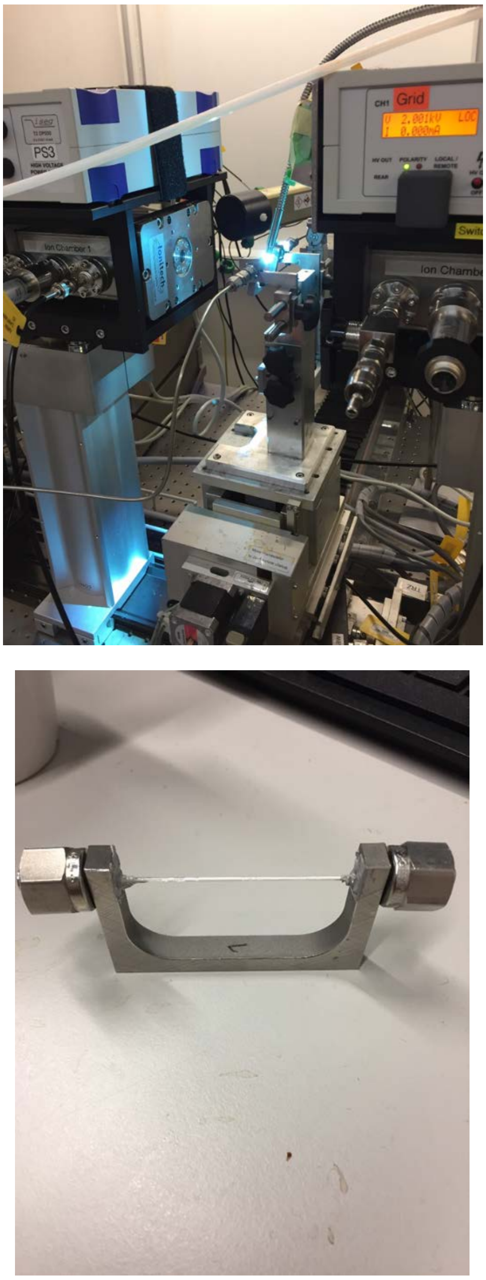

Figure 3. Experimental setup used for in-situ XAS measurements.

2.3 Photocatalytic test

2.3.1 Photocatalytic methane coupling

A commercial 230 mL batch reactor and a home-made flow reactor equipped with a quart window on the top were used for photocatalytic methane coupling tests (**Figure. 4a and b**). The light source was provided by a 400 W Hg-Xe lamp from Newport (66485-500HX-R1) with full irradiation (from ~200 to 1100 nm).

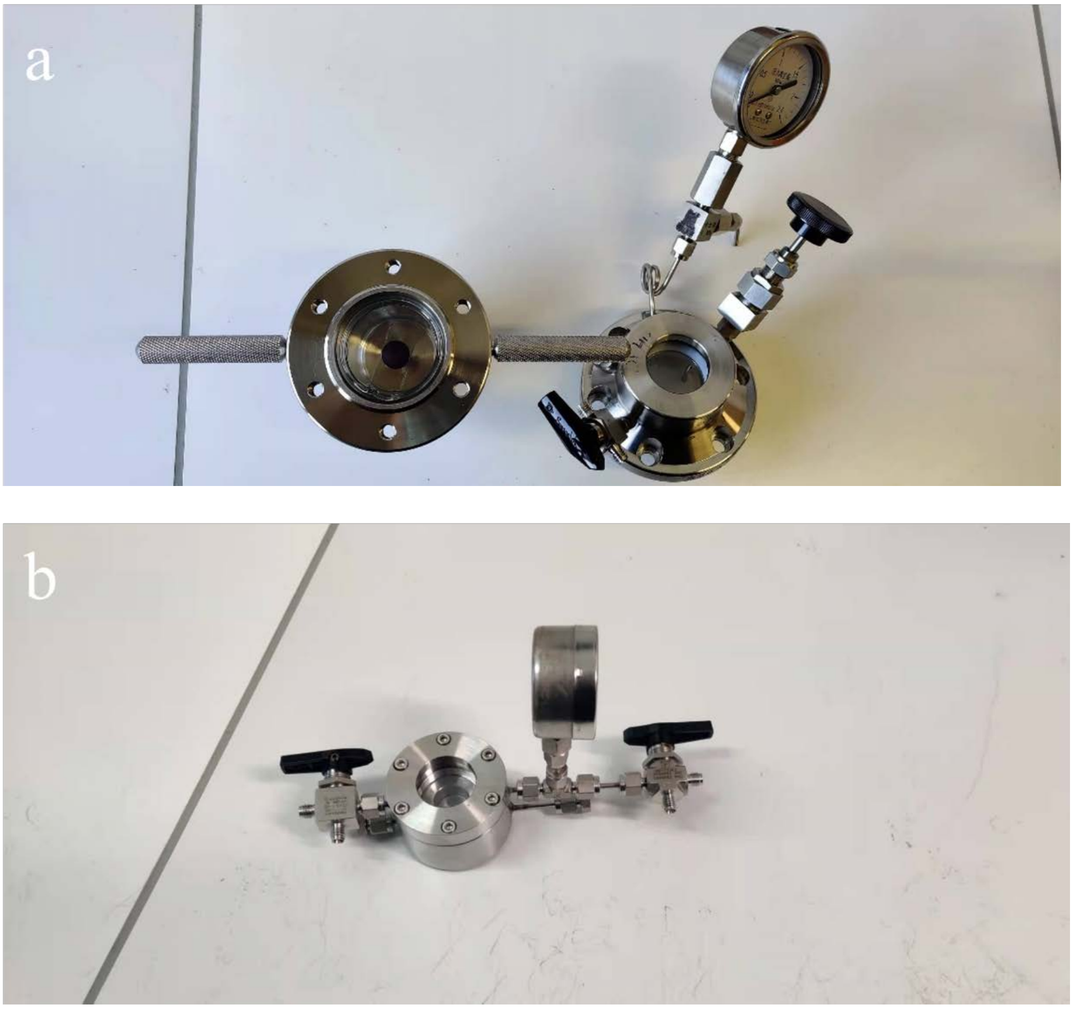

Figure 4. Picture of (a) commercial batch reactor and (b) home-made flow reactor

Typically, in the batch process, 50 mg photocatalyst was placed on a quartz glass holder on the bottom of the batch reactor. The reactor is firstly evacuated using a vacuum pump and filled with methane/air mixture. Nota that methane and air form explosive mixtures with lower explosive limit of 4.4 % CH_4 by volume of air and upper explosive limit of 16.4 % CH_4 by volume of air.

The gas pressure was then increased up to 0.3 MPa and the reactor was kept in the dark for 30 min to ensure an adsorption–desorption equilibrium between the photocatalysts and reactants before irradiation. During the reaction, the temperature was maintained at 20±3 °C by an attached cooling system (Minichiller 300). After reaction, the gas was directly injected into GC (PerkinElmer Clarus 580 GC) through Swagelok tube and analyzed by PoraBOND Q and ShinCarbon ST 100/120 columns with Ar as the carrier gas, accompanied by a flame ionization detector and a thermal conductivity detector.

In the continuous gas flow process, 20 mg photocatalyst was firstly dispersed on the bottle of flow reactor. Then, reaction gas CH_4/synthetic air (20 vol.% O_2/N_2) with a total flowing rate of 41 ml min^{-1} (gas ratio CH_4/air, 40/1) was introduced to the reactor. After catalytic performance became stable, the gas products were analyzed as in batch process.

The surface temperature of photocatalyst was measured by a thermocouple. In the batch process, the temperature of samples was ~ 40 °C. In the continuous gas flow process, the temperature of samples was ~ 75 °C. The conducted experiments showed that these temperatures in neither batch process nor continuous gas flow process are incapable to drive methane conversion in the absence of irradiation.

The apparent quantum yield (AQY) at 360 nm was calculated according to the following equation.

$$\text{AQY} = \frac{R(electron) * N_A}{ISt/E_\lambda} * 100\%$$

where N_A, I, S and t stand for the Avogadro's constant, light irradiance on the sample (W cm^{-2}), irradiation area (cm^{-2}) and reaction time (s), respectively. E_λ (J) is given by hc/λ (λ = 362 nm). R(electron) represents the number of electrons used in the formation of the products. RC_2(electron) and RC_3(electron) are the number of moles of electrons used for the formations of C_2H_6 and C_3H_8, respectively. R(electron) = RC_2(electron) + RC_3(electron) = $2n(C_2H_6) + 3n(C_3H_8)$, where $n(C_2H_6)$ and $n(C_3H_8)$ are the number of moles of C_2H_6 and C_3H_8, respectively.

2.3.2 Photocatalytic methane oxidation

A commercial 230 mL batch reactor equipped with a quart window on the top was used for photocatalytic methane oxidation reaction tests (**Figure. 4a**). The light source was provided by a 400 W Hg-Xe lamp from Newport (66485-500HX-R1) with full irradiation (from ~200 to 1100 nm) The spectrum of light source of 400 W Hg-Xe lamp and characteristics of filter FSQ-GG435 and filter FSQ-U340 are shown below, respectively.

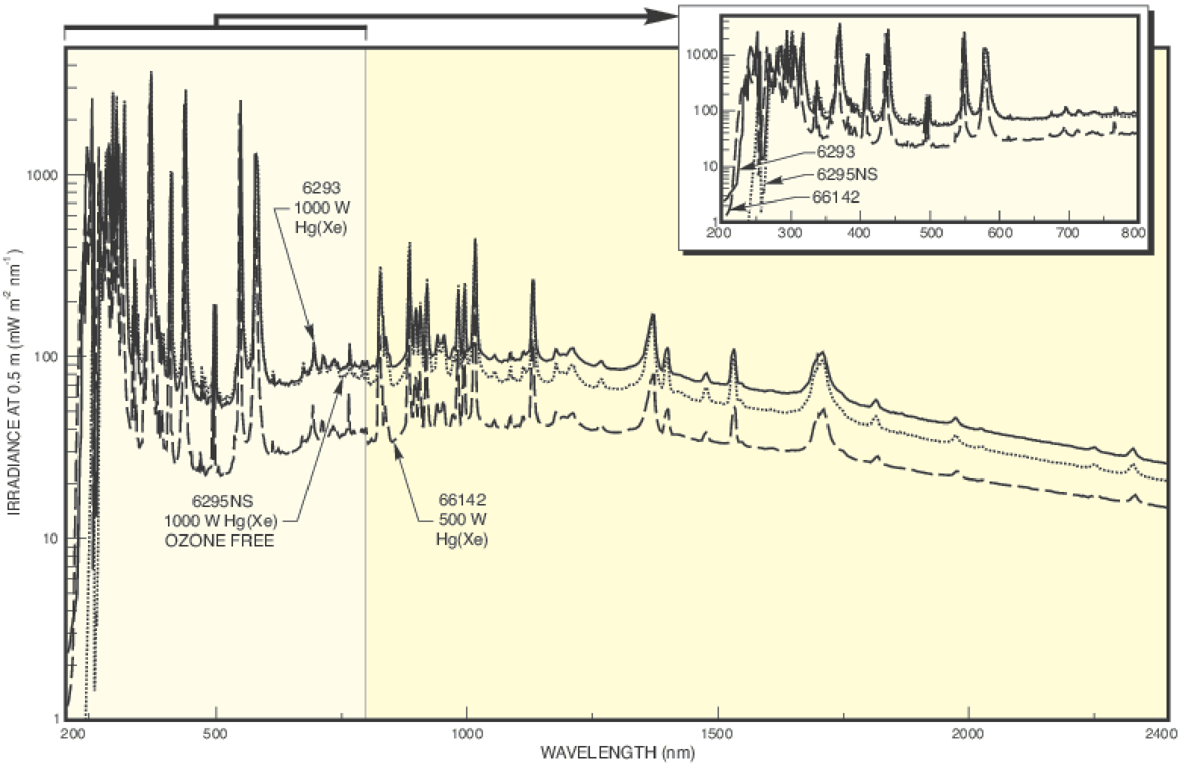

The spectrum of light source of 400 W Hg-Xe lamp

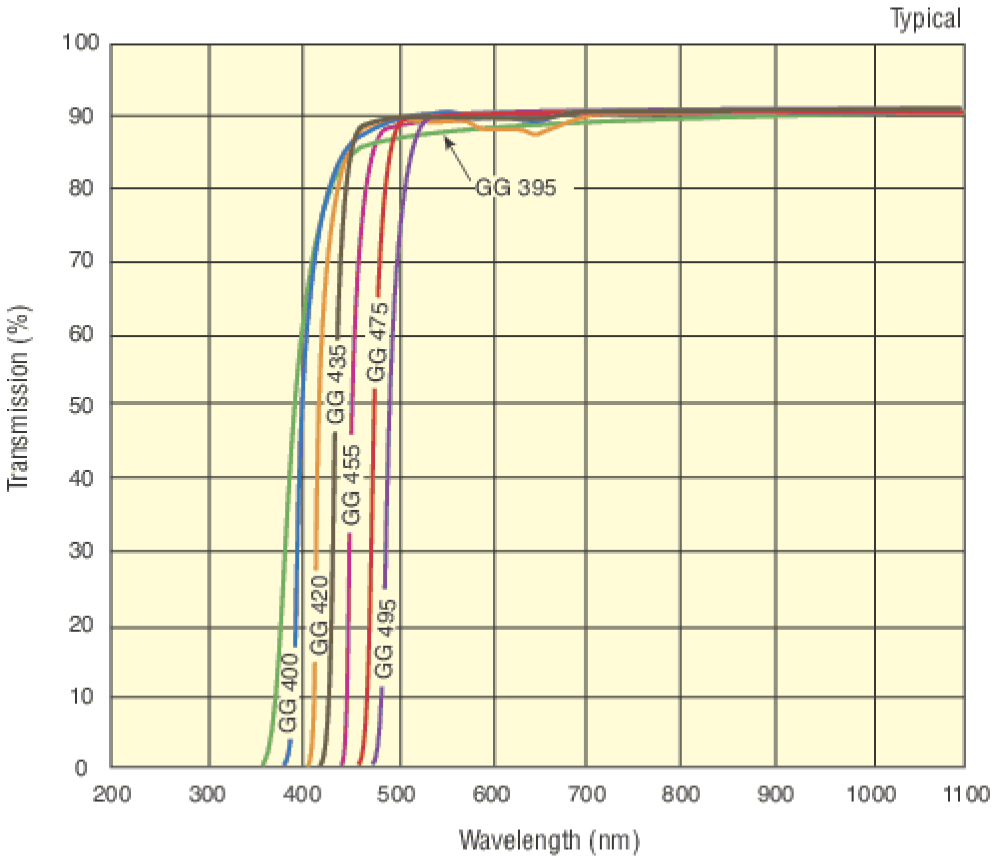

The characteristics of filter FSQ-GG435

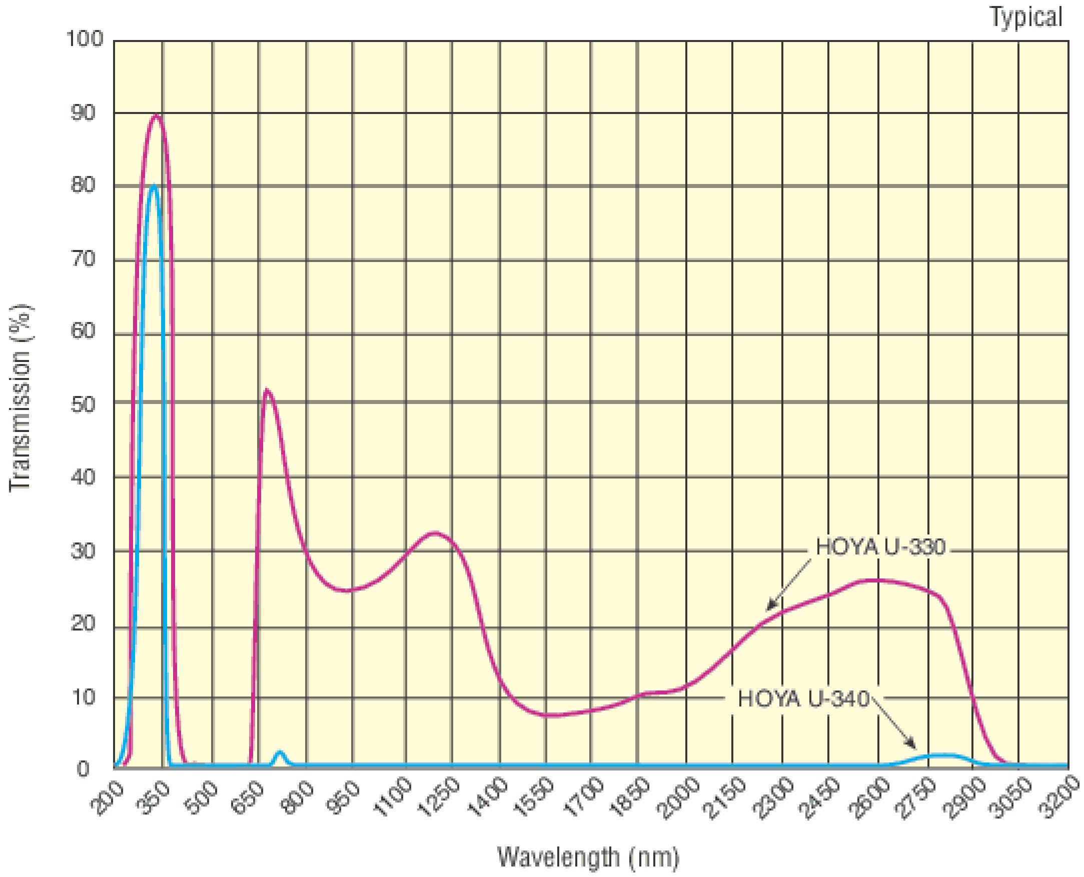

The characteristics of filter FSQ-U340

Typically, 10 mg sample was dispersed in 100 mL deionized water in a quartz cup, after which the quartz cup was placed into reactor, pressurized with 0.1 MPa air and 0.6 MPa methane and keep for 0.5 h to ensure a dissolution equilibrium with 1000 rpm min^{-1} magnetic stirring. Subsequently, the reactor was irradiated by 400W Hg-Xe lamp for 2 h. During the reaction, the temperature of the liquid was maintained at 20±3 °C by an attached cooling system (Minichiller 300). After reaction, the reactor was cooled to 5 °C for another 0.5 h without stirring. Then the gas and liquid products were collected and analysed.

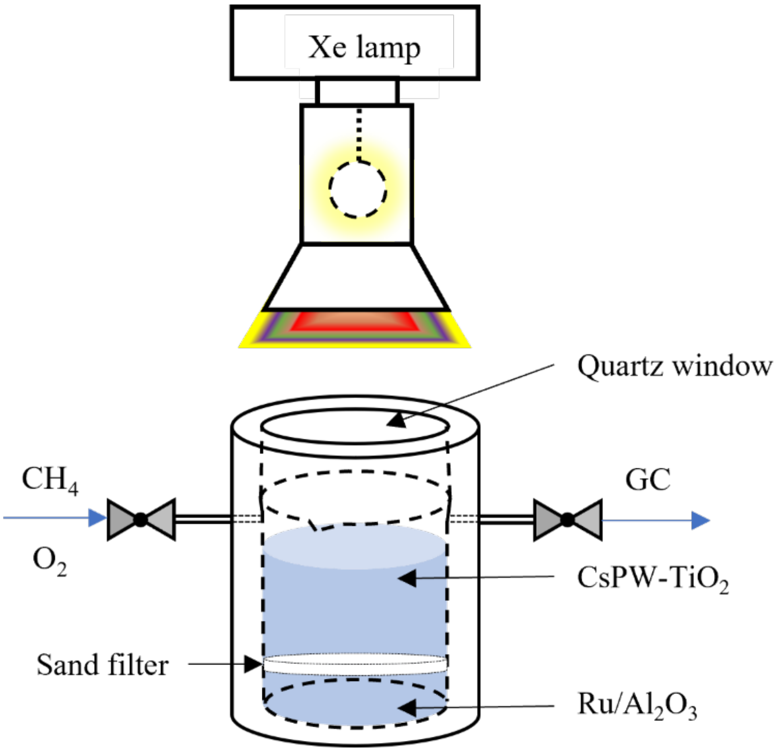

Figure 5. Sketch of the reactor for cascade process

In the cascade photo-chemocatalytic process, the photoreactor was equipped with a sand filter to isolate CsPW-TiO$_2$ photocatalyst and Ru/Al$_2$O$_3$ (**Fig. 5**), in which all the conditions were the same with the typical process described above, except 1 g commercial 5% Ru/Al$_2$O$_3$ was placed in a small glass container on the bottom of reactor. Consequently, photocatalysts CsPW-TiO$_2$ and Ru/Al$_2$O$_3$ can be separated. After irradiation, the 5% Ru/Al$_2$O$_3$ was immediately released out from the small glass container by vigorous stirring (1800 rpm min^{-1}) to oxidize the liquid oxygenates into formic acid at 20 °C. Then the gas and liquid products were collected and analysed.

The gas products were directly injected into GC (PerkinElmer Clarus 580 GC) through Swagelok tube and analysed by PoraBOND Q and ShinCarbon ST 100/120 columns with Ar as the carrier gas, accompanied by a flame ionization and a thermal conductivity detector.

The liquid products (formic acid, methanol, methyl hydroperoxide) were quantified by ^{1}H NMR (BRUKER, Avance HD 300 MHz). Typically, 0.5 mL liquid product was mixed with 0.1 mL D$_2$O containing 0.05 μL dimethyl sulfoxide (DMSO, Sigma-Aldrich, >99.9%) as internal standard. The formaldehyde was quantified by colorimetric method as reported[2]. The concentration of formaldehyde was determined by the standard curve (**Fig 6**).

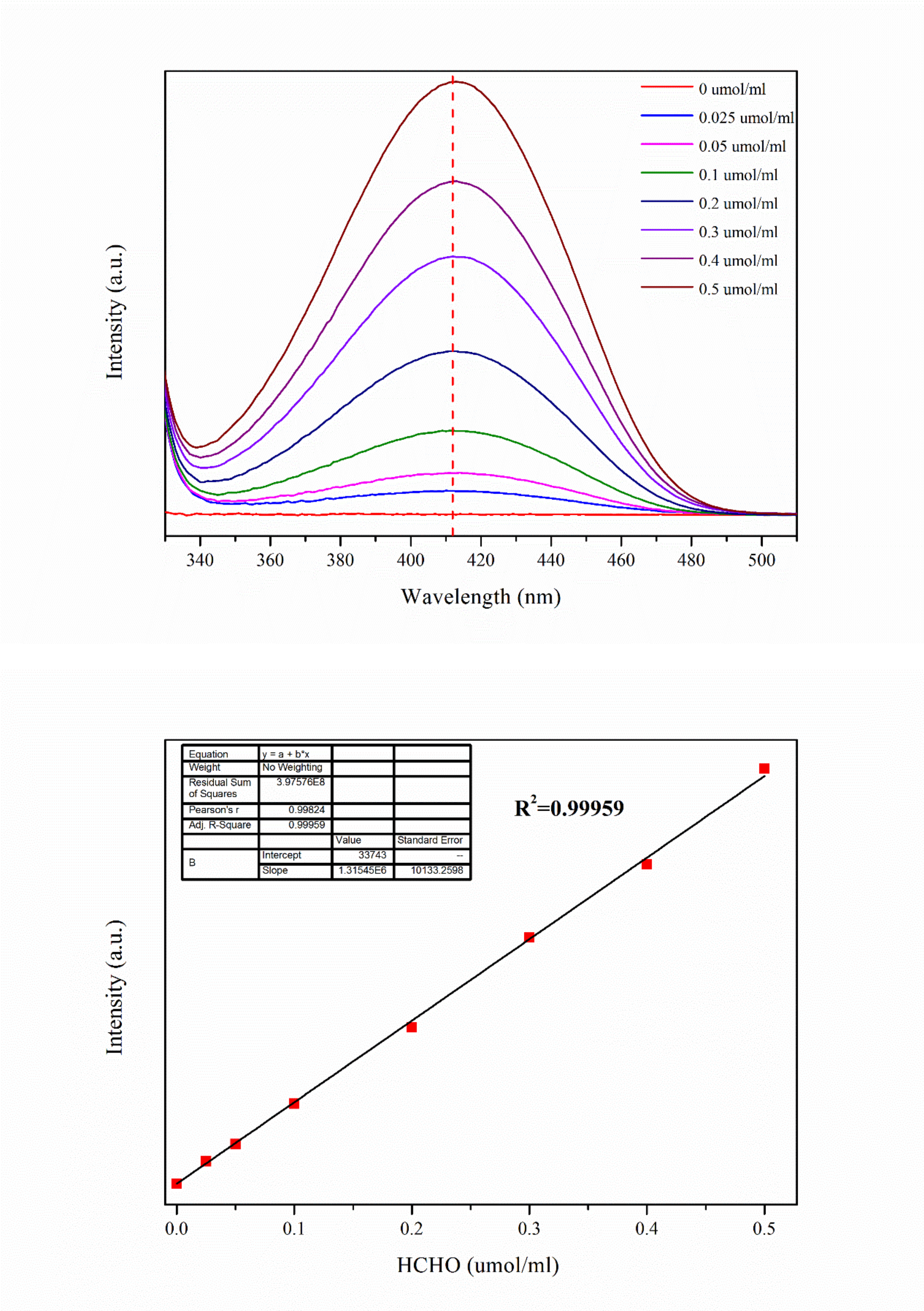

Equation	y = a + b*x		
Weight	No Weighting		
Residual Sum of Squares	3.97576E8		
Pearson's r	0.99824		
Adj. R-Square	0.99959		
		Value	Standard Error
B	Intercept	33743	--
	Slope	1.31545E6	10133.2598

Figure 6. Calibration curve for the quantification of HCHO by colorimetric method.

2.4 References

[1] S.A. Belhout, J.Y. Kim, D.T. Hinds, N.J. Owen, J.A. Coulter, S.J. Quinn, Multifunctional and robust composite materials comprising gold nanoparticles at a spherical polystyrene particle surface, Chem. Commun. 52 (2016) 14388–14391. https://doi.org/10.1039/c6cc07947d.

[2] H. Song, X. Meng, S. Wang, W. Zhou, X. Wang, T. Kako, J. Ye, Direct and Selective Photocatalytic Oxidation of CH4 to Oxygenates with O2 on Cocatalysts/ZnO at Room Temperature in Water, J. Am. Chem. Soc. 141 (2019) 20507–20515. https://doi.org/10.1021/jacs.9b11440.

Chapter 3. Selective photochemical methane coupling to ethane at ambient conditions on AgPW-TiO$_2$

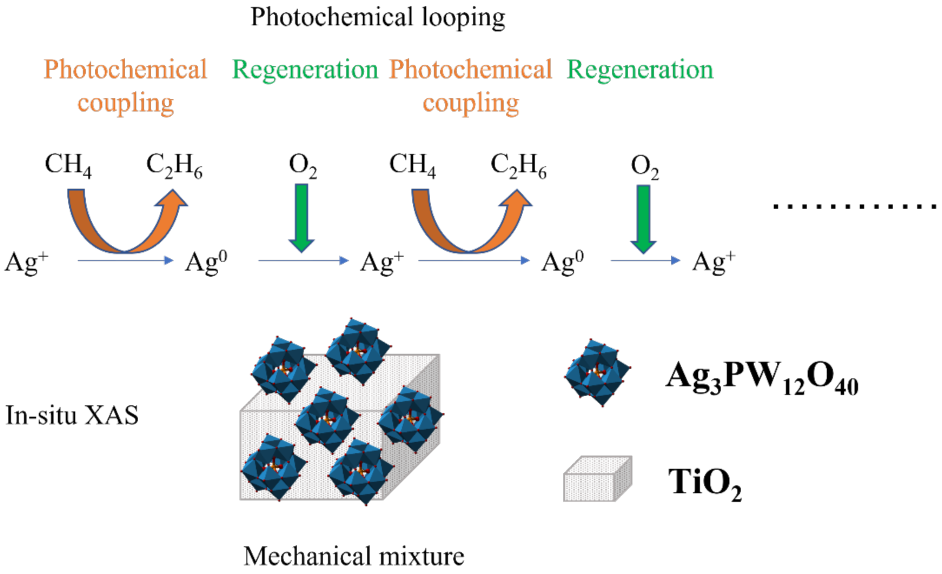

Abstract

Methane, one of the most abundant molecules on Earth and a major greenhouse gas, comes from various renewable and fossil resources. The transformation of methane into ethane and other hydrocarbons requires hash temperature due to high thermodynamic stability and extreme inertness of methane and results in massive emissions of CO_2. Mechanical mixtures of silver salt of phosphotungstic aicd (AgPW) and titania have been prepared for photochemical methane coupling at ambient temperature with high ethane yield and coupling selectivity. The methane conversion requires band gap transition in both the AgPW and TiO_2 excited by UV irradiation, as well the charge transfer between AgPW and TiO_2 with intimate contact. Introducing even small amount of AgPW to TiO_2 significantly enhanced the coupling rate. In-situ XAS showed that during photochemical methane coupling, cationic Ag^+ species were reduced to metallic Ag and resulted in photoactivity decrease, while Ag^+ species and photoactivity can be regenerated from the spent AgPW-TiO_2 exposing to light in the presence of air. The chemical looping process achieved ethane production of 64 μmol/g with coupling selectivity above 95%.

3.1 Introduction

Methane is an important source of energy as well as chemical raw material with huge reserves, which comes from renewable and fossil resources[1][2][3][4]. The activation and utilization of methane still encounters great challenges in modern science due to its extremely inert nature[5][6][7]. To overcome the thermodynamic barriers for methane activation, high temperature is required, however, coke deposition and methane overoxidation are more thermodynamic favorable, resulting in low selectivity towards target products and rapid catalyst deactivation[8]. Consequently, most of methane is currently burnt for energy supply, resulting in large amounts of carbon dioxide emission[9].

Commercially, methane is converted into fuels and chemicals using an energy-intensive indirect route involving the production of syngas (CO and H_2)[10]. However, a direct route has been the subject of intense interest for many decades[11]. Additionally, photocatalysis has appeared recently as a promising strategy in converting solar energy into chemical energy under mild conditions[12][13][14][15], as photocatalysis could break the thermodynamic barriers and thus avoid the drawbacks existing at harsh temperature. We previously demonstrated a great potential in photocatalytic methane conversion into chemicals and fuels under mild conditions by three major routes[10], in which photocatalytic methane coupling to ethane represents an attractive path for methane upgrading with highest selectivity, while it shows meanwhile significantly low productivity. To achieve both efficient and selective methane conversion is the major challenge in photocatalytic methane coupling.

Previously, the photocatalytic non-oxidative coupling of methane (NOCM) was investigated over some metal oxides with significantly lower yield, such as Zn, Ti, Al and Ga oxides[16][17], as well as the highly dispersed mixed metal oxide species[18]. Recently, NOCM has shown higher ethane yield when exploiting the metal co-catalysts supported on semiconductors, especially for Au owning to its special properties. In peer works, Long et al[19]. reported an ethane yield of 11.3 μmol g^{-1} h^{-1} over Au/ZnO benefitting from the plasma resonance of Au nanoparticles and the surface polarization of ZnO. Hu et al[20]. achieved an ethane yield of 81.7 μmol g^{-1} h^{-1} with 95% selectivity over Au/TiO_2 with light-diffuse-reflection surface in a continuous flow system. In addition, an optimized ZnO-AuPd hybrid has also achieved a methane conversion of 536.0 μmol g^{-1} with a C_{2+} compound selectivity of 96% after long term irradiation[21]. However, either the consumption of lattice oxygen or excessive accumulation of holes in semiconductors would eventually result in the photoactivity decay, and a regeneration process is often necessarily required to regain photoactivity[22].

Selective photochemical looping has obtained the proof of concept in our very recent work[22] using the model reaction of methane coupling to ethane. We uncovered quasi stoichiometric coupling (selectivity >90%) of methane to ethane over silver-heteropolyacid-titania nanocomposites (Ag-HPW/TiO_2) prepared by impregnation using 12- tungstophosphoric acid and silver nitrate at room temperature in the absence of oxygen in the gaseous phase. In the reaction stage, methane under irradiation is stoichiometrically coupled to ethane with silver being simultaneously reduced to the metallic state. The nanocomposites can be reversibly regenerated numerous times in air under illumination at ambient temperature.

Herein, we synthesized the silver salt of phosphotungstic acid (AgPW) in one step by ion exchange ($AgNO_3 + H_3PW_{12}O_{40} \rightarrow 3HNO_3 + Ag_3PW_{12}O_{40}\downarrow$). Different to previous work, the catalysts were prepared from silver salt of heteropolyacid and titania using mechanical mixing. The AgPW salt mechanically mixed with TiO_2 (AgPW-TiO_2) exhibits significantly enhanced photochemical methane coupling activity. The Ag cations in AgPW play important role in methane activation. The presence of phosphotungstic acid helps cationic Ag^+ species regeneration. We performed in-situ synchrotron based XAS investigation of the evolution of oxidation state of silver during photochemical methane coupling and regeneration. In methane coupling process, Ag cations were reduced to metallic Ag and results in photoactivity decrease, while exposing the spent AgPW-TiO_2 to air under light treatment can re-oxidize metallic Ag into Ag^+ and regenerate methane coupling activity.

3.2 Results and Discussion

3.2.1 Photochemical coupling of methane on the AgPW-TiO_2 mechanical mixtures

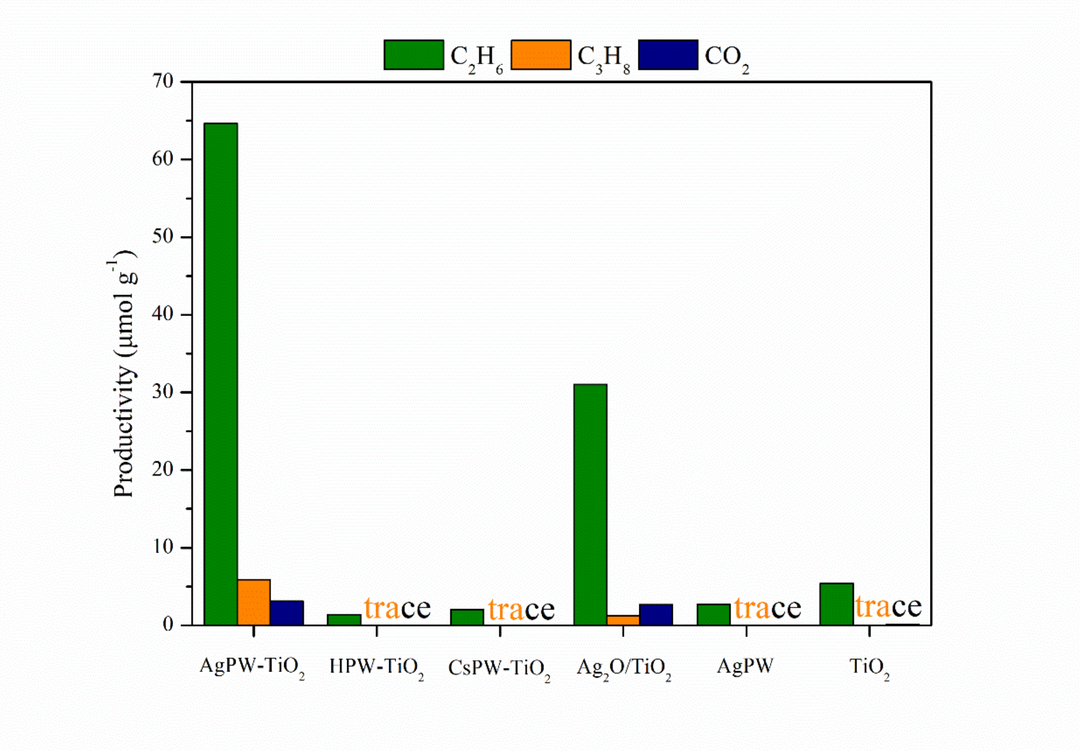

Fig 1. Photochemical methane coupling on different materials

Firstly, we investigated photochemical conversion of methane over TiO_2, AgPW and AgPW-TiO_2 as shown in **Fig 1**. No methane conversion was detected in the absence of light or without studied composites, indicating methane conversion was driven by light over solids. The exposure of TiO_2 and AgPW to light irradiation only resulted in small amount of methane conversion. Interestingly, a significantly enhanced productivity and selectivity to ethane were observed over the AgPW-TiO_2 nanocomposite. Besides ethane, small amount of propane was detected, which can be produced from further methane-ethane cross coupling[22][23].

To investigate the role of Ag, two component composites Ag_2O/TiO_2, HPW-TiO_2 and CsPW-TiO_2 were further studied under identical conditions. Both the HPW-TiO_2 and CsPW-TiO_2 composites show even negligible promotion for methane coupling compared to pristine TiO_2. Ag_2O/TiO_2 shows enhanced methane coupling, but twice lower than AgPW-TiO_2. These catalytic results demonstrate the important role of Ag species in AgPW deposited on TiO_2 for methane coupling.

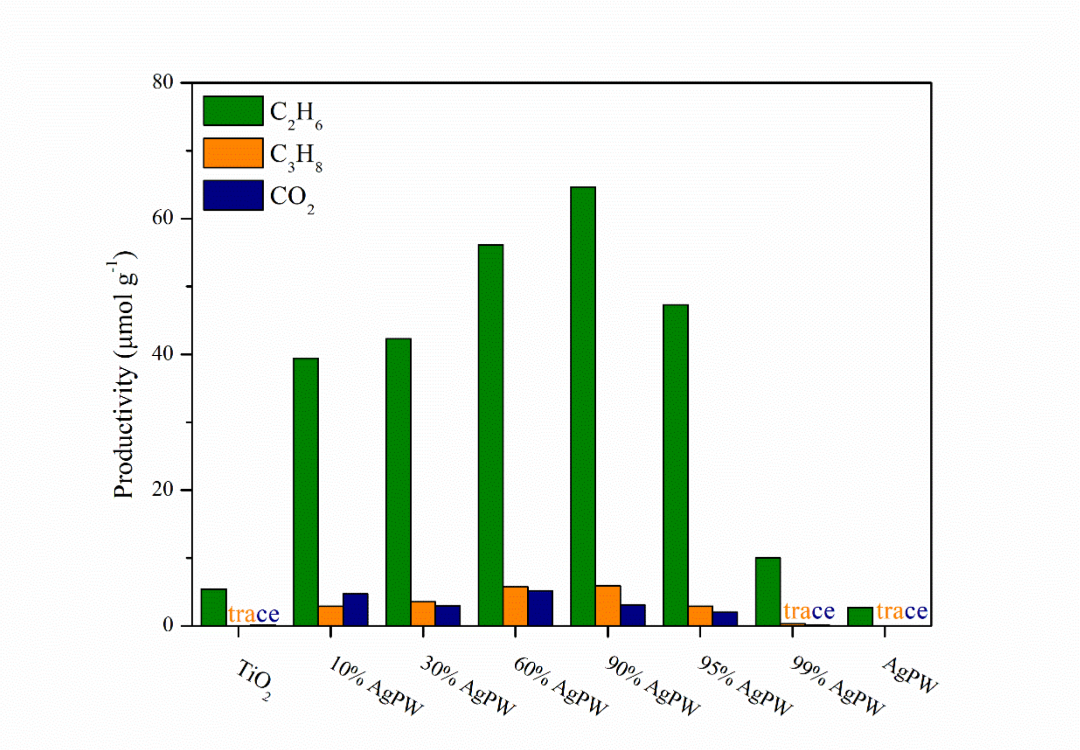

Fig 2. Photochemical methane coupling on AgPW-TiO_2 prepared by mechanical mixing with different AgPW mass ratio

The methane coupling activity as a function of AgPW content in the AgPW-TiO_2 composite prepared by mechanical mixing displays a volcano-type curve as shown in **Fig 2**. Addition of even small amount of AgPW (10%) to TiO_2 or small amount of TiO_2 (5%) to AgPW results in a major increase in the rate of methane coupling. The highest rate of methane coupling was observed at the AgPW content of 90% AgPW, while the coupling rate decreases at higher AgPW content. The enhanced methane coupling can be attributed to the formation of a p-n semiconductor heterojunction between TiO_2 and AgPW as reported in previous work[22][24][25]. This heterojunction may facilitate the separation of e^-/h^+ and slows down charge carrier recombination, making electrons and holes available for reaction.

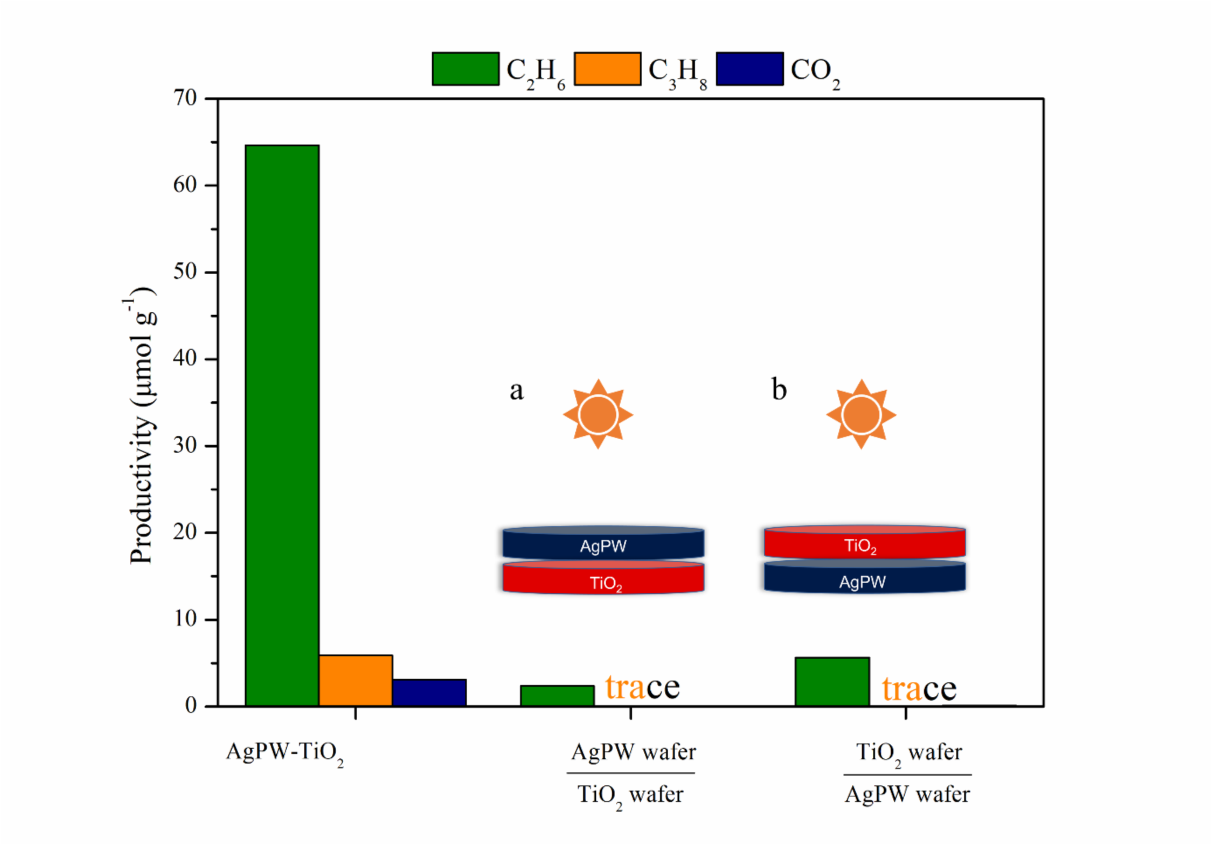

Fig 3. Photochemical methane coupling performance on AgPW and TiO_2 with different configuration.

To further investigate the interaction between AgPW and TiO_2 in methane coupling, AgPW wafer and TiO_2 wafer were overlapped with each other and exposed to light irradiation respectively for methane conversion as shown in **Figure 3**. The methane coupling performance of the overlapped wafers are however similar with the exposed component on the top (**Figure 1**), indicating the importance of close contact between AgPW and TiO_2 for photoactivity enhancement.

In addition, semiconductors, such as ZnO, PCN and $SrTiO_3$ have been introduced into AgPW to evaluate methane coupling (**Figure 4**). The methane conversion is however significantly low on the composites containing ZnO, PCN and $SrTiO_3$. Interestingly, only TiO_2 shows efficient methane coupling activity when in contact with AgPW. These results suggest that the synergy between AgPW and TiO_2 is essential for methane coupling.

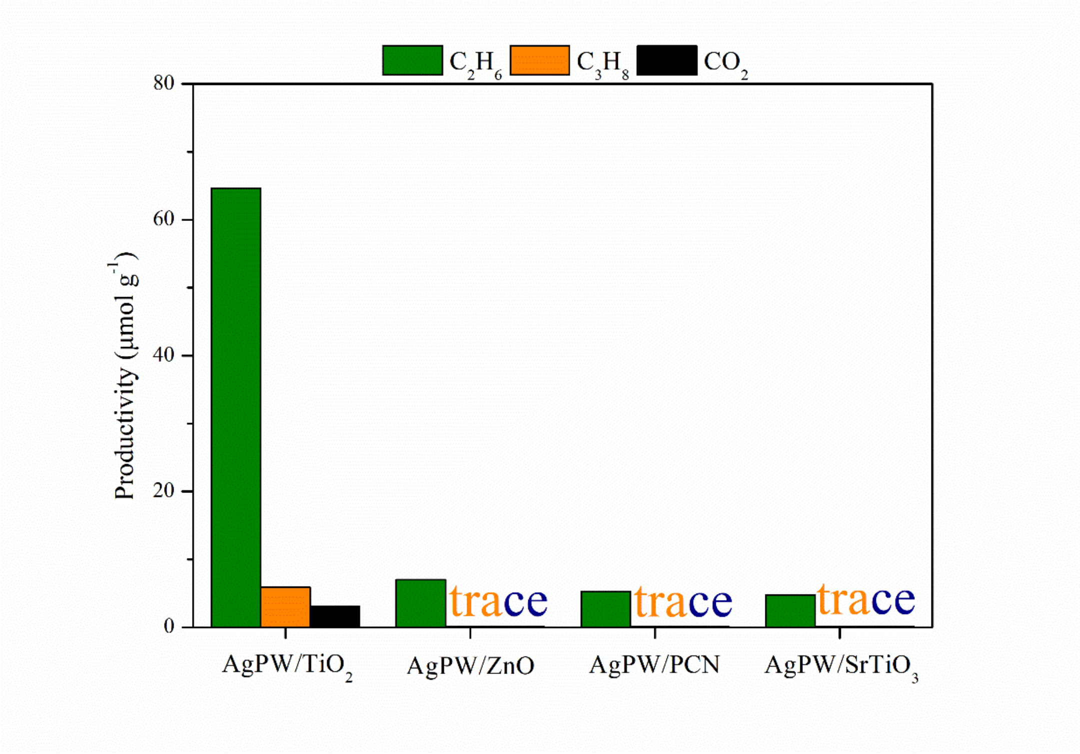

Fig 4. Methane conversion on AgPW mechanically mixed with different semiconductors

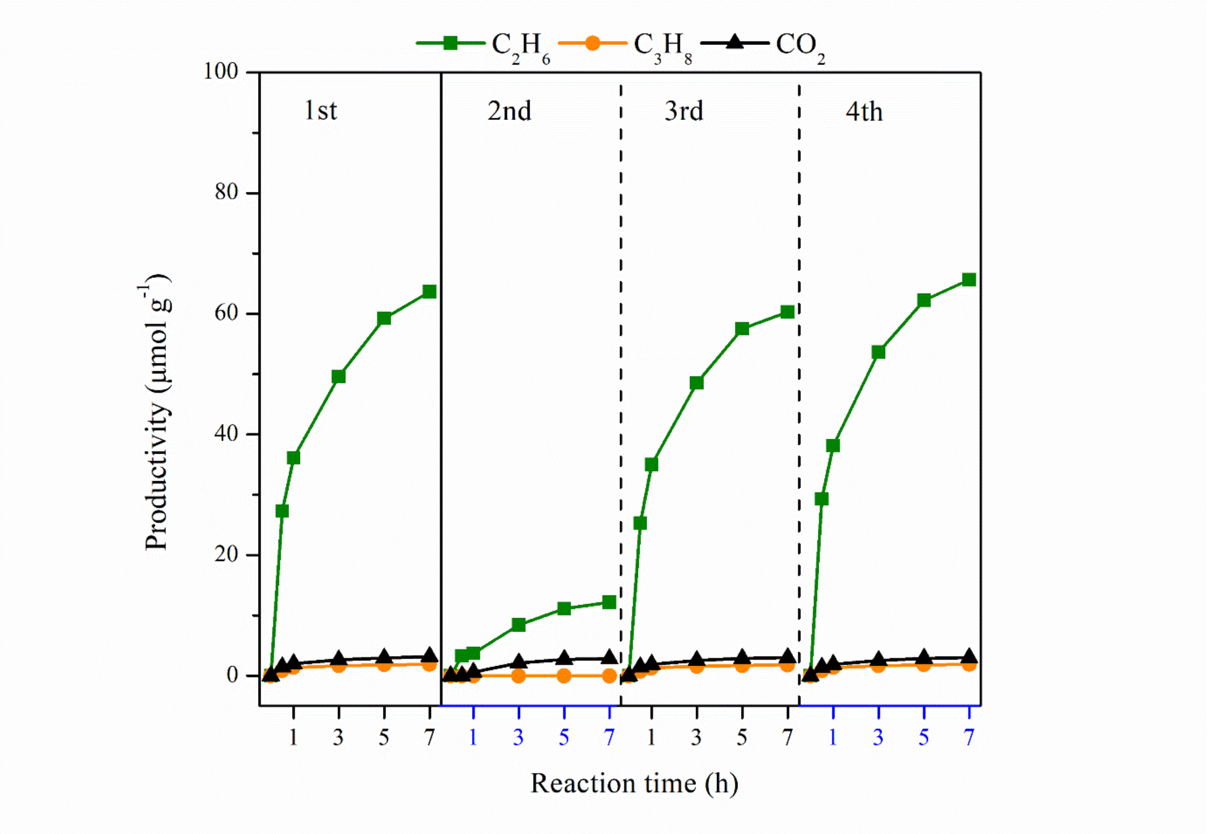

Fig 5. Cycle experiments in anaerobic methane coupling on AgPW-TiO_2 without (2nd) and with regeneration (3rd and 4th). Dashed lines represent nanocomposite regeneration.

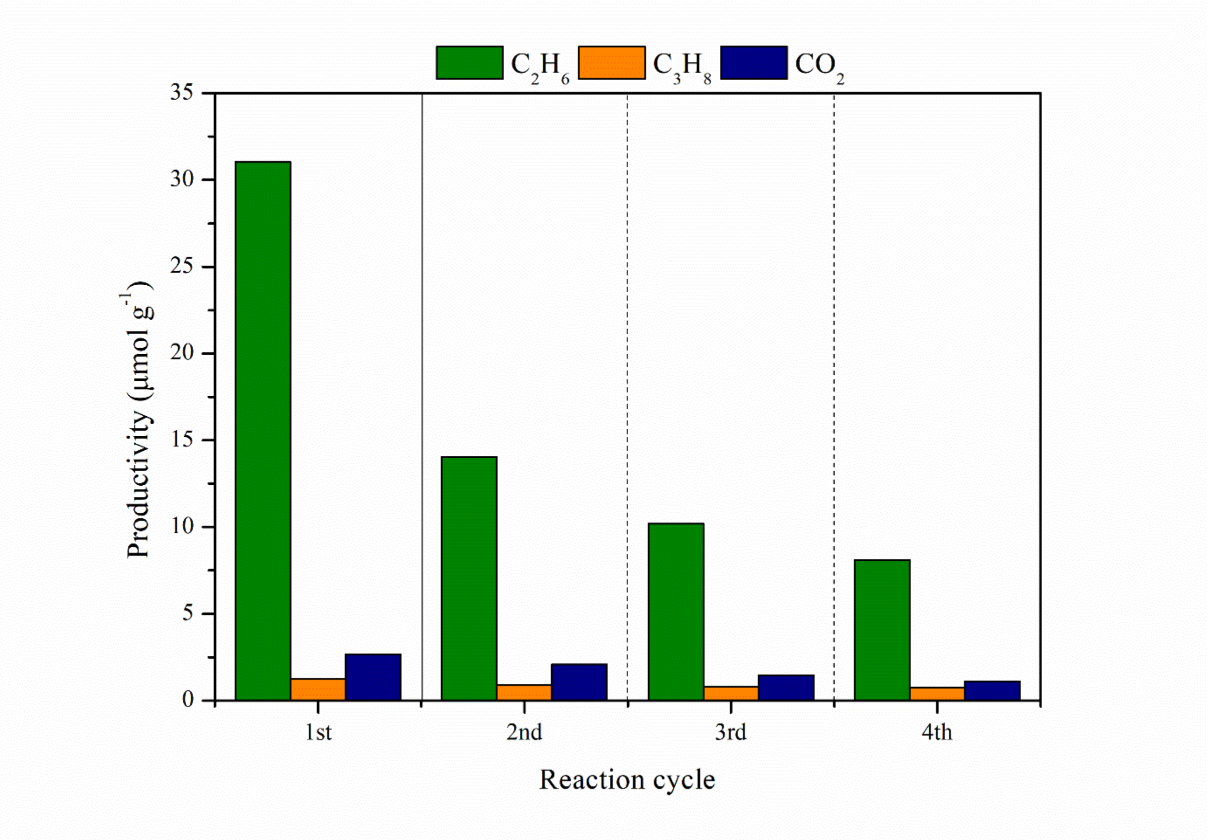

Fig 6. Cycle experiments in methane coupling on Ag_2O-TiO_2 without (2nd) and with regeneration (3rd and 4th). Dashed lines represent nanocomposite regeneration.

The time course of photochemical methane coupling performance on AgPW-TiO_2 is shown in **Figure 5.** The exposure of AgPW-TiO_2 to light in the presence of methane results in sharp increase in hydrocarbon production during the first 2 h and then decreases slowly. The decrease in methane coupling is attributed to the reduction of Ag as the color of composite turns to black from white during reaction, which is further proven below by XAS in **Figure 12**. Consequently, a significantly decreased methane conversion is observed in the 2nd cycle. Alternatively, after the regeneration of spent composite after 1st cycle under light irradiation in the presence of air, the methane coupling performance can be recovered as in the 1st cycle.

A different behavior was however observed for Ag_2O/TiO_2 as shown in **Figure 6**. The methane coupling activity still decreased after regeneration processes in the 3rd and 4th cycle, indicating an irreversibility of Ag_2O/TiO_2. These results suggest that the presence of phosphotungstic aicd is not only important for enhancing photoactivity, but also critical for composite regeneration.

3.2.2 Characterization of the AgPW-TiO₂ prepared by mechanical mixing

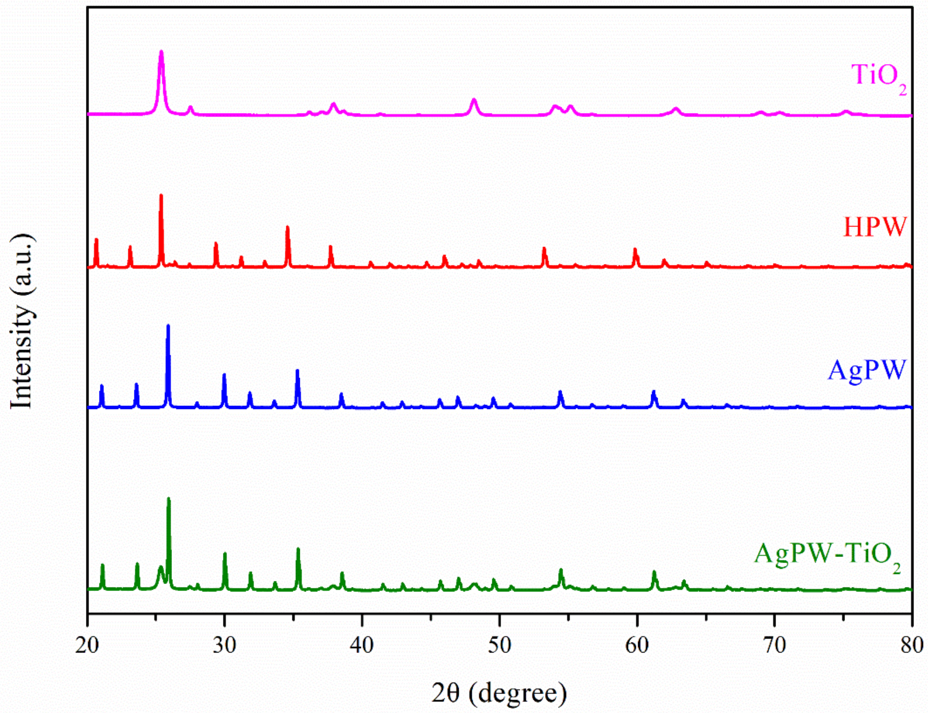

Fig 7. X-ray diffraction patterns of materials

The XRD patterns of AgPW-TiO_2, AgPW, HPW and TiO_2 are shown in **Figure 7**. All the samples containing TiO_2 exhibit characteristic XRD peaks of the anatase and rutile phase[26]. The parent HPW exhibits the typical X-ray diffractograms of the body-centered cubic secondary structure of Keggin anions[27][28]. AgPW exhibits similar diffraction patterns as that of HPW. In addition, a slight shift toward higher angles was observed for AgPW and no diffraction peaks of pure HPW were detected, indicating that Ag^+ was incorporated into HPW cluster with the remaining of Keggin structure with good crystalline. The AgPW-TiO_2 mixture shows distinguishing X-ray diffraction peaks of both the TiO_2 and AgPW.

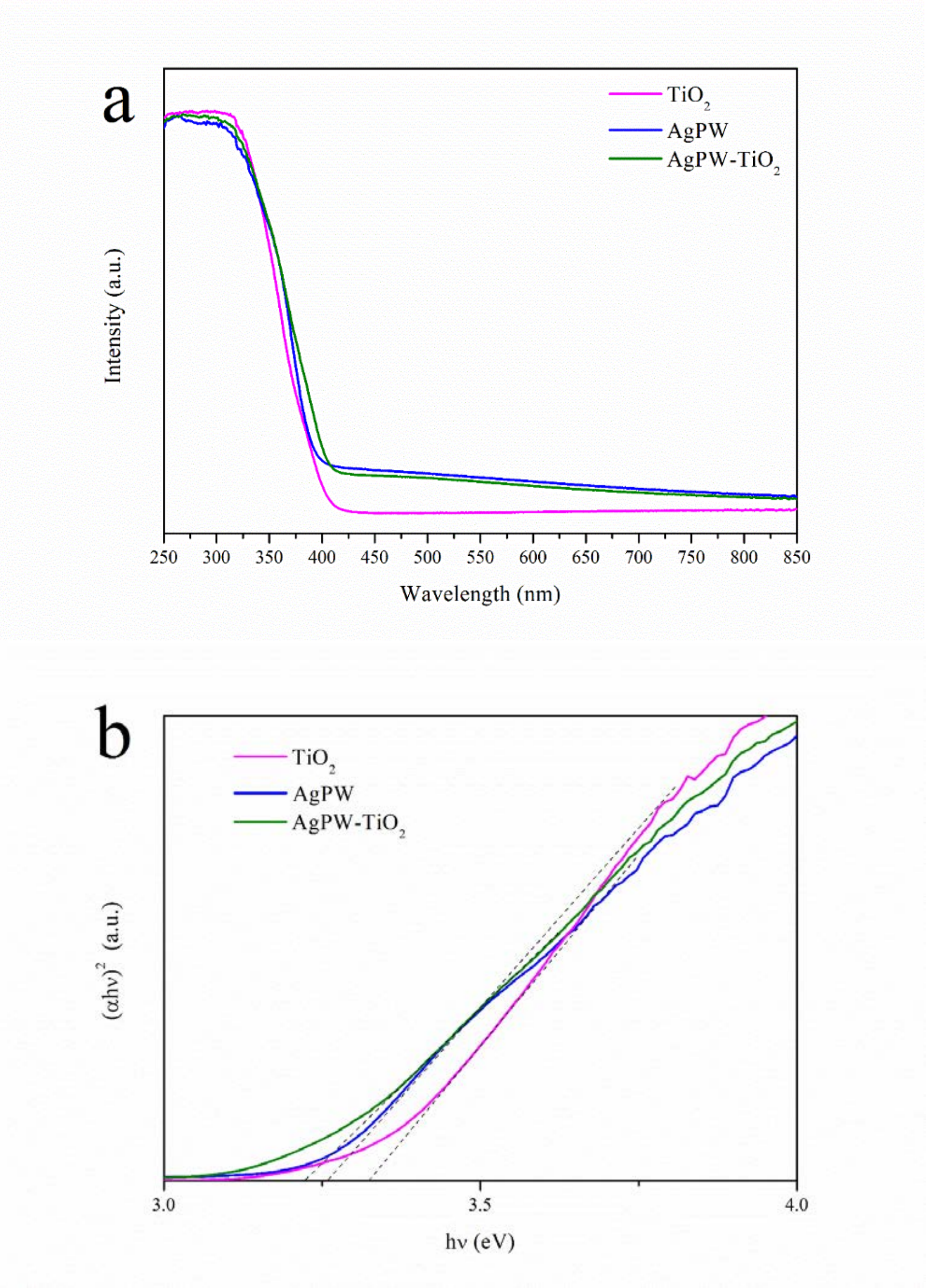

Fig 8. UV-visible DRS spectra of TiO_2, AgPW and AgPW-TiO_2

The UV-visible spectra of TiO_2, AgPW and AgPW-TiO_2 are displayed in **Figure 8**. The samples show intense absorption in the ultraviolet region (<400 nm). Interestingly, the bandgap estimated using Tauc's plot are almost the same for both TiO_2, AgPW and AgPW-TiO_2 (3.32 eV for TiO_2, 3.26 eV for AgPW and 3.22 eV for AgPW-TiO_2). They show no photoactivity under visible light irradiation as these materials can not be photoexcited for methane conversion.

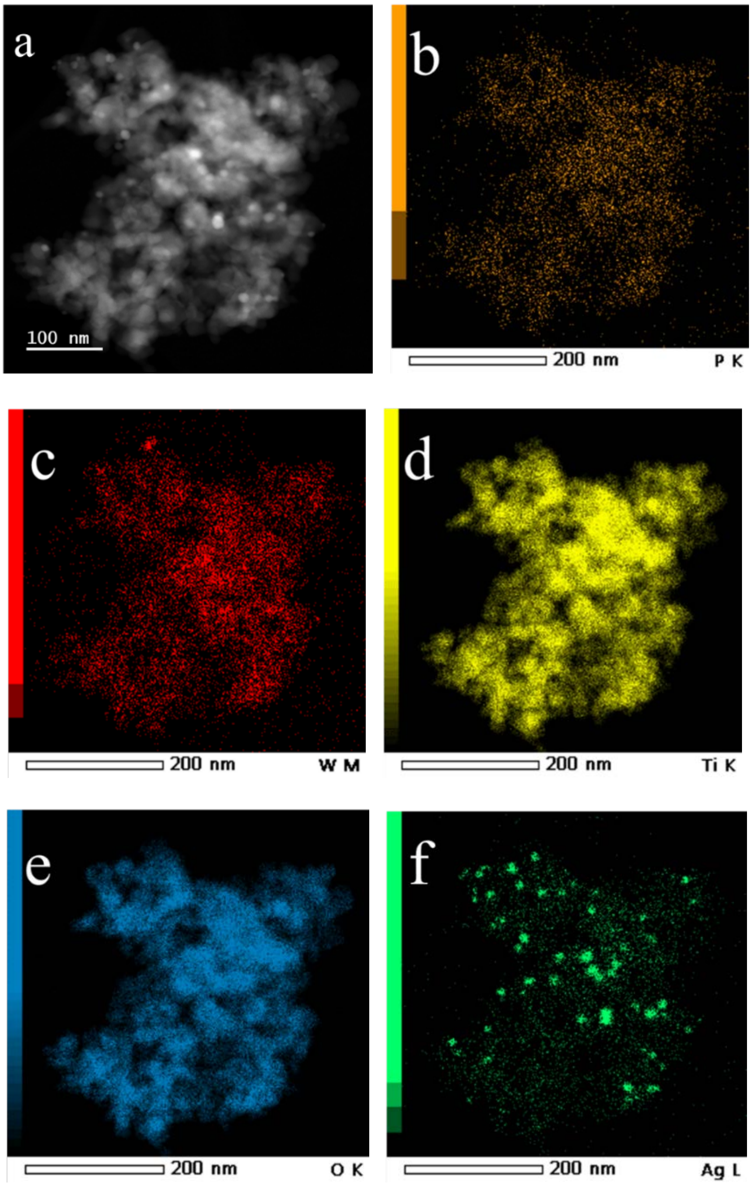

Fig 9. STEM-HAADF (a) and corresponding EDX mapping images with intensity scale corresponding to the concentration of the elements and edges: P and K edge (b), W and M edge (c), Ti and K edge (d), O and K edge (e) and Ag and L edge (f).

The scanning transmission electron microscopy high-angle annular dark-field imaging (STEM-HAADF) and STEM energy dispersive X-ray spectroscopy (STEM-EDX) elemental maps of AgPW-TiO_2 are shown in **Figure 9**. The pictures show that extremely small silver species with the diameter of around 2 nm within AgPW are uniformly dispersed on the surface of TiO_2. They identify close contact but distinct separation of TiO_2 and AgPW semiconductor phase, confirming the presence of the p-n heterojunction.

3.2.3 In-situ XAS investigation of silver evolution in nanocomposites

To provide further insight into the variation of silver oxidation state during the photochemical process in methane and regeneration process in air, in-situ synchrotron X-ray absorption spectroscopy (XAS) has been used to characterize the evolution of silver species in AgPW-TiO_2 mechanical mixture during the photochemical looping. The procedure of photochemical looping is shown in **Figures 10**.

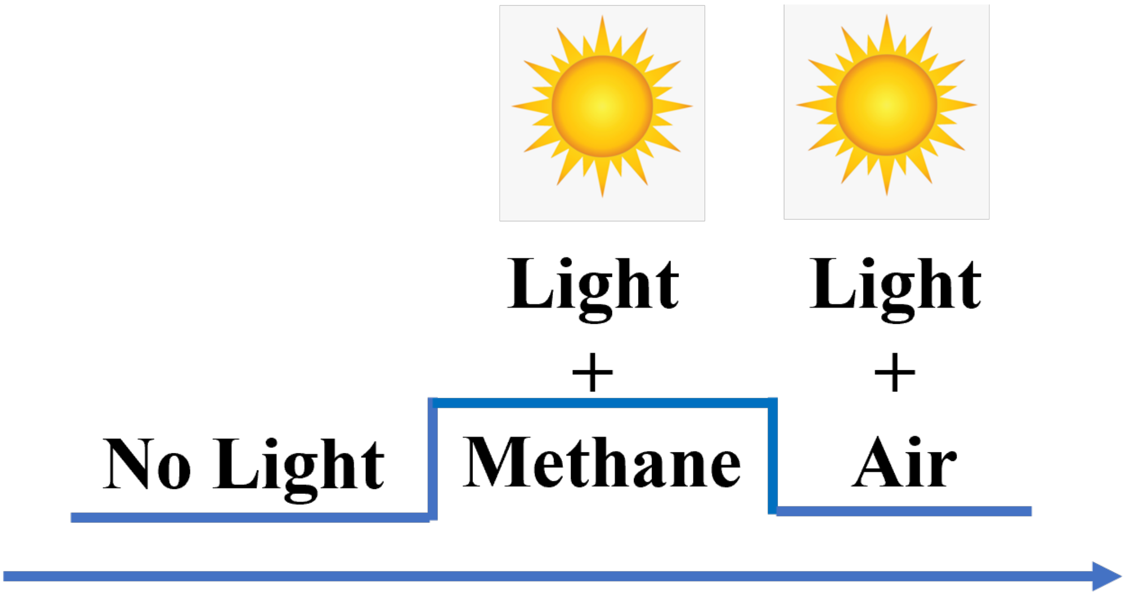

Figure 10. Experimental procedure in the in-situ XAS experiments

The XANES spectra at Ag K-absorption edge of reference Ag_2O, Ag foil together with that of the freshly prepared by mechanical mixing AgPW-TiO_2 sample are given in **Figure 11**. Fresh AgPW-TiO_2 shows spectral features that are similar to that of $AgNO_3$, indicating the presence of single Ag^+ cations, probably localized in the cationic sites of heteropolyacid. When AgPW-TiO_2 was exposed to light in methane, the silver K-edge XANES spectra evolved from that characteristic of isolated Ag^+ cations to those typical of silver foil (**Figure 12a**). The color of the samples also changed from white to black. This suggests gradual reduction of silver during methane photochemical coupling:

$$2CH_4+Ag^+\rightarrow C_2H_6+2H^++Ag^0$$

Further exposure of the sample to air under UV irradiation leads to oxidation of metallic silver to the cationic Ag^+ species (**Figure 12b**).

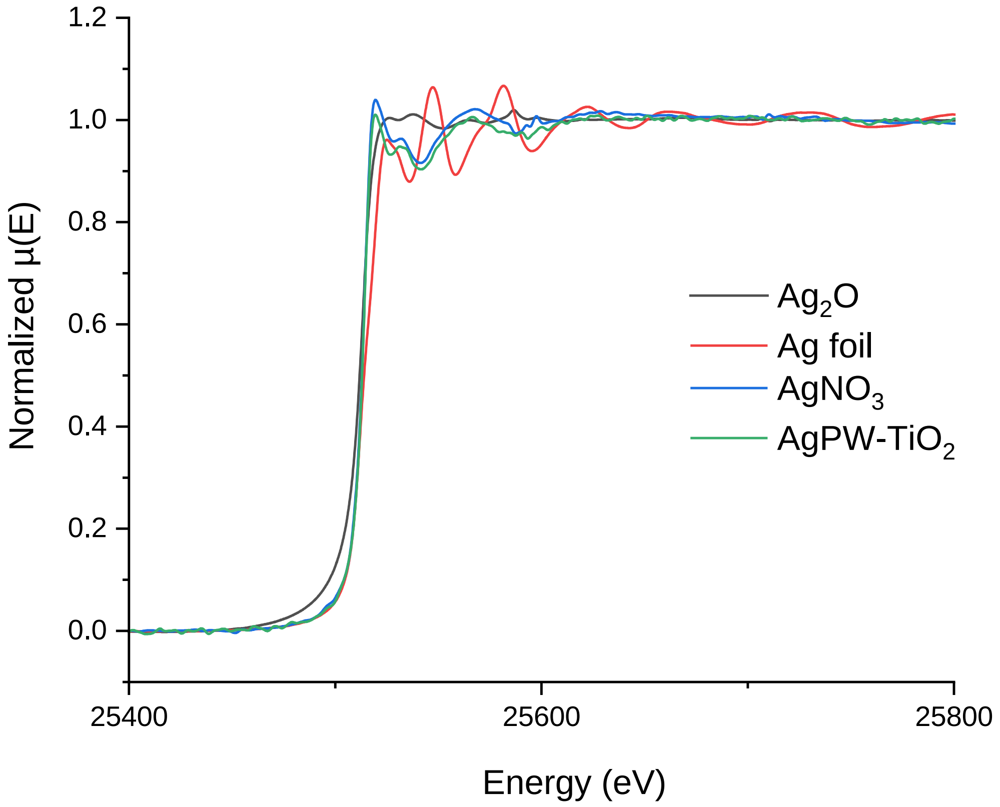

Figure 11. XANES spectra at Ag K-absorption edge of reference Ag_2O, Ag foil $AgNO_3$ and mechanically mixed AgPW-TiO_2 sample

The XANES spectra were quantitatively analyzed using a linear combination of XANES spectra of reference compounds (**Figure 13**). The analysis was indicative of the increase in the fraction of metallic silver gradually during the nanocomposite exposure in methane atmosphere to light to almost 70%. The subsequent exposure to air results in a sharp decrease in the fraction of sliver metallic species from 70 to 20%. Thus, a major faction of Ag changes the oxidation state from Ag^+ to Ag^0 during light treatment in methane and back during subsequent contact with air. The silver reduction-oxidation cycles in methane and air under irradiation can be repeated several times.

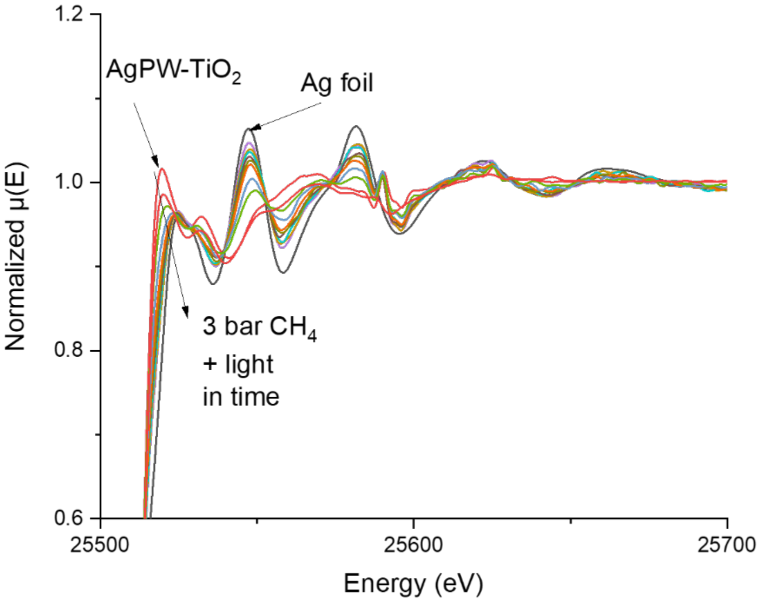

(a)

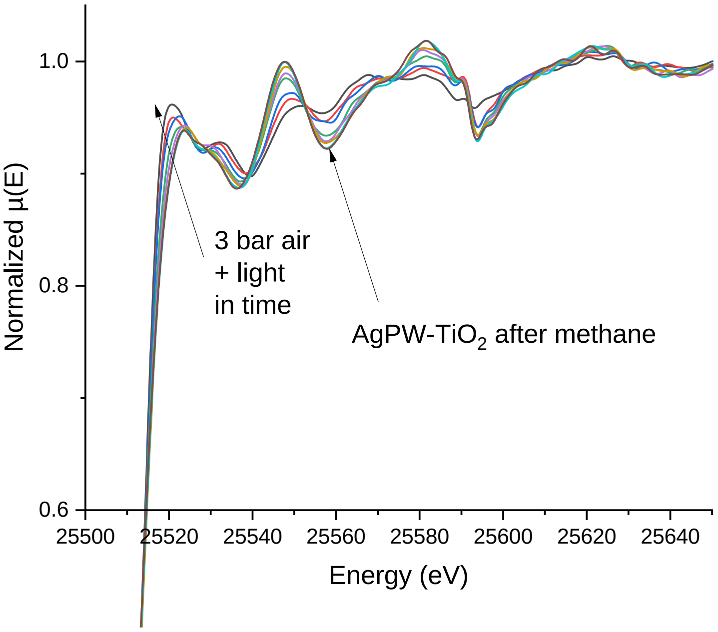

(b)

Figure 12. Evolution of silver K-edge XANES spectra during photochemical looping. (a) methane coupling process in the presence of light and methane and (b) regeneration process in the presence of light and air

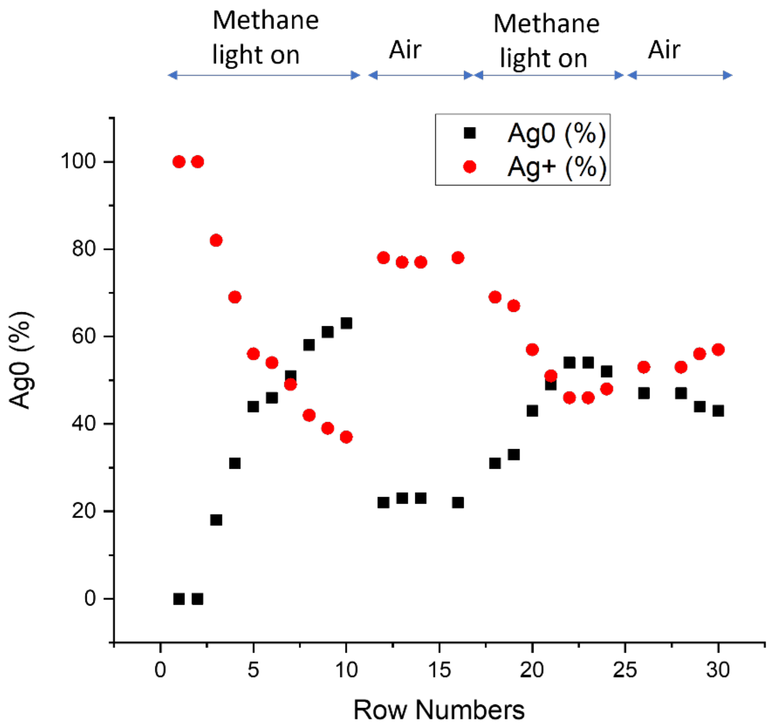

Figure 13. Evolution of oxidized and metallic silver species in AgPW-TiO_2 nanocomposite during the photochemical looping

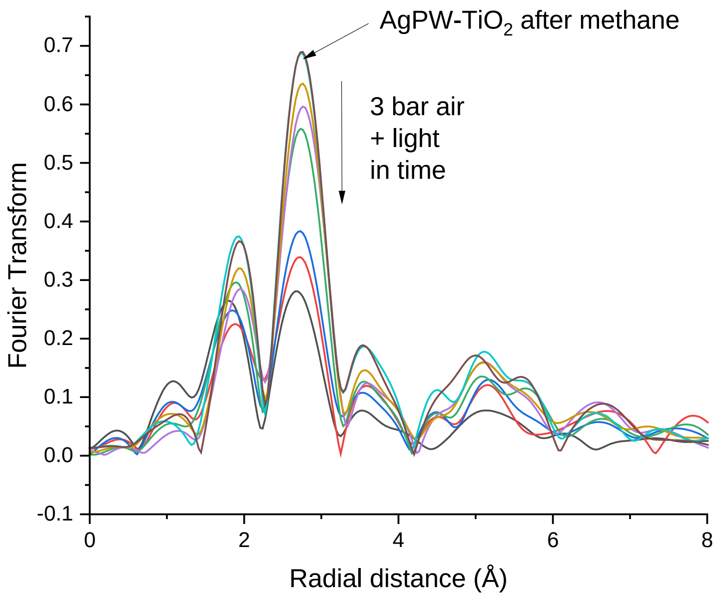

Figure 14. EXAFS Fourier transform moduli of AgPW-TiO_2 nanocomposite measured in-situ during the regeneration process in the presence of light and air

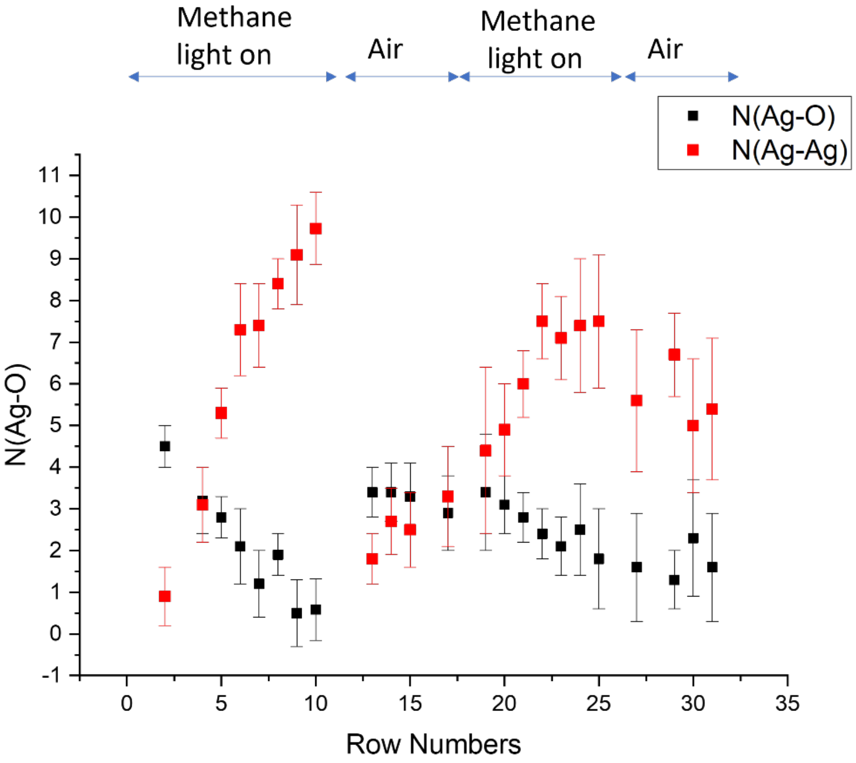

Figure 15. Evolution of Ag-O and Ag-Ag coordination numbers calculated from EXAFS in $AgPW-TiO_2$ nanocomposite during the photochemical looping

The EXAFS Fourier transform moduli during the regeneration in air under irradiation are shown in **Figure 14**. They exhibit peaks at 1.9 Å and 2.4 Å attributed respectively to the Ag-O and Ag-Ag coordination shells. The exposure of the $AgPW-TiO_2$ sample to air results in the decrease in the intensity of EXAFS FT transform peak at 2.4 Å and in the increase in the intensity of 1.9 Å Fourier transform peaks. This corresponds to the oxidation of silver metallic state to the oxidation state. **Figure** 15 shows variation of AgO and Ag-Ag coordination numbers calculated from EXAFS Fourier transform. The amount of oxygen in the shell of silver decreases during the exposure of the nanocomposite to light in the presence of methane, which could be due to the silver reduction. The amount of Ag atoms in coordination shell of silver increases during reduction due to the growth of silver metallic phase and increase in the size of Ag nanoparticles.

3.3 Conclusion

High selectivity of methane coupling to hydrocarbons and high ethane yield were observed over AgPW-TiO_2 composite. The efficient methane coupling requires AgPW and TiO_2 components with intimate contact. This intimate contact can be reached either by co-impregnation or mechanical mixing. The presence of even small amount of TiO_2 (5%) helps charge transfer and separation between AgPW and TiO_2 via the p-n heterojunction and significantly enhances the methane coupling. The optimized nanocomposite achieved an ethane production of 64 μmol/g with coupling selectivity above 95%. The existence of cationic Ag species is critical for efficient methane activation. The in-situ XAS revealed the gradual reduction of cationic Ag^+ species to metallic Ag at room temperature in the presence of methane, which resulted in methane coupling slowing down, while their subsequent re-oxidation form metallic Ag to silver cations in the presence of air can regenerate photoactivity.

3.4 References

[1] J. Ma, X. Tan, Q. Zhang, Y. Wang, J. Zhang, L. Wang, Exploring the size effect of Pt nanoparticles on the photocatalytic nonoxidative coupling of methane, ACS Catal. 11 (2021) 3352–3360. https://doi.org/10.1021/acscatal.0c04943.

[2] Q. Li, Y. Ouyang, H. Li, L. Wang, J. Zeng, Photocatalytic Conversion of Methane: Recent Advancements and Prospects, Angew. Chemie Int. Ed. 61 (2022). https://doi.org/10.1002/anie.202108069.

[3] J. Yang, W. Xiao, X. Chi, X. Lu, S. Hu, Z. Wu, W. Tang, Z. Ren, S. Wang, X. Yu, L. Zhang, A. Rusydi, J. Ding, Y. Guo, P.X. Gao, Solar-driven efficient methane catalytic oxidation over epitaxial ZnO/La0.8Sr0.2CoO3 heterojunctions, Appl. Catal. B Environ. 265 (2020) 118469. https://doi.org/10.1016/j.apcatb.2019.118469.

[4] H. Song, X. Meng, T.D. Dao, W. Zhou, H. Liu, L. Shi, H. Zhang, T. Nagao, T. Kako, J. Ye, Light-Enhanced Carbon Dioxide Activation and Conversion by Effective Plasmonic Coupling Effect of Pt and Au Nanoparticles, ACS Appl. Mater. Interfaces. 10 (2018) 408–416. https://doi.org/10.1021/acsami.7b13043.

[5] H. Song, X. Meng, Z. jun Wang, H. Liu, J. Ye, Solar-Energy-Mediated Methane Conversion, Joule. 3 (2019) 1606–1636. https://doi.org/10.1016/j.joule.2019.06.023.

[6] X. Meng, X. Cui, N.P. Rajan, L. Yu, D. Deng, X. Bao, Direct Methane Conversion under Mild Condition by Thermo-, Electro-, or Photocatalysis, Chem. 5 (2019) 2296–2325. https://doi.org/10.1016/j.chempr.2019.05.008.

[7] L. Meng, Z. Chen, Z. Ma, S. He, Y. Hou, H.H. Li, R. Yuan, X.H. Huang, X. Wang, X. Wang, J. Long, Gold plasmon-induced photocatalytic dehydrogenative coupling of methane to ethane on polar oxide surfaces, Energy Environ. Sci. 11 (2018) 294–298. https://doi.org/10.1039/c7ee02951a.

[8] B.L. Farrell, V.O. Igenegbai, S. Linic, A Viewpoint on Direct Methane Conversion to Ethane and Ethylene Using Oxidative Coupling on Solid Catalysts, ACS Catal. 6 (2016) 4340–4346. https://doi.org/10.1021/acscatal.6b01087.

[9] P. Tang, Q. Zhu, Z. Wu, D. Ma, Methane activation: The past and future, Energy Environ. Sci. 7 (2014) 2580–2591. https://doi.org/10.1039/c4ee00604f.

[10] D. Hu, V. V Ordomsky, A.Y. Khodakov, Major routes in the photocatalytic methane

conversion into chemicals and fuels under mild conditions, Appl. Catal. B Environ. 286 (2021). https://doi.org/10.1016/j.apcatb.2021.119913.

[11] Y. Wang, Room-Temperature Conversion of Methane Becomes True, Joule. 2 (2018) 1399–1401. https://doi.org/10.1016/j.joule.2018.07.013.

[12] X. Yu, V. De Waele, A. Löfberg, V. Ordomsky, A.Y. Khodakov, Selective photocatalytic conversion of methane into carbon monoxide over zinc-heteropolyacid-titania nanocomposites, Nat. Commun. 10 (2019) 700. https://doi.org/10.1038/s41467-019-08525-2.

[13] L. Yuliatiw, H. Yoshida, L. Yuliati, H. Yoshida, L. Yuliatiw, H. Yoshida, L. Yuliati, H. Yoshida, Photocatalytic conversion of methane, Chem. Soc. Rev. 37 (2008) 1592–1602. https://doi.org/10.1039/b710575b.

[14] G. Chen, G.I.N. Waterhouse, R. Shi, J. Zhao, Z. Li, L.Z. Wu, C.H. Tung, T. Zhang, From Solar Energy to Fuels: Recent Advances in Light-Driven C1 Chemistry, Angew. Chemie - Int. Ed. 58 (2019) 17528–17551. https://doi.org/10.1002/anie.201814313.

[15] X. Chen, Y. Li, X. Pan, D. Cortie, X. Huang, Z. Yi, Photocatalytic oxidation of methane over silver decorated zinc oxide nanocatalysts, Nat. Commun. 7 (2016) 1–8. https://doi.org/10.1038/ncomms12273.

[16] L. Yuliati, T. Hattori, H. Itoh, H. Yoshida, Photocatalytic nonoxidative coupling of methane on gallium oxide and silica-supported gallium oxide, J. Catal. 257 (2008) 396–402. https://doi.org/10.1016/j.jcat.2008.05.022.

[17] G.N. Kuzmin, M. V. Knatko, S. V. Kurganov, Light and X-ray-induced chemistry of methane on TiO2, React. Kinet. Catal. Lett. 23 (1983) 313–317. https://doi.org/10.1007/BF02065581.

[18] L. Yuliati, T. Hattori, H. Yoshida, Highly dispersed magnesium oxide species on silica as photoactive sites for photoinduced direct methane coupling and photoluminescence, Phys. Chem. Chem. Phys. 7 (2005) 195–201. https://doi.org/10.1039/b410089a.

[19] L. Meng, Z. Chen, Z. Ma, S. He, Y. Hou, H.H. Li, R. Yuan, X.H. Huang, X.X. Wang, X.X. Wang, J. Long, Gold plasmon-induced photocatalytic dehydrogenative coupling of methane to ethane on polar oxide surfaces, Energy Environ. Sci. 11 (2018) 294–298. https://doi.org/10.1039/c7ee02951a.

[20] J. Lang, Y. Ma, X. Wu, Y. Jiang, Y.H. Hu, Highly efficient light-driven methane coupling under ambient conditions based on an integrated design of a photocatalytic system, Green Chem. 22 (2020) 4669–4675. https://doi.org/10.1039/d0gc01608j.

[21] W. Jiang, J. Low, K. Mao, D. Duan, S. Chen, W. Liu, C. Pao, J. Ma, S. Sang, C. Shu, X. Zhan, Z. Qi, H. Zhang, Z. Liu, X. Wu, R. Long, L. Song, Y. Xiong, Pd-Modified ZnO–Au Enabling Alkoxy Intermediates Formation and Dehydrogenation for Photocatalytic Conversion of Methane to Ethylene, J. Am. Chem. Soc. 143 (2021) 269–278. https://doi.org/10.1021/jacs.0c10369.

[22] X. Yu, V.L. Zholobenko, S. Moldovan, D. Hu, D. Wu, V. V Ordomsky, A.Y. Khodakov, Stoichiometric methane conversion to ethane using photochemical looping at ambient temperature, Nat. Energy. (2020). https://doi.org/10.1038/s41560-020-0616-7.

[23] S. Song, H. Song, L. Li, S. Wang, W. Chu, K. Peng, X. Meng, Q. Wang, B. Deng, Q. Liu, Z. Wang, Y. Weng, H. Hu, H. Lin, T. Kako, J. Ye, A selective Au-ZnO/TiO2 hybrid photocatalyst for oxidative coupling of methane to ethane with dioxygen, Nat. Catal. (2021). https://doi.org/10.1038/s41929-021-00708-9.

[24] X. Yu, S. Moldovan, V. V. Ordomsky, A.Y. Khodakov, Design of core-shell titania-heteropolyacid-metal nanocomposites for photocatalytic reduction of CO2 to CO at ambient temperature, Nanoscale Adv. 1 (2019) 4321–4330. https://doi.org/10.1039/c9na00398c.

[25] X. Yu, V. De Waele, A. Löfberg, V. Ordomsky, A.Y. Khodakov, Selective photocatalytic conversion of methane into carbon monoxide over zinc-heteropolyacid-titania nanocomposites, Nat. Commun. 10 (2019) 700. https://doi.org/10.1038/s41467-019-08525-2.

[26] D. Hu, C. Liu, L. Li, K. Le Lv, Y.H. Zhang, J.L. Li, Carbon dioxide reforming of methane over nickel catalysts supported on TiO2(001) nanosheets, Int. J. Hydrogen Energy. 3 (2018) 21345–21354. https://doi.org/10.1016/j.ijhydene.2018.09.188.

[27] S. Zhu, X. Gao, F. Dong, Y. Zhu, H. Zheng, Y. Li, Design of a highly active silver-exchanged phosphotungstic acid catalyst for glycerol esterification with acetic acid, J. Catal. 306 (2013) 155–163. https://doi.org/10.1016/j.jcat.2013.06.026.

[28] F. Hashemi, M. Taghizadeh, M.D. Rami, Polyoxometalate modified SAPO-34: A highly

stable and selective catalyst for methanol conversion to light olefins, Microporous Mesoporous Mater. 295 (2020) 109970. https://doi.org/10.1016/j.micromeso.2019.109970.

Chapter 4. Room temperature methane photocatalytic coupling over titania with gold nanoparticles: Does the plasmonic effect matter?

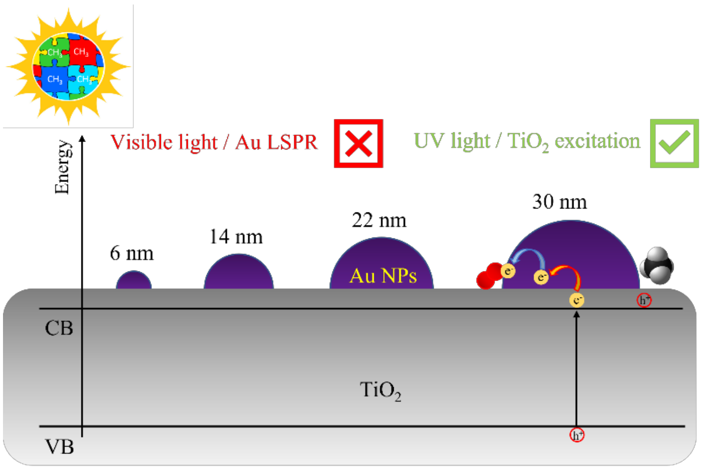

Abstract

Methane, one of the most abundant molecules on Earth and a major greenhouse gas, comes from renewable and fossil resources. The activation and utilization of methane are attractive, but encounters numerous challenges due to high thermodynamic stability and extreme inertness of methane.

Gold nanoparticles with a size from 6 to 29 nm supported on titania have been prepared for photocatalytic non-oxidative and oxidative methane couplings in both batch and continuous gas flow reactors. A hydrocarbon productivity of 1864 μmol g^{-1} h^{-1} with a coupling selectivity higher than 86% was achieved in the continuous oxidative methane coupling flow process. The photocatalytic performance in both non-oxidative and oxidative methane couplings is only slightly affected by the gold nanoparticle size. The plasmonic effect of gold nanoparticles cannot alone drive the methane conversion. Methane conversion requires synergy between the band gap transition in titania excited by UV irradiation and the inhibition of charge carrier recombination by gold nanoparticles. A combination of techniques showed that the methane activation occurred over titania oxygen vacancies, while oxygen was likely activated by gold nanoparticles.

4.1 Introduction

Methane is an important source of energy as well as chemical raw material, which comes from vast renewable and fossil resources [1–4]. Methane is a greenhouse gas (GHG) with an effect on the climate 30 times more significant [5,6] than carbon dioxide. The activation and utilization of methane still encounters numerous challenges due to methane high thermodynamic stability and extreme inertness [7–9]. In conventional thermocatalytic processes, high temperature is required to overcome the kinetic barriers for methane activation. However, at high temperatures, coke deposition and methane re-oxidation become more thermodynamically advantageous compared to the conversion of methane into valuable products such as longer chain hydrocarbons or oxygenates. Consequently, low selectivity and rapid catalyst deactivation have been often observed [10]. These are the reasons, why currently the main way of utilizing methane remains combustion for energy production, which emits large quantities of carbon dioxide [11].

Photocatalysis has emerged as a promising strategy for converting solar energy into chemical energy under mild conditions [12–15]. The great potential of photocatalytic conversion of methane to chemicals and fuels under mild conditions has been demonstrated in recent publications [16]. Among different methane conversion routes, the photocatalytic methane coupling to ethane is particularly attractive. Methane coupling usually exhibits higher selectivity compared to reforming/oxidation to CO or methanol [16]. The major challenge in photocatalytic methane coupling is to achieve simultaneously high productivity and high selectivity to ethane and other long-chain hydrocarbons.

At the same time, semiconductor photocatalysis currently faces two major challenges: limited absorption of photons by semiconductors in the visible range and fast recombination of the photoinduced charge carriers. In this context, the use of metal nanoparticles (NPs) has played several important roles in spectacularly improving the catalytic performance of semiconductor photocatalysts. The Au, Ag, Cu, Pt, Rh, Pd, Mg, Ni, and Al NPs have been extensively used [17], because of their attractive catalytic or electron trapping properties. The term “plasmonic” [18] usually refers to metal NPs, which absorb irradiation in the visible and near-infrared ranges due to the localized surface plasmon resonance (LSPR) excitation. LSPR is the collective oscillation of free electrons in metal NPs under resonant conditions in response to an incoming electromagnetic wave. Excitation of LSPR on plasmonic NPs can accelerate a variety of chemical reactions via the activation of surface molecules and bonds [19]. Moreover, the interaction of plasmonic metal NPs with semiconductors may result in the formation of different metal-semiconductor junctions. The Schottky barrier at the interface between metal NPs and a semiconductor allows hot electrons with the appropriate energy to pass [20] through the interface, resulting in the enhanced separation of electrons and holes. The intensity and resonance wavelength of LSPR over plasmonic metal nanostructures are tunable by modifying particle morphology and size. Besides, metal NPs can also operate as co-catalysts for photocatalytic reactions [21,22].

Previously, the non-oxidative photocatalytic coupling of methane (NOCM) was investigated over both bulk Zn, Ti, Al and Ga oxides [23,24] and highly dispersed mixed metal oxide species [25]. Recently, NOCM has shown a higher ethane yield over metal co-catalysts supported on semiconductors. Long et al. [26] reported an ethane yield of 11.3 μmol g^{-1} h^{-1} over Au/ZnO. The reaction benefited from LSPR of Au NPs and surface polarization of ZnO. Hu et al. [27] achieved an ethane yield of 81.7 μmol g^{-1} h^{-1} with 95% selectivity over Au/TiO_2 with the light-diffuse-reflection surface in a continuous flow system. In addition, an optimized ZnO-AuPd hybrid catalyst has also achieved a methane conversion of 536.0 μmol g^{-1} with a C_{2+} hydrocarbon selectivity of 96% [28]. However, in NOMC, the rapid photoactivity decay was observed which was probably due to the consumption of lattice oxygen or excessive accumulation of holes in semiconductors. A regeneration process is often required to recover the photocatalytic activity. Similarly, we demonstrated [29] a photochemical looping process for quantitative methane conversion to ethane, which involved reaction and regeneration steps on Ag-HPW/TiO_2.

Alternatively, the photocatalytic oxidative coupling of methane (OCM) with the commonly used oxidant such as O_2, provides a facile technology of methane chemical utilization, which has been however rarely investigated. Additionally, Au NPs have also been efficient in oxygen activation into moderately reactive oxidative species, which could further enhance charge transfer and contribute to selective methane oxidation. Besides, recent studies have revealed that the continuous gas flow process is likely to be a better alternative to the batch process for highly active OCM catalysts. Tang et al. [30] reported an OCM process, in which optimized $Cu_{0.1}Pt_{0.5}$/PC-50 achieved in the flow system a C_2 product yield of 68.0 μmol g^{-1} h^{-1} with 60% selectivity. Very recently, Song et al.[31] achieved an ethane production of over 5000.0 μmol g^{-1} h^{-1} with 90% selectivity over Au-ZnO/TiO_2 in an OCM process using a flow reactor. No decay in photoactivity was observed during the long-term test in these processes.

Despite the major progress in photocatalytic methane coupling, very few information about the contribution of the plasmonic effect and influence of the plasmonic NP size on OCM and NOCM has been available in the literature. Herein, a series of Au NPs with various sizes supported on titania have been prepared for the photocatalytic NOCM and OCM reactions in both batch and continuous gas flow reactors. We found that the catalytic conversion of methane occurred over the oxygen vacancies in titania. The charge separation and recombination prohibition in titania are enhanced by the interaction with metallic NPs. A hydrocarbon productivity of 1864 μmol g^{-1} h^{-1} with a coupling selectivity over 86 % was observed in the continuous gas flow process.

4.2 Results and Discussion

4.2.1 Characterization of the Au-TiO$_2$ catalysts

The TEM images of colloidal gold NPs (**Figure 1, Chapter 2**) show isolated spherical gold NPs with relatively narrow distributions with an average size from 5 to 32 nm. The images of Au/TiO$_2$ catalysts prepared from gold colloidal NPs (**Figure 2, Chapter 2**) display TiO$_2$ crystallites with irregular morphology with mean sizes of 20–30 nm. The catalysts contain gold NPs with the sizes from 6 to 35 nm similar to those in colloidal systems.

The electron microscopy images of the calcined **Au/TiO$_2$** are shown respectively in **Figures 1**. The **Au/TiO$_2$** samples contained about 5 wt. % Au (**Table S1, Chapter 2**). After calcination, a small increase in the Au NP size was observed (**Figure 1**) for all samples, while the particle morphology remains largely intact. The average gold particle size varies in the calcined catalysts from 9 to 29 nm.

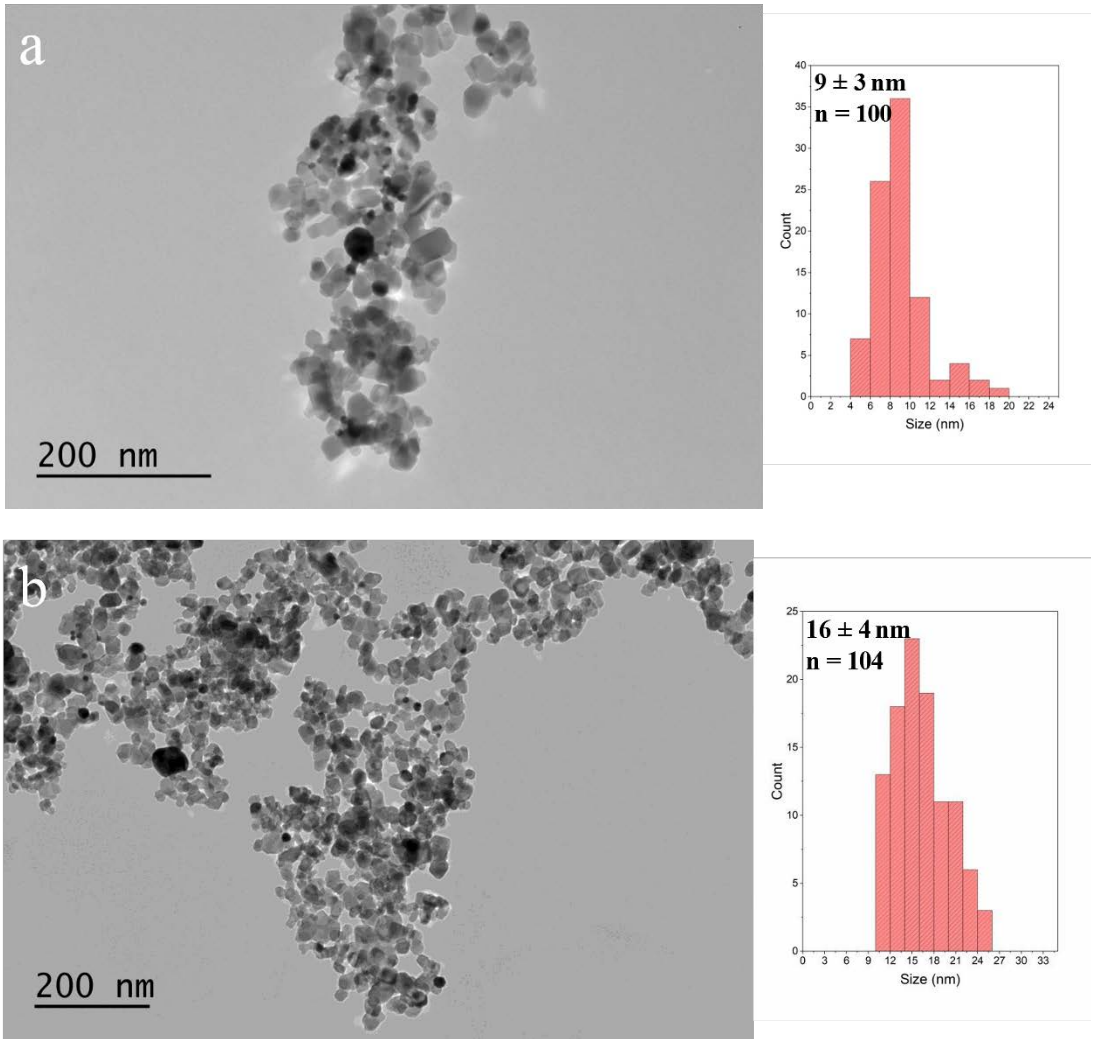

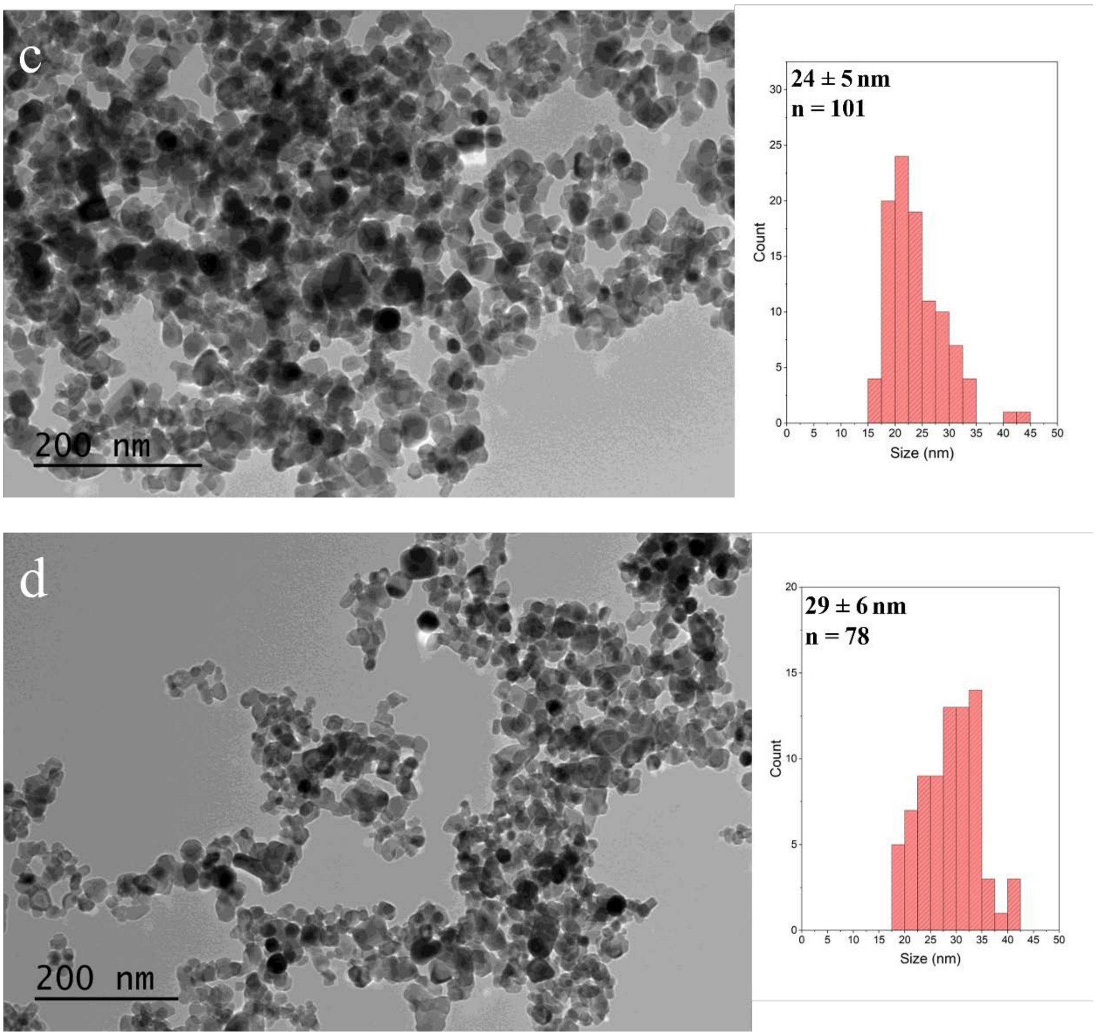

Figure 1. TEM images and histograms of size distribution for Au particle size in calcined (a) 6 nm Au/TiO_2, (b) 14 nm Au/TiO_2, (c) 22 nm Au/TiO_2 and (d) 30 nm Au/TiO_2.

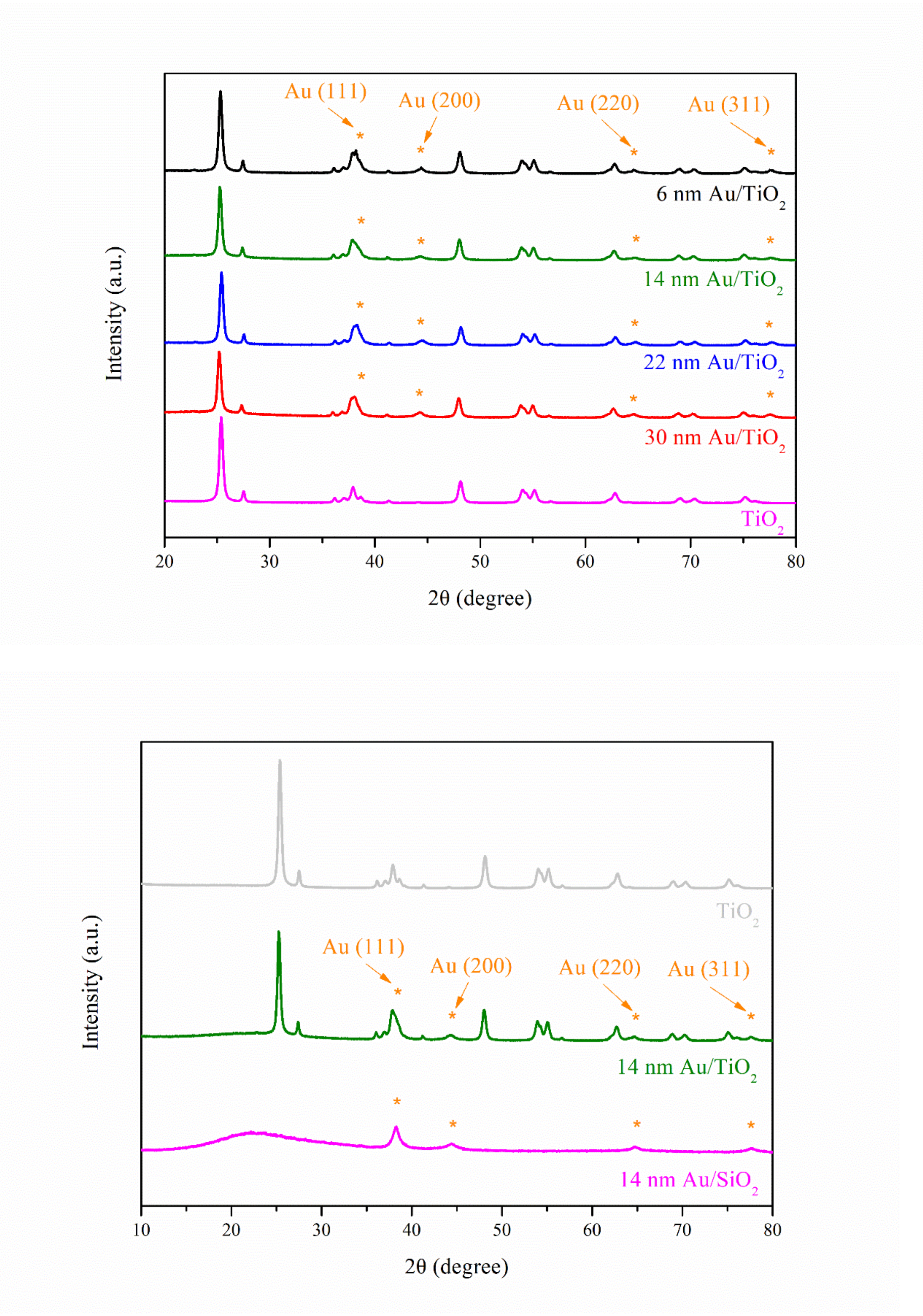

Figure 2. X-ray diffraction patterns of (a) TiO_2 and Au/TiO_2 samples with average Au NPs size ranging from 6 nm to 30 nm and (b) 14 nm Au/SiO_2.

The X-ray diffraction (XRD) patterns of **Au/TiO$_2$** samples are shown in **Figure 2a**. All the **Au/TiO$_2$** samples exhibit intense XRD peaks of the TiO$_2$ anatase and rutile phases, while the silica-based samples exhibit a broad peak centered at around 22° ascribed to amorphous SiO$_2$ (**Figure 2b**). Meanwhile, the diffraction peaks located at 38.2, 44.3, 64.6, and 77.5° were assigned to the Au NPs [32]. The **Au/TiO$_2$** samples with metal NPs of 6 nm, 14 nm, 22 nm and 30 nm show broad diffraction peaks attributed to the gold metallic phase. In agreement with TEM results, the broad XRD patterns indicate the presence of relatively small gold NPs. Interestingly, gold NPs of 14 nm supported on titania or silica exhibit similar XRD patterns suggesting the presence of gold NP size of similar size in both oxides.

The Au NPs supported on TiO$_2$ were further investigated by XPS (**Figure 3).** The two Au 4f binding energies, corresponding to 4f$_{5/2}$ and 4f$_{7/2}$ at around 87 and 83 eV, indicate the metallic Au phase [33].

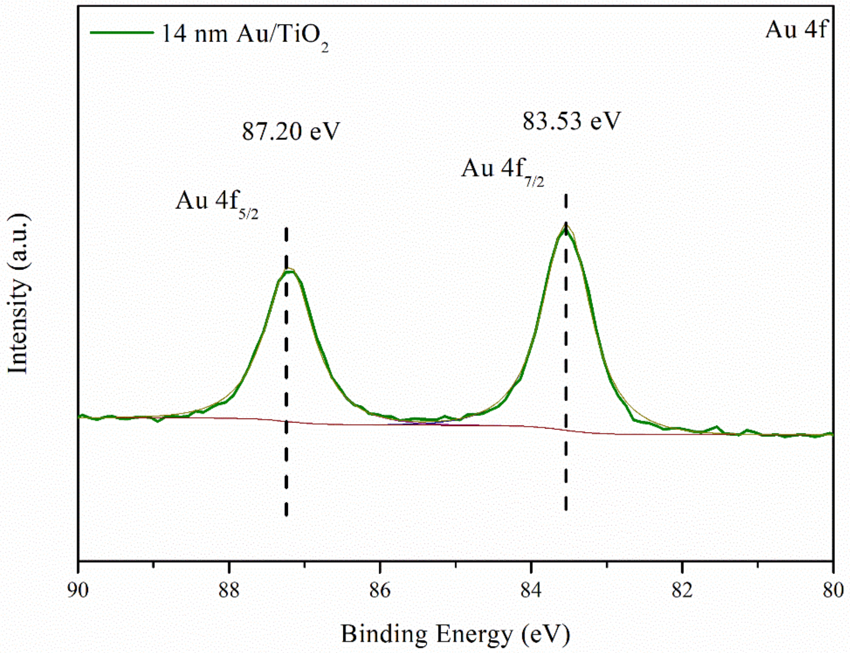

Figure 3. XPS analysis of the Au 4f of 14 nm Au/TiO$_2$ samples.

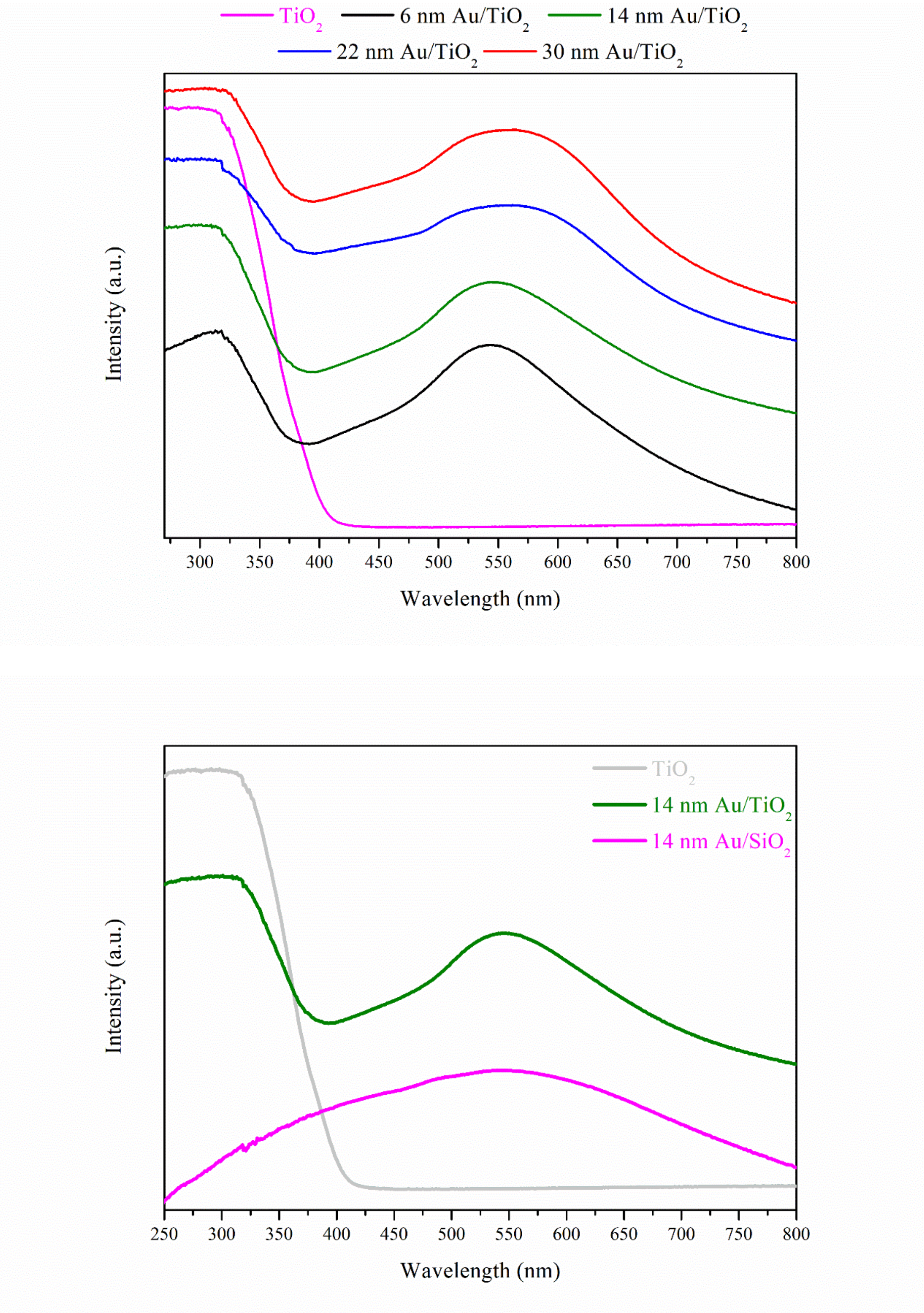

Figure 4. UV-Vis absorption spectra of (a) TiO_2 and Au/TiO_2 samples with average Au NPs size ranging from 6 nm to 30 nm and (b) 14 nm Au/SiO_2.

Figure 4a shows results from UV-Vis spectroscopy for all the titania-based samples. They exhibit the absorption peaks located at the UV region due to the photoexcitation of TiO_2. In addition, all the **Au/TiO_2** samples display a broad surface plasmon resonance (SPR) absorption peak of Au NPs at 400-700 nm and centered at around 550 nm. A red-shift of the SPR absorption peaks is observed in **Au/TiO_2** samples with large gold NPs (**22 nm Au/SiO_2** and **30 nm Au/SiO_2**) relative to the samples with smaller Au NPs. The observation is consistent [34] with the shift of LSPR to longer wavelengths with an increase in NPs size. Interestingly, the **14 nm Au/SiO_2** and **14 nm Au/TiO_2** samples with gold NPs of 14 nm exhibit similar Au SPR absorption peak (**Figure 4b**).

The photocurrent tests were conducted using irradiation close the band gap of titania and SPR absorption in order to evaluate the charge separation behavior of photocatalyst (**Figure 5**). For the pristine **TiO_2**, a negligible photocurrent density was observed. **14 nm Au/TiO_2** exhibited significantly high photocurrent density at both excitation wavelengths. This indicates a more effective charge separation in 14 nm **Au/TiO_2** compared to **TiO_2** caused by the band gap and plasmonic absorption.

The charge separation and charge transfer between TiO_2 and Au NPs were investigated using photoluminescence (PL) spectra (**Figure 6**). Pristine **TiO_2** exhibited a strong PL emission peak at 440 nm, which correlated with the severe charge recombination occurring in TiO_2 nanocrystal. After the decoration with the Au NPs, the PL emission peaks were greatly quenched, suggesting the pronounced charge separation within Au/TiO_2 samples. The weakest PL peak observed for **14 nm Au/TiO_2** demonstrates obvious suppression of charge recombination rate, which is well consistent with the photocurrent analysis (**Figure 5**). These results emphasize the role of Au NPs in charge transfer and separation between Au and **TiO_2** in the supported **Au/TiO_2** catalysts.

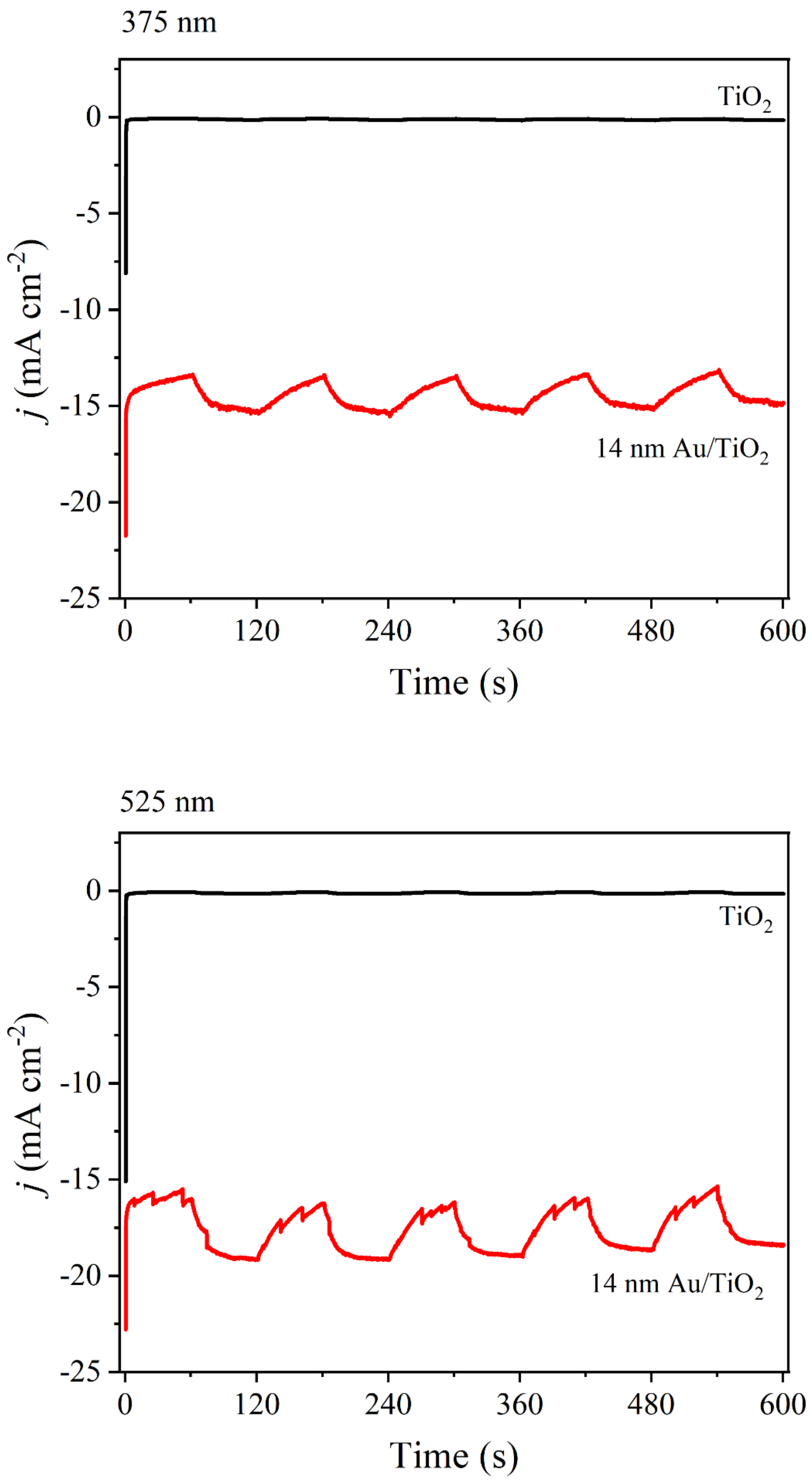

Figure 5. Photocurrent measured for **14nm Au/TiO$_2$** and **TiO$_2$** samples

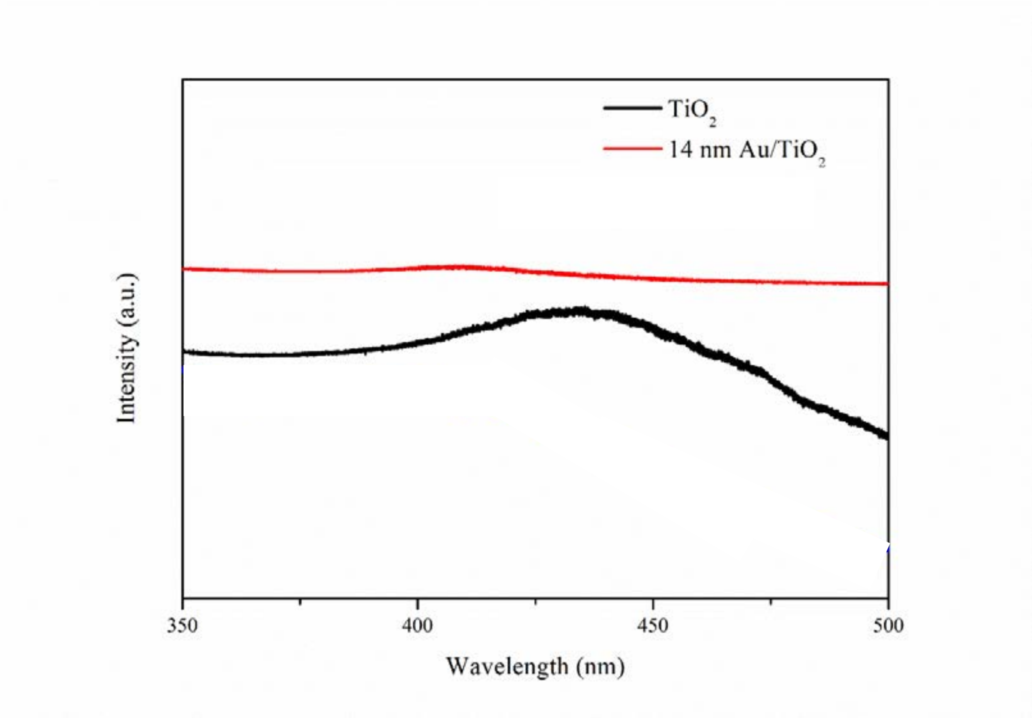

Figure 6. Photoluminescence (PL) spectra of TiO_2 and 14 nm Au/TiO_2

4.2.2 Photocatalytic NOCM over Au/TiO_2

Table 1. Control experiments results of the methane coupling over the 14 nm Au/TiO_2

Reactant	Catalyst	Light	Products
-	√	√	None
CH_4 or CH_4 + Air	×	√	None
	√	×	None
	√	√	Yes

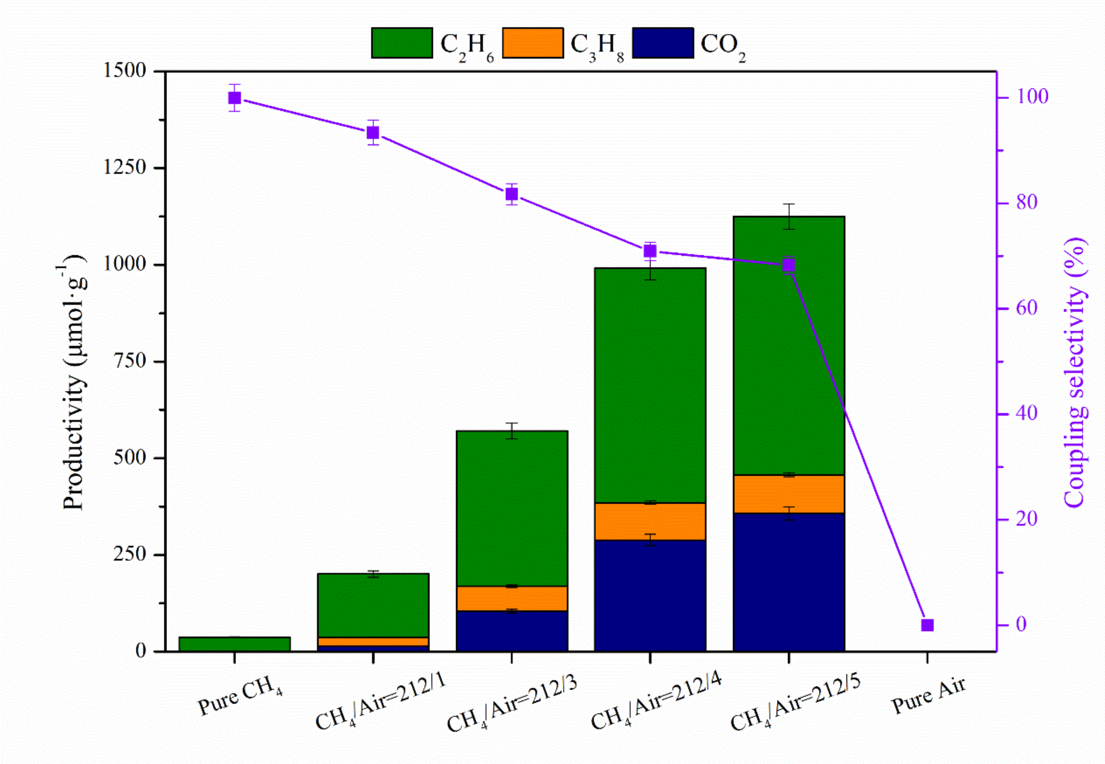

Figure 7. Photocatalytic NOCM and OCM performance of 14 nm Au/TiO_2. Reaction conditions: 50 mg catalyst, 0.3 MPa, 3 h, 20 ± 2 °C, 400 W Xe lamp with full irradiation

The photocatalytic NOCM over the **Au/TiO_2** and **Au/SiO_2** samples was studied in the batch reactor (**Figure 4a, Chapter 2**). No product was detected in the blank experiments without light or without catalyst (**Table 1**). This suggests that methane conversion is indeed driven by photocatalysis. The photocatalytic performance of **14 nm Au/TiO_2** in anaerobic conditions (without air) is presented in **Figure 7**. Under pure methane, a small amount of ethane and traces of propane are produced in NOCM over the **14 nm Au/TiO2** sample. In addition to ethane, stoichiometric amounts of hydrogen were produced in NOCM:

$2\ CH_4 \rightarrow C_2H_6 + H_2$

For comparison, we also studied NOCM in pure methane on bare **TiO2** (**Figure 8)**. Only negligible methane conversion was detected over **TiO2** under the same conditions in the absence of air.

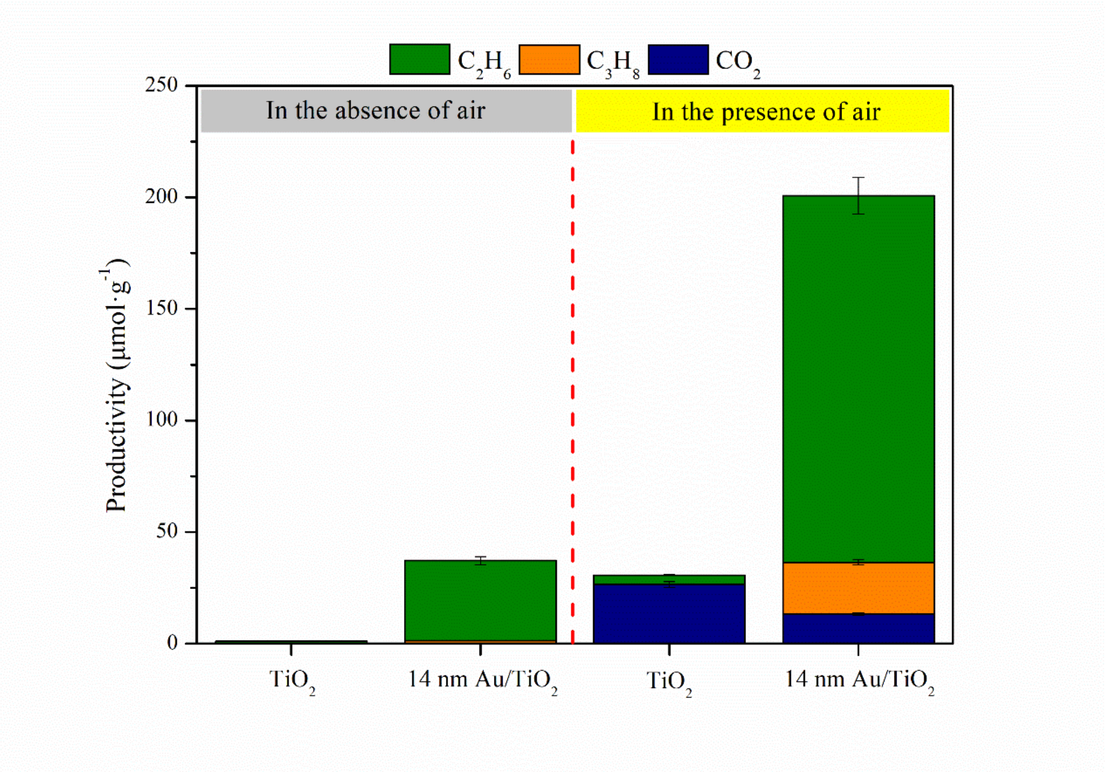

Figure 8. Photocatalytic methane coupling performance over 14 nm Au/TiO2 and TiO2; Reaction conditions: 50 mg catalyst, 0.3 Mpa pure CH_4 or CH_4/Air= 212/1, 3 h, 20 ± 2 °C, 400 W Xe lamp with full irradiation.

Furthermore, NOCM was investigated over the **Au/TiO2** samples with a gold average NP size ranging from 6 nm to 30 nm (**Figure 9**). The **6 nm Au/TiO2** sample exhibits slightly higher methane coupling activity than the Au/TiO2 catalysts with larger NPs (**22 nm Au/TiO2** and **30 nm Au/TiO2**). Interestingly, the catalytic performance of **Au/TiO2** catalysts with gold NPs of **22 nm** and **30 nm** was indistinguishable. It is well known that smaller NPs would expose more active surface sites and may engender stronger metal-support interaction. The slightly higher

NOCM activities observed on the **6 nm Au/TiO2** and **14 nm Au/TiO2** samples would be due to better gold dispersion.

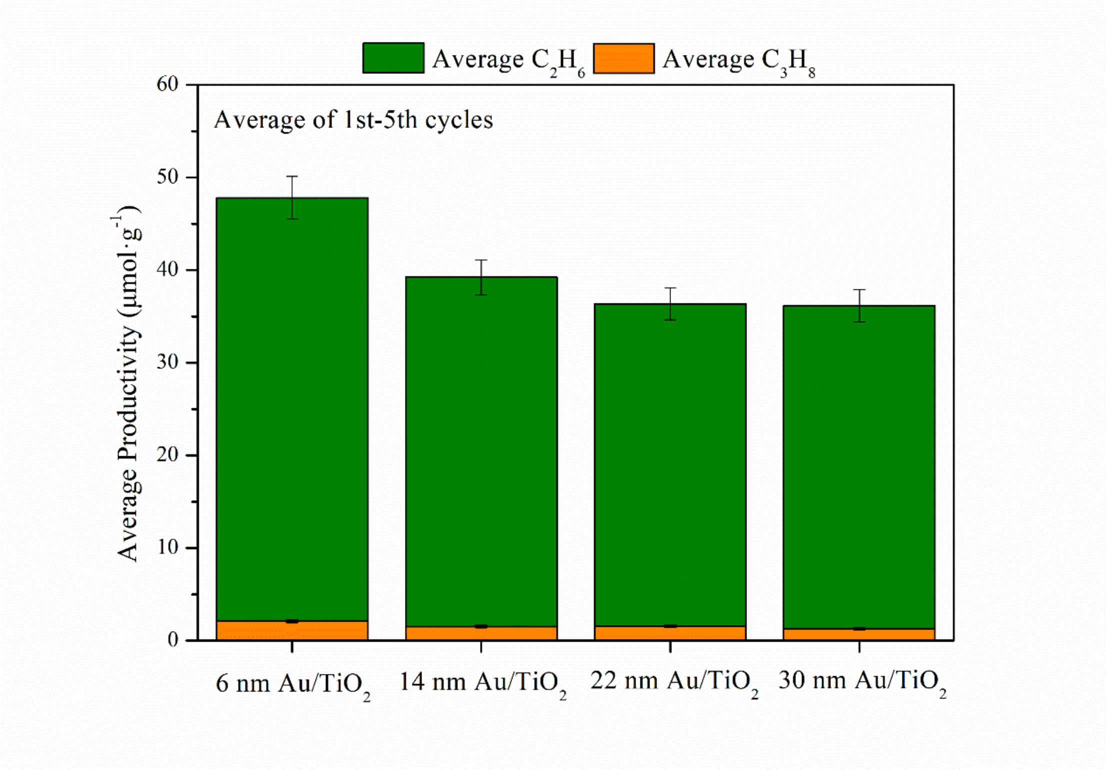

Figure 9. Average photocatalytic NOCM performance over Au/TiO_2 with different Au nanoparticle size; Reaction conditions: 50 mg catalyst, 0.3 Mpa CH_4, 3 h, 20 ± 2 °C, 400 W Xe lamp with full irradiation

Figure 10 shows the ethane and propane production as a function of reaction time in NOCM over **14 nm Au/TiO2**. The hydrogen to hydrocarbon ratio does not change with the reaction time. All the **Au/TiO2** samples showed excellent stability in NOCM. No obvious deactivation was observed after 5 consecutive NOCM reaction runs performed in the batch reactor (**Figure 11**).

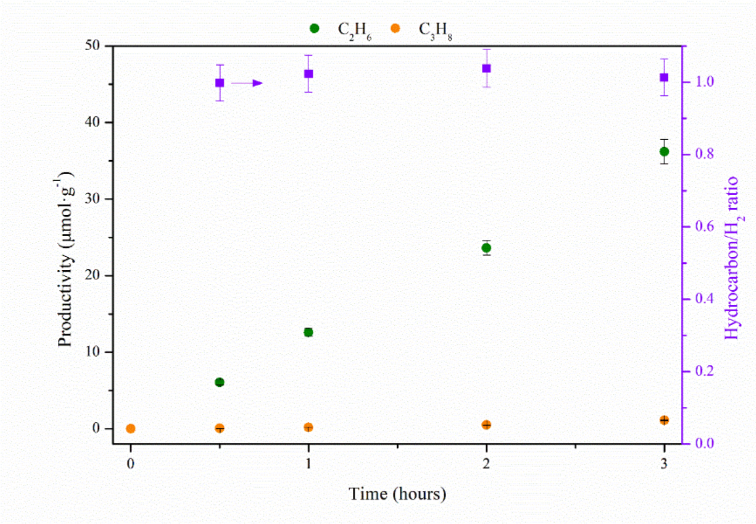

Figure 10. Time course of photocatalytic NOCM performance over 14 nm Au/TiO_2. Reaction conditions: 50 mg catalyst, 0.3 Mpa CH_4, 0-3 h, 20 ± 2 °C, 400 W Xe lamp with full irradiation

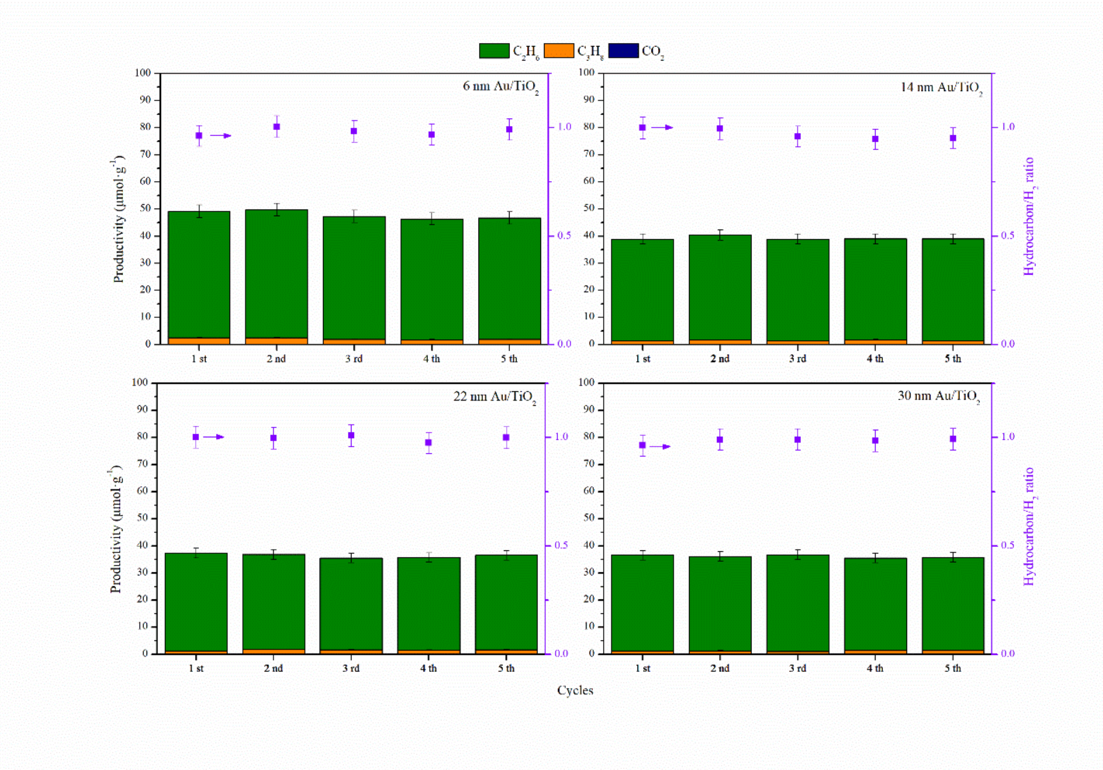

Figure 11. Photocatalytic NOCM performance over Au/TiO_2 with different Au nanoparticle size; Reaction conditions: 50 mg catalyst, 0.3 Mpa CH_4, 3 h, 20 ± 2 °C, 400 W Xe lamp with full irradiation.

4.2.3 Photocatalytic OCM over Au/TiO2

The presence of air spectacularly boosts methane coupling on both **TiO_2** and **Au/TiO_2** samples. In **OCM** in the batch reactor, **Au/TiO_2** produces ethane with a coupling selectivity higher than 90% (**Figure 7**). CO_2 is also produced, while the amount of hydrogen generated from methane, strongly diminishes. Besides ethane, small amounts of propane were detected over **Au/TiO_2**, possibly resulting from methane-ethane oxidative cross-coupling. Furthermore, more carbon oxides were detected at a higher O_2 content over **Au/TiO_2**. Thus, the optimized methane to O_2 ratio seems crucial for selective and efficient OCM. This might be due to the fact that O_2 is more reactive than methane [35]. In the present study, the methane to air ratio was fixed at 212/1 in all the OCM tests in the batch reactor.

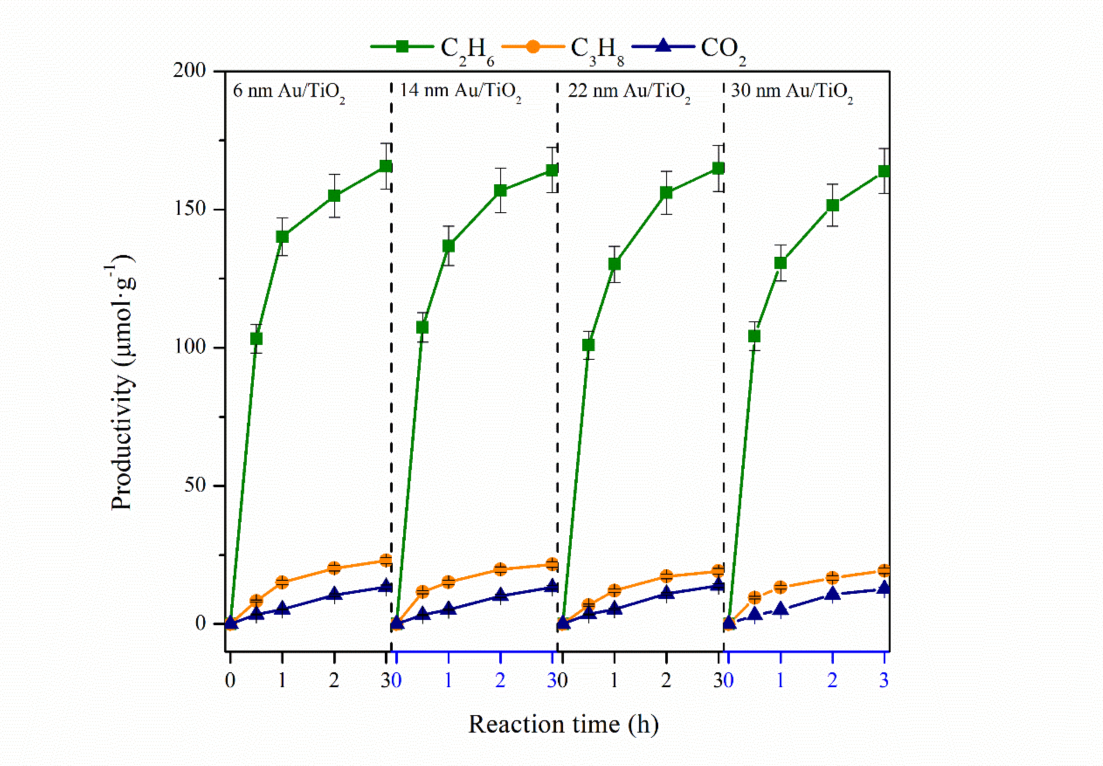

Figure 12. Photocatalytic OCM performance over Au/TiO_2 with different Au nanoparticle size; Reaction conditions: 50 mg catalyst, 0.3 MPa, CH_4/Air= 212/1, 0-3 h, 20 ± 2 °C, 400 W Xe lamp with full irradiation.

Then, we measured methane coupling as a function of gold NP size in titania (**Figure 12**). All the **Au/TiO_2** samples with different Au particle sizes exhibited nearly identical catalytic performance in the OCM reaction. Besides ethane, small amounts of CO_2 and propane were detected with almost the same selectivities. Note that **TiO_2** predominately yields CO_2 from methane in the presence of oxygen. Only very small amounts of ethane were detected in OCM over **TiO_2** under the same conditions.

Evaluation of the long-term OCM performance of **14 nm Au/TiO_2** shows a gradual increase in the amount of produced ethane with O_2 consumption during the first 7 h of reaction (**Figure 13**). The coupling selectivities were stable during the first 7 h of reaction and exceeded 90%.

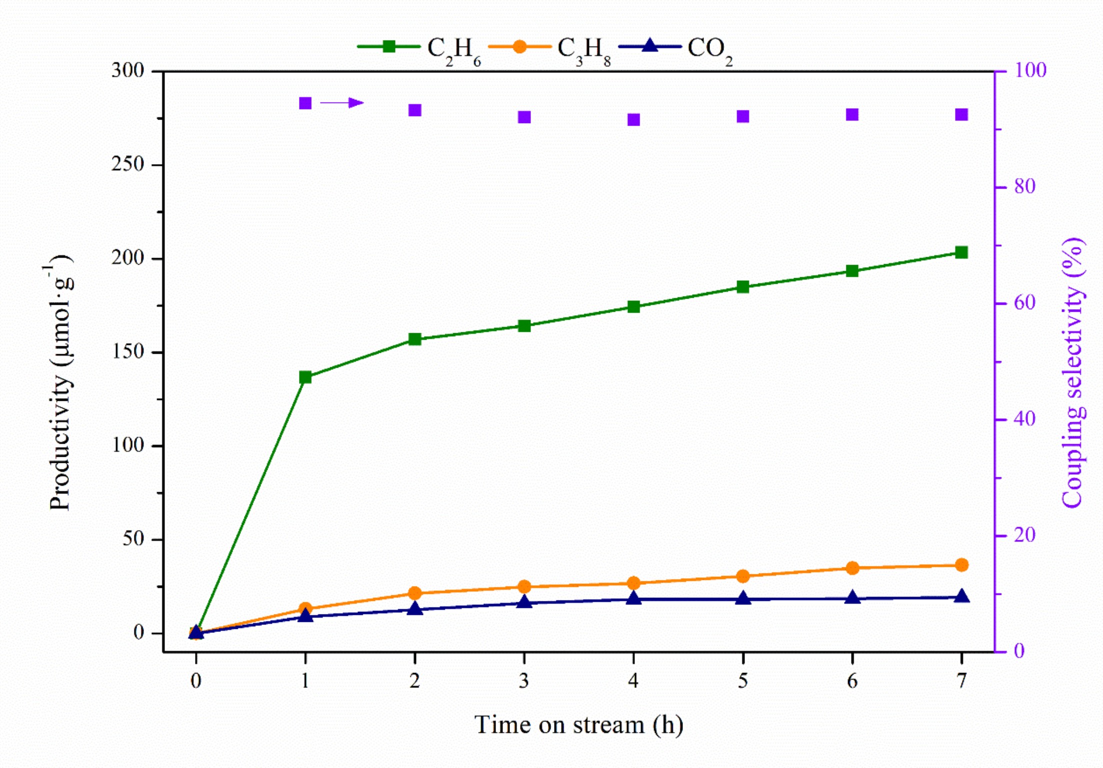

Figure 13. Time course of photocatalytic OCM over 14 nm Au/TiO_2- Reaction conditions: 50 mg catalyst, 0.3 MPa, CH_4/Air= 212/1, 0-7 h, 20 ± 2 °C, 400 W Xe lamp with full irradiation.

The photocatalytic activity of Au/TiO_2 in OCM can be initiated either by UV irradiation, which excites the band-band transition in TiO_2, or by visible light, which is adsorbed by Au plasmonic NPs. In order to evaluate the effect of different wavelength on the photocatalytic activity, the **14 nm Au/TiO_2** sample was illuminated using either full irradiation of Xe lamp, UV or visible light (**Figure 14)**. It turns out that noticeable methane conversion was observed only in the presence of full irradiation or UV light. No methane conversion was detected under only visible light. The photocatalytic activity under UV irradiation was slightly lower compared to that under full irradiation, which could be due to lower UV irradiation intensity due to the use of a filter. Interestingly, the same methane coupling selectivity was observed in the methane conversion under full irradiation or UV.

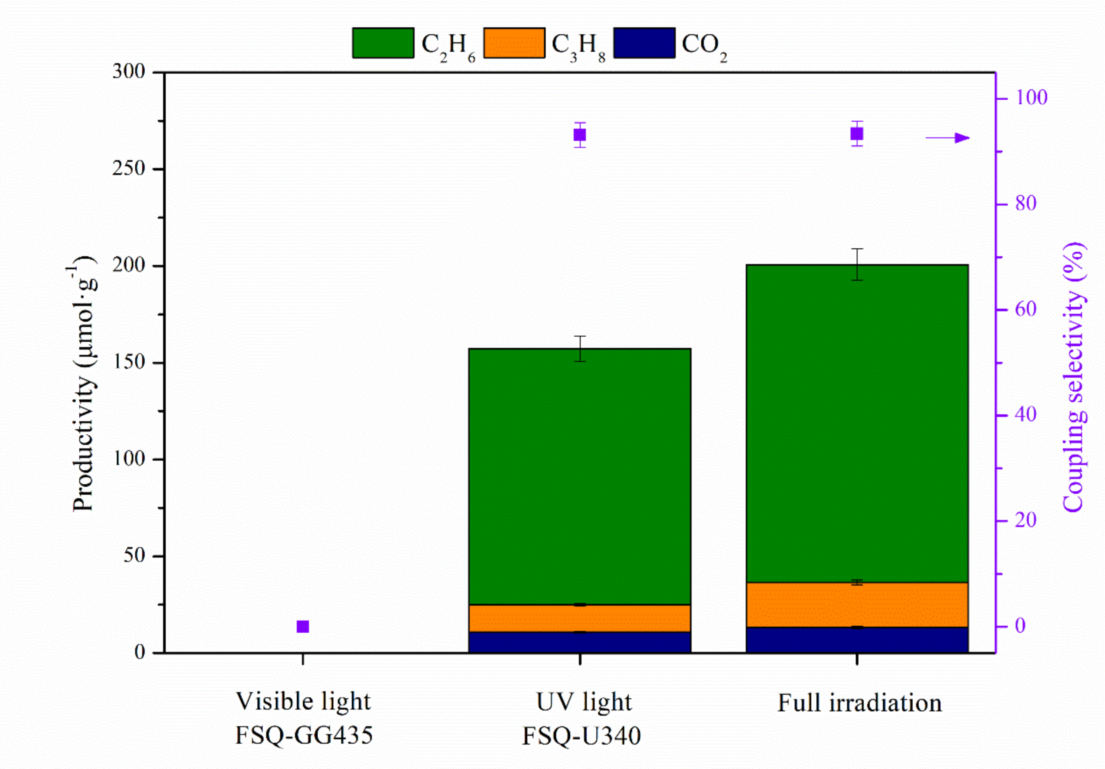

Figure 14. Photocatalytic OCM over 14 nm Au/TiO_2 under different irradiation; Reaction conditions: 50 mg catalyst, 0.3 MPa, CH_4/Air= 212/1, 3 h, 20 ± 2 °C, 400 W Xe lamp with visible light, UV light and full irradiation.

In order to further evaluate the contribution of plasmonic effect of gold NPs on the methane conversion, the silica-based catalyst (**14 nm Au/SiO_2**) was tested in methane conversion under the identical conditions as titania-based counterpart with the same size of gold NP (**14 nm Au/TiO_2**). Silica is an insulator and no contribution of silica to the photocatalytic methane conversion is expected under these conditions. No methane conversion was detected over **14 nm Au/SiO_2** under neither visible light, UV light nor full irradiation. This suggests that the Au plasmonic effect alone induced by visible light cannot trigger the methane conversion. This is possibly due to the lower oxidation potential of holes in the Au plasmonic NPs, which is insufficient for methane activation [36]. At the same time, the plasmonic effect of gold NPs can be synergistic and can contribute to enhancing charge separation and accelerating charge transfer in the **TiO_2** supported catalysts.

The type of reactor can have a strong influence on the photocatalytic reaction [27,37]. The irradiation intensity, flow rate, methane and O_2 concentrations in the photoreactor play important roles in the OCM performance. OCM over **14 nm Au/TiO_2** was further studied in a continuous gas flow reactor (**Figure 4b, Chapter 2**).

The results in the flow reactor were then compared to those obtained in the batch reactor. High flowing rates could cause insufficient contact time of reactants with the catalyst, leading to lower methane conversion. Under the optimized irradiation and composition of methane-air mixture with a total flowing rate of 41 ml min^{-1}, the ethane production in the flow reactor reaches 1638 μmol g^{-1} h^{-1} with a coupling selectivity up to 86% (**Figure 15**). Thus, the ethane productivity is 30 times higher in the flow reactor than that in the batch reactor (**Figure 16**).

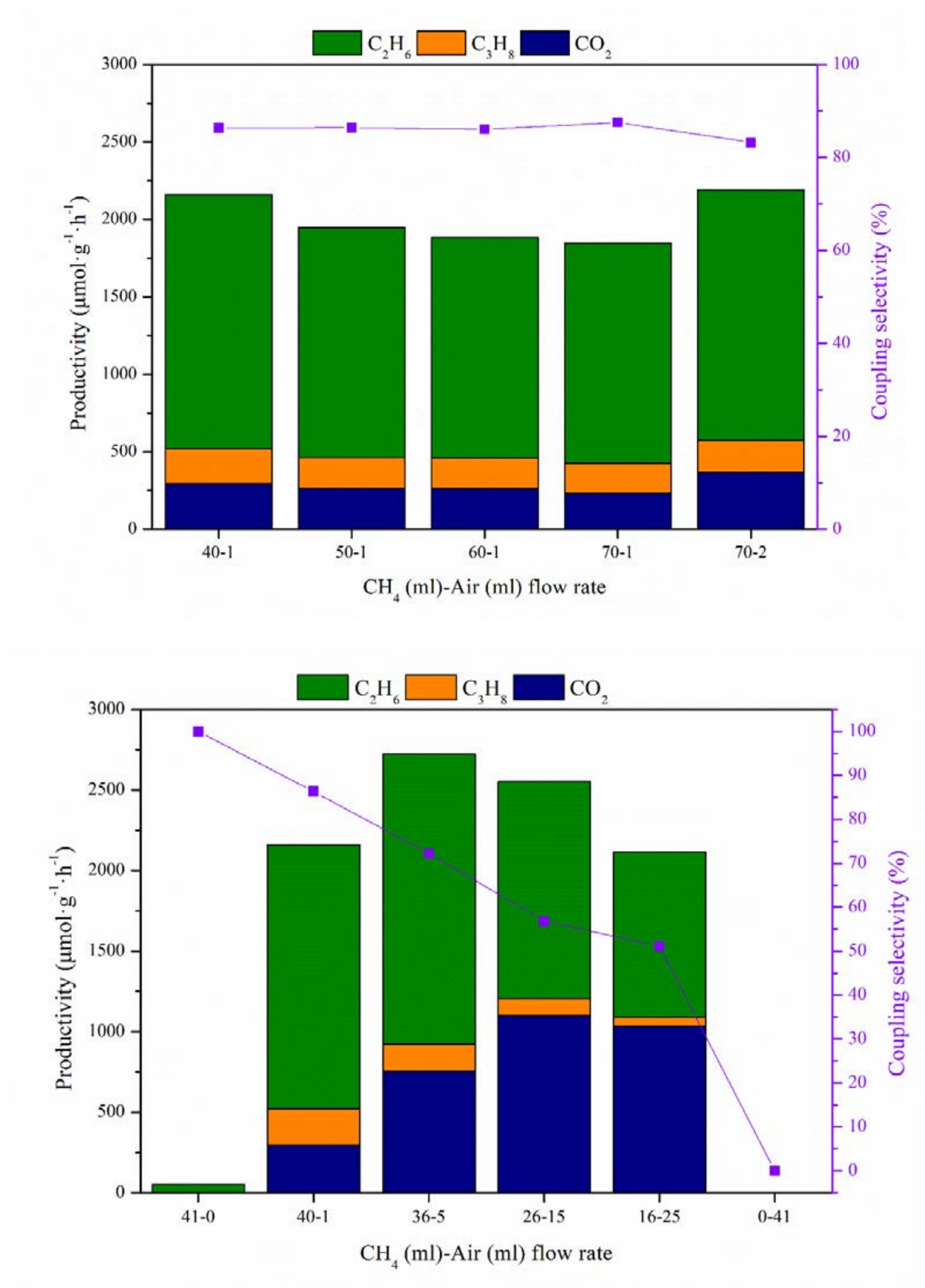

Figure 15. Photocatalytic OCM performance over 14 nm Au/TiO_2 with different methane to air ratio in continuous gas flow process; Reaction conditions: 20 mg catalyst, atmospheric pressure, 400 W Xe lamp with full irradiation.

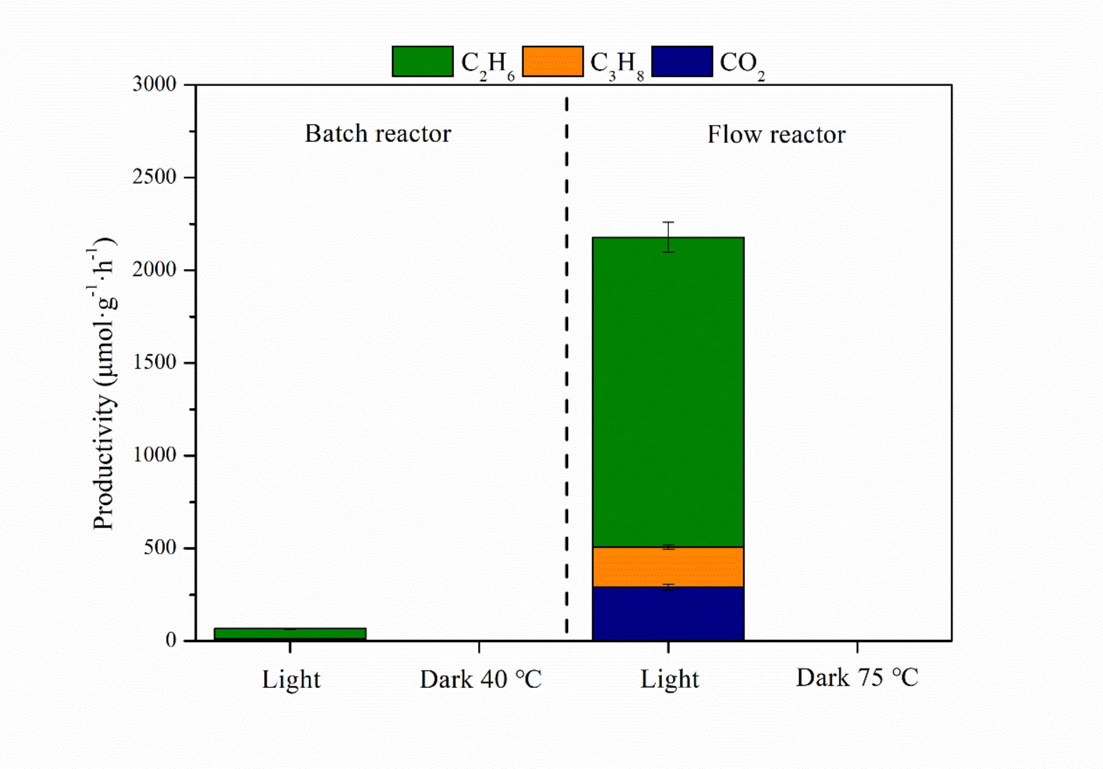

Figure 16. Photocatalytic and thermal OCM performance over 14 nm Au/TiO_2 in batch and flow reactor; Reaction conditions in batch reactor: 50 mg catalyst, 0.3 Mpa, CH_4/Air= 212/1, 3 h. Reaction conditions in flow reactor: 20 mg catalyst, atmospheric pressure, CH_4/Air= 40 ml min^{-1}/1 ml min^{-1}.

We measured apparent quantum yields (AQY) in both batch and flow reactors. Despite higher overall productivity in the flow reactor, AQY at 360 nm in OCM remain similar in both batch and flow reactors (**Figure 17)**. In the batch process, the AQY was 2.40 % in the first 1 h, while it decreased to 1.83% in 3 h due to the consumption of oxygen. In the flow reactor, a stable AQY of 2.36 % was observed in 2 h. Note that the batch process showed similar AQY in comparison with the flow process in the first 1 h. The higher OCM productivity of the flow reactor is likely due to the higher intensity of irradiation. Interestingly, the decrease in the gold content in the **14 nm Au/TiO_2** catalyst from 5 to 0.5 wt. % does not result in lower rate or selectivity of methane conversion (**Figure 18**). Some decrease in methane conversion is only observed when the gold content in the catalyst drops to less than 0.5 wt. %.

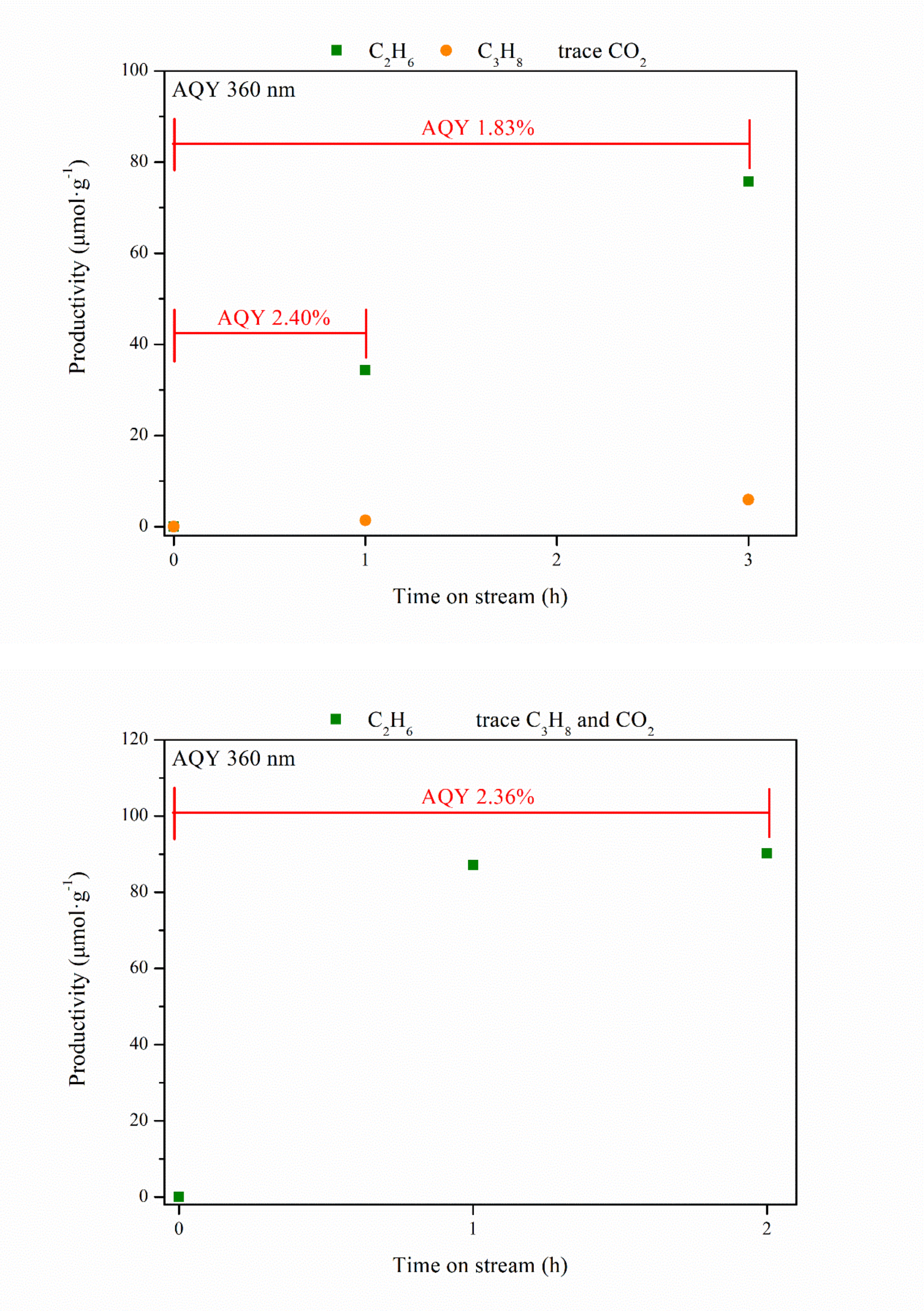

Figure 17. The apparent quantum yield (AQY) at 360 nm during photocatalytic OCM over 14 nm Au/TiO_2 in the (a) batch reactor and (b) flow reactor.

Interestingly, the decrease in the gold content in the **14 nm Au/TiO2** catalyst from 5 to 0.5 wt. % does not result in lower rate or selectivity of methane conversion (**Figure 18**). Some decrease in methane conversion is only observed when the gold content in the catalyst drops to less than 0.5 wt. %.

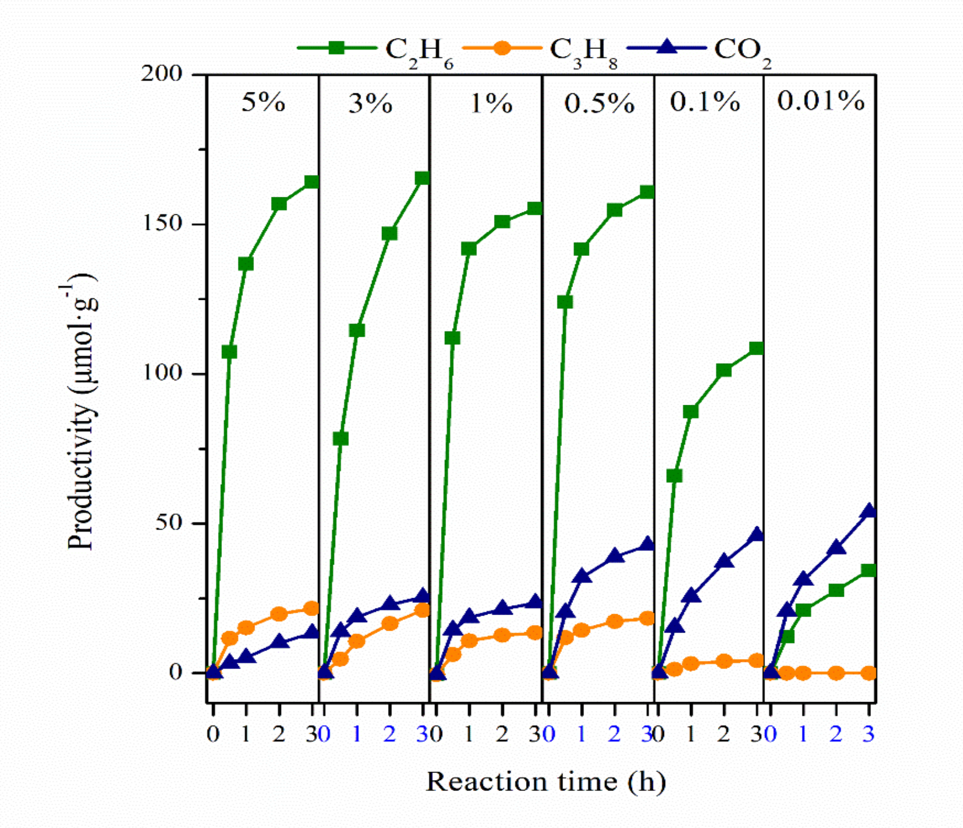

Figure 18. Time course of photocatalytic OCM over Au/TiO2 with different Au contents. Reaction conditions: 50 mg catalyst, 0.3 MPa, CH_4/Air= 212/1, 0-3 h, 20 ± 2 °C, 400 W Xe lamp with full irradiation.

In addition, stable OCM photocatalytic activity without noticeable deactivation was observed in the flow reactor for 8 h (**Figure 19**). The stability of photocatalytic performance seems to be due to the stability of catalyst structure. Indeed, undistinguishing XRD patterns were observed for the spent and fresh **14 nm Au/TiO2** catalysts (**Figure 20**).

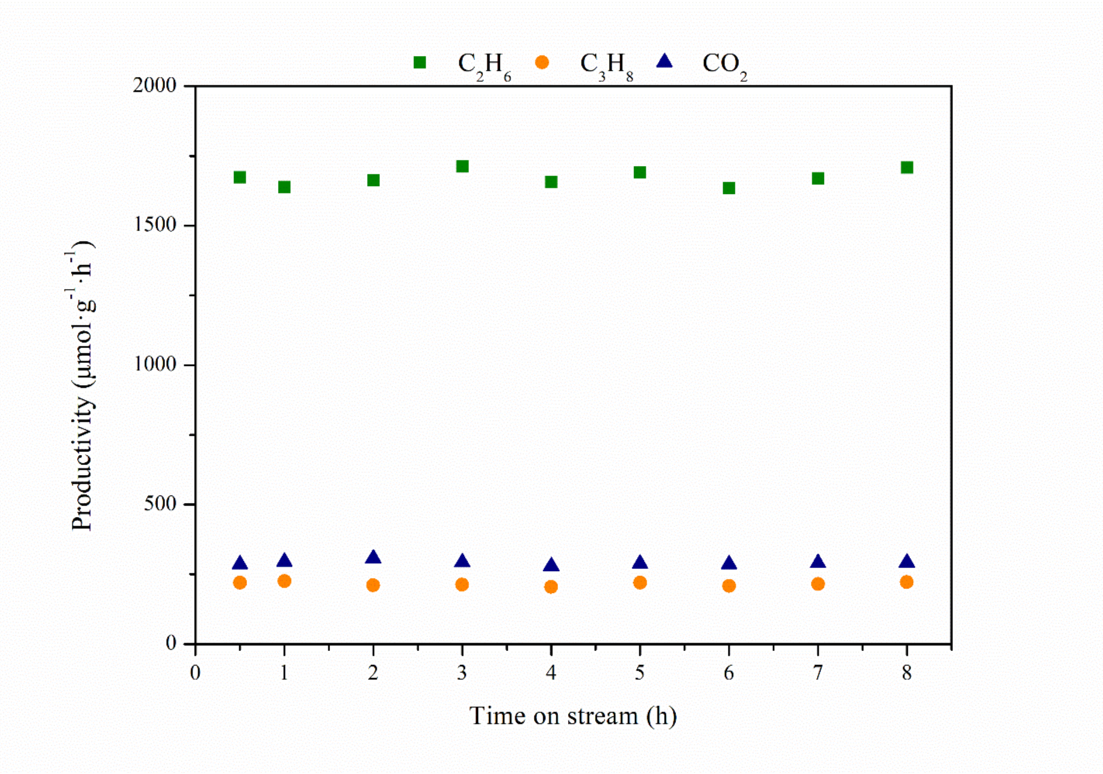

Figure 19. Stability test of photocatalytic OCM reaction over 14 nm Au/TiO_2 in the continuous gas flow process; Reaction conditions: 20 mg catalyst, atmospheric pressure, 0-8 h, 400 W Xe lamp with full irradiation.

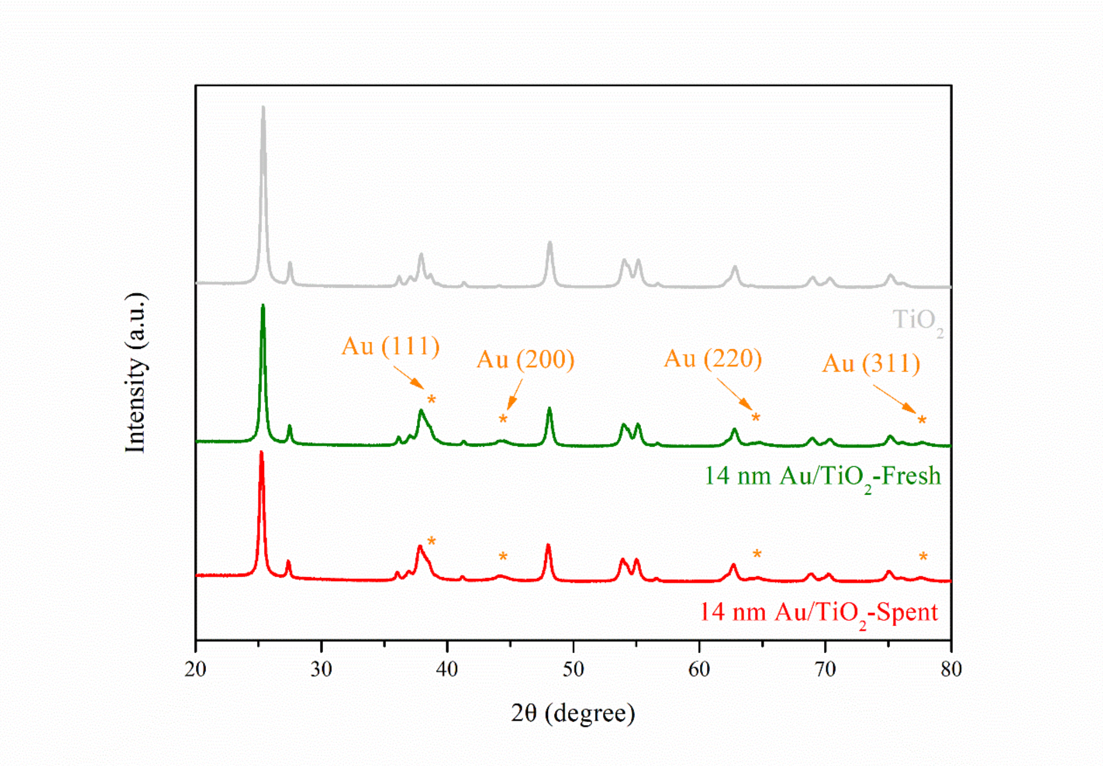

Figure 20. XRD patterns of the fresh and spent 14 nm Au/TiO_2

The thermal gravimetric analysis shows negligible carbon deposition on the spent catalyst after 8 h of OCM reaction (**Figure 21**). Hence, the continuous gas flow OCM process with optimized catalyst irradiation could be a promising alternative to the commonly used batch photocatalytic process.

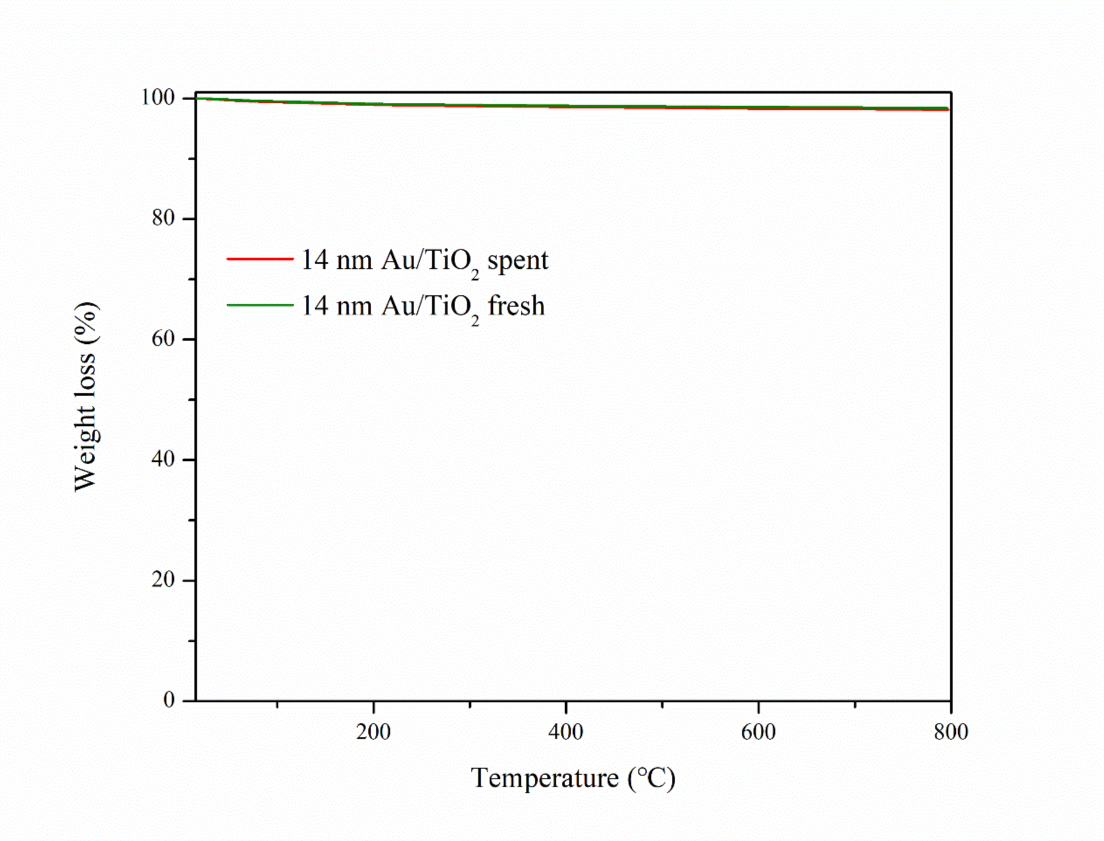

Figure 21. TG spectra of the fresh and spent 14 nm Au/TiO_2.

4.2.4 Mechanism of OCM over Au/TiO$_2$

The activation of molecular methane and O_2 over **TiO$_2$** and **Au/TiO$_2$** can be regarded as key steps in the efficient and selective OCM. These molecules can be activated either on gold NPs or on **TiO$_2$** oxygen vacancies.

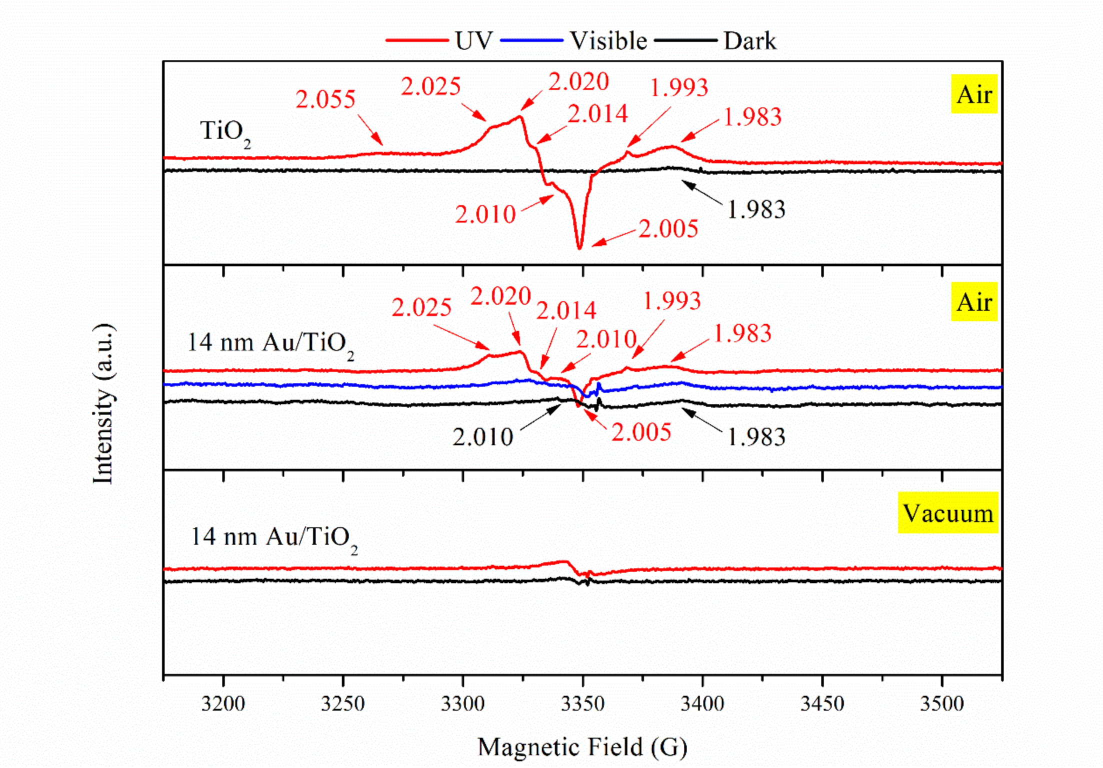

Figure 22. In situ EPR spectra of **TiO$_2$** and **14 nm Au/TiO$_2$** in air or in vacuum under dark conditions (black line), visible light (blue line) and UV light irradiation (red line)

It is well known that O_2 adsorbed on the surface of catalysts is a strong electron scavenger forming the superoxide anion (O_2^-)[38], which contributes to charge separation and methane oxidation. As shown in **Figure 22**, in the dark, two weak EPR signals with g=2.010 and g=1.983 are assigned[39][40] to oxygen vacancies and Ti^{3+}. Upon UV irradiation in the presence of air, two types of paramagnetic species were detected: reactive oxygen species (ROS) and Ti^{3+}, with a series of new signals (g=1.983-2.055), revealing the generation of surface species, because of the interaction between catalyst surface sites and O_2. The signals at $g < 2.00$ (g=1.993 and 1.983) were assigned to the surface electron trapping site Ti^{3+}, and the signals with $g > 2.00$ (g=2.005, 2.010, 2.014, 2.020, 2.025 and 2.055) were assigned to the reactive oxygen species (ROS)

[39][40]. For **14 nm Au/TiO_2**, almost no new EPR signal was observed neither under visible light in the presence of air nor under UV light in vacuum. These results confirm that the produced EPR signals with $g > 2.00$ can be assigned to the O_2^- radical [31][39][40]. Visible light can therefore, hardly activate O_2. In addition, note that under UV light in the presence of air, the EPR signal intensities of O_2^- radical over **TiO_2** are stronger than that over **Au-TiO_2**, while the **Au-TiO_2** shows better oxidative methane coupling productivity as well as selectivity. This suggests that deposition of gold NPs can neutralize some sites on the TiO_2 surface, which may activate oxygen.

To better elucidate the role of the Au NPs and **TiO_2** in the photocatalytic OCM, **14 nm Au/TiO_2** was pretreated by TEOS with a goal to cover selectively the surface of **TiO_2** by silica. The surface of **TiO_2** contains acid sites, which are necessary for the hydrolysis of TEOS to silica. The preferential localization of silica generated by TEOS hydrolysis has been further confirmed by imaging techniques (**Figure 23**). The STEM-EDS images of **14 nm Au/TiO_2** pretreated with TEOS show gold NPs localized on titania. STEM-EDS suggests a uniform distribution of silica species produced via TEOS hydrolysis over **TiO_2**. It is important to note that no localization of silica over gold NPs was observed (**Figure 23)**.

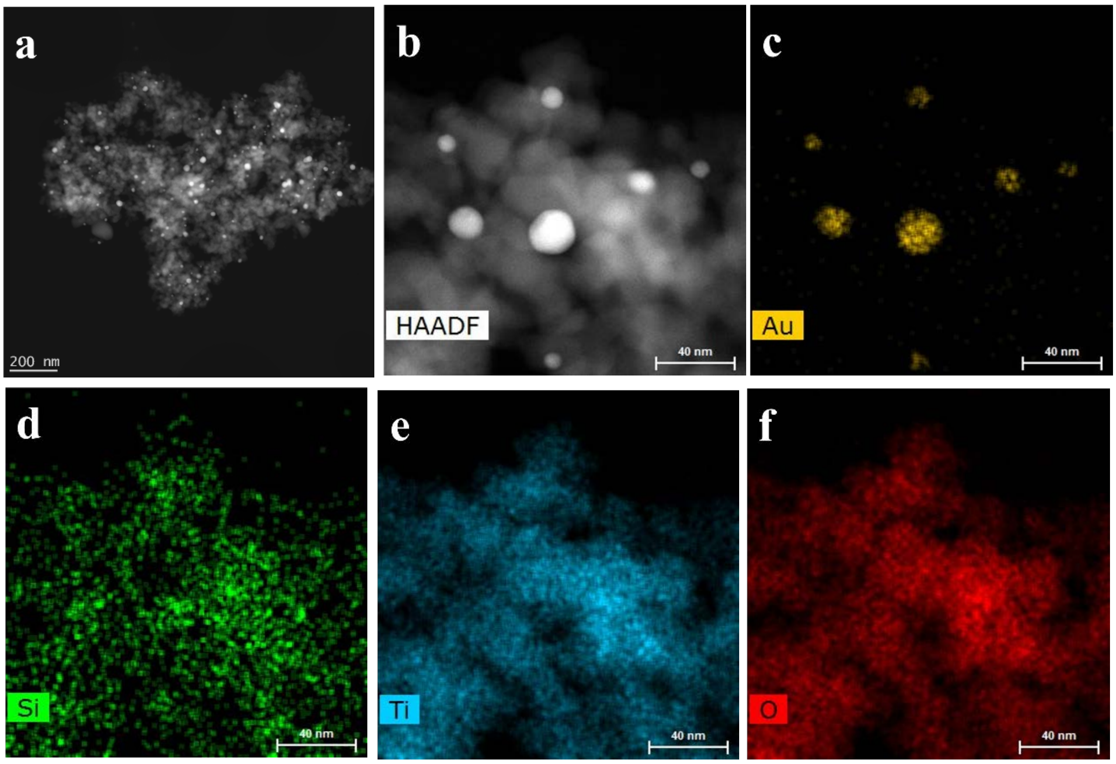

Figure 23. STEM (a, b) and STEM-EDS mapping images (c-f) of 14 nm Au/TiO_2 treated by TEOS

To provide further insights into the localization of silica introduced during the TEOS pretreatment, the **Au/TiO_2** catalyst before and after the pretreatment with TEOS was characterized by CO-FTIR (**Figure 24**). The IR bands of carbon monoxide at around 2186 cm^{-1}, which appear after the carbon monoxide adsorption over the catalysts, are attributed to CO adsorbed on Lewis acid sites (presumably oxygen vacancies linked to the Ti cations), while the bands at 2113 cm^{-1} and 2127 cm^{-1} are assigned to the CO chemisorption over metallic Au NPs [41][42]. Interestingly, the intensity of the band at around 2186 cm^{-1} attributed to the CO adsorption over titania oxygen vacancies strongly decreases after the TEOS treatment. Important, the intensity of IR bands due to the CO adsorption on Au NPs remains almost the same. A slight red shift of the CO adsorption bands on Au NPs can be possibly due to some modification of gold NPs by the **SiO_2** species. It seems that the **TiO_2** surface is effectively coated with **SiO_2**, while the surface of Au NPs is less affected by TEOS pretreatment. Besides, the spectrum of **14 nm Au/TiO_2** exhibits an additional band at 2350 cm^{-1}, which is assigned to physically adsorbed CO_2, while this peak is absent in the IR spectra of the same catalyst after

TEOS treatment. The presence of CO_2 could be due to the presence of reactive surface oxygen species, which oxidize CO to CO_2.

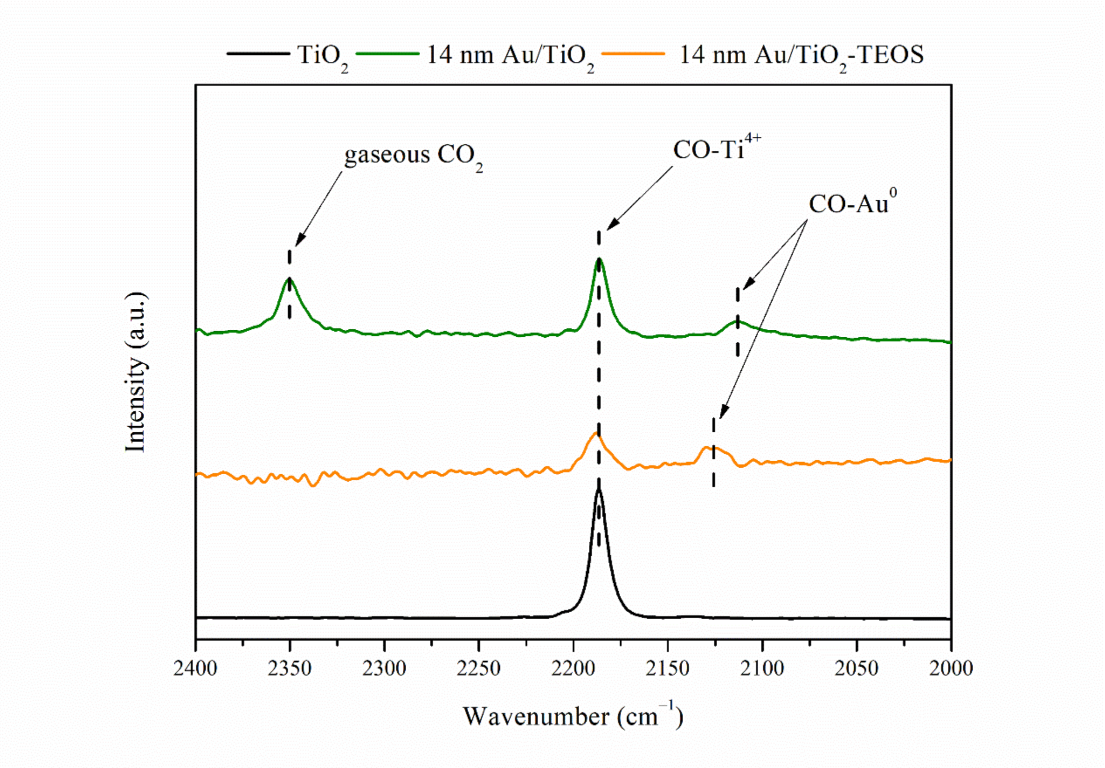

Figure 24. CO-FTIR spectra of TiO_2, 14 nm Au/TiO_2, and 14 nm Au/TiO_2 – TEOS samples.

Interestingly, **14 nm Au/TiO_2** after TEOS treatment showed twice lower activity in the methane photocatalytic conversion compared to the untreated counterpart (**Figure 25**). Considering selective coverage of the titania surface by silica, the decrease in the photocatalytic activity after TEOS pretreatment emphasizes the role of **TiO_2** surface sites in methane photocatalytic coupling. It can also be assumed that the presence of only surface sites associated with metallic gold is not sufficient to achieve photocatalytic conversion of methane.

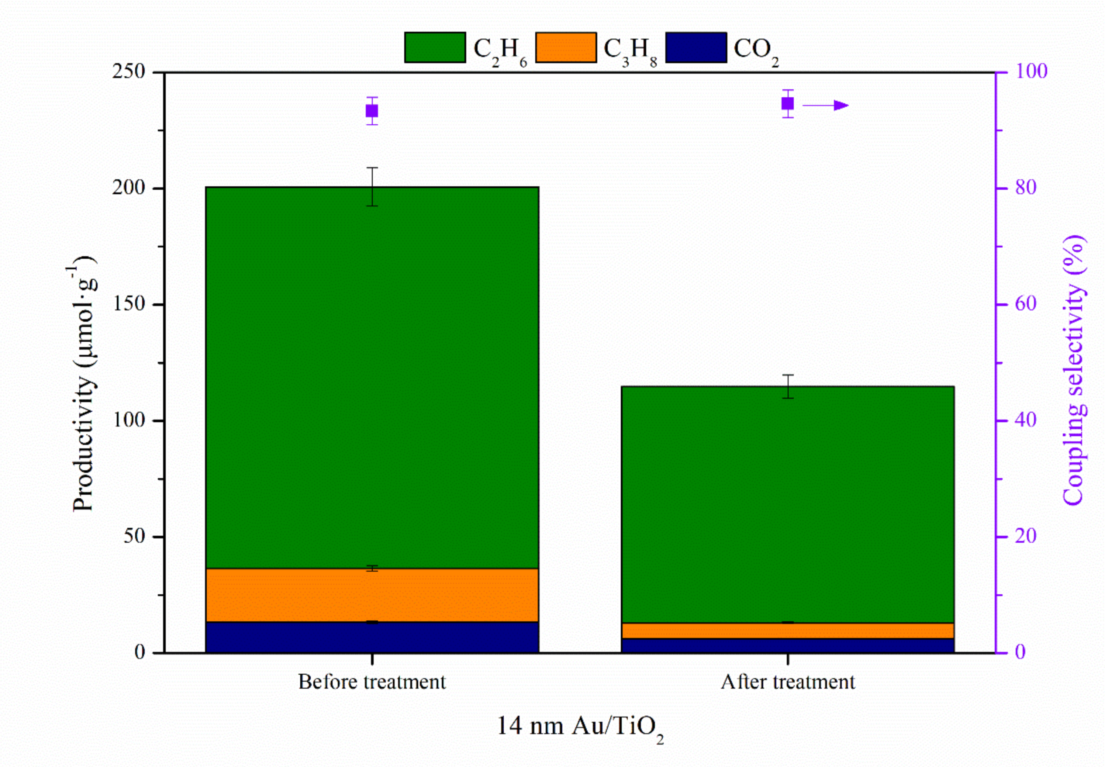

Figure 25. Photocatalytic OCM performance in batch process over 14 nm Au/TiO_2 before and after TEOS treatment. Reaction conditions: 50 mg catalyst, 0.3 Mpa, CH_4/Air= 212/1, 3 h, 20 ± 2 °C, 400 W Xe lamp with full irradiation.

To gain more insights into the photocatalytic OCM process, the *in-situ* diffuse reflectance infrared Fourier transform spectroscopic investigation (in situ DRIFTS) was performed under irradiation in the presence of methane and oxygen. A series of peaks appear after the **14 nm Au/TiO_2** catalyst exposure to methane and oxygen (**Figure 26**). The bands at 1190 cm^{-1} and 1280 cm^{-1} are assigned to the $\rho(CH_2)$ and $\omega(CH_2)$ of adsorbed HCHO* species [43]. The vibration bands at 1369 cm^{-1}, 1446 cm^{-1} and 1532 cm^{-1} are attributed to the $\upsilon_s(OCO)$, δ(CH) and $\upsilon_a(OCO)$ of adsorbed HCOO* and carbonate species [43,44]. The band at 1617 cm^{-1} corresponds to the δ(HOH) of chemisorbed water produced by the methane oxidation [44,45]. In addition, two characteristic vibration bands appear at 2857 cm^{-1} and 2919 cm^{-1}, which can be assigned to $\upsilon_s(CH_3)$ and $\upsilon_a(CH_3)$ of adsorbed $*OCH_3$ species [46,47]. Eventually, a new vibration band located at 2350 cm^{-1} is observed under prolonged irradiation (>13 min), which is assigned to $\upsilon_a(CO)$ of gaseous CO_2 [48].

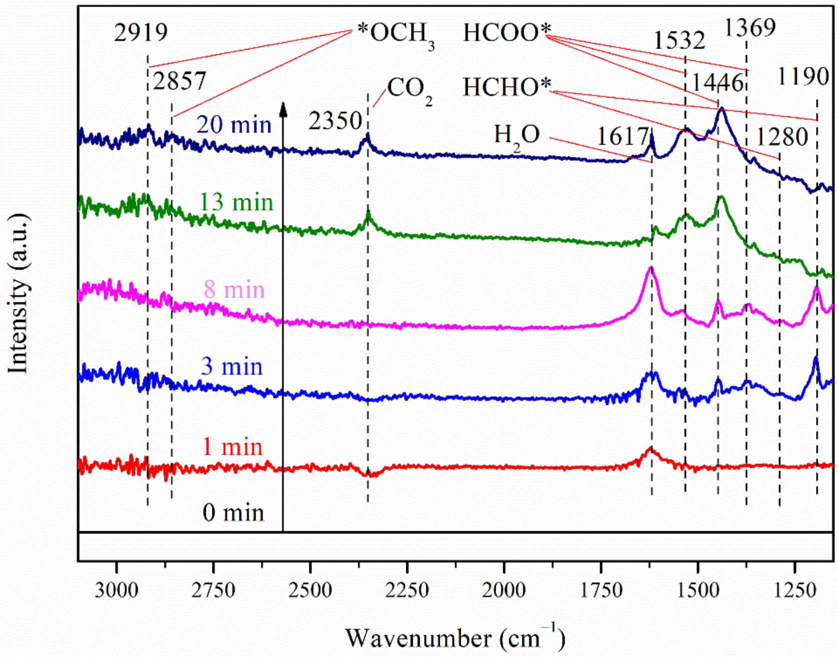

Figure 26. In situ DRIFTS spectra for photocatalytic OCM reaction over 14 nm Au/TiO$_2$

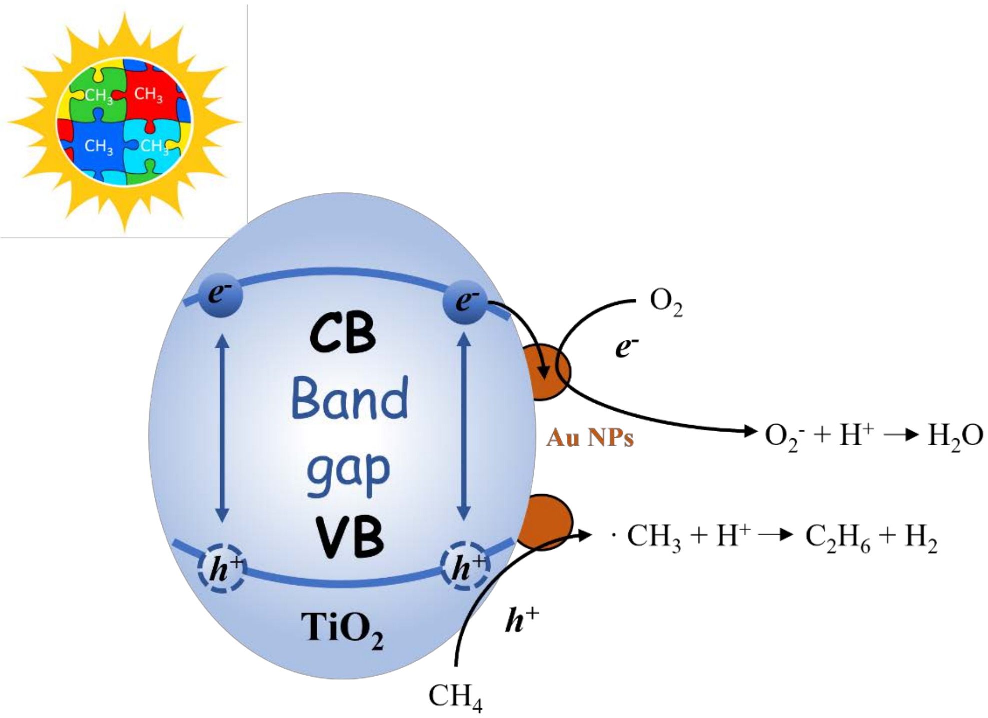

Figure 27. Proposed reaction mechanism for photocatalytic OCM over Au/TiO$_2$

Based on the above results, we propose the following mechanism of photocatalytic OCM over **Au/TiO_2** (**Figure 27).** Upon UV irradiation, the electrons are photoexcited from VB of **TiO_2** to its CB and then migrate to Au NPs. Oxygen activation takes place over Au NPs with the electron transfer to oxygen and formation of anionic O_2^- species. Activation of oxygen over gold NPs does not seem to be a kinetically relevant step in methane coupling. Indeed, a 10 time decrease in the amount of gold in the catalysts from 5 to 0.5 wt. % does not noticeably affect the photocatalytic behavior (**Figure 18**). Meanwhile, the holes in **TiO_2** are involved in the hydrogen atom abstraction from methane molecules, producing the CH_3^* species. Then, the hydrogen atoms are either oxidized by holes yielding protons and react with O_2^- with the formation of water.

The $*CH_3$ species produced on CH_4 activation on titania further combine to form ethane. Some $*CH_3$ species are captured by reactive oxygen species forming $*OCH_3$, HCHO*, and HCOO* species, which eventually decompose into CO_2. In addition, ethane can be additionally activated by holes to form $*C_2H_5$ radicals, which undergo cross-coupling with other $*CH_3$ radicals to form propane.

4.3 Conclusion

The rate and selectivity in OCM and NOCM on titania-based photocatalysts are strongly enhanced by the presence of gold NPs. Methane conversion to ethane takes place in both anaerobic and aerobic conditions. The presence of oxygen results in a multifold increase in the reaction rate in the batch reactor. A hydrocarbon productivity of 1864 μmol g^{-1} h^{-1} with a coupling selectivity higher than 86% was achieved in the continuous gas flow OCM process. The methane conversion requires activation of band gap transition in **TiO_2** by UV irradiation. No methane conversion was observed after activation of plasmonic Au NPs by visible light. The plasmonic effect of gold NPs can contribute to enhancing charge separation and accelerating charge transfer in the catalyst. The photocatalytic performance of titania supported gold catalysts is not affected by the size of gold NPs in the range from 6 to 29 nm. The methane activation and oxidation occur under UV light over titania oxygen vacancies while the oxygen activation probably takes place over gold NPs.

4.4 References

[1] J. Ma, X. Tan, Q. Zhang, Y. Wang, J. Zhang, L. Wang, Exploring the size effect of Pt nanoparticles on the photocatalytic nonoxidative coupling of methane, ACS Catal. 11 (2021) 3352–3360. https://doi.org/10.1021/acscatal.0c04943.

[2] Q. Li, Y. Ouyang, H. Li, L. Wang, J. Zeng, Photocatalytic Conversion of Methane: Recent Advancements and Prospects, Angew. Chemie Int. Ed. 61 (2022). https://doi.org/10.1002/anie.202108069.

[3] J. Yang, W. Xiao, X. Chi, X. Lu, S. Hu, Z. Wu, W. Tang, Z. Ren, S. Wang, X. Yu, L. Zhang, A. Rusydi, J. Ding, Y. Guo, P.X. Gao, Solar-driven efficient methane catalytic oxidation over epitaxial ZnO/La0.8Sr0.2CoO3 heterojunctions, Appl. Catal. B Environ. 265 (2020) 118469. https://doi.org/10.1016/j.apcatb.2019.118469.

[4] H. Song, X. Meng, T.D. Dao, W. Zhou, H. Liu, L. Shi, H. Zhang, T. Nagao, T. Kako, J. Ye, Light-Enhanced Carbon Dioxide Activation and Conversion by Effective Plasmonic Coupling Effect of Pt and Au Nanoparticles, ACS Appl. Mater. Interfaces. 10 (2018) 408–416. https://doi.org/10.1021/acsami.7b13043.

[5] E.G. Nisbet, R.E. Fisher, D. Lowry, J.L. France, G. Allen, S. Bakkaloglu, T.J. Broderick, M. Cain, M. Coleman, J. Fernandez, G. Forster, P.T. Griffiths, C.P. Iverach, B.F.J. Kelly, M.R. Manning, P.B.R. Nisbet-Jones, J.A. Pyle, A. Townsend-Small, A. al-Shalaan, N. Warwick, G. Zazzeri, Methane Mitigation: Methods to Reduce Emissions, on the Path to the Paris Agreement, Rev. Geophys. 58 (2020) 1–51. https://doi.org/10.1029/2019RG000675.

[6] E.A.G. Schuur, A.D. McGuire, C. Schädel, G. Grosse, J.W. Harden, D.J. Hayes, G. Hugelius, C.D. Koven, P. Kuhry, D.M. Lawrence, S.M. Natali, D. Olefeldt, V.E. Romanovsky, K. Schaefer, M.R. Turetsky, C.C. Treat, J.E. Vonk, Climate change and the permafrost carbon feedback, Nature. 520 (2015) 171–179. https://doi.org/10.1038/nature14338.

[7] H. Song, X. Meng, Z. jun Wang, H. Liu, J. Ye, Solar-Energy-Mediated Methane Conversion, Joule. 3 (2019) 1606–1636. https://doi.org/10.1016/j.joule.2019.06.023.

[8] X. Meng, X. Cui, N.P. Rajan, L. Yu, D. Deng, X. Bao, Direct Methane Conversion under Mild Condition by Thermo-, Electro-, or Photocatalysis, Chem. 5 (2019) 2296–2325.

https://doi.org/10.1016/j.chempr.2019.05.008.

[9] L. Meng, Z. Chen, Z. Ma, S. He, Y. Hou, H.H. Li, R. Yuan, X.H. Huang, X. Wang, X. Wang, J. Long, Gold plasmon-induced photocatalytic dehydrogenative coupling of methane to ethane on polar oxide surfaces, Energy Environ. Sci. 11 (2018) 294–298. https://doi.org/10.1039/c7ee02951a.

[10] B.L. Farrell, V.O. Igenegbai, S. Linic, A Viewpoint on Direct Methane Conversion to Ethane and Ethylene Using Oxidative Coupling on Solid Catalysts, ACS Catal. 6 (2016) 4340–4346. https://doi.org/10.1021/acscatal.6b01087.

[11] P. Tang, Q. Zhu, Z. Wu, D. Ma, Methane activation: The past and future, Energy Environ. Sci. 7 (2014) 2580–2591. https://doi.org/10.1039/c4ee00604f.

[12] X. Yu, V. De Waele, A. Löfberg, V. Ordomsky, A.Y. Khodakov, Selective photocatalytic conversion of methane into carbon monoxide over zinc-heteropolyacid-titania nanocomposites, Nat. Commun. 10 (2019) 700. https://doi.org/10.1038/s41467-019-08525-2.

[13] L. Yuliati, H. Yoshida, Photocatalytic conversion of methane, Chem. Soc. Rev. 37 (2008) 1592. https://doi.org/10.1039/b710575b.

[14] G. Chen, G.I.N. Waterhouse, R. Shi, J. Zhao, Z. Li, L.Z. Wu, C.H. Tung, T. Zhang, From Solar Energy to Fuels: Recent Advances in Light-Driven C1 Chemistry, Angew. Chemie - Int. Ed. 58 (2019) 17528–17551. https://doi.org/10.1002/anie.201814313.

[15] X. Chen, Y. Li, X. Pan, D. Cortie, X. Huang, Z. Yi, Photocatalytic oxidation of methane over silver decorated zinc oxide nanocatalysts, Nat. Commun. 7 (2016) 1–8. https://doi.org/10.1038/ncomms12273.

[16] D. Hu, V. V Ordomsky, A.Y. Khodakov, Major routes in the photocatalytic methane conversion into chemicals and fuels under mild conditions, Appl. Catal. B Environ. 286 (2021). https://doi.org/10.1016/j.apcatb.2021.119913.

[17] X. Li, H.O. Everitt, J. Liu, A.A. Kumar, P. Choudhary, A.A. Kumar, P.H.C. Camargo, V. Krishnan, Synergy between thermal and nonthermal effects in plasmonic photocatalysis, Small. 13 (2020) 1268–1280. https://doi.org/10.1002/smll.202101638.

[18] X. Zhang, Y.L. Chen, R.S. Liu, D.P. Tsai, Plasmonic photocatalysis, Reports Prog. Phys. 76 (2013). https://doi.org/10.1088/0034-4885/76/4/046401.

[19] U. Aslam, V.G. Rao, S. Chavez, S. Linic, Catalytic conversion of solar to chemical energy on plasmonic metal nanostructures, Nat. Catal. 1 (2018) 656–665. https://doi.org/10.1038/s41929-018-0138-x.

[20] L. Mascaretti, A. Naldoni, Hot electron and thermal effects in plasmonic photocatalysis, J. Appl. Phys. 128 (2020). https://doi.org/10.1063/5.0013945.

[21] S. Wu, X. Tan, J. Lei, H. Chen, L. Wang, J. Zhang, Ga-Doped and Pt-Loaded Porous TiO 2 –SiO 2 for Photocatalytic Nonoxidative Coupling of Methane, J. Am. Chem. Soc. 141 (2019) 6592–6600. https://doi.org/10.1021/jacs.8b13858.

[22] Y. Ben-Shahar, F. Scotognella, I. Kriegel, L. Moretti, G. Cerullo, E. Rabani, U. Banin, Optimal metal domain size for photocatalysis with hybrid semiconductor-metal nanorods, Nat. Commun. 7 (2016) 1–7. https://doi.org/10.1038/ncomms10413.

[23] L. Yuliati, T. Hattori, H. Itoh, H. Yoshida, Photocatalytic nonoxidative coupling of methane on gallium oxide and silica-supported gallium oxide, J. Catal. 257 (2008) 396–402. https://doi.org/10.1016/j.jcat.2008.05.022.

[24] G.N. Kuzmin, M. V. Knatko, S. V. Kurganov, Light and X-ray-induced chemistry of methane on TiO2, React. Kinet. Catal. Lett. 23 (1983) 313–317. https://doi.org/10.1007/BF02065581.

[25] L. Yuliati, T. Hattori, H. Yoshida, Highly dispersed magnesium oxide species on silica as photoactive sites for photoinduced direct methane coupling and photoluminescence, Phys. Chem. Chem. Phys. 7 (2005) 195–201. https://doi.org/10.1039/b410089a.

[26] L. Meng, Z. Chen, Z. Ma, S. He, Y. Hou, H.H. Li, R. Yuan, X.H. Huang, X.X. Wang, X.X. Wang, J. Long, Gold plasmon-induced photocatalytic dehydrogenative coupling of methane to ethane on polar oxide surfaces, Energy Environ. Sci. 11 (2018) 294–298. https://doi.org/10.1039/c7ee02951a.

[27] J. Lang, Y. Ma, X. Wu, Y. Jiang, Y.H. Hu, Highly efficient light-driven methane coupling under ambient conditions based on an integrated design of a photocatalytic system, Green Chem. 22 (2020) 4669–4675. https://doi.org/10.1039/d0gc01608j.

[28] W. Jiang, J. Low, K. Mao, D. Duan, S. Chen, W. Liu, C. Pao, J. Ma, S. Sang, C. Shu, X. Zhan, Z. Qi, H. Zhang, Z. Liu, X. Wu, R. Long, L. Song, Y. Xiong, Pd-Modified ZnO–Au Enabling Alkoxy Intermediates Formation and Dehydrogenation for Photocatalytic

Conversion of Methane to Ethylene, J. Am. Chem. Soc. 143 (2021) 269–278. https://doi.org/10.1021/jacs.0c10369.

[29] X. Yu, V.L. Zholobenko, S. Moldovan, D. Hu, D. Wu, V. V Ordomsky, A.Y. Khodakov, Stoichiometric methane conversion to ethane using photochemical looping at ambient temperature, Nat. Energy. 5 (2020) 511–519. https://doi.org/10.1038/s41560-020-0616-7.

[30] X. Li, J. Xie, H. Rao, C. Wang, J. Tang, Platinum- and CuOx-Decorated TiO2 Photocatalyst for Oxidative Coupling of Methane to C2 Hydrocarbons in a Flow Reactor, Angew. Chemie - Int. Ed. 59 (2020) 19702–19707. https://doi.org/10.1002/anie.202007557.

[31] S. Song, H. Song, L. Li, S. Wang, W. Chu, K. Peng, X. Meng, Q. Wang, B. Deng, Q. Liu, Z. Wang, Y. Weng, H. Hu, H. Lin, T. Kako, J. Ye, A selective Au-ZnO/TiO2 hybrid photocatalyst for oxidative coupling of methane to ethane with dioxygen, Nat. Catal. (2021). https://doi.org/10.1038/s41929-021-00708-9.

[32] H. Song, X. Meng, T.D. Dao, W. Zhou, H. Liu, L. Shi, H. Zhang, T. Nagao, T. Kako, J. Ye, Light-Enhanced Carbon Dioxide Activation and Conversion by Effective Plasmonic Coupling Effect of Pt and Au Nanoparticles, ACS Appl. Mater. Interfaces. 10 (2018) 408–416. https://doi.org/10.1021/acsami.7b13043.

[33] M. Behl, P.K. Jain, Catalytic activation of a solid oxide in electronic contact with gold nanoparticles, Angew. Chemie - Int. Ed. 54 (2015) 992–997. https://doi.org/10.1002/anie.201409111.

[34] E.A. Coronado, E.R. Encina, F.D. Stefani, Optical properties of metallic nanoparticles: Manipulating light, heat and forces at the nanoscale, Nanoscale. 3 (2011) 4042–4059. https://doi.org/10.1039/c1nr10788g.

[35] T.J. Miao, C. Wang, L. Xiong, X. Li, J. Xie, J. Tang, In Situ Investigation of Charge Performance in Anatase TiO2Powder for Methane Conversion by Vis-NIR Spectroscopy, ACS Catal. 11 (2021) 8226–8238. https://doi.org/10.1021/acscatal.1c01998.

[36] L. Xiong, J. Tang, Strategies and Challenges on Selectivity of Photocatalytic Oxidation of Organic Substances, Adv. Energy Mater. 11 (2021). https://doi.org/10.1002/aenm.202003216.

[37] G. Wang, X. Mu, J. Li, Q. Zhan, Y. Qian, X. Mu, L. Li, Light-Induced Nonoxidative Coupling of Methane Using Stable Solid Solutions, Angew. Chemie. 133 (2021) 20928–20932. https://doi.org/10.1002/ange.202108870.

[38] M.R. Hoffmann, S.T. Martin, W. Choi, D.W. Bahnemann, Environmental Applications of Semiconductor Photocatalysis, Chem. Rev. 95 (1995) 69–96. https://doi.org/10.1021/cr00033a004.

[39] M. Iwamoto, K. Maruyama, N. Yamazoe, T. Selyama, Study of metal oxide catalysts by temperature programmed desorption. 2. Chemisorption of oxygen on copper(II) ion-exchanged Y-type zeolites, J. Phys. Chem. 81 (1977) 622–629. https://doi.org/10.1021/j100522a007.

[40] E. Carter, A.F. Carley, D.M. Murphy, Evidence for O2- radical stabilization at surface oxygen vacancies on polycrystalline TiO2, J. Phys. Chem. C. 111 (2007) 10630–10638. https://doi.org/10.1021/jp0729516.

[41] F. Boccuzzi, A. Chiorino, M. Manzoli, FTIR study of the electronic effects of CO adsorbed on gold nanoparticles supported on titania, Surf. Sci. 454 (2000) 942–946. https://doi.org/10.1016/S0039-6028(00)00160-6.

[42] M.A. Centeno, K. Hadjiivanov, T. Venkov, H. Klimev, J.A. Odriozola, Comparative study of Au/Al2O3 and Au/CeO2-Al2O3 catalysts, J. Mol. Catal. A Chem. 252 (2006) 142–149. https://doi.org/10.1016/j.molcata.2006.02.056.

[43] T. Kecskés, J. Raskó, J. Kiss, FTIR and mass spectrometric studies on the interaction of formaldehyde with TiO2 supported Pt and Au catalysts, Appl. Catal. A Gen. 273 (2004) 55–62. https://doi.org/10.1016/j.apcata.2004.06.012.

[44] J. Raskó, T. Kecskés, J. Kiss, Formaldehyde formation in the interaction of HCOOH with Pt supported on TiO2, J. Catal. 224 (2004) 261–268. https://doi.org/10.1016/j.jcat.2004.03.025.

[45] D.A. Panayotov, J.T. Yates, Depletion of conduction band electrons in TiO2 by water chemisorption - IR spectroscopic studies of the independence of Ti-OH frequencies on electron concentration, Chem. Phys. Lett. 410 (2005) 11–17. https://doi.org/10.1016/j.cplett.2005.03.146.

[46] T. Chen, Z. Feng, G. Wu, J. Shi, G. Ma, P. Ying, C. Li, Mechanistic studies of

photocatalytic reaction of methanol for hydrogen production on Pt/TiO2 by in situ fourier transform IR and time-resolved IR spectroscopy, J. Phys. Chem. C. 111 (2007) 8005–8014. https://doi.org/10.1021/jp071022b.

[47] E.A. Taylor, G.L. Griffin, Product Selectivity during CH3OH Decomposition on Ti02 Powders, J. Phys. Chem. 92 (1988) 477–481.

[48] L. Mino, G. Spoto, A.M. Ferrari, CO2 capture by TiO2 anatase surfaces: A combined DFT and FTIR study, J. Phys. Chem. C. 118 (2014) 25016–25026. https://doi.org/10.1021/jp507443k.

Chapter 5. Beyond the selectivity limit in the photocatalytic oxidation of methane to formic acid at room temperature: Contribution of chemocatalysis

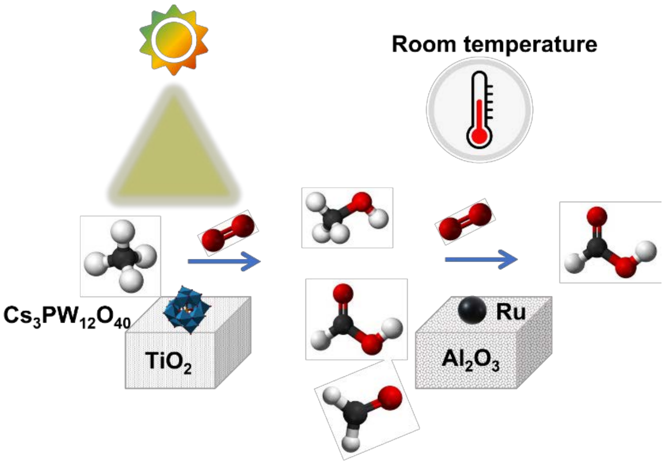

Abstract

Direct oxidation of methane into value-added fuels and chemicals remains a major challenge in modern science. Formic acid is one of the most promising platform-molecules for hydrogen storage, low-temperature membrane fuel cells and different branches of the chemical industry. Photocatalysis proposes an attractive route for methane partial oxidation to value added chemicals under mild conditions. The radical mechanism of methane photocatalytic oxidation often limits the selectivity to the target products. In this paper, we propose a strategy to break the conventional limitations of methane photocatalytic oxidation by adding a chemocatalyst and conducting the whole process in a one-pot reactor. A selectivity of methane oxidation to formic acid of 85 % and a productivity of 5 $\text{mmol}_{\text{formic acid}}\ \text{g}^{-1}_{\text{photocatalyst}}$ were achieved. The formic acid with a concentration of up to 1.1 mM is produced.

In this strategy, the methane selective conversion into formic acid proceeds first over caesium salt of phosphotungstic acid supported on titania, which photocatalytically via radical mechanism oxidizes methane under irradiation into a mixture of C_1 liquid oxygenates (formaldehyde, methyl hydroperoxide, methanol). These oxygenates are then selectively converted into formic acid over the heterogeneous alumina supported ruthenium catalyst. All reactions of selective oxidation of methane to formic acid occur at room temperature in the same reactor.

5.1 Introduction

Methane, the main component of natural and shale gas, gas hydrate and biogas, is a promising feedstock for the chemical industry but at the same time, an extremely inert molecule [1–6]. The chemical stability of methane is closely related to the high C-H bond energy (439 kJ mol^{-1}) and its symmetric tetrahedral molecular geometry, which leads to low polarizability, weak acidity and low affinity for electrons and protons[7–9]. As a result, most methane is currently burned for energy production and accounts for 20-25% of global carbon dioxide emissions into the atmosphere.[10] Moreover, methane "flaring" (methane burning at the oil production sites) consumes around 3.5 % of the global amount of produced natural gas. Methane is itself a greenhouse gas (GHG) with an impact on the climate 30 times[11,12] higher than carbon dioxide.

Currently available industrial technologies of methane utilization involve indirect and direct highly energy-intensive thermochemical processes. The indirect two-step processes occur through the intermediate production of syngas (mixture of hydrogen and carbon monoxide)[5,13,14] by steam reforming (Eq. 1) or partial oxidation (Eq. 2) at a temperature higher than 800°C:

$$CH_4 + H_2O\ (g) \rightarrow CO + 3H_2,\ \Delta H^0_{298K} = 205.9\ kJ\cdot mol^{-1} \quad (1)$$

$$CH_4 + 1/2\ O_2 \rightarrow CO + 2H_2,\ \Delta H\ ^0_{298K} = -36\ kJ\ mol^{-1} \quad (2)$$

The only available industrial technologies for direct thermochemical methane utilization are the Andrussow process and the non-oxidative BMA (or Degussa) process, in which methane reacts with ammonia at extremely high temperatures (>1600°C) and produces hydrogen cyanide[15].

Photocatalysis is a promising strategy for converting solar light into chemical energy and it may enable the activation of C-H bonds in methane under mild conditions[16–19]. Recently, photocatalysis has demonstrated great potential for selective methane conversion to fuels and chemicals at room temperature[13,20–22]. The major routes of methane photocatalytic conversion involve methane selective oxidation to methanol, methane photocatalytic dry or steam reforming to hydrogen and carbon monoxide, and methane coupling leading to the formation of ethane and higher hydrocarbons.

Several photocatalytic systems and oxidants have been explored for methane oxidation to oxygenates. Photocatalytic aerobic oxidation of methane to methanol over Au/ZnO[23,24] and Au-CoO_x/TiO_2[25] has been recently reported. The boosted performance of these catalysts was attributed to mild oxidative hydroperoxyl radicals (•OOH) produced over co-catalysts. Highly selective oxidation of methane to methanol has been observed over FeO_x/TiO_2[26] in the presence of H_2O_2 at ambient conditions, resulting from lower overpotential of H_2O_2 reduction to hydroxyl radicals (•OH) over iron species. Toxic and unstable chlorine dioxide radical was also used[27] for the non-catalytic synthesis of formic acid from methane. Besides, photocatalytic aerobic oxidation of methane to formaldehyde and formic acid was reported over Au_x/c-WO_3[28] and HSiMo/TiO_2[29]. The process, however, required either high pressure or elevated temperature. Multiple liquid oxygenates (methyl hydroperoxide, methanol, formaldehyde, formic acid, etc.) are usually simultaneously produced and can be hardly separated. Most of the current photocatalytic methane oxidation routes suffer, therefore, from low productivity and insufficient selectivity or require highly reactive, unstable and toxic oxidants (H_2O_2, ClO_2 etc).

Formic acid is one of the most promising feedstocks [30,31] for hydrogen storage, fuel cells, grass silage, leather tanning, textile dyeing, finishing, food additives, natural rubber, drilling fluids and various chemical processes. Currently, industrial production of formic acid proceeds via a multistep process such as the carbonylation of methanol with subsequent hydrolysis of methyl formate [28,30]. Direct selective transformation of methane to formic acid occurring at room temperature using renewable energy sources such as solar light and without any toxic oxidants could be, therefore, extremely attractive and valuable.

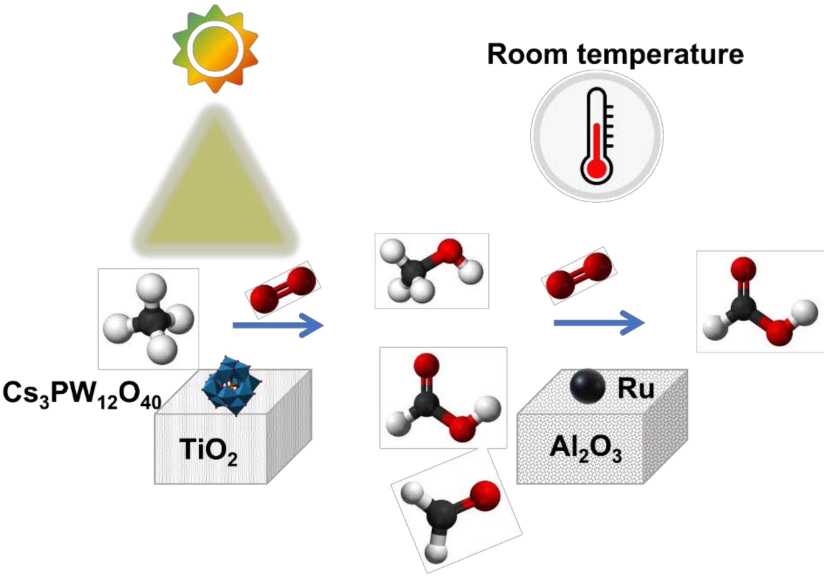

Fig. 1. Cascade photo-chemocatalytic process for selective synthesis of formic acid from methane

Hereby, we propose a strategy for synthesizing formic acid from methane with a selectivity that exceeds the usual limitations of photocatalysis. The process takes place in water at ambient temperature and employs air as an oxidant (**Figure 1**). The process involves two catalytic systems. Methane photocatalytic oxidation over cesium salt of phosphotungstic acid (HPW) supported on titania is used for the synthesis of a mixture of C_1 oxygenates (methyl hydroperoxide, methanol, formaldehyde and formic acid). Insoluble caesium salt was used for heterogenization of soluble heteropolyacid. A heterogeneous ruthenium catalyst supported by aluminium enables chemocatalytic oxidation of C_1 oxygenates to formic acid. Highly selective methane oxidation to formic acid is achieved under ambient temperature. The formic acid productivity has reached 5 $mmol_{formic\ acid}\ g^{-1}_{photocatalyst}$ with a selectivity of 85%. A concentrated formic acid solution of 1.1 mmol/L is produced in this process.

5.2 Result and discussion

5.2.1 Photocatalytic methane oxidation with O_2 in water to a mixture of C_1 oxygenates

First, the photocatalytic methane oxidation was investigated at ambient temperature in the presence of the following catalysts: HPW, caesium salt of HPW (CsPW) and TiO_2 (**Fig. 2**). No methane conversion is observed in the reactor with any of these catalysts in the absence of light, indicating that methane oxidation is driven by photocatalysis. Under irradiation, without a catalyst, only a small amount of formaldehyde has been detected. Some minor formaldehyde formation from CH_4 under UV irradiation has been previously reported in the literature[32,33]. Also, very low methane conversion was observed over the catalysts in the presence of light but without oxygen. The methane oxidation without a catalyst or in the absence of oxygen can be due to the hydroxyl radicals generated[32,33] by UV light in water.

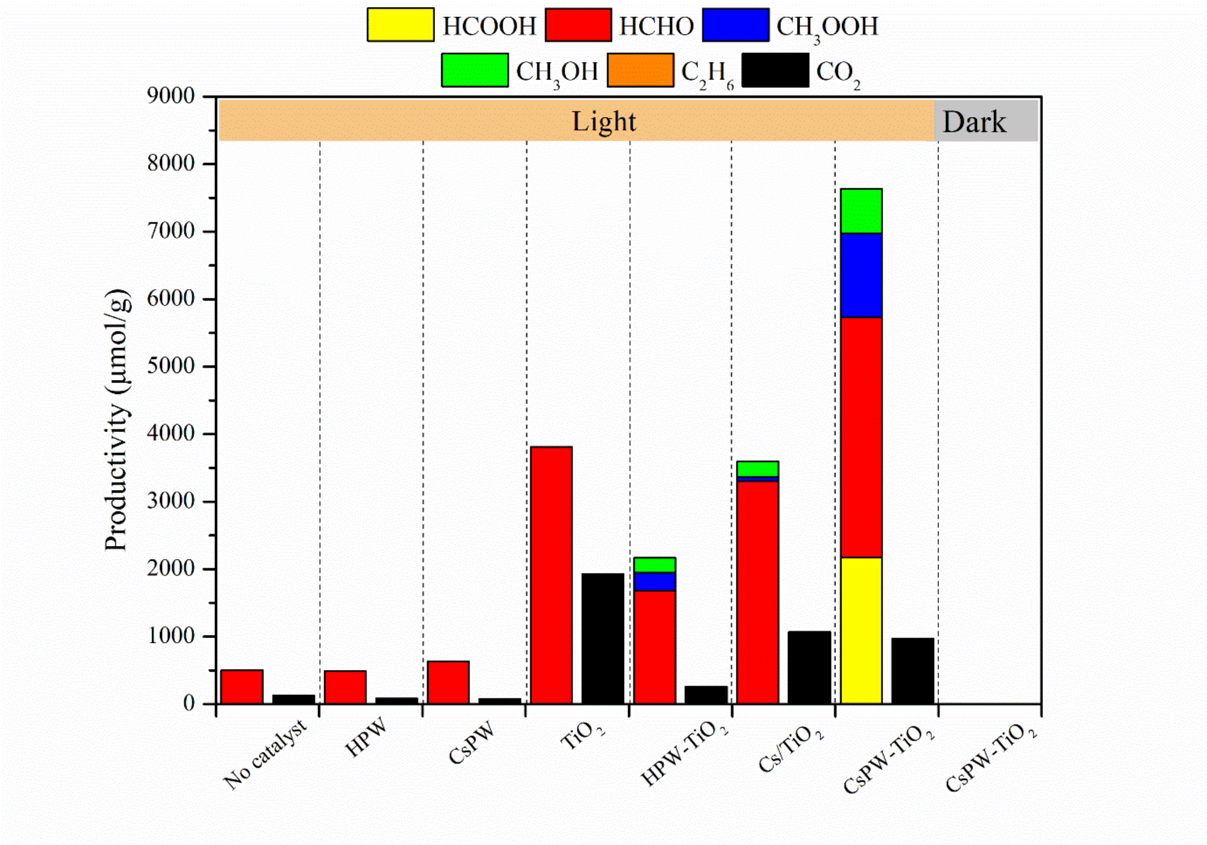

Fig. 2. Methane photocatalytic oxidation with O_2 in water over various composites.

Exposure of the reactor with HPW and CsPW to methane and oxygen under irradiation also results in some formaldehyde generation (**Fig. 2**). The amount of formaldehyde produced over HPW and CsPW was, however, also very small, similar to that detected in the reactor under irradiation, without any catalyst. This suggests that HPW or CsPW are not active in methane photocatalytic oxidation. Much higher amounts of formaldehyde and CO_2 were produced from methane under irradiation in the reactor filled with TiO_2. Note that methane oxidation over TiO_2 is accompanied by a major production of CO_2. The observed photocatalytic activity of TiO_2 in methane oxidation to formaldehyde and CO_2 is consistent with previous works[23].

Very different selectivity patterns were observed in the methane photocatalytic conversion over the CsPW-TiO_2 catalyst. A mixture of C_1 oxygenates with much high productivity was detected on CsPW-TiO_2; formic acid being one of the main oxidation products (**Fig. 2**). Important, the selectivity to undesirable CO_2 was significantly reduced over CsPW-TiO_2 compared to titania.

Note that no formic acid was detected in the methane photocatalytic oxidation over HPW-TiO_2 and Cs/TiO_2 (**Fig. 2**). The selectivity patterns over HPW-TiO_2 are rather similar to that over TiO_2. It is well known that HPW is readily soluble in polar solvents[34]. The observed inferior catalytic performance of HPW-TiO_2 with the selectivities similar to that of TiO_2, is possibly due to leaching HPW from the surface of TiO_2 in HPW-TiO_2 catalysts. Consequently, methane oxidation mainly occurs over TiO_2 surface (**Fig. 3**). Methane oxidation to CO_2 and formaldehyde also occurs on TiO_2 surface sites in Cs/TiO_2.

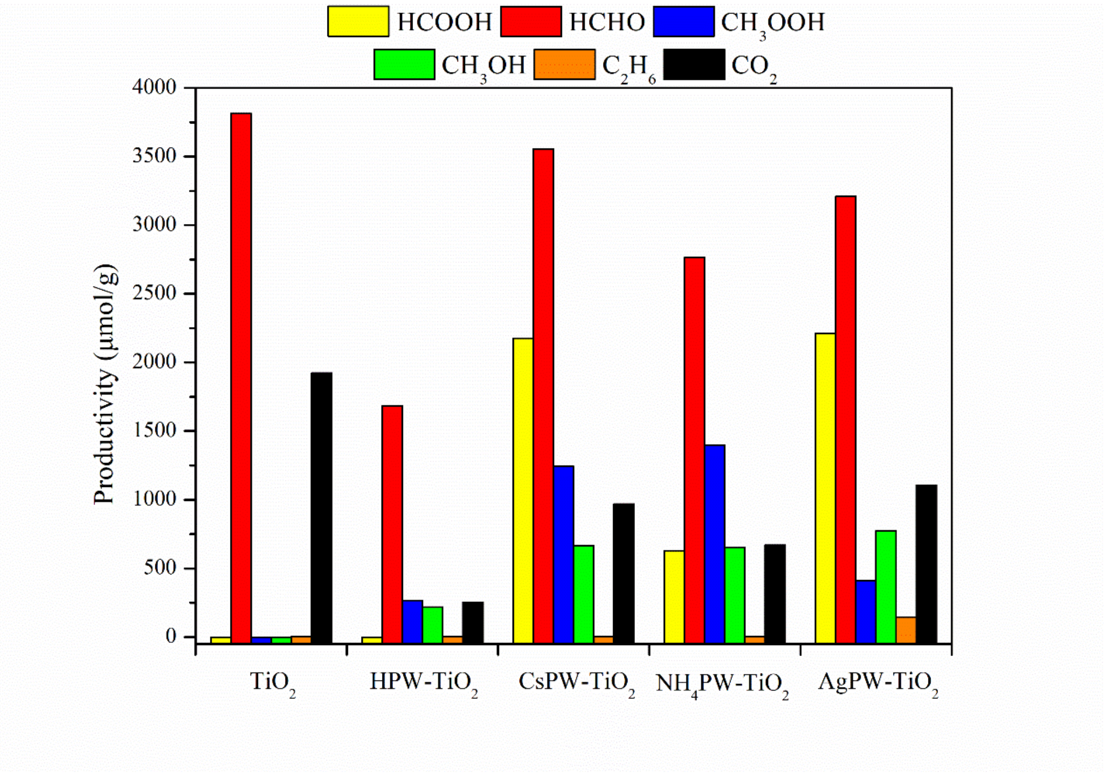

Figure 3. Methane photocatalytic oxidation with O_2 in water over catalysts containing different HPW salts.

Much higher oxygenate yields compared to HPW-TiO_2, accompanied by major production of formic acid are observed on all the insoluble HPW salts (CsPW, AgPW, NH_4PW) mixed with TiO_2 (**Fig. 3**). Note that over the AgPW-TiO_2 and NH_4PW-TiO_2 samples, the formic acid productivity was somewhat lower compared to CsPW-TiO_2. The Ag^+ cations in AgPW may undergo reduction to metallic silver in the presence of methane, while NH_4^+ cations can decompose under irradiation. Both processes may lead to the formation of soluble HPW, its leaching from TiO_2[35,36] and loss of catalytic activity. The formation of the silver metallic phase was uncovered by XRD in the spent AgPW-TiO_2 catalyst (**Fig. 4**).

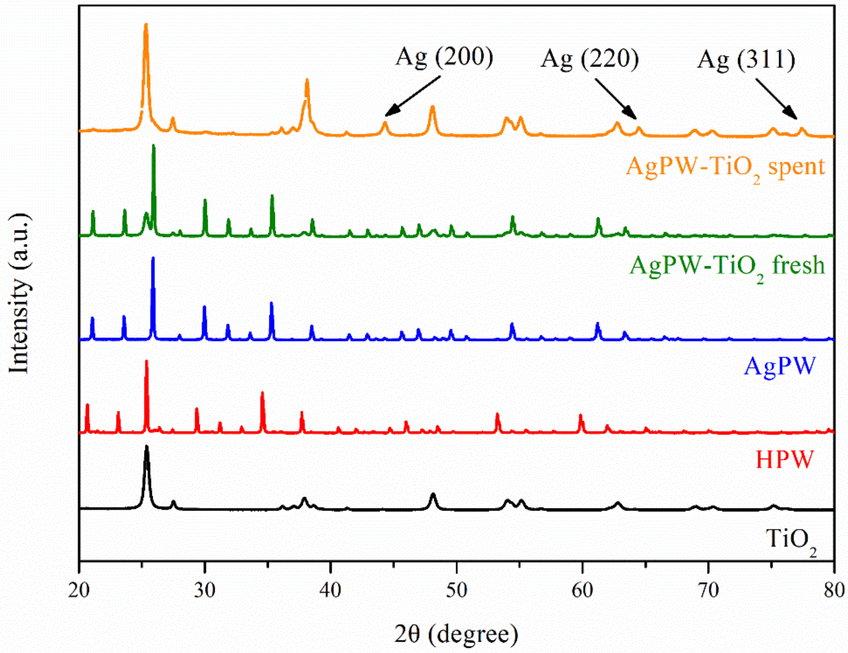

Figure 4. X-ray diffraction patterns of catalysts

Insoluble and stable CsPW demonstrates superior stability in the aqueous solution under irradiation. The X-ray diffraction shows that the spent CsPW-TiO_2 catalyst is intact compared with the fresh one (see **Fig. 24)**. Stable catalytic performance is observed over CsPW-TiO_2 in 4 cycle tests (**Fig. 5)**. These results indicate the indispensable role of Cs^+ ions in stabilizing HPW on the surface of TiO_2 during efficient photocatalytic methane oxidation.

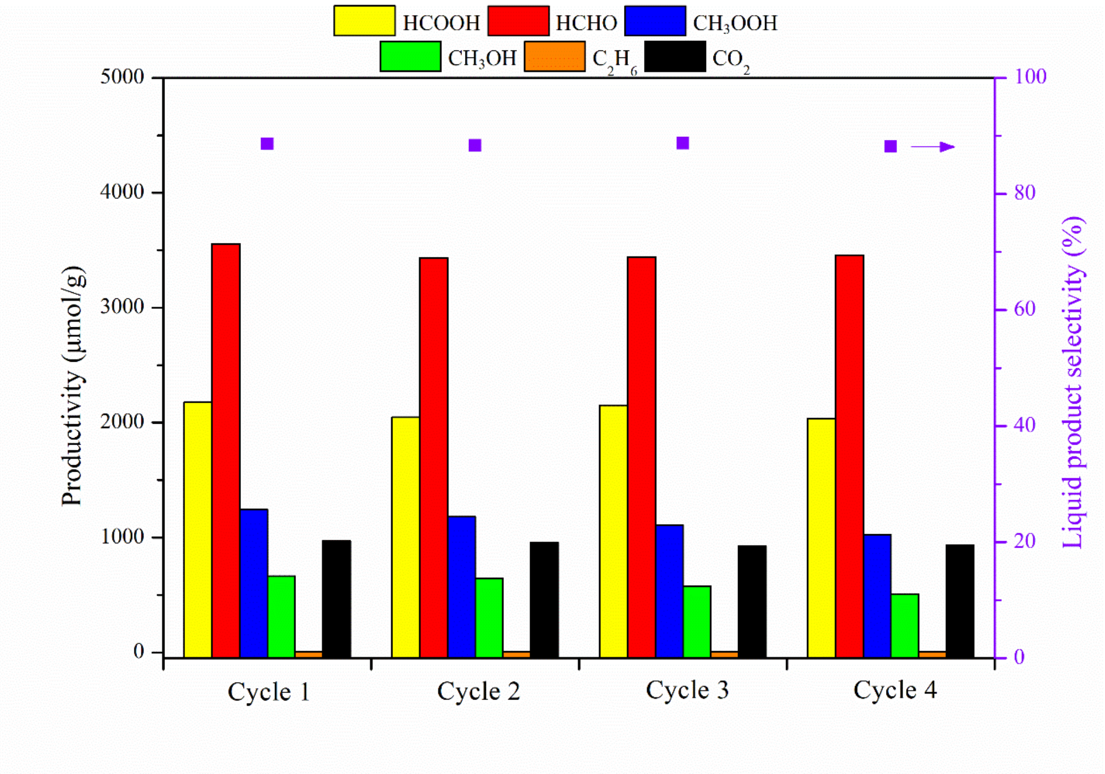

Figure 5. Cycling tests of methane photocatalytic oxidation with O_2 in water over CsPW-TiO_2.

Several types of heteropolyacids such as phosphotungstic acid (HPW), phosphomolybdic acid (HPMo), silicomolybdic acid (HSiMo) and silicotungstic acid (HSiW), were used in the preparation of caesium-heteropolyacid titania nanocomposites (**Fig. 6**). The overall methane conversion is much lower over the catalysts prepared by mixing caesium salts of phosphomolybdic and silicomolybdic acids with TiO_2 compared to CsPW-TiO_2.

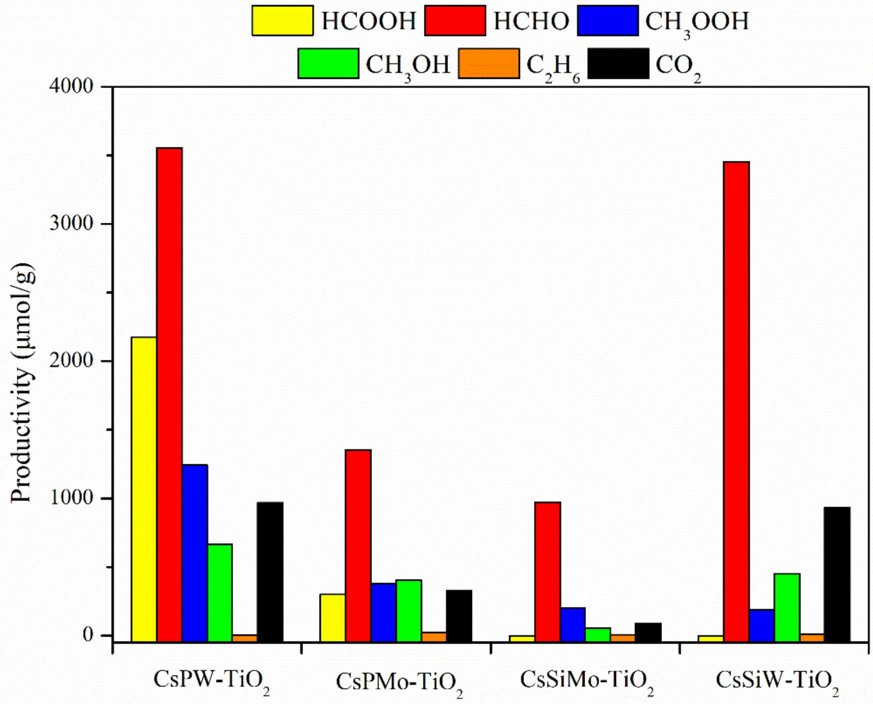

Figure 6. Methane photocatalytic oxidation with O_2 in water over catalysts containing Cs salts of different heteropolyacid.

The formic acid productivity as a function of CsPW content in the CsPW-TiO_2 catalysts displays a volcano-type curve (**Fig. 7**). Lower formic acid productivity at low content of CsPW can be due to the contribution of TiO_2 to methane oxidation to formaldehyde and CO_2, while insufficient light harvesting can explain low formic acid production at higher amount of CsPW in CsPW-TiO_2.

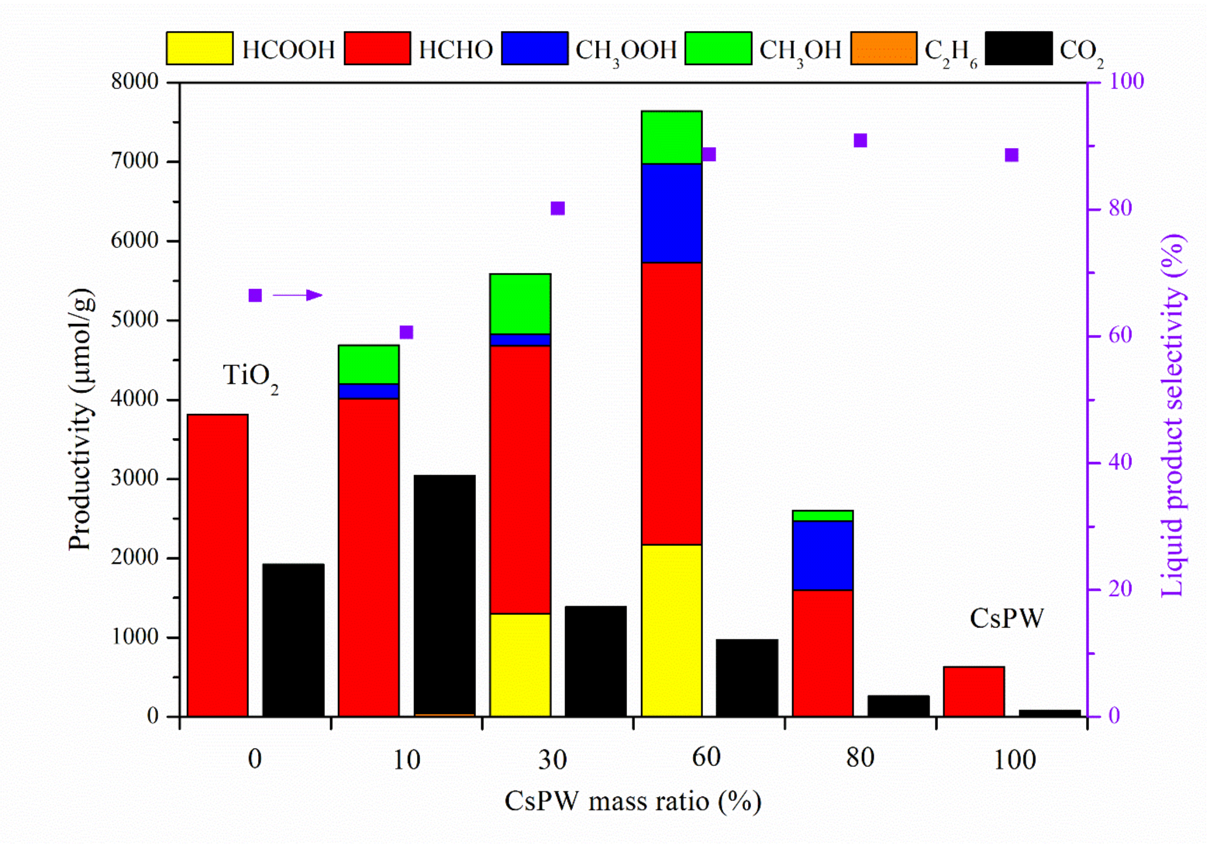

Fig. 7. Methane photocatalytic oxidation with O_2 in water over CsPW-TiO_2 with different CsPW mass ratio.

Very low methane conversion was observed under anaerobic conditions with the formaldehyde being the major product. The oxygenate yield over CsPW-TiO_2 is boosted in the air (**Fig. 8**).

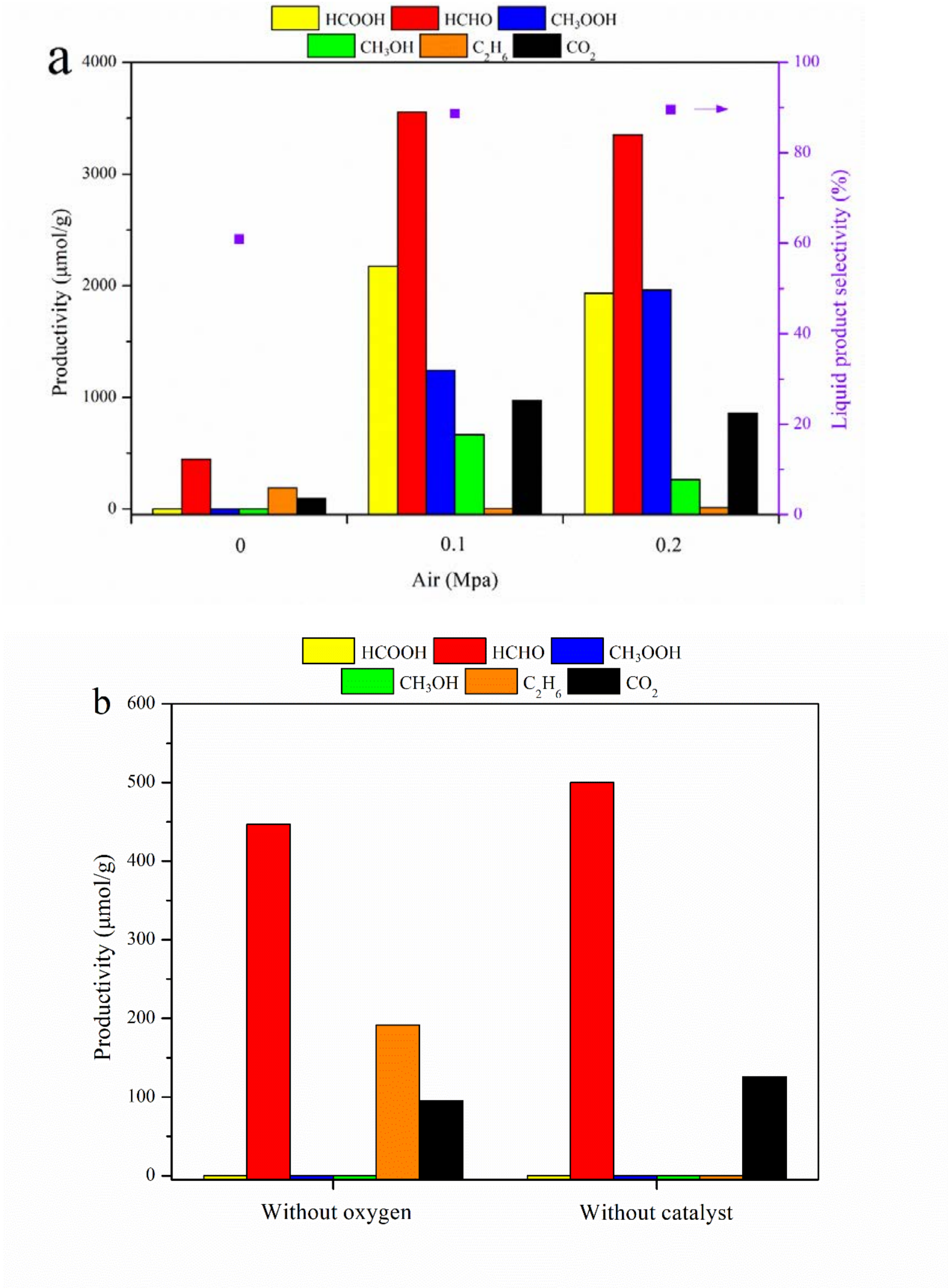

Figure 8. (a) Methane photocatalytic oxidation in water over CsPW-TiO_2 with different O_2 pressure and (b) Methane photocatalytic oxidation in the absence of oxygen and CsPW-TiO_2.

At higher methane relative content, lower formic acid productivity was observed, which can be due to the deficiency of oxygen in the reactor required for methane oxidation (**Fig. 9**).

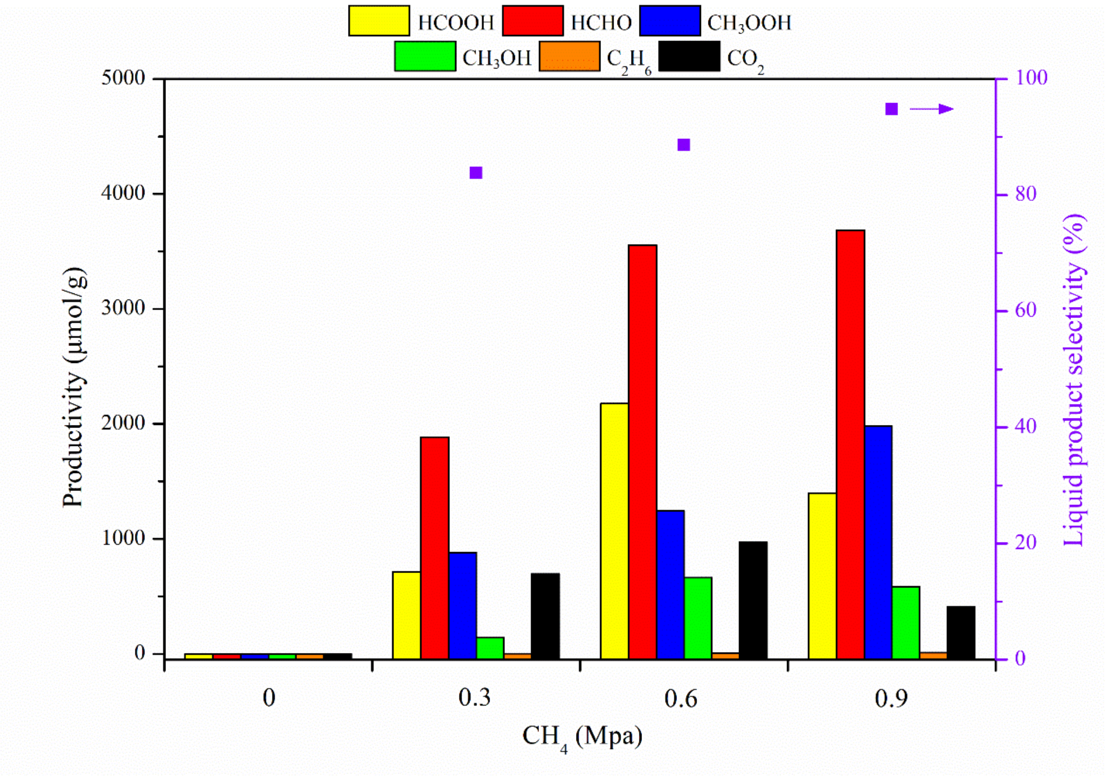

Figure 9. Methane photocatalytic oxidation in water over CsPW-TiO_2 with different CH_4 pressure.

The methane photocatalytic oxidation over CsPW-TiO_2 is studied as a function of reaction time (**Fig. 10**). As expected, methane conversion increases with irradiation time. At a shorter reaction time, the methane conversion mostly leads to formaldehyde and methyl hydroperoxide. Formic acid has been only observed at a longer reaction time. This suggests that formic acid is principally produced by re-oxidation of formaldehyde and possibly methyl hydroperoxide. The selectivity to CO_2 also increases with reaction time most probably due to re-oxidation of C_1 oxygenates.

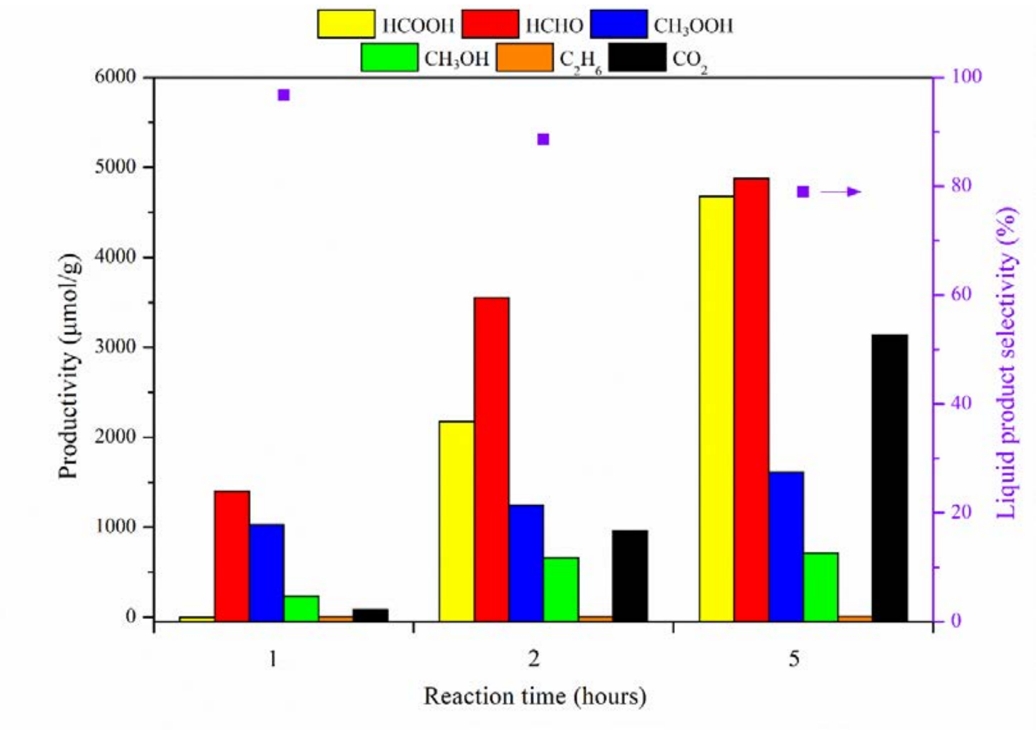

Figure 10. Time course of productivity and liquid product selectivity of methane photocatalytic oxidation with O_2 in water over CsPW-TiO$_2$.

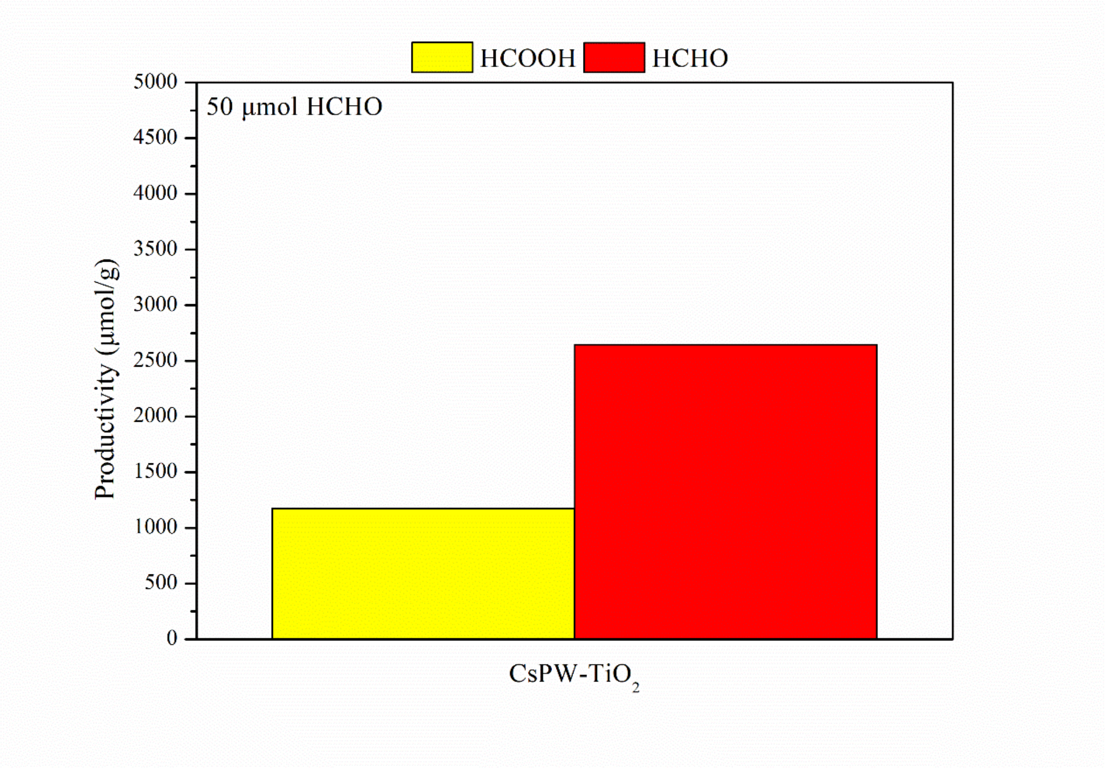

Figure 11. Photocatalytic oxidation in HCHO solution over CsPW-TiO$_2$.

To prove possible re-oxidation of HCHO to HCOOH and CO_2 under light irradiation, CsPW-TiO_2 was dispersed in HCHO solution (500 μmol/L) (**Fig. 11**). The HCOOH yield of 11.76 μmol was achieved from the direct HCHO oxidation in 2 h. The suggestion about re-oxidation of C_1 oxygenates generated by methane photocatalytic oxidation is also confirmed by the experiments with larger amounts of water added to the reactor. The selectivity to formic acid increases with the increase in water amount in the reactor, because of lower probability of its re-oxidation to CO_2 in the diluted solution (**Fig. 12**).

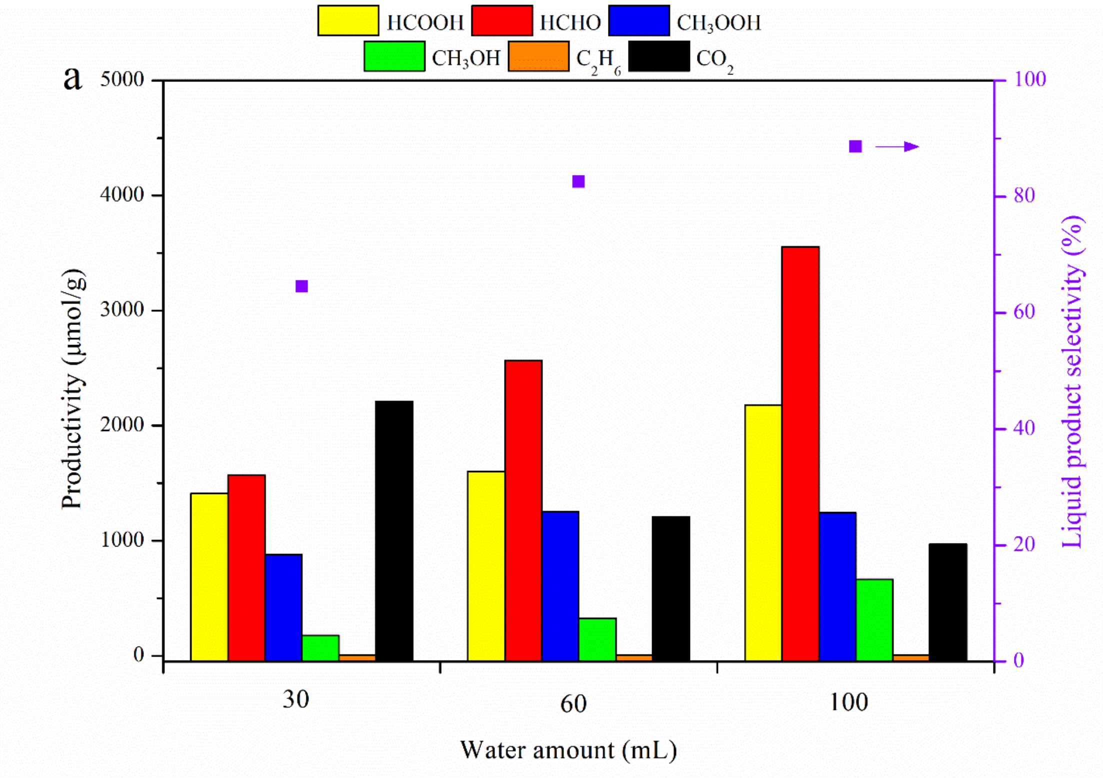

Figure 12. Methane photocatalytic oxidation with O_2 in water over CsPW-TiO_2 with different water amount.

The enhanced CsPW-TiO_2 photocatalytic performance in the methane oxidation to C_1 oxygenates and formic acid can be attributed to the formation of a p-n semiconductor heterojunction between TiO_2 and CsPW reported in previous works[16,35,37,38]. This heterojunction may facilitate the separation of e^-/h^+ and slows down charge carrier recombination, making electrons and holes available for photocatalytic processes. On the photo-excited CsPW-TiO_2, the electrons are transferred to the conduction band of the p-type semiconductor (CsPW) and the holes to the valence band of the n-type semiconductor (TiO_2) via the heterojunction, which increases the electron concentration in CsPW and hole concentration in TiO_2 (**Fig. 13**).

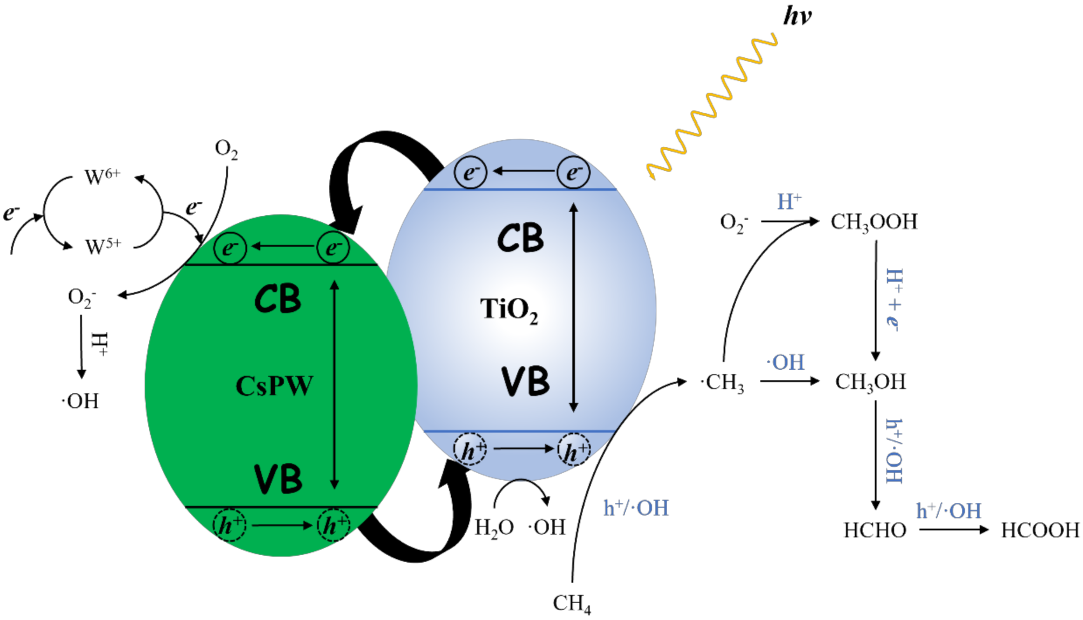

Figure 13. Sketch of the proposed reaction mechanism for photocatalytic methane oxidation to CH_3OOH, CH_3OH, HCHO and HCOOH over CsPW-TiO_2. CB, conduction band, VB, valence band.

Methane oxidation is then improved by the higher concentration of holes on the surface of TiO_2, while O_2 reduction into different reactive oxygen species is enhanced by the higher electron density over CsPW. The HPW acid stabilized by Cs^+ ions also play a role of cocatalyst for methane conversion to C_1 oxygenates with low CO_2 selectivity and the reaction can involve the formation of tungsten lower oxidation states.

Interestingly, after the exposure to methane without air in the presence of light, the CsPW-TiO_2

sample becomes blue, indicating a partial reduction of W species. The catalyst gets white again after exposure to air (**Fig. 14**). The colour remains unchanged during the methane photocatalytic oxidation in the presence of air.

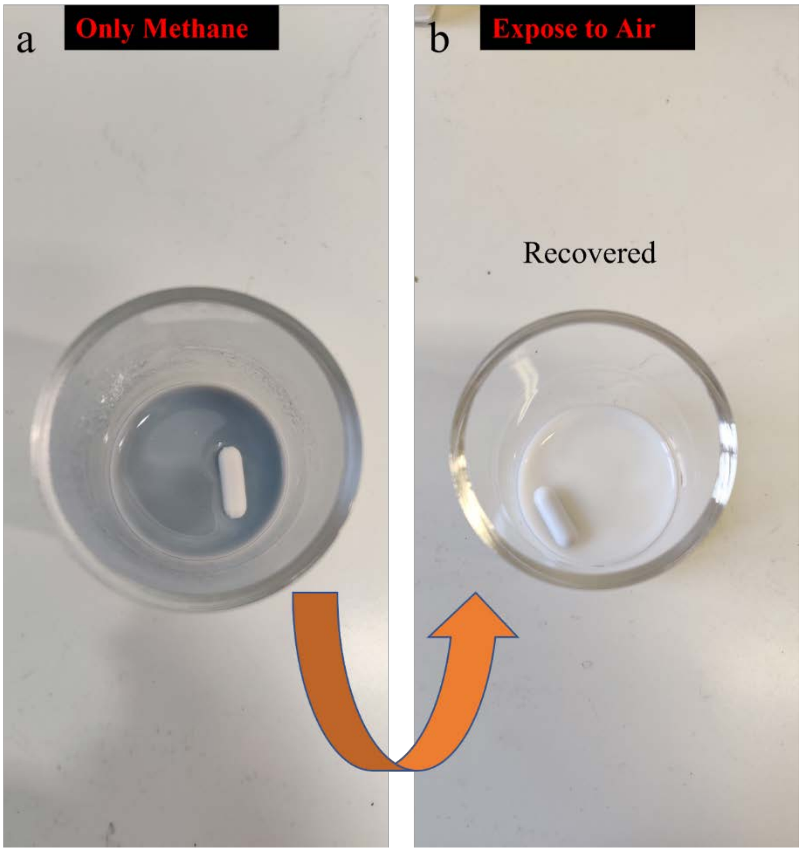

Figure 14. Reaction solution after irradiation in pure methane (a) and then exposed to air (b)

Methane oxidation experiments were carried out under both visible and UV light (**Figure 15**). No methane conversion was observed under visible light and the methane oxidation at 360 nm UV light only produced small amounts of HCHO, CH_3OOH and CH_3OH mixture, indicating that UV light was necessary to photoexcite CsPW-TiO_2 for methane activation. The AQY (apparent quantum yield) was 4.5% at 360 nm for CsPW-TiO_2.

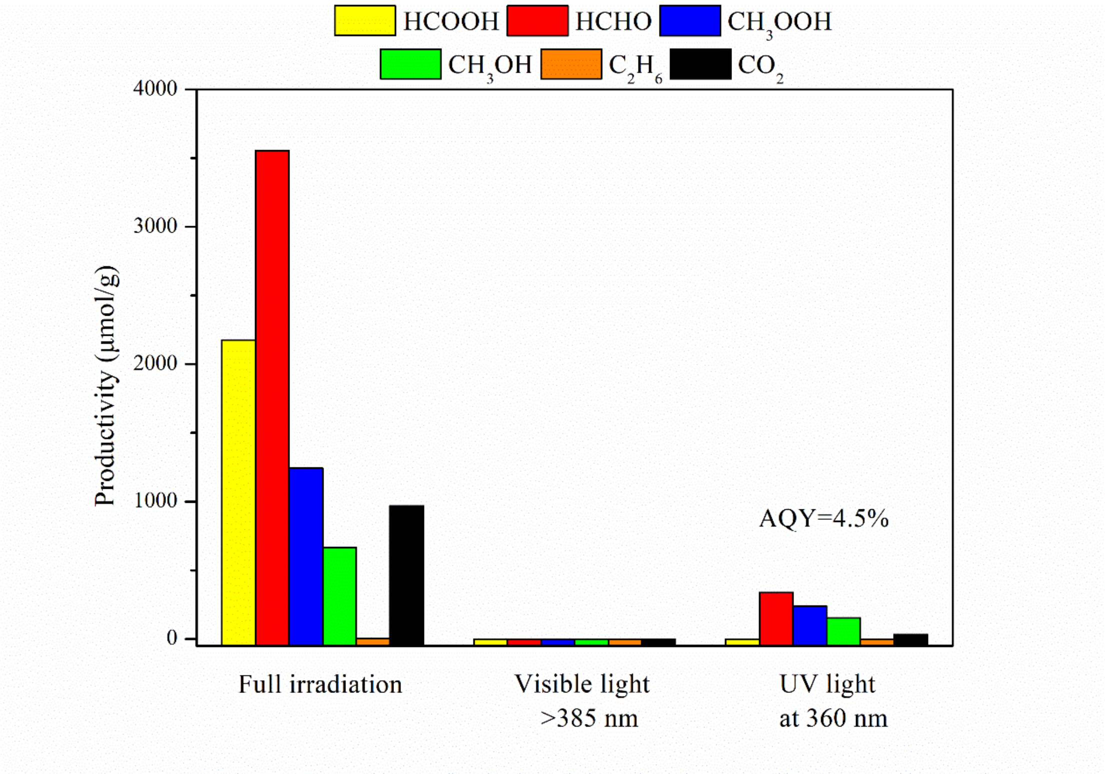

Figure 15. Photocatalytic methane oxidation over CsPW-TiO_2 under different light irradiation

The reactive oxygen species scavenging experiments were conducted during photocatalytic methane oxidation using salicylic acid and sodium sulphite (Na_2SO_3) as ·OH radicals and holes (h^+) sacrificial agents, respectively. The addition of both salicylic acid and sodium sulphite significantly suppressed methane conversion (**Figure 16**), suggesting that both the •OH radicals and holes (h^+) are the main reactive species for methane conversion.

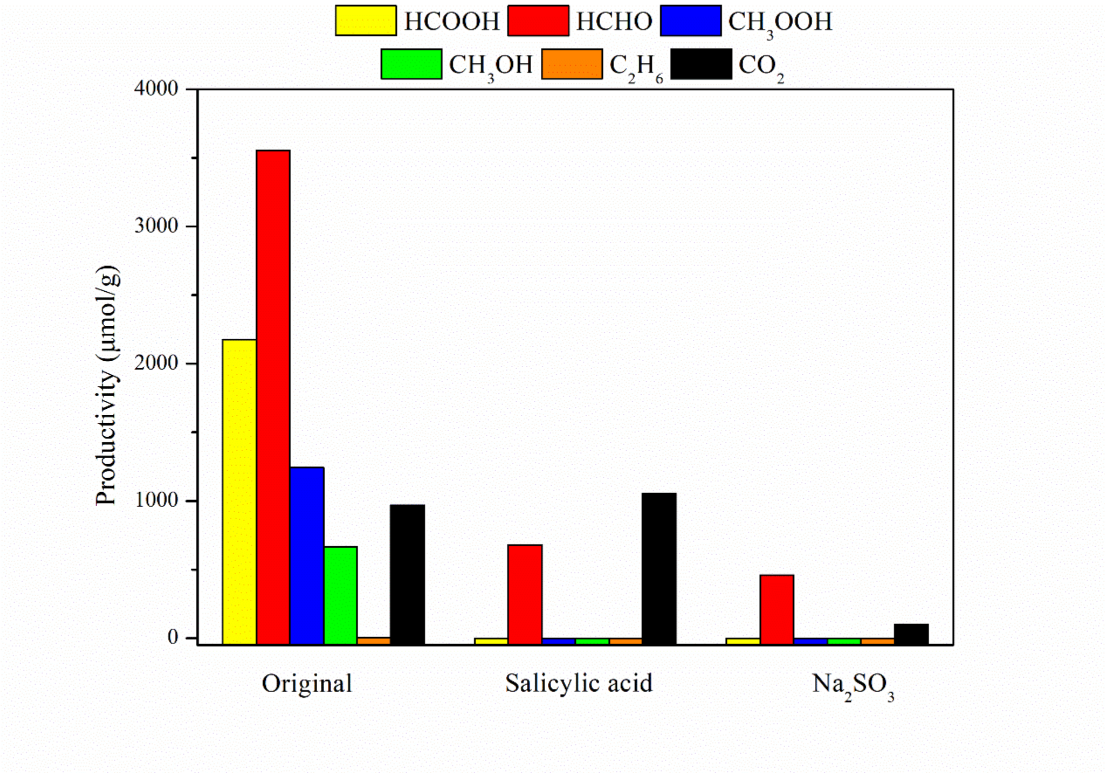

Figure 16. photocatalytic methane oxidation over CsPW-TiO_2 with the addition of salicylic acid and Na_2SO_3

To further investigate the mechanism of methane photooxidation, we used an in-situ electron paramagnetic resonance (EPR) spin-trapping technique with the spin trap 5,5-dimethyl-1-pyrroline N-oxide (DMPO). Before the introduction of CH_4, only the 1:2:2:1 quartet signal ascribed to the DMPO-OH adduct was observed on illuminated CsPW-TiO_2 (**Figure 17a**), revealing the presence of •OH. Upon introducing CH_4, both •CH_3 and •OH were detected (**Figure 17b**), which indicates that photocatalytic CH_4 oxidation over CsPW-TiO_2 is radically based and involves generation of •CH_3. In addition, CsPW-TiO_2 shows higher DMPO-OH signal intensity than bare TiO_2 (**Figure 17a**), which can be due to better charge separation via the p-n heterojunction. Interestingly, when air is removed from the system, CsPW-TiO_2 shows a decreased DMPO-OH signal intensity (**Figure 17a**). This indicates that O_2 also plays an important role in •OH production. This phenomenon is consistent with the photoluminescence (PL) spectra (**Figure 27**) and methane photooxidation performance.

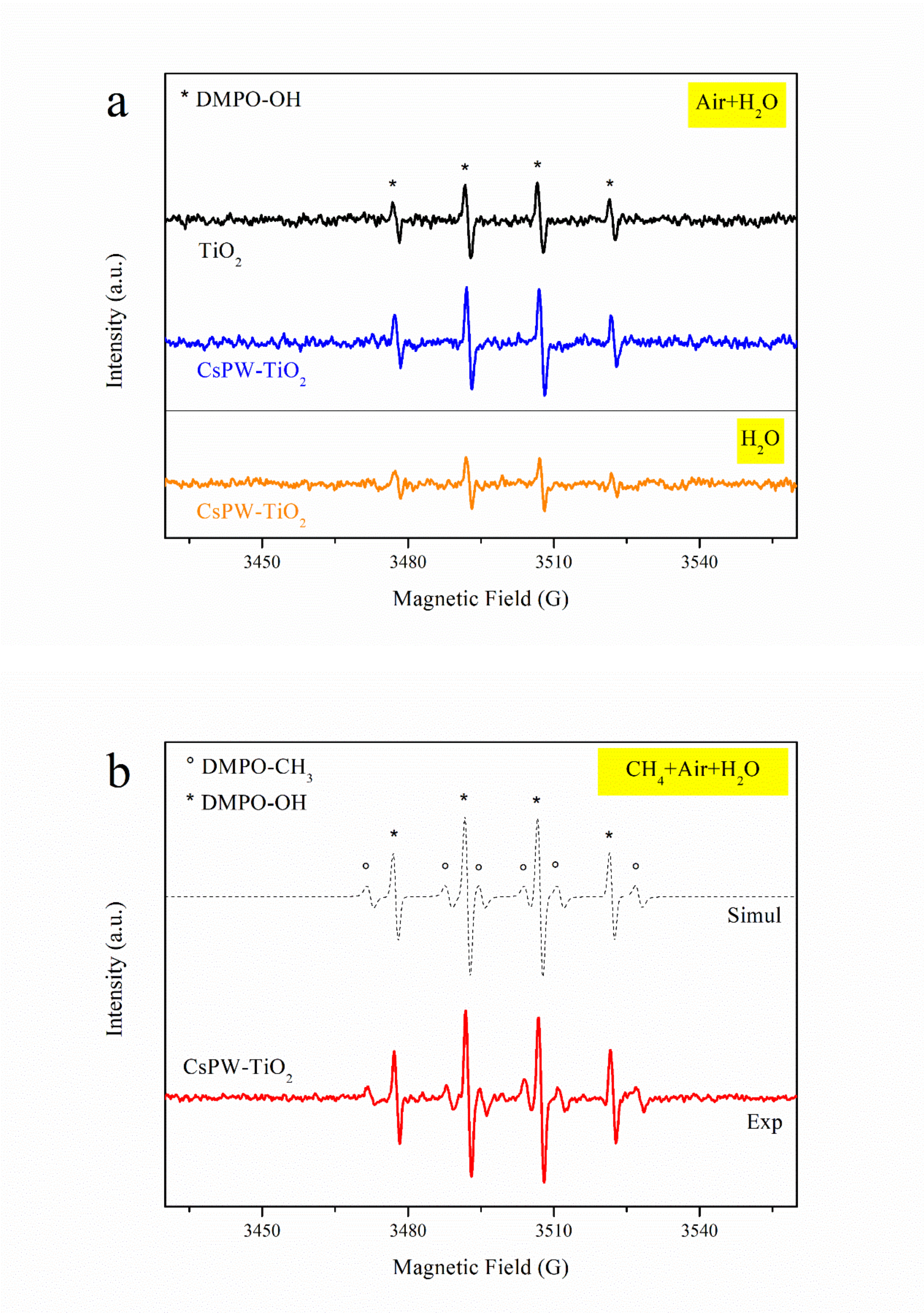

Figure 17. EPR spectra of CsPW-TiO_2 and TiO_2 under irradiation in air and H_2O (**a**) and in methane, air and H_2O (**b**). DMPO was added to the reaction mixture as the radical trapping agent.

It is well-known that the adsorbed O_2 on the surface of catalysts is a strong electron scavenger forming the superoxide anion (O_2^{-})[39], which can produce •OH radicals[40] and contribute to charge separation and methane oxidation. To investigate the activation of O_2 over catalysts and understand the underlying mechanism in photocatalytic methane oxidation, in situ EPR experiments were carried out in air or a vacuum. The EPR spectra were recorded under dark and light irradiation conditions at 120 K (**Figure 18**). They show the presence of Ti^{3+} and O_2^{-} species over both TiO_2 and CsPW-TiO_2 under irradiation. Note that under irradiation in air, the signal intensities of O_2^{-} radical over TiO_2 are stronger than that over CsPW-TiO_2, while the DMPO-OH intensity of TiO_2 is lower than CsPW-TiO_2 (**Figure 17a**). This suggests that abundant O_2^{-} radical might be the main cause for the overoxidation to CO_2 over TiO_2 instead of •OH radicals.

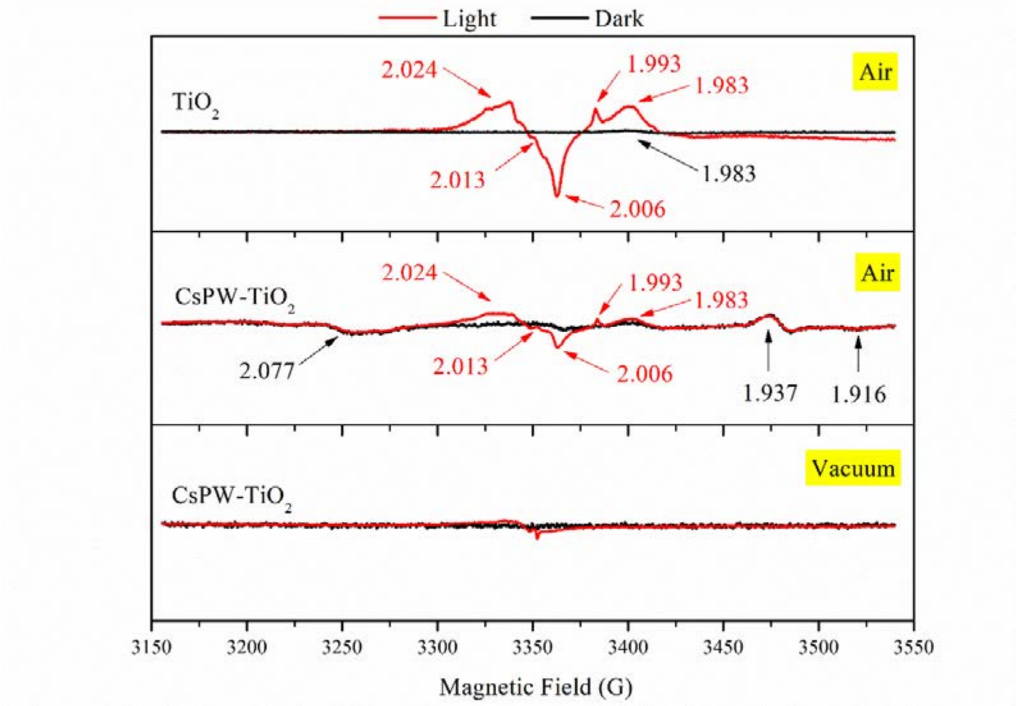

Figure 18. In situ EPR spectra of TiO_2 and CsPW-TiO_2 in air or in vacuum under dark conditions (black line) and light irradiation (red line).

In the dark with air, the signal with g=1.983 assigned to Ti^{3+} was observed[41]. In addition, some signals on CsPW-TiO_2 with g=1.916, 1.937 and 2.077 can be due to the absorption of O_2 on the catalyst surface as they did not show in a vacuum. Upon irradiation, two types of paramagnetic species were detected: reactive oxygen species (ROS) and Ti^{3+}, with a series of new signals (g=1.993-2.024). The signals at g < 2.00 (g=1.993 and 1.983) were assigned to the surface electron trapping site Ti^{3+}, and the signals with g= 2.024, g= 2.013 and g= 2.006 were assigned to the reactive oxygen species[42]. The EPR results reveal the generation of surface species, because of the interaction between catalyst surface sites and O_2, while almost no EPR signal assigned to ROS was observed over CsPW-TiO_2 in the vacuum under both dark and light irradiation. These results confirm that produced EPR signals with g= 2.024, g= 2.013 and g= 2.006 can be assigned to the O_2^- radical[43][44].

On the basis of the above results, we propose a potential mechanism for photocatalytic methane oxidation over CsPW-TiO_2, as illustrated in **Figure 13**. Under irradiation, the charge separation is enhanced thanks to the p-n heterojunction, the photogenerated electrons can efficiently transfer to CsPW while holes migrate to TiO_2. As a result, more electrons and holes are available for methane oxidation, which simultaneously oxidize H_2O via photoholes and reduce O_2 via photoelectrons for the formation of •OH radicals (**Figure 17**), a key factor for CH_4 activation. The reduction of O_2 may involve a partial reduction of W species, which can also play a role as a co-catalyst. The formed •OH radicals and holes next activate methane to $•CH_3$ which reacts with O_2 to form CH_3OOH. The CH_3OH can derive from either the CH_3OOH precursor through a photoreduction process or the coupling of $•CH_3$ and •OH. Finally, HCHO and HCOOH can be produced from the photooxidation of CH_3OH by photogenerated holes or •OH.

Our results show that photocatalytic oxidation of methane, which occurs at room temperature, suffers from insufficient selectivity. Indeed, methane photocatalytic oxidation over CsPW-TiO_2 results in a mixture of C_1 oxygenates (**Figure 2**). The separation of individual liquid oxygenates from the reaction solution can be a difficult task and prohibitively expensive. It is much more attractive and promising to achieve a selective one-pot synthesis of concentrated formic acid production in the liquid phase directly from methane. That was the reason, why we attempted to further convert the mixture of C_1 oxygenates produced by photocatalysis into formic acid.

5.2.2 Chemo-catalytic oxidation of methanol and formaldehyde over commercial Ru/Al_2O_3 heterogeneous catalyst at room temperature

A series of heterogeneous supported transition metal catalysts have been investigated in a batch reactor in the formaldehyde and methanol chemo-oxidation (without irradiation) to formic acid at ambient temperature in the presence of air. No conversion of methanol and formaldehyde was observed in the absence of the catalyst.

Table 1. Formaldehyde oxidation to formic acid over transition metal composites in aqueous solution[a]

Entry	Catalyst	Final concentration of oxygenates (μmol L^{-1})	
		HCHO	HCOOH
1	CuO	474	0
2	Fe_2O_3	486	0
3	Cu-ZnO-Al_2O_3	484	0
4	5% Pt/C	0	0
5	5% Pd/Al_2O_3	0	0
6	5% Ru/Al_2O_3	0	355
7[b]	5% Ru/Al_2O_3	0	355
8[c]	-	500	0

[a]Reaction conditions: 0.1g catalyst, 0.1 MPa air, 5.0 g solution, 20 ± 2 °C reaction temperature, 2 h reaction time, no light irradiation. [b]Entry 7: 12 h reaction time. [c]Entry 8: no catalyst. The initial concentration of formaldehyde in all tests was 500 μmol L^{-1}.

No noticeable formaldehyde oxidation was either observed over CuO, Fe_2O_3, and CuZnAl (**Table 1, Entry 1-3**). Interestingly, only supported noble metals (Pt, Pd and Ru) were found effective in the formaldehyde oxidation (**Table 1, Entry 4-7**). The Pt/C and Pd/Al_2O_3 catalysts produced from formaldehyde only CO_2, as no liquid products were even observed.

To study the oxidation efficiency of C_1 oxygenates mixture to formic acid, different amounts of Ru/Al_2O_3 catalyst were dispersed into 5 g (500 μmol L^{-1}) of HCHO solution as a reference. **Figure 19** shows that the rate of HCHO oxidation into HCOOH increase with increase of the amount of Ru/Al_2O_3 catalyst. The complete oxidation of HCHO with 0.01 g Ru/Al_2O_3 took rather long time (about 48 h). We chose 0.1 g Ru/Al_2O_3 for efficient oxygenate oxidation in the cascade process. Important, Ru/Al_2O_3 showed selective chemocatalytic oxidation of formaldehyde to formic acid with a selectivity of 71 %. Interestingly, even with increasing the reaction time from 2 h to 12 h (**Table 1, Entry 6** and **7**), no further oxidation of formic acid to CO_2 has been detected.

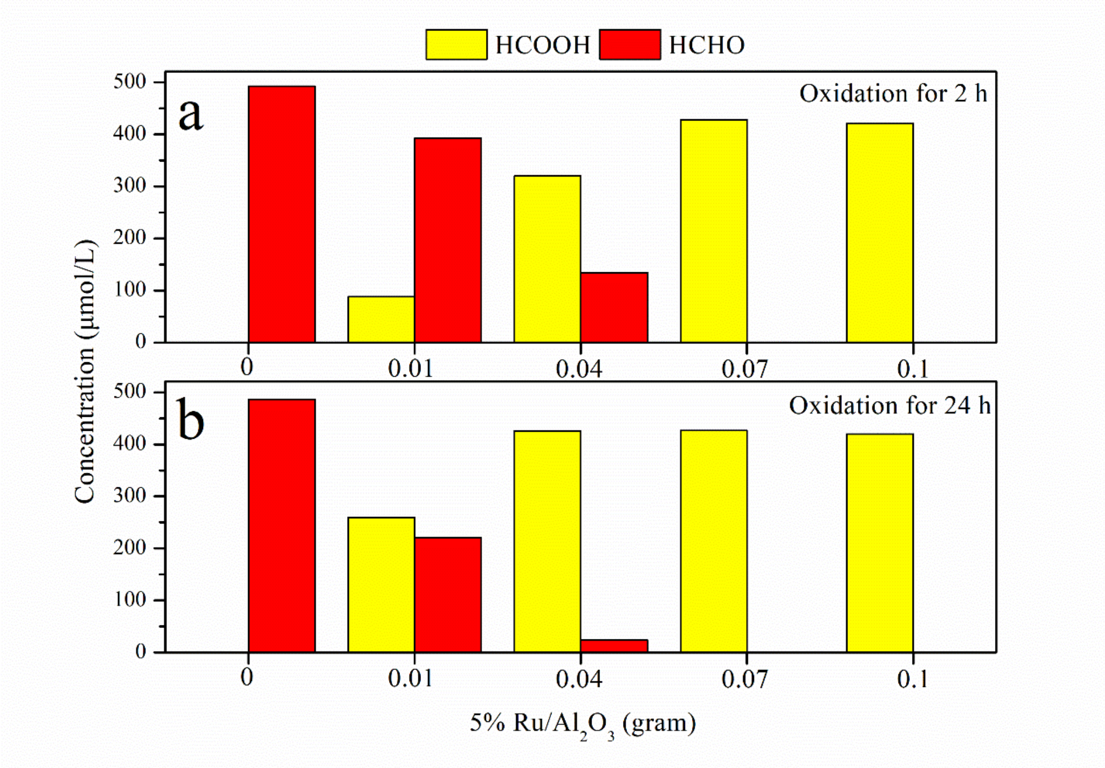

Figure 19. formaldehyde (HCHO) solution oxidation over a series amount of Ru/Al_2O_3 catalyst with time

Table 2. Methanol and formaldehyde oxidation to formic acid over 5% Ru/Al_2O_3 in aqueous solution[a]

Entry	Original concentration of oxygenates (µmol L^{-1})			Final concentration of oxygenates (µmol L^{-1})		
	CH_3OH	HCHO	HCOOH	CH_3OH	HCHO	HCOOH
1	186	0	0	0	0	120
2[b]	186	0	0	186	0	0
3	0	500	0	0	0	355
4[b]	0	500	0	0	500	0
5[c]	0	0	0	0	0	0

[a]Reaction conditions: 0.1g 5% Ru/Al_2O_3 catalyst, 0.1 MPa air, 5.0 g solution, 20 ± 2 °C reaction temperature, 2 h reaction time, no light irradiation. [b]Entry 2 and 4: no 5% Ru/Al_2O_3 catalyst. [c]Entry 5: pure water.

In addition to formaldehyde, the supported Ru/Al_2O_3 catalyst was evaluated in the methanol chemocatalytic oxidation at room temperature in the presence of air. The catalytic results are presented in **Table 2**. In the presence of Ru/Al_2O_3, methanol is oxidized with a selectivity of 64% to formic acid. The catalytic results suggest, therefore, that Ru/Al_2O_3 can be an efficient catalyst for selective oxidation of a mixture of C_1 oxygenates produced by photocatalytic oxidation of methane to formic acid at ambient temperature. The commercial 5 wt.% Ru/Al_2O_3 catalyst was characterized using a combination of techniques: XRD, imaging techniques, XPS and TPR. The details of the characterization of $CsPW\text{-}TiO_2$ and Ru/Al_2O_3 are given in **Figures 24-31**.

5.2.3 Cascade photo-chemo-catalytic conversion of methane to formic acid

After elaboration of photo-catalytic methane oxidation to C_1 oxygenates and chemo-catalytic oxidation of C_1 oxygenates to formic acid, we tried to combine the two processes by mechanically mixing the CsPW-TiO_2 photocatalyst with the Ru/Al_2O_3 heterogeneous catalyst (**Table 3**).

Table 3. Methane oxidation over the CsPW-TiO_2+Ru/Al_2O_3 catalysts prepared by mechanical mixing and in the cascade process

Entry	Catalyst	Catalyst weight composition, g		Productivity (μmol $g_{photocatalyst}^{-1}$ h^{-1})			
		CsPW-TiO_2	Ru/Al_2O_3	CH_3OH/ CH_3OOH	HCHO	HCOOH	CO_2
1[a]	CsPW-TiO_2	0.01	0	332.21/621.94	1777.01	1088.12	484.38
2[a]	CsPW-TiO_2+ Ru/Al_2O_3	0.01	0.1	0/0	0	0	Trace
3[b]	CsPW-TiO_2+ Ru/Al_2O_3	0.01	0.01	195.75/0	300.00	0	151.80
4	Cascade process: Separated CsPW-TiO_2 and Ru/Al_2O_3	0.01	1	0/0	0	2528.13	446.79

Reaction conditions: 0.6 MPa CH_4, 0.1 MPa air, 100 mL water, 20 ± 2 °C reaction temperature, 400 W Xe lamp, full irradiation.

[a] 2 h reaction time.

[b] 5h reaction time.

No liquid product, but only traces of CO_2 were observed over the mixed composites containing 0.1 g Ru/Al_2O_3 and 0.01 g CsPW-TiO_2 (**Table 3, Entry 2**). Small amounts of methanol and formaldehyde were eventually detected by reducing the Ru/Al_2O_3 amount in the mixed composite and extending the irradiation time (**Table 3, Entry 3**). However, an extremely lower methane conversion over the mechanically mixed catalysts, compared to the photocatalytic performance of CsPW-TiO_2 (**Table 3, Entry 1**) indicates that the mechanical mixing completely suppresses the photocatalytic process. The low activity of the mechanical mixture of CsPW-TiO_2 and Ru/Al_2O_3 may be due to the covering of the photocatalyst by its alumina-supported counterpart, making it inaccessible to irradiation. The UV-visible spectra (**Fig. 20**) show almost complete disappearance of adsorption due to the band gap transition in the TiO_2 and CsPW semiconductors after mixing with Ru/Al_2O_3.

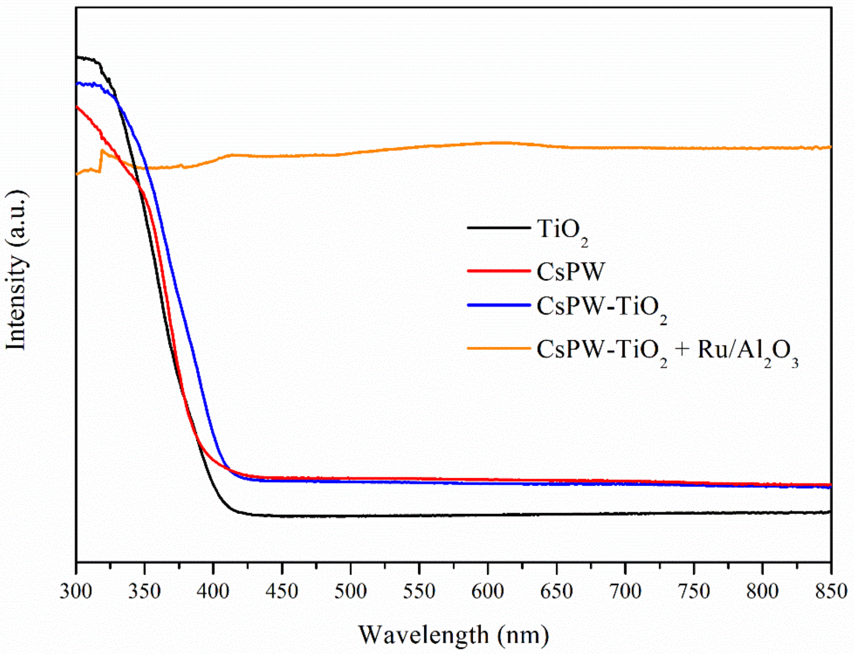

Figure 20. UV-visible DRS spectra of TiO_2, CsPW, CsPW-TiO_2 and mechanical mixture of CsPW-TiO_2 and Ru/Al_2O_3.

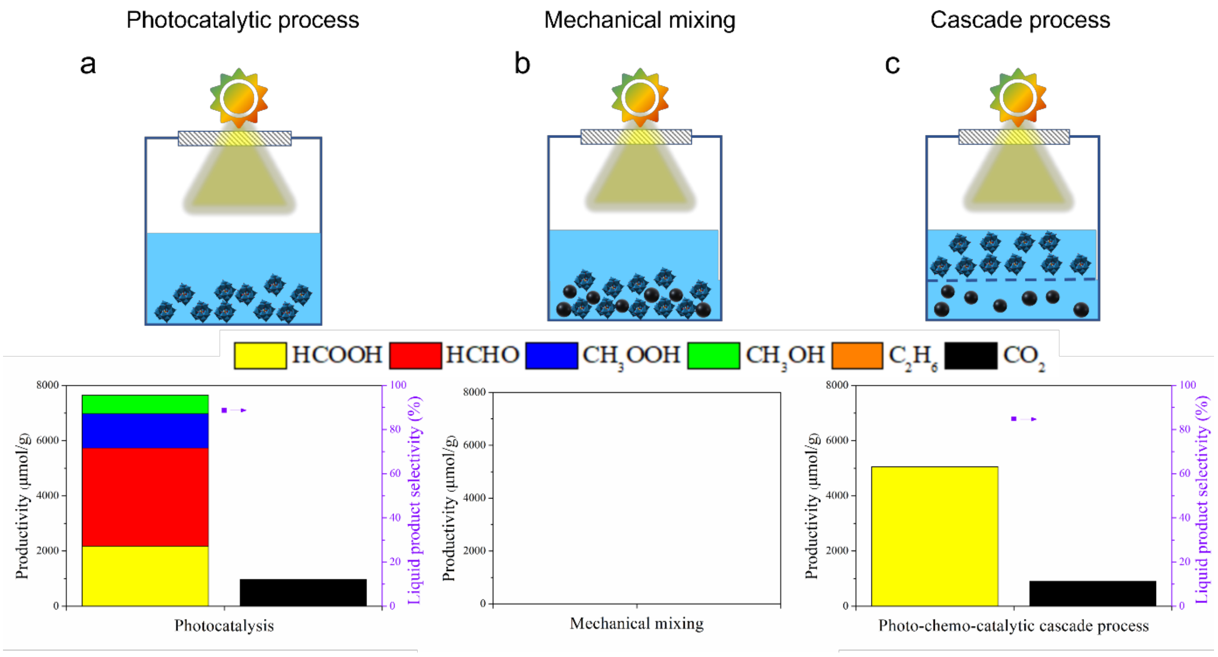

Fig. 21. Photocatalytic (a), mechanical mixing (b) and cascade photo-chemo-catalytic process (c) for methane oxidation

Photocatalytic process: 10 mg CsPW-TiO_2, 100 mL water, 0.6 MPa CH_4, 0.1 MPa air, 2 h irradiation time, 20 ± 2 °C reaction temperature, light source: 400 W Xe lamp, full irradiation.

Mechanical mixing: 10 mg CsPW-TiO_2, 100 mg 5% Ru/Al_2O_3, 100 mL water, 0.6 MPa CH_4, 0.1 MPa air, 2 h irradiation time, 20 ± 2 °C reaction temperature, light source: 400 W Xe lamp, full irradiation

Cascade process: 10 mg CsPW-TiO_2, 1 g 5% Ru/Al_2O_3, 100 mL water, 0.6 MPa CH_4, 0.1 MPa air, 2 h irradiation time, 20 ± 2 °C reaction temperature, light source: 400 W Xe lamp, full irradiation

Then, the CsPW-TiO_2 and Ru/Al_2O_3 were loaded in the same reactor but separately from each other. The reactor configuration is shown in **Figure 21** and **Figure 5** (**In Chapter 2**). The photocatalyst is located at the top of the reactor and exposed to irradiation. The ruthenium catalyst is placed under a sand filter at the bottom of the reactor. The productivities to oxygenates attained in the photocatalytic process with the CsPW-TiO_2 catalysts and in the cascade photo-chemo-catalytic process are shown in **Table 3, Entry 1** and **4** and **Fig. 21**. Different to the photocatalytic reaction, which produced a multitude of C_1 oxygenates (**Fig. 21a**), methane conversion in the cascade process selectively yields formic acid (**Fig. 21c**). After the optimization of the reaction conditions, in the cascade process, the productivity of HCOOH reached 5000 μmol g^{-1} after 2 h irradiation with a total selectivity ~85%. CO_2 was the only gaseous compound, which was released during methane oxidation.

The isotopic labelling experiments using $^{13}CH_4$ were conducted to confirm the carbon source of C_1 oxygenates. The three ^{13}C NMR signals at 168, 82, 65 and 48 ppm (**Figure 22a)** were attributed to $H^{13}COOH$, $H^{13}CHO$, $^{13}CH_3OOH$ and $^{13}CH_3OH$, respectively. In addition, the existence of $H^{13}COOH$ alone after oxygenates oxidation over Ru/Al_2O_3 suggests that oxygenates derived from methane were selectively oxidized into formic acid (**Figure 22b**). These results confirm that all the oxygenates indeed originate from methane.

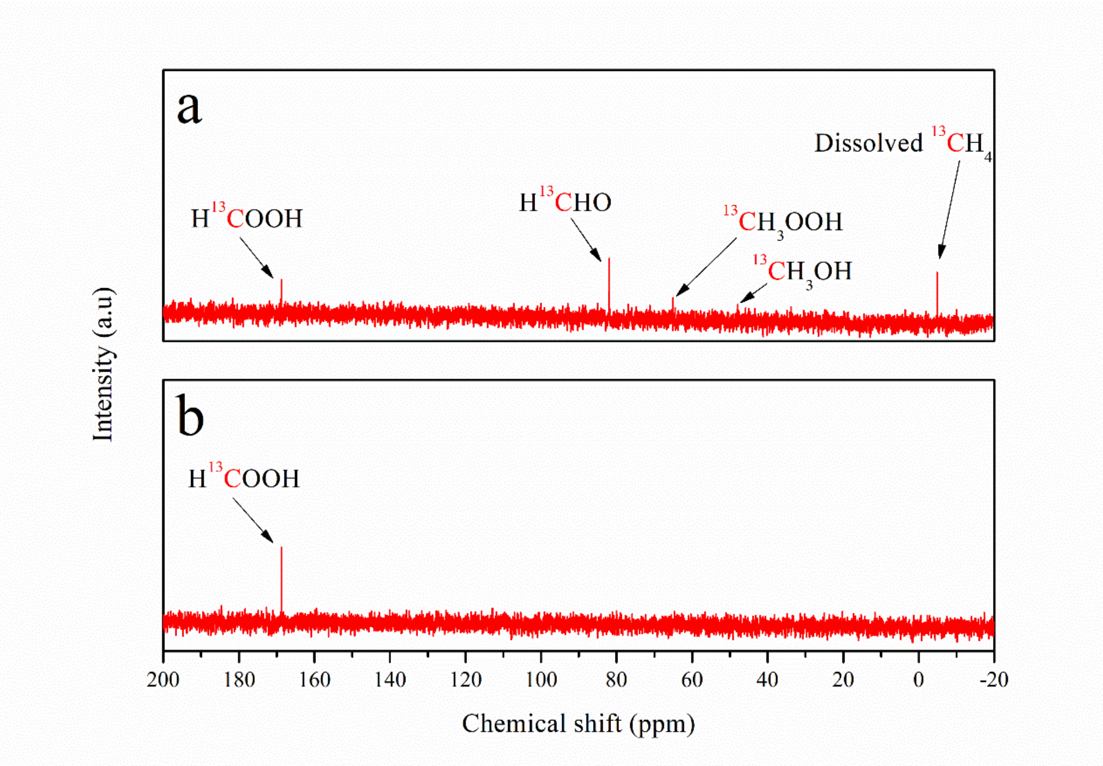

Figure 22. ^{13}C NMR spectrum of the product obtained from photocatalytic methane oxidation over CsPW-TiO_2 using $^{13}CH_4$ (**a**) and subsequent oxygenates oxidation over Ru/Al_2O_3 (**b**)

Numerous applications of formic acid require concentrated solutions. Separation of formic acid from water can be prohibitively expensive if the concentration of the target product in the post-reaction mixture is low. To reach a higher concentration of the formic acid in the liquid phase, we reduced the amount of water (30 mL) in the cascade process. With some decrease in the selectivity, a concentrated HCOOH solution of 1.1 mmol/L was obtained **(Fig. 23)**.

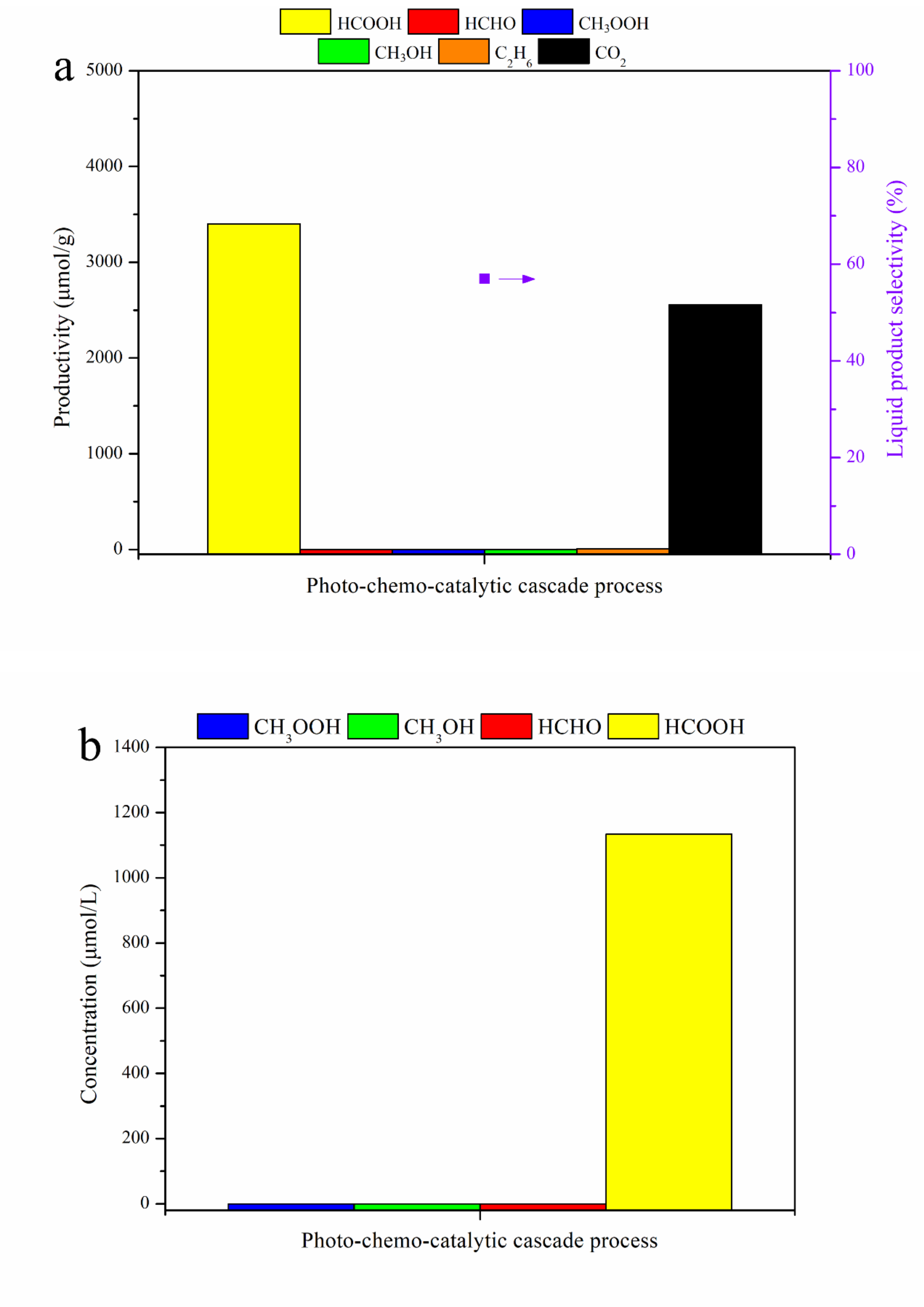

Figure 23. Concentrated HCOOH production over cascade process.

5.3 Catalyst Characterization

5.3.1 Characterisation of CsPW-TiO$_2$

All the TiO$_2$ containing samples exhibit X-ray diffraction peaks of rutile and anatase phases (**Figure 24**). The obtained X-ray diffraction reflections in CsPW and CsPW-TiO$_2$ are similar to those of the HPW, indicating the formation of crystalline Keggin structure[45,46]. The peak broadening in CsPW-TiO$_2$ suggests possible disordering and formation of smaller crystalline domains of HPW.

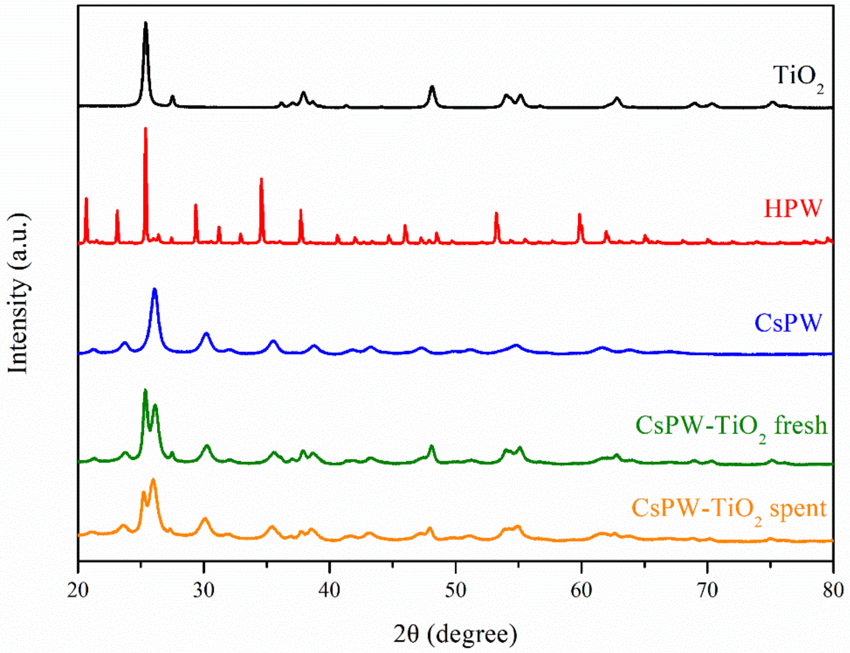

Figure 24. X-ray diffraction patterns of catalysts

Fig. 25 displays the images of scanning transmission electron microscopy (STEM), scanning transmission electron microscopy high-angle annular dark-field (STEM-HAADF) and STEM energy dispersive X-ray spectroscopy (STEM-EDX) elemental maps of the CsPW-TiO_2 sample. The STEM images (**Fig. 25a)** show an irregular morphology of TiO_2 crystallites with a mean size of 20–30 nm. Besides, some smaller CsPW particles are well dispersed on TiO_2 with distinct interfaces between them. The STEM-EDX maps (**Fig. 25 b-d**) indicate a uniform distribution of Cs, P and W elements in the CsPW small particles dispersed on TiO_2. At the same time, the catalysts contain larger CsPW particles, which exhibit characteristic X-ray diffraction peaks, in contact with TiO_2. The images show close contact but distinct separation of TiO_2 and CsPW semiconductor phases, confirming the presence of the heterojunction.

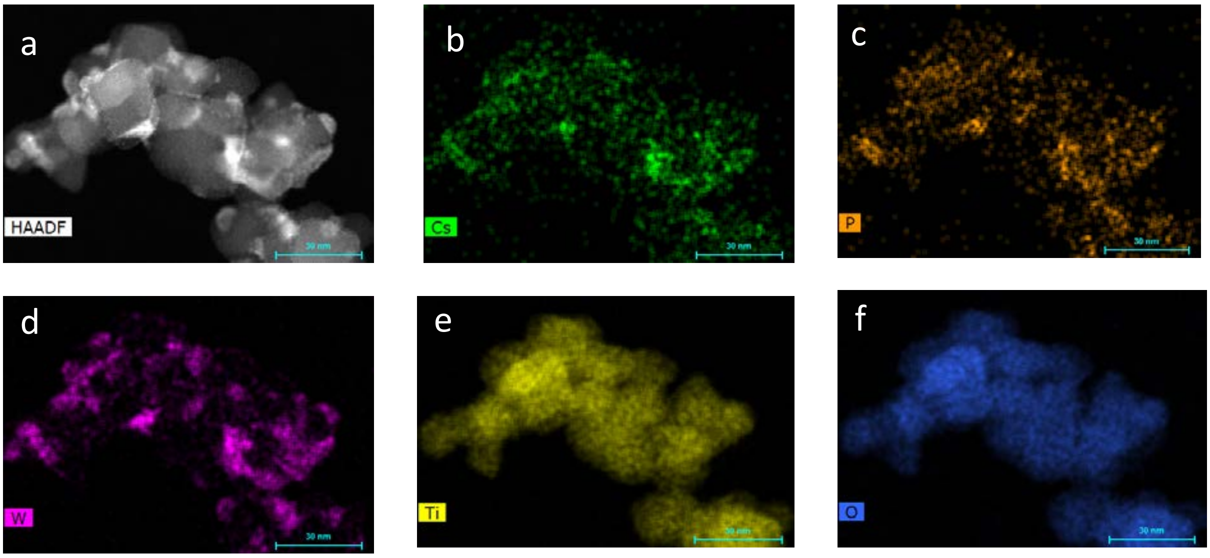

Fig. 25. STEM and STEM-EDX mapping images of fresh CsPW-TiO_2 sample. **a**, STEM-HAADF and corresponding EDX mapping images of the elements: Cs (**b**), P (**c**), W (**d**), Ti (**e**) and O (**f**).

The UV-visible spectra of TiO_2, CsPW and CsPW-TiO_2 are displayed in **Figure 20**. The samples show intense absorption in the ultraviolet region (< 400 nm). Interestingly, the band gaps estimated using Tauc's plots (**Figure 26**) are almost the same for both TiO_2, CsPW and CsPW-TiO_2 (3.33 eV for TiO_2, 3.27 for CsPW and 3.20 for CsPW-TiO_2).

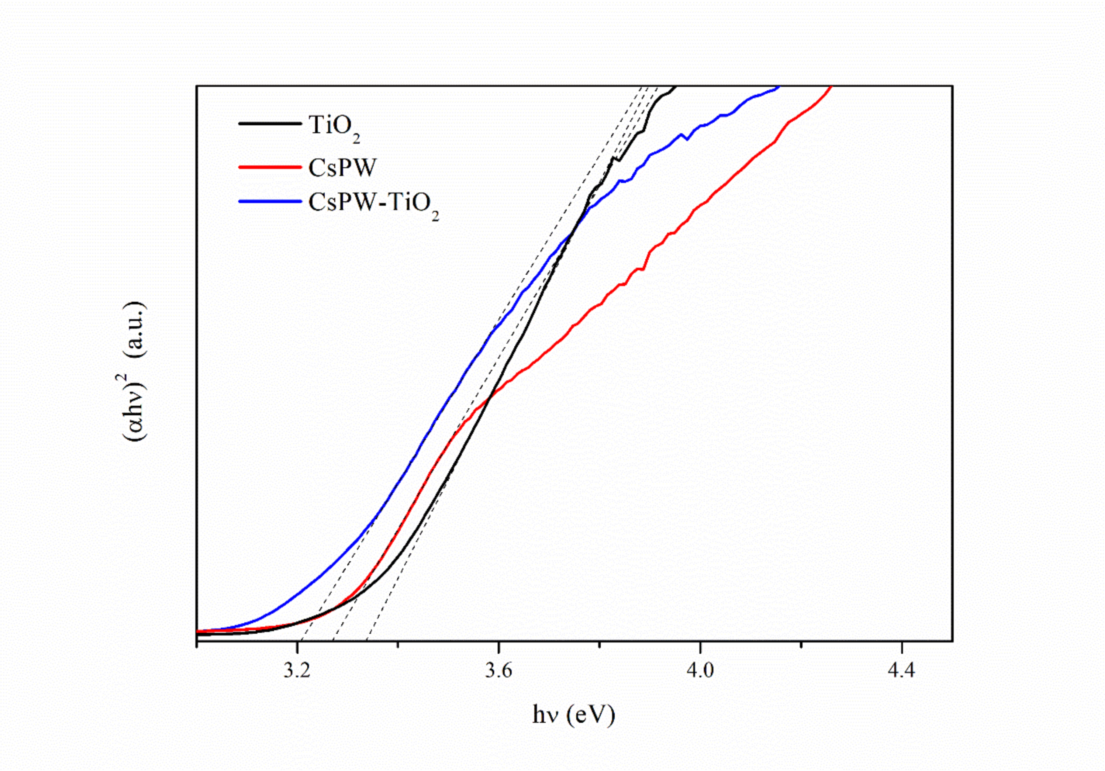

Figure 26. Tauc's plots of TiO_2, CsPW and CsPW-TiO_2

The charge separation in CsPW-TiO_2, CsPW and TiO_2 was followed by photoluminescence (PL) spectroscopy, which provides information about the surface processes involved in the recombination of photogenerated charge carriers (**Figure 27**). An obvious visible luminescence band at around 475 nm is observed for TiO_2, due to the recombination of photogenerated e^-/h^+ pairs [5,47]. The intensity of the luminescence band at ~475 nm decreases in the order of TiO_2 > CsPW-TiO_2 > CsPW (**Figure 27**). This suggests that the CsPW-TiO_2 composite is the most efficient for the separation of photogenerated electron-hole pairs. This can be explained by the migration of excited electrons from TiO_2 to CsPW, preventing the electron−hole recombination. This effect has been observed earlier for other photocatalytic reactions in the presence of HPW and TiO_2[48].

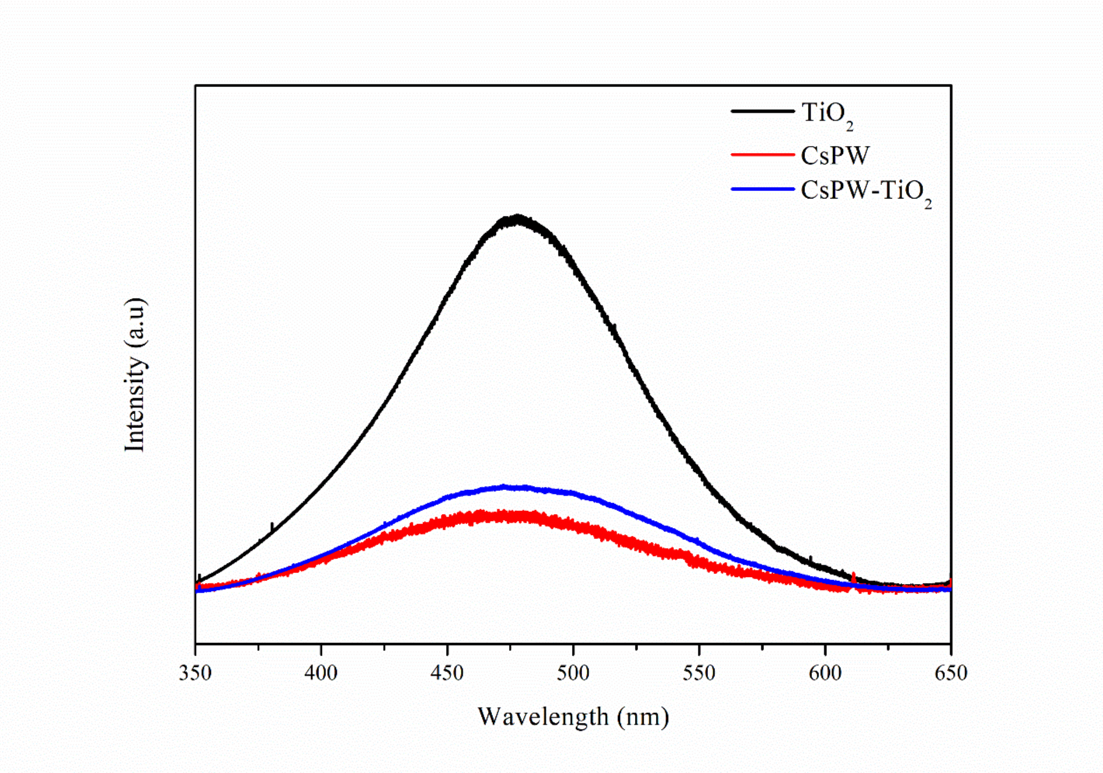

Figure 27. Photoluminescence spectra of TiO_2, CsPW and CsPW-TiO_2.

5.3.2 Characterization of Ru/Al_2O_3

The commercial 5 wt.% Ru/Al_2O_3 catalyst was characterized using a combination of techniques: XRD, imaging techniques, XPS and TPR.

The XRD patterns of oxidized 5 wt. % Ru/Al_2O_3 catalyst are shown in **Figure 28**. They exhibit the peaks characteristic of γ-alumina and RuO_2.

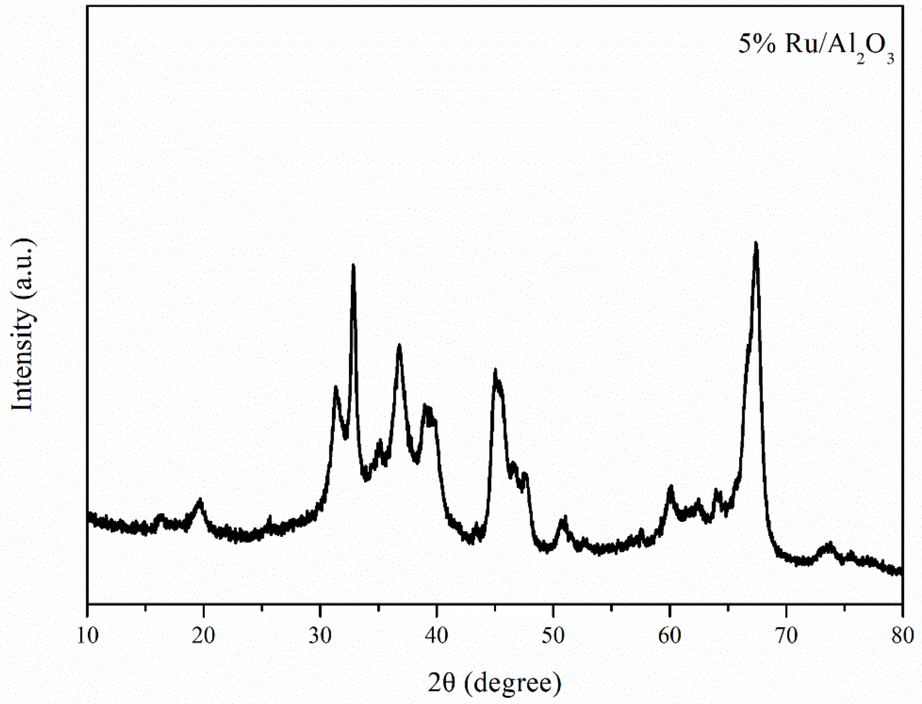

Figure 28. XRD patterns of oxidized 5 wt. % Ru/Al_2O_3 catalyst

The STEM, HAADF-STEM images and corresponding STEM-EDX mapping (**Figure 29**) indicate the presence of small Ru nanoparticles dispersed over the alumina support. The histograms of Ru nanoparticles calculated from STEM-HAADF images display the average size of Ru nanoparticles of 5-6 nm.

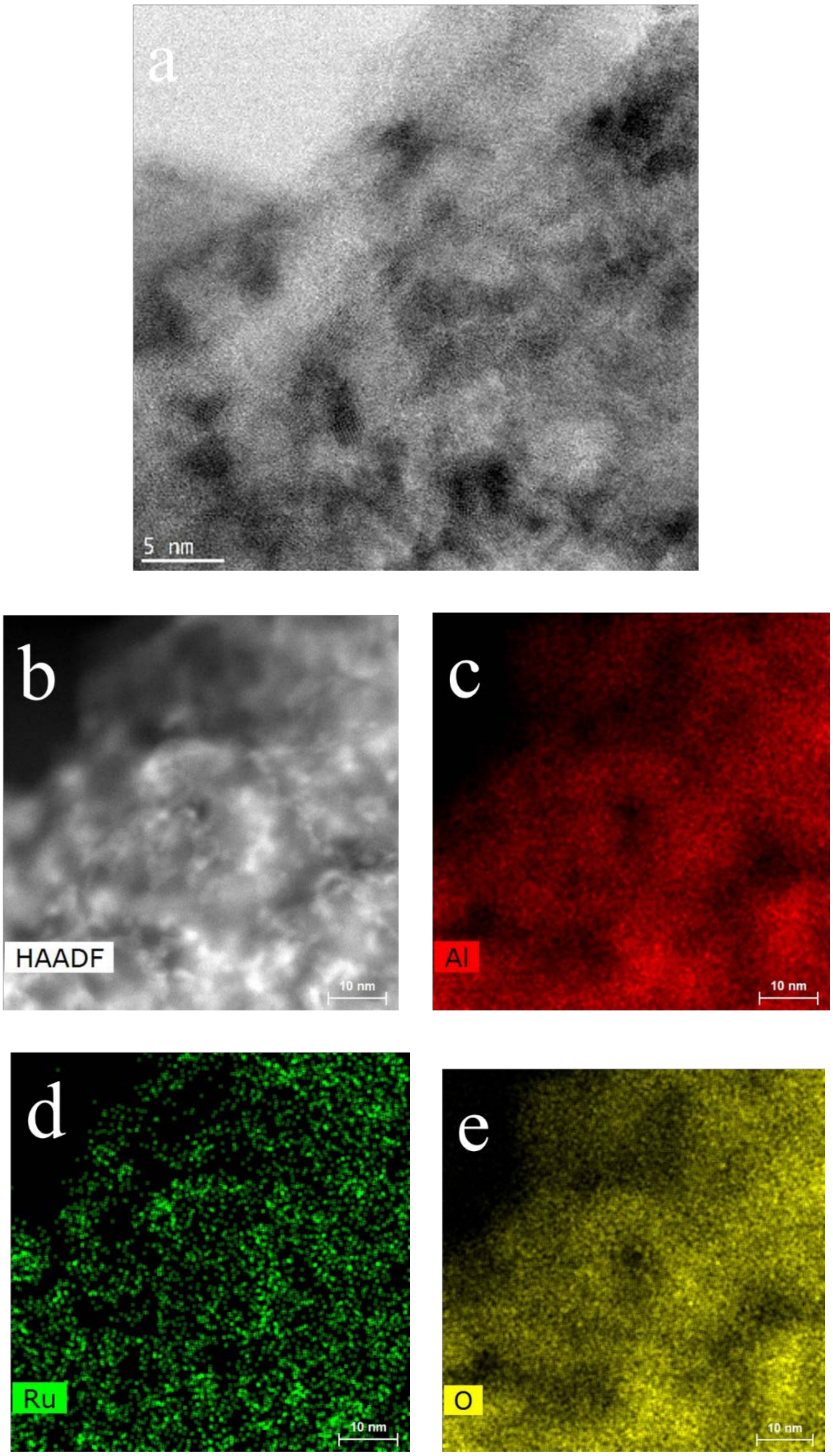

Figure 29. STEM, HAADF-STEM image and corresponding STEM-EDX mapping of Ru/Al_2O_3 catalyst. **a,** STEM image of Ru/Al_2O_3 catalyst. **b-e**, STEM-HAADF (**b**), and corresponding EDX mapping images of the elements: Al (**c**), Ru (**d**), O (**e**).

The XPS spectra of Ru/Al_2O_3 catalyst (**Figure 30**) shows the existence of small amount of RuO_2 species, while most ruthenium nanoparticles are metallic state.

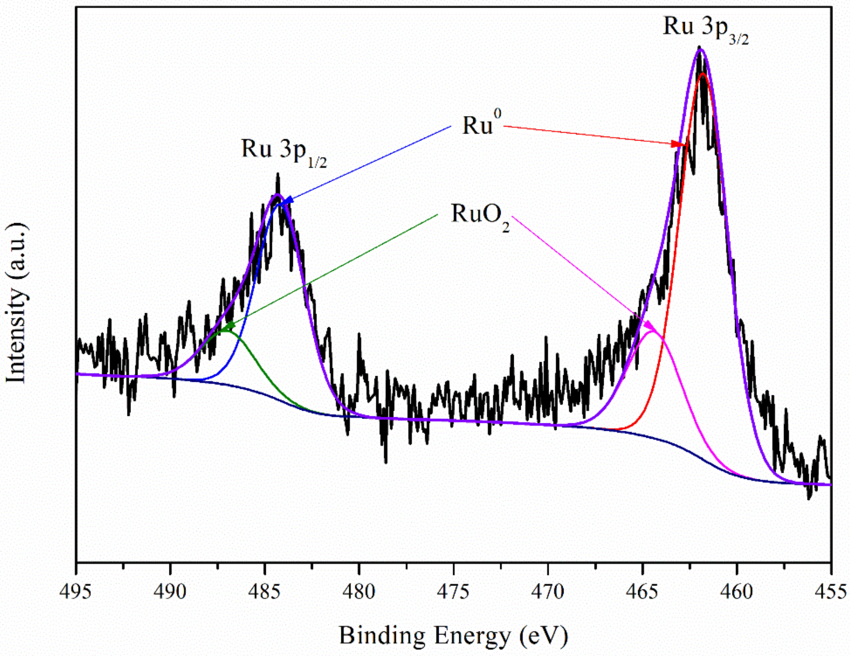

Figure 30. XPS spectra of Ru/Al_2O_3

The TPR profiles of Ru/Al_2O_3 catalyst (**Figure 31**) exhibit two hydrogen absorption peaks. The low temperature peaks at 114°C can be attributed to the reduction of small highly dispersed ruthenium oxide species, while the high temperature shoulder at 217°C is assigned to the reduction of well-crystallized larger ruthenium oxide nanoparticles. The catalyst characterization results are is in general accordance with the previous findings[49–51].

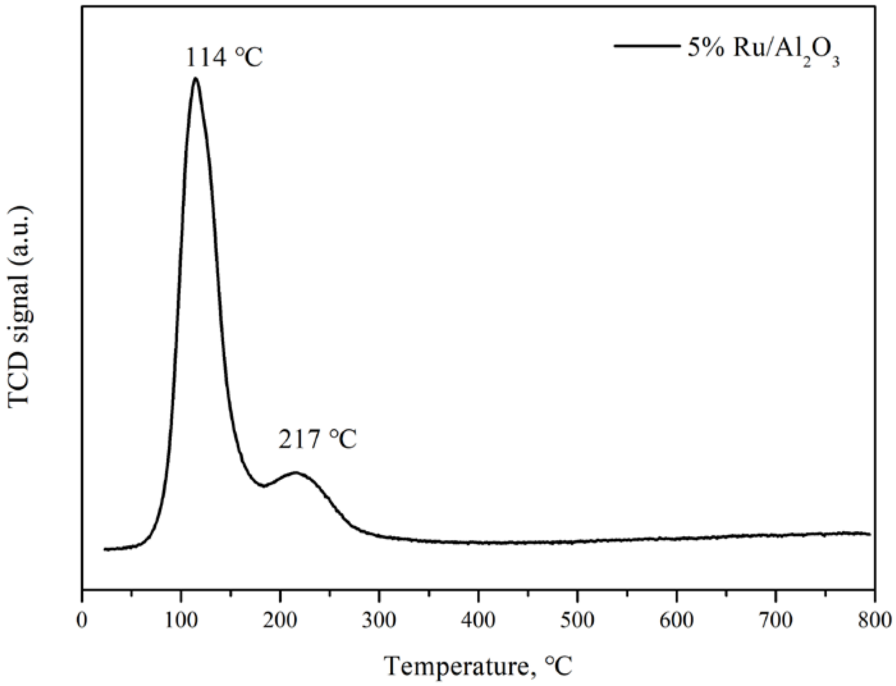

Figure 31. TPR profile of Ru/Al$_2$O$_3$

5.4 Conclusion

In this work, we propose a one-pot photo-chemocatalytic process for selective synthesis of formic acid from methane with air as an oxidant at ambient temperature. A yield of formic acid over 5000 μmol g^{-1} and a selectivity of 85% were achieved. CO_2 is the only gaseous compound in methane oxidation. Optimization of reaction conditions allows the synthesis of HCOOH solution with a concentration of 1.1 mmol/L

The process involves a photocatalyst prepared from caesium salt of phosphotungstic acid mixed with titania and a heterogeneous alumina supported ruthenium catalyst. Methane photocatalytic oxidation results in a mixture of C_1 oxygenates, which then are selectively oxidized to formic acid. Our findings offer valuable guidance for the direct and highly selective methane oxidation to HCOOH in water using O_2 as an oxidant.

This strategy can be particularly suitable for selective conversion of extremely inert molecules such as methane, light alkanes or CO_2 under mild conditions.

5.5 References

[1] J. Ma, X. Tan, Q. Zhang, Y. Wang, J. Zhang, L. Wang, Exploring the size effect of Pt nanoparticles on the photocatalytic nonoxidative coupling of methane, ACS Catal. 11 (2021) 3352–3360. https://doi.org/10.1021/acscatal.0c04943.

[2] W. Jiang, J. Low, K. Mao, D. Duan, S. Chen, W. Liu, C. Pao, J. Ma, S. Sang, C. Shu, X. Zhan, Z. Qi, H. Zhang, Z. Liu, X. Wu, R. Long, L. Song, Y. Xiong, Pd-Modified ZnO–Au Enabling Alkoxy Intermediates Formation and Dehydrogenation for Photocatalytic Conversion of Methane to Ethylene, J. Am. Chem. Soc. 143 (2021) 269–278. https://doi.org/10.1021/jacs.0c10369.

[3] Q. Li, Y. Ouyang, H. Li, L. Wang, J. Zeng, Photocatalytic Conversion of Methane: Recent Advancements and Prospects, Angew. Chemie Int. Ed. 61 (2022). https://doi.org/10.1002/anie.202108069.

[4] J. Yang, W. Xiao, X. Chi, X. Lu, S. Hu, Z. Wu, W. Tang, Z. Ren, S. Wang, X. Yu, L. Zhang, A. Rusydi, J. Ding, Y. Guo, P.X. Gao, Solar-driven efficient methane catalytic oxidation over epitaxial ZnO/La0.8Sr0.2CoO3 heterojunctions, Appl. Catal. B Environ. 265 (2020) 118469. https://doi.org/10.1016/j.apcatb.2019.118469.

[5] X. Li, J. Xie, H. Rao, C. Wang, J. Tang, Platinum- and CuOx-Decorated TiO2 Photocatalyst for Oxidative Coupling of Methane to C2 Hydrocarbons in a Flow Reactor, Angew. Chemie - Int. Ed. 59 (2020) 19702–19707. https://doi.org/10.1002/anie.202007557.

[6] H. Song, X. Meng, T.D. Dao, W. Zhou, H. Liu, L. Shi, H. Zhang, T. Nagao, T. Kako, J. Ye, Light-Enhanced Carbon Dioxide Activation and Conversion by Effective Plasmonic Coupling Effect of Pt and Au Nanoparticles, ACS Appl. Mater. Interfaces. 10 (2018) 408–416. https://doi.org/10.1021/acsami.7b13043.

[7] H. Song, X. Meng, Z. jun Wang, H. Liu, J. Ye, Solar-Energy-Mediated Methane Conversion, Joule. 3 (2019) 1606–1636. https://doi.org/10.1016/j.joule.2019.06.023.

[8] X. Meng, X. Cui, N.P. Rajan, L. Yu, D. Deng, X. Bao, Direct Methane Conversion under Mild Condition by Thermo-, Electro-, or Photocatalysis, Chem. 5 (2019) 2296–2325. https://doi.org/10.1016/j.chempr.2019.05.008.

[9] L. Meng, Z. Chen, Z. Ma, S. He, Y. Hou, H.H. Li, R. Yuan, X.H. Huang, X. Wang, X. Wang, J. Long, Gold plasmon-induced photocatalytic dehydrogenative coupling of methane to ethane on polar oxide surfaces, Energy Environ. Sci. 11 (2018) 294–298. https://doi.org/10.1039/c7ee02951a.

[10] P. Tang, Q. Zhu, Z. Wu, D. Ma, Methane activation: The past and future, Energy Environ. Sci. 7 (2014) 2580–2591. https://doi.org/10.1039/c4ee00604f.

[11] E.G. Nisbet, R.E. Fisher, D. Lowry, J.L. France, G. Allen, S. Bakkaloglu, T.J. Broderick, M. Cain, M. Coleman, J. Fernandez, G. Forster, P.T. Griffiths, C.P. Iverach, B.F.J. Kelly, M.R. Manning, P.B.R. Nisbet-Jones, J.A. Pyle, A. Townsend-Small, A. al-Shalaan, N. Warwick, G. Zazzeri, Methane Mitigation: Methods to Reduce Emissions, on the Path to the Paris Agreement, Rev. Geophys. 58 (2020) 1–51. https://doi.org/10.1029/2019RG000675.

[12] E.A.G. Schuur, A.D. McGuire, C. Schädel, G. Grosse, J.W. Harden, D.J. Hayes, G. Hugelius, C.D. Koven, P. Kuhry, D.M. Lawrence, S.M. Natali, D. Olefeldt, V.E. Romanovsky, K. Schaefer, M.R. Turetsky, C.C. Treat, J.E. Vonk, Climate change and the permafrost carbon feedback, Nature. 520 (2015) 171–179. https://doi.org/10.1038/nature14338.

[13] D. Hu, V. V Ordomsky, A.Y. Khodakov, Major routes in the photocatalytic methane conversion into chemicals and fuels under mild conditions, Appl. Catal. B Environ. 286 (2021). https://doi.org/10.1016/j.apcatb.2021.119913.

[14] J. Lang, Y. Ma, X. Wu, Y. Jiang, Y.H. Hu, Highly efficient light-driven methane coupling under ambient conditions based on an integrated design of a photocatalytic system, Green Chem. 22 (2020) 4669–4675. https://doi.org/10.1039/d0gc01608j.

[15] G.E. Johnson, W.A. Decker, A.J. Forney, J.H. Field, Hydrogen cyanide produced from coal and ammonia, Ind. Eng. Chem. Process Des. Dev. 7 (1968) 137–143. https://doi.org/10.1021/i260025a027.

[16] X. Yu, V. De Waele, A. Löfberg, V. Ordomsky, A.Y. Khodakov, Selective photocatalytic conversion of methane into carbon monoxide over zinc-heteropolyacid-titania nanocomposites, Nat. Commun. 10 (2019) 700. https://doi.org/10.1038/s41467-019-08525-2.

[17] L. Yuliati, H. Yoshida, Photocatalytic conversion of methane, Chem. Soc. Rev. 37 (2008) 1592. https://doi.org/10.1039/b710575b.

[18] G. Chen, G.I.N. Waterhouse, R. Shi, J. Zhao, Z. Li, L.Z. Wu, C.H. Tung, T. Zhang, From Solar Energy to Fuels: Recent Advances in Light-Driven C1 Chemistry, Angew. Chemie - Int. Ed. 58 (2019) 17528–17551. https://doi.org/10.1002/anie.201814313.

[19] X. Chen, Y. Li, X. Pan, D. Cortie, X. Huang, Z. Yi, Photocatalytic oxidation of methane over silver decorated zinc oxide nanocatalysts, Nat. Commun. 7 (2016) 1–8.

https://doi.org/10.1038/ncomms12273.

[20] M.D. Ward, J.F. Brazdil, S.P. Mehandru, A.B. Anderson, Methane photoactivation on copper molybdate. An experimental and theoretical study, J. Phys. Chem. 91 (1987) 6515–6521. https://doi.org/10.1021/j100310a019.

[21] W. Zhu, M. Shen, G. Fan, A. Yang, J.R. Meyer, Y. Ou, B. Yin, J. Fortner, M. Foston, Z. Li, Z. Zou, B. Sadtler, Facet-Dependent Enhancement in the Activity of Bismuth Vanadate Microcrystals for the Photocatalytic Conversion of Methane to Methanol, ACS Appl. Nano Mater. 1 (2018) 6683–6691. https://doi.org/10.1021/acsanm.8b01490.

[22] Y. Zhou, L. Zhang, W. Wang, Direct functionalization of methane into ethanol over copper modified polymeric carbon nitride via photocatalysis, Nat. Commun. 10 (2019). https://doi.org/10.1038/s41467-019-08454-0.

[23] H. Song, X. Meng, S. Wang, W. Zhou, X. Wang, T. Kako, J. Ye, Direct and Selective Photocatalytic Oxidation of CH4 to Oxygenates with O2 on Cocatalysts/ZnO at Room Temperature in Water, J. Am. Chem. Soc. 141 (2019) 20507–20515. https://doi.org/10.1021/jacs.9b11440.

[24] W. Zhou, X. Qiu, Y. Jiang, Y. Fan, S. Wei, D. Han, L. Niu, Z. Tang, Highly selective aerobic oxidation of methane to methanol over gold decorated zinc oxide: Via photocatalysis, J. Mater. Chem. A. 8 (2020) 13277–13284. https://doi.org/10.1039/d0ta02793f.

[25] H. Song, X. Meng, S. Wang, W. Zhou, S. Song, T. Kako, J. Ye, Selective Photo-oxidation of Methane to Methanol with Oxygen over Dual-Cocatalyst-Modified Titanium Dioxide, ACS Catal. 10 (2020) 14318–14326. https://doi.org/10.1021/acscatal.0c04329.

[26] J. Xie, R. Jin, A. Li, Y. Bi, Q. Ruan, Y. Deng, Y. Zhang, S. Yao, G. Sankar, D. Ma, J. Tang, Highly selective oxidation of methane to methanol at ambient conditions by titanium dioxide-supported iron species, Nat. Catal. 1 (2018) 889–896. https://doi.org/10.1038/s41929-018-0170-x.

[27] K. Ohkubo, K. Hirose, Light-Driven C−H Oxygenation of Methane into Methanol and Formic Acid by Molecular Oxygen Using a Perfluorinated Solvent, Angew. Chemie - Int. Ed. 57 (2018) 2126–2129. https://doi.org/10.1002/anie.201710945.

[28] S. Wei, X. Zhu, P. Zhang, Y. Fan, Z. Sun, X. Zhao, D. Han, L. Niu, Aerobic oxidation of methane to formaldehyde mediated by crystal-O over gold modified tungsten trioxide via photocatalysis, Appl. Catal. B Environ. 283 (2021) 119661. https://doi.org/10.1016/j.apcatb.2020.119661.

[29] Z. Sun, C. Wang, Y.H. Hu, Highly selective photocatalytic conversion of methane to liquid oxygenates over silicomolybdic-Acid/TiO2under mild conditions, J. Mater. Chem. A. 9 (2021) 1713–1719. https://doi.org/10.1039/d0ta09226f.

[30] M.D. Rojas-Andrade, S. Chen, Structural Engineering of Nanoparticle Catalysts for Electrochemical Oxidation of Formic Acid, in: Encycl. Interfacial Chem., Elsevier, 2018: pp. 863–880. https://doi.org/10.1016/B978-0-12-409547-2.13319-0.

[31] H. Kawanami, Y. Himeda, G. Laurenczy, Formic Acid as a Hydrogen Carrier for Fuel Cells Toward a Sustainable Energy System, in: 2017: pp. 395–427. https://doi.org/10.1016/bs.adioch.2017.04.002.

[32] K. Ogura, M. Kataoka, Photochemical conversion of methane, J. Mol. Catal. 43 (1988) 371–379. https://doi.org/10.1016/0304-5102(88)85148-4.

[33] S. Murcia-López, K. Villa, T. Andreu, J.R. Morante, Partial Oxidation of Methane to Methanol Using Bismuth-Based Photocatalysts, ACS Catal. 4 (2014) 3013–3019. https://doi.org/10.1021/cs500821r.

[34] R.F. Cotta, K.A. da Silva Rocha, E.F. Kozhevnikova, I. V. Kozhevnikov, E. V. Gusevskaya, Heteropoly acid catalysts in upgrading of biorenewables: Cycloaddition of aldehydes to monoterpenes in green solvents, Appl. Catal. B Environ. 217 (2017) 92–99. https://doi.org/10.1016/j.apcatb.2017.05.055.

[35] X. Yu, V.L. Zholobenko, S. Moldovan, D. Hu, D. Wu, V. V Ordomsky, A.Y. Khodakov, Stoichiometric methane conversion to ethane using photochemical looping at ambient temperature, Nat. Energy. 5 (2020) 511–519. https://doi.org/10.1038/s41560-020-0616-7.

[36] L. Matachowski, M. Zimowska, D. Mucha, T. Machej, Ecofriendly production of ethylene by dehydration of ethanol over Ag 3PW 12O 40 salt in nitrogen and air atmospheres, Appl. Catal. B Environ. 123–124 (2012) 448–456. https://doi.org/10.1016/j.apcatb.2012.05.003.

[37] P. Meng, H. Heng, Y. Sun, J. Huang, J. Yang, X. Liu, Positive effects of phosphotungstic acid on the in-situ solid-state polymerization and visible light photocatalytic activity of polyimide-based photocatalyst, Appl. Catal. B Environ. 226 (2018) 487–498. https://doi.org/10.1016/j.apcatb.2018.01.004.

[38] H. Wang, L. Zhang, Z. Chen, J. Hu, S. Li, Z. Wang, J. Liu, X. Wang, Semiconductor heterojunction photocatalysts: Design, construction, and photocatalytic performances, Chem. Soc.

Rev. 43 (2014) 5234–5244. https://doi.org/10.1039/c4cs00126e.

[39] M.R. Hoffmann, S.T. Martin, W. Choi, D.W. Bahnemann, Environmental Applications of Semiconductor Photocatalysis, Chem. Rev. 95 (1995) 69–96. https://doi.org/10.1021/cr00033a004.

[40] Y. Fan, W. Zhou, X. Qiu, H. Li, Y. Jiang, Z. Sun, D. Han, L. Niu, Z. Tang, Selective photocatalytic oxidation of methane by quantum-sized bismuth vanadate, Nat. Sustain. 4 (2021) 509–515. https://doi.org/10.1038/s41893-021-00682-x.

[41] A.R. Koirala, S. Docao, K.B. Yoon, Photocatalytic homolysis of methyl formate to dry formaldehyde on PdO/TiO2: Photocatalytic reverse Tishchenko reaction of methyl formate, RSC Adv. 4 (2014) 33144–33148. https://doi.org/10.1039/c4ra05744a.

[42] C.P. Kumar, N.O. Gopal, T.C. Wang, EPR Investigation of TiO 2 Nanoparticles with Temperature-Dependent Properties, (2006) 5223–5229.

[43] M. Iwamoto, K. Maruyama, N. Yamazoe, T. Selyama, Study of metal oxide catalysts by temperature programmed desorption. 2. Chemisorption of oxygen on copper(II) ion-exchanged Y-type zeolites, J. Phys. Chem. 81 (1977) 622–629. https://doi.org/10.1021/j100522a007.

[44] E. Carter, A.F. Carley, D.M. Murphy, Evidence for O2- radical stabilization at surface oxygen vacancies on polycrystalline TiO2, J. Phys. Chem. C. 111 (2007) 10630–10638. https://doi.org/10.1021/jp0729516.

[45] S. Zhu, X. Gao, F. Dong, Y. Zhu, H. Zheng, Y. Li, Design of a highly active silver-exchanged phosphotungstic acid catalyst for glycerol esterification with acetic acid, J. Catal. 306 (2013) 155–163. https://doi.org/10.1016/j.jcat.2013.06.026.

[46] R. Liu, T. Wang, C. Liu, Y. Jin, Highly selective and stable CsPW/Nb2O5 catalysts for dehydration of glycerol to acrolein, Cuihua Xuebao/Chinese J. Catal. 34 (2013) 2174–2182. https://doi.org/10.1016/s1872-2067(12)60666-4.

[47] X. Yu, S. Moldovan, V. V. Ordomsky, A.Y. Khodakov, Design of core-shell titania-heteropolyacid-metal nanocomposites for photocatalytic reduction of CO2 to CO at ambient temperature, Nanoscale Adv. 1 (2019) 4321–4330. https://doi.org/10.1039/c9na00398c.

[48] H. Shi, T. Zhang, T. An, B. Li, X. Wang, Enhancement of photocatalytic activity of nano-scale TiO2 particles co-doped by rare earth elements and heteropolyacids, J. Colloid Interface Sci. 380 (2012) 121–127. https://doi.org/10.1016/j.jcis.2012.04.069.

[49] J. RYNKOWSKI, T. PARYJCZAK, M. LENIK, Characterization of alumina supported nickel-

ruthenium systems, Appl. Catal. A Gen. 126 (1995) 257–271. https://doi.org/10.1016/0926-860X(95)00035-6.

[50] M.G. Cattania, F. Parmigiani, V. Ragaini, A study of ruthenium catalysts on oxide supports, Surf. Sci. 211–212 (1989) 1097–1105. https://doi.org/10.1016/0039-6028(89)90880-7.

[51] L. Guczi, Z. Schay, K. Matusek, I. Bogyay, Surface structure and selectivity control in the CO + H2 reaction over FeRu Bimetallic catalysts, Appl. Catal. 22 (1986) 289–309. https://doi.org/10.1016/S0166-9834(00)82637-8.

Chapter 6. General Conclusion and Perspectives

Methane, one of the most abundant molecules on Earth and a major greenhouse gas, comes from renewable and fossil resources: biogas, natural gas, coal gas, shale gas and clathrates in the ocean floors. The activation and utilization of methane as a starting material to other chemicals is attractive, but encounters numerous challenges due to high thermodynamic stability and extreme inertness of methane. Most of methane chemical reactions occur at high temperature and coincide with major emissions of CO_2. Photocatalysis has been considered as a promising way for methane conversion by renewable energy-solar energy at ambient conditions. There are three major routes of photocatalytic methane conversion: photocatalytic methane dry reforming to syngas, photocatalytic methane oxidation to methanol and photocatalytic methane coupling to ethane. This thesis mainly focuses on the photocatalytic methane oxidation and photocatalytic methane coupling, in which ethane and high value formic acid were produced with high yield and selectivity by chemical looping strategies, oxidative/non-oxidative coupling and cascade process on AgPW-TiO_2, Au/TiO_2 and CsPW-TiO_2, respectively.

6.1 General Conclusion

6.1.1 Photocatalytic methane coupling

Photocatalytic methane coupling to ethane has showed high selectivity but often encounters low yield. We demonstrate a photochemical looping strategy for highly selective methane coupling to ethane at ambient temperature over silver salt of phosphotungstic acid (AgPW)–titania nanocomposites. The efficient methane coupling requires composites which combine with intimate contact between both the cationic Ag species in phosphotunstic acid and TiO_2 components. The presence of even small amount of TiO_2 (5%) facilitates charge transfer and separation between AgPW and TiO_2 via the p-n heterojunction and significantly enhances the methane coupling. The optimized nanocomposite achieved an ethane productivity of 64 μmol g^{-1} with a coupling selectivity above 95%. The existence of cationic Ag species is critical for efficient methane activation. During methane coupling, the Ag cationic species are reduced to metallic silver and methane coupling slows down, while the metallic Ag can be re-oxidized back into Ag^+ in air under illumination at ambient temperature and regenerate methane coupling activity.

In addition, a series of Au NPs with various average sizes from 6 nm to 30 nm supported on titania have been prepared for the photocatalytic non-oxidative coupling of methane (NOCM) and oxidative coupling of methane (OCM) reactions in both batch and continuous gas flow reactors. The plasmonic effect of gold nanoparticles cannot alone drive the methane photocatalytic conversion. The methane conversion requires band gap transition in TiO2 excited by UV irradiation. Moreover, almost no gold particle size effect was observed on methane oxidative and non-oxidative coupling. The charge separation and recombination prohibition in titania are enhanced by the interaction with metallic Au NPs. We found that the catalytic conversion of methane occurred over the oxygen vacancies in titania, while oxygen was activated by gold nanoparticles. A high hydrocarbon productivity of 1864 $\mu mol\ g^{-1}\ h^{-1}$ with a coupling selectivity over 86 % was observed in the continuous gas flow process.

6.1.2 Photocatalytic methane oxidation

Methanol has been the major target product of photocatalytic methane oxidation in water. However, a mixture of methanol, methyl hydroperoxide and formaldehyde has been often produced in most photocatalytic methane oxidation process. We developed a cascade strategy achieving highly selective formic acid production from methane at ambient conditions in an environmental and sustainable way. In this strategy, the methane selective conversion into formic acid proceeds first over caesium salt of phosphotungstic acid supported on titania, which photocatalytically oxidizes methane under irradiation into a mixture of C_1 liquid oxygenates containing formic acid, formaldehyde, methyl hydroperoxide and methanol. The C_1 liquid oxygenates produced by photocatalysis are then selectively converted into formic acid over the heterogeneous alumina supported ruthenium catalyst.

Cs plays important role in stabilizing phosphotungstic acid from leaching out in the presence of water. The p-n heterojunction between CsPW and TiO_2 accelerated charge separation/transfer and enhanced methane oxidation, as more electrons and holes were available for driving reduction and oxidation reaction, respectively. Ru/Al_2O_3 selectively oxidized C_1 oxygenate mixture produced by photocatalysis into formic acid. All reactions of selective oxidation of methane to formic acid occur at room temperature in the same reactor using O_2 as oxidant. A yield of formic acid over 5000 μmol $g_{photocatalyst}^{-1}$ and a selectivity of 85% were achieved. CO_2 is the only gaseous compound in the methane oxidation. Optimisation of reaction conditions allows synthesis of HCOOH solution with a concentration of 1.1 mmol/L.

6.2 Perspectives

Despite the major development in photocatalysis, most semiconductor materials encounter low efficiency in light harvesting, especially for visible light utilization. More stable, efficient, and clean semiconductor materials are urgently required to be developed. The photocatalysis is a rather complex process, better understanding of the semiconductor materials as well as the reaction mechanism in photocatalytic process are needed for further studies. In addition, the optimization of photo-reactor and new photocatalytic reactions also requires more development.

6.2.1 Photocatalytic methane conversion

There are three major routes for photocatalytic methane conversion: photocatalytic methane dry reforming to syngas, photocatalytic methane oxidation to methanol and photocatalytic methane coupling. The methane oxidation has been extensively studied as it has higher productivity and efficiency. Among different oxidation processes, methane partial oxidation to methanol and methane complete oxidation to CO_2 have attracted particular attention. The complete oxidation of methane to CO_2 seems to be an attractive option to reduce the concentration of methane present in the atmosphere. Note that methane is a GHG, which is 30 times more potent than carbon dioxide. Methane photocatalytic oxidation is an exothermic process. The methane photocatalytic oxidation to CO_2 can reduce, on the one hand, global warming and on other hand, because of the exothermic effect, it can produce renewable electricity under mild conditions.

The current scientific immaturity of the methane photochemical conversion processes does not allow to envision industrial or practical utilization in the near future. Among the discussed methane photocatalytic conversion routes to value-added chemicals, the most promising could be photocatalytic methane oxidation to methanol, formaldehyde, and formic acid. As they are valuable platform molecule and they have much higher cost compared to ethane produced by methane coupling or to syngas, which is manufactured by methane reforming. The separation of methane and products of methane photocatalytic conversion can be only feasible for practical purposes if the yield of target products can reach a few per cent. Another challenge is the stability of photocatalysts, though it has been rarely addressed in most of publications.

Direct mild conversion of methane is one of the main targets in the modern society. The photochemical processes such as methane partial oxidation, methane reforming and methane coupling should provide opportunities to perform methane conversion to value-added products, under mild conditions, instead of methane combustion. This should significantly decrease the GHG effects due to the uncontrollable emission of methane and carbon dioxide and will contribute to the optimized utilization of fossil and renewable methane feedstocks.

6.2.2 Development of new efficient photocatalysts

The highest apparent quantum yield (AQY) reported in photocatalytic methane conversion has been 60% over Pt/black TiO_2[1], but the majority of photocatalysts have exhibited a much lower AQY, some even less than 10%. By contrast, a high AQY is commonly reported in other photocatalytic processes, in particular, for water splitting (up to 96%, $350 < \lambda < 360$ nm)[2], indicating that significant improvement is needed for photocatalytic methane conversion. There are a few strategies to address this problem, beginning with the optimization of the most promising photocatalysts reported for analogous processes (water splitting, CO_2 conversion, nitrogen reduction) for methane conversion. Types of photocatalysts other than inorganic materials can also be explored. Emerging polymeric photocatalysts, including graphitic carbon nitride, covalent triazine frameworks and covalent organic frameworks, have already shown enormous potential, owing to their light absorption properties, band structure and surface characteristics, which can all be easily tuned by molecular engineering[3]. Based on the needs of the specific experiment, the catalyst structure can also be modified through the construction of hierarchical structures, facet control, size adjustments and interface chemistry[4].

Co-catalysts play a pivotal role in manipulating products' yield and selectivity. Although the reported co-catalysts cover a wide field, including nanoparticles, clusters and single atoms, the function of the real active sites and the reaction steps on each type of active site are still ambiguous. Understanding the function of single-atom materials in both photocatalytic and thermocatalytic reactions is expected to assist the development of economical co-catalysts for photocatalytic methane conversion; a few examples of single-atom co-catalysts have been reported in photocatalytic methane conversion, such as single Ru atoms on plasmonic Cu for DRM[5]. On the other hand, a single-component co-catalyst may not meet the requirement of organic synthesis from methane, owing to the diversity of the products. Therefore, the field is trending towards combining multiple components with complementary functions. Mixing single Pt atoms with Pt_n clusters provides balanced activity and durability for the water–gas shift reaction[6], for example, suggesting that such a combination may be an attractive strategy for co-catalyst design in methane conversion.

6.2.3 Reaction system design

Currently, the majorities of photocatalytic methane conversion reactions are carried out in home-made or commercial batch reactors with various volumes. Relatively high residence time in batch reactors leads to the over-oxidation of the methane conversion intermediates. Design of new photoreactors with continuous operation such as fluidized, slurry, fixed bed, membrane, optical-fiber, monolith or internally illuminated monolith photoreactors can also enhance the efficiency of light collection, exposure of the photocatalyst to the irradiation, heat and mass transfer. Most of available results were obtained with a tiny amount of catalyst (a few mg). The scale up seems to be a major challenge for most of photocatalytic processes. Particular attention should be paid to the efficient light collection, precise temperature control and absence of even very tiny leaks. Uncontrollable temperature increase can strongly contribute to the rate of photocatalytic reactions. Even a very small amount of excess oxygen can affect the reaction rate and selectivity.

6.3 References

[1] B. Han, W. Wei, M. Li, K. Sun, Y.H. Hu, R. Li, / Chemcomm, C. Communication, A thermo-photo hybrid process for steam reforming of methane: Highly efficient visible light photocatalysis, Chem. Commun. 55 (2019) 7816–7819. https://doi.org/10.1039/c9cc04193a.

[2] T. Takata, J. Jiang, Y. Sakata, M. Nakabayashi, N. Shibata, V. Nandal, K. Seki, T. Hisatomi, K. Domen, Photocatalytic water splitting with a quantum efficiency of almost unity, Nature. 581 (2020) 411–414. https://doi.org/10.1038/s41586-020-2278-9.

[3] Y. Wang, A. Vogel, M. Sachs, R.S. Sprick, L. Wilbraham, S.J.A. Moniz, R. Godin, M.A. Zwijnenburg, J.R. Durrant, A.I. Cooper, J. Tang, Current understanding and challenges of solar-driven hydrogen generation using polymeric photocatalysts, Nat. Energy. 4 (2019) 746–760. https://doi.org/10.1038/s41560-019-0456-5.

[4] C. Xie, Z. Niu, D. Kim, M. Li, P. Yang, Surface and Interface Control in Nanoparticle Catalysis, Chem. Rev. 120 (2020) 1184–1249. https://doi.org/10.1021/acs.chemrev.9b00220.

[5] L. Zhou, J.M.P. Martirez, J. Finzel, C. Zhang, D.F. Swearer, S. Tian, H. Robatjazi, M. Lou, L. Dong, L. Henderson, P. Christopher, E.A. Carter, P. Nordlander, N.J. Halas, Light-driven methane dry reforming with single atomic site antenna-reactor plasmonic photocatalysts, Nat. Energy. 5 (2020) 61–70. https://doi.org/10.1038/s41560-019-0517-9.

[6] X. Zhang, M. Zhang, Y. Deng, M. Xu, L. Artiglia, W. Wen, R. Gao, B. Chen, S. Yao, X. Zhang, M. Peng, J. Yan, A. Li, Z. Jiang, X. Gao, S. Cao, C. Yang, A.J. Kropf, J. Shi, J. Xie, M. Bi, J.A. van Bokhoven, Y.W. Li, X. Wen, M. Flytzani-Stephanopoulos, C. Shi, W. Zhou, D. Ma, A stable low-temperature H2-production catalyst by crowding Pt on α-MoC, Nature. 589 (2021) 396–401. https://doi.org/10.1038/s41586-020-03130-6.

Author Introduction

Di Hu was born in October 1994 in Wuhan City, Hubei Province, China. He received his bachelor’s degree in chemical engineering and technology from Jianghan University in June 2016. Shortly, he did undergraduate research under the supervision of Prof. Lin Li focused on the methane dry reforming into syngas over supported nickel nanoparticles with anti-coke and sintering resistance, in the Key Laboratory of Catalysis and Energy Materials Chemistry of Ministry of Education & Hubei Key Laboratory of Catalysis and Materials Science, South-Central University for Nationalities. Hereafter, he received his master's degree in chemical engineering from South-Central University for Nationalities in June 2019.

In September 2019, he started the PhD programs which was sponsored by the China scholarship Council studying at Unité de Catalyse et Chimie du Solide (UCCS, UMR 8181), Université de Lille, France. His PhD thesis was supervised by Dr. Andrei Khodakov and Dr. Vitaly Ordomsky. His PhD research focuses on the photocatalytic methane conversion into chemicals and fuels under ambient conditions.

List of papers during PhD

1. **Hu, D.**, Ordomsky, V. V., Khodakov, A. Y. Major routes in the photocatalytic methane conversion into chemicals and fuels under mild conditions. *Appl. Catal. B: Environ*. 286, 119913 (2021).
2. **Hu, D.**, Addad, A., Ben Tayeb, K., Ordomsky, V. V., Khodakov, A. Y. Beyond the selectivity limit in the photocatalytic oxidation of methane to formic acid at room temperature: Contribution of chemocatalysis. *Angew. Chem. Int. Ed. Submitted*.
3. **Hu, D.**, Belhout, S., Dong, C., Shetty, S., Ng, H., Brasseur, P., Bezerra, L. S., Ben Tayeb, K., Virginie, M., Wojcieszak, R., Ordomsky, V. V., Camargo, P., Khodakov, A. Y. Smaller and larger gold nanoparticles supporte on titania for selective photocatalytic methane coupling at ambient temperature. *ACS Catal. Submitted.*

Conference paper

4. **Hu, D.**, Ordomsky, V. V., Khodakov, A. Y. Cascade photo-chemo-catalytic process for selective methane oxidation to formic acid at ambient temperature. Netherland’s Catalysis and Chemistry Conference (NCCC), Netherland, 2022, poster.
5. **Hu, D.**, Ordomsky, V. V., Khodakov, A. Y. Breaking selectivity limits in the photocatalytic oxidation of methane to formic acid: Contribution of chemocatalysis. French Conference on Catalysis (FCCat), France, 2022, oral presentation.

Acknowledgement

The completion of the thesis is attributed to the support of many people and their company. First and foremost, I would like to appreciate the patient guidance, insightful suggestion, and constant encouragement from my supervisor, Dr. Andrei Khodakov and Dr. Vitaly Ordomsky. They gave me plenty of help, advice, and instruction during the whole process of my PhD in experiments, paper writing and other scientific activities. Their conscientious academic spirit and modest, open-minded personality inspire me both in academic study and daily life. Also, I would like to thank the researchers and professors in the UCCS, Institute Chevreul, University of Lille, Centrale Lille, University of Helsinki, Jerzy Haber Institute of Catalysis and Surface Chemistry and Polish Academy of Science for their professional instruction, devoted collaboration, and kind help in academic research.

Additional, thanks to the China Scholarship Council for providing me a PhD stipend. Thanks to the French National Research Agency and the ANR SolarMethaChem project (ANR-20-SODR-0002) supporting the research. Thanks to the French government for the living welfare allowance.

Last but not least, I would like to express my heartfelt gratitude to my parents, Mr. Rongsheng Hu and Ms. Jiaxi Fan and the people ever accompanied and helped me.

Time flies, but the memories are so deep. Thanks to all the precious moments.

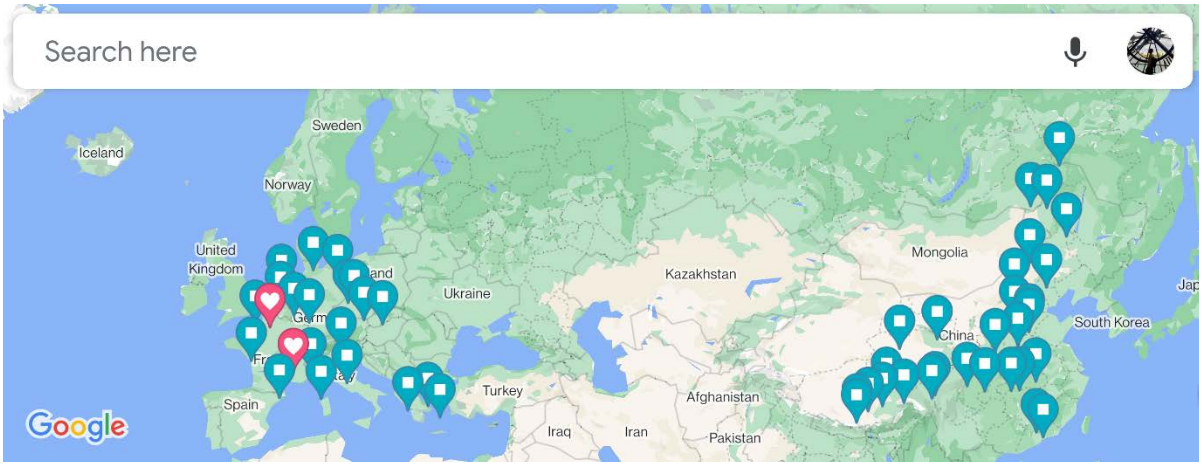
Search here
Sweden
Iceland
Norway
United Kingdom
Ukraine
Kazakhstan
Mongolia
South Korea
China
Turkey
Afghanistan
Spain
Iraq
Iran
Pakistan
Google